Novel Methods and Applications of Weak Measurements in Optics

Thomas Bailey

A thesis submitted to the University of Ottawa in partial fulfillment of the requirements of

Doctorate in Philosophy degree in Physics

Under the supervision of
Prof. Jeff S. Lundeen

uOttawa
Department of Physics
Faculty of Science
University of Ottawa

Contents

List of Tables

List of Figures

Legend

List of Abbreviations

Abbreviation	Definition
BCH	Baker-Campbell-Hausdorff
DBR	Distributed Bragg Grating
FWHM	Full Width Half Maximum
GPU	Graphics Processing Unit
HWP	Half Waveplate
KD	Kirkwood-Dirac
LCOS	Liquid Crystal on Silicon
NPBS	Non-Polarizing Beam Splitter
N-POVM	Non-Positive Operator-Valued Measure
PBS	Polarizing Beam Splitter
PD	Photodiode
POVM	Positive Operator-Valued Measure
QWP	Quarter Waveplate
SLM	Spatial Light Modulator
SPDC	Spontaneous Parametric Down Conversion

List of Symbols

Symbol	Description
$\mathbb{1}$	The identity.
$\hat{A}$	Generic observable operator.
A_w	The weak value of the observable $\hat{A}$.
$\lvert A\rangle$	Anti-diagonal polarized state.
$\hat{a}$	Lowering/annihilation operator for mode a.
$\hat{a}^\dagger$	Raising/creation operator for mode a.
$\lvert\alpha\rangle$	A coherent state with amplitude α.
$\hat{B}$	Generic observable operator.
$\hat{b}$	Lowering/annihilation operator for mode b.
$\hat{b}^\dagger$	Raising/creation operator for mode b.
$\lvert\beta\rangle$	A coherent state with amplitude β.
$\hat{c}$	Lowering/annihilation operator for mode c
$\hat{c}^\dagger$	Raising/creation operator for mode c.
$\chi^{(n)}$	The n^{th} order nonlinear electric susceptibility.
$\hat{d}$	Lowering/annihilation operator for mode d
$\hat{d}^\dagger$	Raising/creation operator for mode d.
$\lvert D\rangle$	Diagonal polarized state.
E	Electric field amplitude.
$\hat{E}_k$	The effect for outcome k.
f	Focal length of a lens.
$\lvert f^k\rangle$	The pointer state corresponding to measurement outcome k.
G	Coupling strength of a strong interaction.
g	Coupling strength of an interaction.
$\lvert\gamma\rangle$	A coherent state with amplitude γ.
$\lvert H\rangle$	Horizontal polarized state.

Continued on next page

(Continued)

Symbol	Description
$\hat{\mathcal{H}}$	A Hamiltonian operator.
$\hbar$	Reduced Planck constant, $\hbar = 1.055 \times 10^{-34}\,\mathrm{J\,s}$.
I	Intensity.
$\mathcal{J}$	Translation operator.
$\hat{K}_k$	The Kraus operator corresponding to measurement outcome k.
k	The wavenumber of light. May refer to the total wavenumber or the transverse component.
κ	Coupling strength of an interaction.
$\|L\rangle$	Left circular polarized state.
λ	Wavelength.
$\hat{M}$	Count operator.
n	Either number of photons or the refractive index.
$\hat{n}$	The number operator for a quantum harmonic oscillator.
$\|n\rangle$	A number state with n photons.
$\hat{O}$	Generic observable operator.
ω	Angular frequency.
Ω	Block matrix.
$\hat{p}$	Momentum operator.
p_k	The probability of the outcome k.
$\|\mathcal{P}\rangle$	The ket for the initial pointer state.
ϕ	Typically a phase. Occasionally can refer to a different angle.
$\hat{\pi}_\lambda$	Projector operator for state $\|\lambda\rangle$.
$\|\Psi\rangle$	The ket for the total quantum system.
$\|\psi\rangle$	The ket for a quantum state. Typically the state being measured.
$\|\psi_i\rangle$	The system state before measurement.
$\|\psi_f\rangle$	The postselected state.
$\hat{q}$	Canonical momentum or field quadrature operator.

Continued on next page

(Continued)

Symbol	**Description**
r	Squeezing strength.
$\|R\rangle$	Right circular polarized state.
$\hat{\rho}$	The density matrix.
S	Symplectic matrix.
σ	Standard deviation.
$\hat{\sigma}$	Pauli matrix.
t	Thickness of a glass sliver.
θ	An angle.
$\hat{U}$	Unitary operator.
$\|V\rangle$	Vertical polarized state.
x	Horizontal transverse position.
$\hat{X}$	Dimensionless field quadrature.
y	Vertical transverse position.
$\hat{Y}$	Dimensionless field quadrature.

0.1 Abstract

As quantum technologies grow in complexity, the need for efficient, non-destructive measurement schemes become increasingly important. Photonic systems, while in many ways ideal for quantum information processing, offer only a limited number of degrees of freedom per mode – placing fundamental restrictions on the number and type of observables that can be simultaneously accessed. Weak measurement provides a framework to circumvent some of these limitations, enabling joint measurements, minimal back-action, and alternative pathways for quantum state characterization.

This thesis presents two contributions to the theory and implementation of weak measurements in optics. First, we design, simulate, and experimentally realize a scheme to measure joint weak values of position and momentum projectors – building on Lundeen and Bamber's framework. We employ a glass sliver to weakly measure x position and use a spatial light modulator (SLM) to couple polarization to x momentum in a way that the strength this interaction is conditional on the y position. We show that a binary conditionality is able to achieve the same results as the linear conditionality initially proposed, while enabling simpler setups and larger signals.

Second, we analyze how weak interactions arising from bulk optical nonlinearities can be harnessed for quantum measurements. Using both the von Neumann and Positive Operator-Valued Measure (POVM) formalisms, we explore a range of nonlinear processes. We identify that information about photon number and field quadratures are accessible via nonlinear interactions, and propose that certain POVM based schemes may offer practical alternatives to standard homodyne detection of field quadratures.

This work contributes to the ongoing development of quantum measurement techniques in optics and presents how weak measurements provide a useful framework in which to consider alternative measurement schemes.

THIS TEXT HAS BEEN MACHINE TRANSLATED
USING ChatGPT & DeepL

À mesure que les technologies quantiques gagnent en complexité, le besoin de schémas de mesure efficaces et non destructifs devient plus crucial. Les systèmes photoniques, bien que souvent idéaux pour le traitement de l'information quantique, n'offrent qu'un nombre limité de degrés de liberté par mode — imposant ainsi des restrictions fondamentales sur le nombre et le type d'observables accessibles simultanément. La mesure faible offre un cadre permettant de contourner certaines de ces limitations, en rendant possibles les mesures conjointes, un effet de retour minimal, et de nouvelles approches pour la caractérisation des états quantiques.

Cette thèse présente deux contributions à la théorie et à la mise en œuvre des mesures faibles en optique. Premièrement, nous concevons, simulons et réalisons expérimentalement un schéma pour mesurer les valeurs faibles conjointes des projecteurs de position et de quantité de mouvement – en nous appuyant sur le cadre de Lundeen et Bamber. Nous utilisons un éclat de verre pour mesurer faiblement la position x et un modulateur spatial de lumière (MSL) pour coupler la polarisation à quantité de mouvement de manière conditionnelle selon la position y. Nous montrons qu'une conditionnalité binaire permet d'obtenir les mêmes résultats qu'une conditionnalité linéaire, tout en simplifiant le montage et en amplifiant le signal.

Deuxièmement, nous analysons comment les interactions faibles issues des non-linéarités optiques en volume peuvent être exploitées pour des mesures quantiques. En utilisant les formalismes de von Neumann et des mesures à valeurs d'opérateurs positifs (POVM), nous explorons divers processus non linéaires. Nous montrons que des informations sur le nombre de photons et les quadratures du champ peuvent être extraites via ces interactions, et proposons que certains schémas basés sur les POVM pourraient offrir des alternatives pratiques à la détection homodyne.

Ce travail contribue au développement des techniques de mesure quantique en optique et souligne l'utilité du cadre des mesures faibles.

0.2 Acknowledgments

I would like to thank my supervisor, Professor Jeff Lundeen, for his invaluable guidance, support, and for fostering an open and productive research environment. His mentorship has been instrumental in shaping both this thesis and my development as a researcher.

I am deeply grateful to all members of the Lundeen Lab for forming such a collaborative and supportive team. Special thanks to Raphael Abrahao and Michael Weil, whose insightful ideas and constructive feedback significantly enhanced the quality of this research.

I extend my appreciation to the entire CERC group for their generosity in sharing equipment, organizing enlightening weekly talks, and bringing us together for social activities that provided much-needed breaks from research. Similarly, I wish to thank the Physics Graduate Student Association (PGSA) and the Optica/SPIE student chapter for providing me with opportunities to contribute more broadly to the department.

I am also grateful to the Ottawa Science Policy Network and Support Our Science for the opportunities to broaden my expertise outside of physics and engage more deeply with Canadian society.

I would like to thank Professor Jeff Lundeen and Professor Michele Godin for being exceptional teaching assistantship supervisors. Their guidance and support made my teaching experiences truly rewarding and helped me develop valuable skills in education and communication.

For their assistance with this thesis specifically, I am thankful to Arman Mansouri and Michael Weil, who provided thoughtful feedback on the introduction, and to my mother, who meticulously reviewed the entire thesis line by line.

I acknowledge the use of generative AI tools, including OpenAI's ChatGPT, Anthropic's Claude, Alphabet's Gemini, and xAI's Grok, which assisted in generating initial ideas for code segments, diagrams, and section summaries throughout the writing process.

All source files used in this thesis can be found at: `https://gitlab.com/tjbailey/phd-thesis`.

0.2.1 Author Contributions

The research presented in this thesis represents collaborative efforts with several contributors, whose specific contributions are:

Professor Jeff Lundeen provided conceptualization for the projects in both Chapter 2 and Chapter 3. He was involved in discussions throughout the entirety of the research process and provided critical guidance at key decision points.

Dr Raphael Abrahao contributed to discussions during the work described in Section 3.1 and Section 3.2. He was also involved in the initial design of the experiment detailed in Chapter 2.

Michael Weil was involved in discussions during the final stages of the conditional weak measurement project. He collected the data and performed the analysis of the direct camera measurements presented in this work.

Kyle Jordan suggested that using two pumps could enable a Hamiltonian of the correct form in Section 3.1.6.

Throughout this thesis, I have clearly noted when presenting theoretical results developed by others. Unless otherwise stated, I was responsible for all other aspects of the research, including experimental design, data collection, analysis, and the writing of this thesis.

0.2.2 Financial Support

This research would not have been possible without financial support from the Natural Sciences and Engineering Research Council of Canada (NSERC) through Professor Lundeen's research grants. I also gratefully acknowledge the University of Ottawa for its financial support throughout my doctoral studies.

0.3 Preface

This thesis represents a journey that, like many in experimental physics, did not unfold as initially envisioned. While I had hoped to produce definitive experimental results demonstrating the conditional weak measurement scheme before submitting, the path proved more challenging than anticipated.

The experimental work described in these pages encountered several substantial technical obstacles. Pervasive interference effects in the beam made it challenging to determine the source of errors and correct the setup. A critical component in our setup, the cylindrical lenses, are a much more specialized component than standard spherical lenses and generally seemed to underperform. A number of different lenses had to be tried before we found a set that seemed to perform adequately. We also made use of a spatial light modulator in the zeroth order. Not only does this mode of operation have more challenges than more typical usage, but the SLM often failed to act reproducibly and required extensive calibration procedures. Perhaps most fundamentally, we faced the intrinsic challenge of detecting and characterizing a signal that was, by design, exceedingly small and only at a relatively late stage did we determine an approach that would enable this to be significantly larger.

These technical challenges were compounded by circumstances that limited collaborative work. The COVID-19 pandemic limited how collaborative the project was from its start, and contributed to several years where I worked largely independently on the experimental aspects of this research. While the Lundeen lab consistently provided an intellectually stimulating and supportive environment, the direct day-to-day collaboration that often accelerates experimental progress was limited during this period. Since Michael Weil began actively collaborating on this project in the summer of 2024, our progress accelerated significantly, underscoring the value of sharing and discussing ideas in experimental physics.

Chapter 1

Introduction

As the ‘second quantum revolution’ [1] continues, the need for new techniques to measure and observe quantum systems has never been more important. Optics, in particular, remains a compelling platform for quantum technologies, especially due to the natural advantage of photons to fulfill the DiVincenzo criterion [2] of decoherence and their ease to be used as flying qubits.

Many techniques have already been developed to measure different observables of photonic systems. For instance, the use of diffraction gratings [3] or chromatic dispersion [4] to measure frequency; or polarizing beam splitters [3] to measure polarization. However, these techniques are typically destructive – with the photon absorbed by a detector. This means that for each observable, a different internal degree of freedom of the photon must be used (see Section 1.1.1). Quantum non-demolition measurements [5–7], where a property can be observed without the destruction of the photon, would overcome this limitation. Demonstrations of quantum non-demolition measurements have largely been focused on using strong optical fields or systems with large optical nonlinearities (such as atoms in a cavity). This limits the range of photonic systems where these techniques are feasible. Therefore, alternative techniques that either enable a more efficient use of the internal degrees of freedom of a photon, or which are able to make use of bulk material nonlinearities are desired.

One approach is to consider weak measurements (see Section 1.1.2). Since the nonlinearities in bulk materials are typically small [8], any measurement that is able to make use of these nonlinearities would, inevitably, be weak. Alternatively, weak measurements could allow for a more efficient use of the internal degrees of freedom of a photon when measuring ‘compound observables’, such as a joint value $\langle \hat{A}\hat{B} \rangle$. Using weak measurements also provides advantages such as being able to monitor the evolution of a system over time through the use of quantum trajectories [9].

Joint expectation values are particularly valuable in quantum technologies because they encode information about correlations between different degrees of freedom that is fundamentally inaccessible from separate measurements of $\langle \hat{A} \rangle$ and $\langle \hat{B} \rangle$. Measurements of this type can be used for quantum state characterization, enabling the characterization of correlations between observables to reconstruct phase-space distributions such as the Wigner or Kirkwood-Dirac distributions. These can reveal non-classical features [10, 11] and be used to verify quantum algorithm outputs and diagnose state preparation errors [12]. In addition, entanglement quantification relies on joint measurements between systems [13] – for example, Bell inequality violations that can certify secure quantum communication channels are measured through correlators between observables [14].

This thesis covers two projects: an experiment to demonstrate a conditional scheme for measuring the joint value of two observables (Chapter 2), and a theoretical analysis of the use of bulk optical nonlinearities to perform quantum measurements (Chapter 3). The remainder of this chapter will provide an overview of the fundamentals of quantum measurement and optics used in the two projects.

The introduction is structured as follows:

- Section 1.1: Quantum Measurement – Presents the von Neumann measurement formalism, weak measurements, and Positive Operator-Valued Measures (POVMs), providing the theoretical foundation for both the joint weak averages in Chapter 2 and the nonlinear measurement approach in Chapter 3.
- Section 1.2: Optics – Discusses optical degrees of freedom relevant to both projects and the theory of the propagation of light used to design the experiment in Chapter 2.
- Section 1.3: Quantum Optics – Examines the quantum harmonic oscillator, field quantization, quantum states of light, quantum phase operators, and nonlinear quantum optics operators, establishing the theoretical framework essential for the bulk optical nonlinearities analyzed in Chapter 3.
- Section 1.4: Quasi-probability Distributions – Introduces Wigner and Kirkwood-Dirac distributions, which are used to motivate and interpret the measurements made by the experiment in Chapter 2.

1.1 Quantum Measurement

A quantum measurement is a process whereby some classical information about a quantum system is obtained, often by coupling to another quantum system. This is a broad definition, which will be outlined in a more formal way in Section 1.1.3.

However, the formalism of projective measurement is often used, where an observable of a system is measured. An observable is described by a Hermitian operator, $\hat{O}$, which can be diagonalized as a set of projector operators, $\hat{\pi}_\lambda$ [15, 16]:

$$\hat{O} = \sum_\lambda \lambda \hat{\pi}_\lambda \,. \tag{1.1}$$

When the eigenvectors of the operator, $\hat{O}$, are non-degenerate, $\hat{\pi}_\lambda = |\lambda\rangle\langle\lambda|$ projects onto the state with eigenvalue λ.

'Measuring an observable' can correspond to two possible actions. One is a 'single shot' – where a specific eigenvalue is found for the system. The probability, p_λ, to measure each particular eigenvalue is dependent on the quantum state, $|\psi\rangle$, according to $p_\lambda = \langle\psi|\hat{\pi}_\lambda|\psi\rangle$. An example of this kind of measurement is whether an individual electron is deflected up or down in the Stern-Gerlach experiment [16, 17].

The other meaning of 'measuring an observable' is to find the observable's expectation value:

$$\langle\hat{O}\rangle = \langle\psi|\hat{O}|\psi\rangle = \sum_\lambda \lambda\langle\psi|\hat{\pi}_\lambda|\psi\rangle \,. \tag{1.2}$$

This is the weighted average of the measured eigenvalues if the 'single shot' measurement was repeated many times.

For clarity, in this introduction the second of these will be referred to as *finding the expectation of an observable* and the 'single shot' measurement will be called *measuring an observable.*

1.1.1 The Von Neumann Formalism

The standard definition of a projective measurement, as stated above, is somewhat limited. It is unable to account for classical uncertainty and implies that after measurement the system is in an eigenstate of the observable (when in many cases – especially for light – the measurement process is more destructive).

One approach to overcome these issues is to make use of an additional quantum system, called the pointer [18]. In this thesis, this approach will be referred to as *the von Neumann formalism of quantum measurement* (in contrast to other sources, such as [15], which use that term to refer to the projective measurements outlined above).

In this framework of measurement, the world is split into 3 parts: I, the quantum system being measured, $|\psi\rangle$; II, the measuring instrument (pointer); and III, the observer. Before the measurement, II is initialized into some state. This state can be a classical mixture of different quantum states to account for classical uncertainty. The measurement itself then proceeds in two steps. In the first, I and II interact to displace the 'position' of II by an amount that corresponds to the value of the observable being measured. In the second step, III performs a projective measurement of the 'position' of II. It is from this 'position' measurement, that information about the initial state of I can be inferred.

The interaction between I and II can be described by a unitary (as can all evolutions of a closed quantum system [19, 20]). For the 'position' of the pointer (II) to correspond to a particular observable, the unitary must have the form:

$$\hat{U} = \mathrm{e}^{-ig\hat{p}\hat{O}/\hbar}\,, \tag{1.3}$$

where $\hat{O}$ is the observable to be measured, p is the canonical momentum of the pointer system, and g is a parameter that describes the strength of the interaction. This is very similar to the translation operator, $\mathscr{J}$, for a translation of $\Delta x'$ in the $\hat{\mathbf{x}}$ direction [20]:

$$\mathscr{J}(\Delta x'\hat{\mathbf{x}}) = \exp\left(-\frac{ip_x\Delta x'}{\hbar}\right)\,. \tag{1.4}$$

Hence the unitary results in a displacement of the canonical pointer position, q, by an amount equal to $g\hat{O}$. This is an abuse of notation, with $\hat{O}$ being an operator and not any specific value. However, since this is an entirely coherent process entangling I and II, the displacement of the pointer 'position' does not 'collapse' until the projective measurement by III, as outlined below.

When the state being measured (I) is represented in the basis of the observable eigenstates, $|\psi\rangle = \sum_\lambda c_\lambda|\lambda\rangle$, and the pointer is intitalized as a pure state, $|\mathcal{P}\rangle$, the combined state of I and II before the interaction can be written as:

$$|\Psi\rangle = \mathcal{P}(q) \otimes \sum_\lambda c_\lambda|\lambda\rangle\,, \tag{1.5}$$

where $\mathcal{P}(q)$ is the initial wave function of the pointer, c_λ are the amplitudes of the measured state (I) when expressed in the basis of observable eigenstates, $|\lambda\rangle$.

After the unitary interaction, the combined system of I and II will then be in state:

$$\begin{aligned}
|\Psi'\rangle = \hat{U}|\Psi\rangle &= \mathrm{e}^{-ig\hat{p}\hat{O}/\hbar} \sum_\lambda c_\lambda \left(\mathcal{P}(q) \otimes |\lambda\rangle\right) \, , \\
&= \mathcal{J}(g\hat{O}) \sum_\lambda c_\lambda \left(\mathcal{P}(q) \otimes |\lambda\rangle\right) \, , \\
&= \sum_\lambda c_\lambda \left(\mathcal{J}(g\hat{O})\mathcal{P}(q) \otimes |\lambda\rangle\right) \, , \\
&= \sum_\lambda c_\lambda \left(\mathcal{P}(q - g\lambda) \otimes |\lambda\rangle\right) \, .
\end{aligned} \tag{1.6}$$

For a 'single shot', the pointer displacement will be measured to be an eigenvalue of $\hat{O}$ rescaled by g (assuming that there is no initial uncertainty in the pointer position), with the probability $|c_\lambda|^2$ to measure the displacement corresponding to the eigenvalue λ.

When repeated many times the expectation of the pointer's displacement will be found to be:

$$\Delta q = \sum_\lambda g|c_\lambda|^2\lambda = g\langle\hat{O}\rangle \, . \tag{1.7}$$

An example of this process is illustrated in Figure 1.1.

1.1.2 Weak Measurement

In the above scheme, it is generally implied that any uncertainty (whether classical or quantum) in the pointer position is smaller than the difference in displacement caused by two adjacent eigenvalues of $\hat{O}$. This means that each eigenvalue can be distinguished by a projective measurement of the pointer position. This will be referred to as a *standard quantum measurement*.

However, there is no need for this to be the case. If the uncertainty in the pointer position is large, or if the pointer displacement is small, then it will no longer be possible to make an unambiguous measurement of the observable eigenvalue. However, the expectation of the observable can still be found in the same way – Equation 1.7 still applies but now with a smaller value of g [21]. This means that, to obtain the same level of confidence in the expectation estimate, many more 'single shot' measurements must be performed. For measurements of this type, the expectation value is sometimes called the *weak average*. These

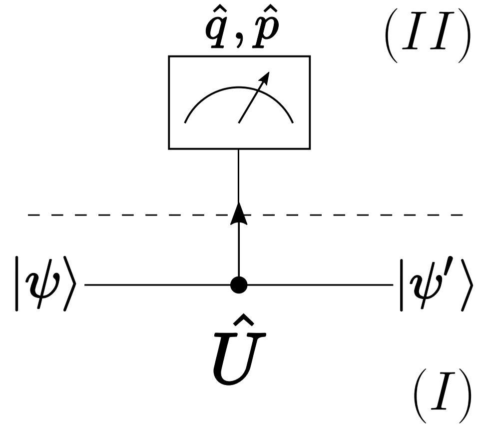

Figure 1.1: A quantum system (I), represented here by $|\psi\rangle$, interacts with a pointer (II) in a way described by the unitary operator $\hat{U}$. The pointer 'position', q, is displaced and the quantum system is modified in someway by the interaction to give $|\psi'\rangle$.

unpostselected measurements also require detection of very small changes to the pointer position, making them particularly sensitive to experimental noise.

Another consequence of performing these weak measurements is that the back-action – the change caused to the system by the process of measurement – on the measured state can be reduced. Since reading out the pointer no longer results in the state collapsing into an eigenstate of $\hat{O}$, after measurement there can still be significant information about the original state. As the strength of the measurement (parameterized by g) goes to zero, the state after the measurement will become indistinguishable from the state before as no information has been extracted (see Figure 1.2 for an illustration). This in no way violates the uncertainty principle – each weak measurement yields only a very imprecise estimate of the observable, with correspondingly large uncertainty.

The reduced back-action does allow sequences of measurements to be considered that would not be of interest within standard quantum measurements. For instance, performing sequential weak measurements of two incompatible observables (such as position and momentum) provides information about both [22], while for a standard measurement only information about the first observable would be found.

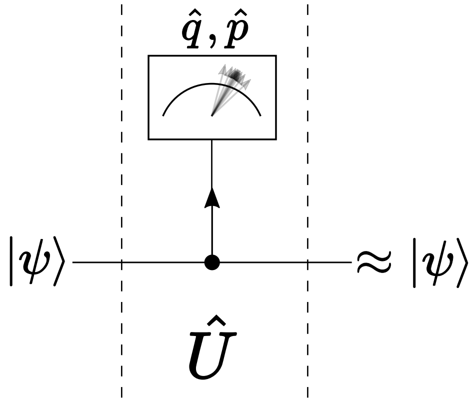

Figure 1.2: A quantum system, represented here by $|\psi\rangle$, interacts weakly with a pointer in a way described by the unitary operator $\hat{U}$. The pointer 'position', q, is displaced by an amount much less than its uncertainty, and the quantum system is minimally modified by the interaction.

Weak Values

One area where weak measurements are often performed is in the context of postselection, where only a subset of possible outcomes are considered. In particular, the concept of a weak value occurs when postselecting on a particular state of the system after measurement.

First introduced by Aharonov, Albert and Vaidman in 1988 [21] (under the provocative title "How the result of a measurement of a component of the spin of a spin-1/2 particle can turn out to be 100"), weak values can result in some counter intuitive results – such as weak values larger than the result of any single measurement of the corresponding operator, or which are complex.

This initially created controversy [23, 24], especially to what degree these weak values are 'measurements' in the normal understanding of the word. However, weak values have proven themselves as a tool to amplify small physical effects in precision experiments [25, 26] and making use of their complex nature to determine additional information about a system [22, 27–29]. The practical advantages of weak value based schemes are still limited, though in some situations, such as in the presence of certain types of noise [30], there appear to be some.

The expression for the weak value is given by [21]:

$$O_w = \frac{\langle\psi_f|\hat{O}|\psi_i\rangle}{\langle\psi_f|\psi_i\rangle}\,, \tag{1.8}$$

where $|\psi_i\rangle$ is the state before measurement, $|\psi_f\rangle$ is the state postselected onto after measurement, and $\hat{O}$ is the observable being measured in each shot.

The 'anomalous' weak values, larger than the result of any single measurement of the corresponding operator, occur when there is limited overlap between $|\psi_i\rangle$ and $|\psi_f\rangle$, resulting in the denominator being a very small value.

We can show that the pointer displacement is given by this weak value by starting from Equation 1.6 and postselecting by a state $|\psi_f\rangle = \sum_\lambda d_\lambda |\lambda\rangle$, to find that the pointer state after the postselection is:

$$\langle\psi_f|\Psi'\rangle = \sum_\lambda c_\lambda d_\lambda^* \mathcal{P}(q - g\lambda)\,. \tag{1.9}$$

If we now Taylor expand the wave function of the pointer we get:

$$\mathcal{P}(q - g\lambda) = \mathcal{P}(q) - g\lambda\mathcal{P}'(q)\,. \tag{1.10}$$

This then gives a pointer state after the postselection of:

$$\langle\psi_f|\Psi'\rangle = \sum_\lambda c_\lambda d_\lambda^* \left(\mathcal{P}(q) - g\lambda\mathcal{P}'(q)\right)\,. \tag{1.11}$$

When we express the weak value, O_w, in the λ basis we see:

$$O_w = \frac{\langle\psi_f|\hat{O}|\psi_i\rangle}{\langle\psi_f|\psi_i\rangle} = \frac{\sum_\lambda c_\lambda d_\lambda^* \lambda}{\sum_\lambda c_\lambda d_\lambda^*}\,. \tag{1.12}$$

This allows us to then rewrite Equation 1.11 as:

$$\langle\psi_f|\Psi'\rangle = \langle\psi_f|\psi_i\rangle \left(\mathcal{P}(q) - gO_w\mathcal{P}'(q)\right)\,, \tag{1.13}$$

which we can see is the Taylor series expansion of:

$$\langle\psi_f|\Psi'\rangle = \langle\psi_f|\psi_i\rangle\mathcal{P}(q - gO_w) \approx \mathrm{e}^{-ig\frac{\mathcal{P}'(q)}{\mathcal{P}(q)}\mathrm{Im}[O_w]}\mathcal{P}(q - g\mathrm{Re}\left[O_w\right])\,. \tag{1.14}$$

When appropriately normalized, this then gives the pointer displacement to be:

$$\Delta q = g\mathrm{Re}\left[O_w\right]\,, \tag{1.15}$$

since the weak value can be complex and only the real part contributes to the shift in pointer position.

The complex part of the weak value results in a shift in momentum of the pointer [21, 31, 32]. This can be expressed as [27]:

$$\Delta p = 2g\mathrm{Im}\left[O_w\right]\mathrm{Var}_{\mathrm{p}}\,, \tag{1.16}$$

where $\mathrm{Var}_{\mathrm{p}} = \langle\mathcal{P}|\hat{p}^2|\mathcal{P}\rangle - \langle\mathcal{P}|\hat{p}|\mathcal{P}\rangle^2$.

Thus, in the weak regime with postselection, the pointer encodes the weak value: $\Delta q = g\mathrm{Re}[O_w]$ and $\Delta p = 2g\mathrm{Im}[O_w]\mathrm{Var}_p$, where these displacements can be large.

1.1.3 Positive Operator-Valued Measures

Until this point, we have considered quantum measurement in the context of observables – quantities that behave in a similar way to classical parameters. However, a more general approach would be to consider all the possible outcomes of reading out the pointer after it interacts in an arbitrary way with a quantum system. This can be done using the positive operator-valued measure (POVM) approach [15, 16].

We can consider the unitary interaction between the quantum systems in terms of a ‘blackbox’ with two input and two output ports, as shown in Figure 1.3. The system to be measured enters port a and the initial pointer state into port c [33].

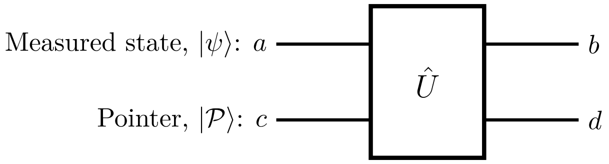

Figure 1.3: A diagram indicating the relationship between the inputs and outputs of the type of unitary being considered. The port a is the state to be measured, b the state after the interaction, and c & d are the pointer before and after the action of the unitary, respectively.

For an input state $|\psi\rangle_a|\mathcal{P}\rangle_c$, the output will be: $|\Psi\rangle = \hat{U}|\psi\rangle_a|\mathcal{P}\rangle_c$. If an orthonormal basis, $|f^k\rangle_d$, is chosen for the Hilbert space of port d then this output state can be written as:

$$|\Psi\rangle = \sum_k \left(\hat{K}_k|\psi\rangle_a\right)|f^k\rangle_d\,. \tag{1.17}$$

This expression is valid for any state to be measured, $|\psi\rangle_a$, but the set of $\hat{K}_k$ (Kraus or measurement operators) depends on the unitary interaction, $\hat{U}$, choice of basis, $|f^k\rangle_d$, and input pointer state, $|\mathcal{P}\rangle_c$. They are given by:

$$\hat{K}_k = \langle f^k|\hat{U}|\mathcal{P}\rangle \,. \tag{1.18}$$

Here $\hat{K}_k$ is an operator because the expectation value above takes a partial trace of $\hat{U}$ over the pointer system only.

The probability of getting the result k, when the pointer state in port d is measured in the orthonormal basis $\{|f^k\rangle_d\}$ is:

$$p_k = \langle\psi|\hat{K}_k^\dagger \hat{K}_k|\psi\rangle \,, \tag{1.19}$$

with an operator defined as:

$$\hat{E}_k = \hat{K}_k^\dagger \hat{K}_k \,. \tag{1.20}$$

The set of positive operators $\{\hat{E}_k\}$ (also referred to as *effects*) is the POVM for this pointer state and readout basis; and sum to the identity,

$$\sum_k \hat{E}_k = \mathbb{1} \,. \tag{1.21}$$

These operators enable the calculation of the probability of each measurement outcome for a state $|\psi\rangle$.

1.1.4 Postselection of POVMs

Postselecting after a POVM can result in similar outcomes as postselections create for weak values (including weak values themselves appearing in expressions for probability of outcomes). Broadly, postselected POVMs enable an even more general class of measurements known as Non-Positive Operator-Valued Measures (N-POVM) [34]. While the formalism presented below follows naturally from established theory, to the best of my knowledge, this specific formulation has not been previously published in the literature.

The state after a measurement interaction is given by Equation 1.17.

$$|\Psi'\rangle = \sum_k \left(\hat{K}_k|\psi_i\rangle_a\right)|f^k\rangle_d \tag{1.17 revisited}$$

The probability to measure the outcome k after postselecting the output port b into the state $|\psi_f\rangle_b$ is found to be:

$$p_k = \frac{|\langle\psi_f|\hat{K}_k|\psi_i\rangle|^2}{p_f} \,, \tag{1.22}$$

where p_f is the probability to successfully postselect into state $|\psi_f\rangle$,

$$p_f = \sum_k |\langle\psi_f|\hat{K}_k|\psi_i\rangle|^2 \,. \tag{1.23}$$

Equation 1.22 can then be rearranged to give:

$$p_k = \frac{\langle\psi_i|\hat{K}_k^\dagger|\psi_f\rangle\langle\psi_f|\hat{K}_k|\psi_i\rangle}{\sum_k |\langle\psi_f|\hat{K}_k|\psi_i\rangle|^2} = \langle\psi_i|\hat{E}_k^f|\psi_i\rangle \,, \tag{1.24}$$

with the postselected effects:

$$\hat{E}_k^f = \frac{\hat{K}_k^\dagger|\psi_f\rangle\langle\psi_f|\hat{K}_k}{\sum_k |\langle\psi_f|\hat{K}_k|\psi_i\rangle|^2} \,. \tag{1.25}$$

To this point we have made no assumptions about the strength of the interaction – measurements of any strength can be described by these postselected POVM effects. In the case of weak measurements the denominator can be replaced with the overlap of the postselected and initial states to give:

$$\hat{E}_k^f \approx \frac{\hat{K}_k^\dagger|\psi_f\rangle\langle\psi_f|\hat{K}_k}{|\langle\psi_f|\psi_i\rangle|^2} \,. \tag{1.26}$$

The effects now bear a closer resemblance to weak values, with the probabilities being the absolute square of the weak value of the Krauss operators.

1.1.5 Measurement Formalisms in This Thesis

The measurement formalisms presented above – von Neumann measurements and more general POVMs – provide the theoretical framework for measurement used throughout this thesis.

The conditional scheme to measure joint weak averages in Chapter 2 makes use of the von Neumann formalism. In Chapter 3, both formalisms are used to analyze how optical nonlinearities can be used to perform measurements.

1.2 Optics

1.2.1 The Degrees of Freedom of Light

When making a von Neumann measurement on a photon, one challenge is that photons typically only interact weakly with other photons (and many other quantum systems). This limits the systems that can easily be used as a pointer to the other degrees of freedom of the photon.

A photon has four independent degrees of freedom: polarization (spin) and the three components of momentum [35]. For a beam of light traveling in the z direction, these degrees of freedom are typically considered as: polarization; x transverse position (or momentum); y transverse position (or momentum); and frequency (or time).

There are a variety of choices of bases in which to consider these degrees of freedom. For polarization, usually horizontal/vertical, diagonal/anti-diagonal or circular basis states are used (more details below). For the transverse spatial degrees of freedom, some common bases are Hermite-Gaussian or Laguerre-Guassian modes [36]. The latter enables orbital angular momentum to be considered as a degree of freedom – though this is not independent of x and y transverse position/momentum [37, 38]. Another possibility for spatial modes is to use the Dirac basis [39].

Polarization and the Poincaré Sphere

The polarization of a photon can be treated as a qubit: although the photon is a spin-1 boson, the longitudinal $S_z = 0$ state is forbidden for a massless particle, leaving only two helicity states, which mathematically behave like a spin-$\frac{1}{2}$ system [16]. Generally, the polarization states aligned with the horizontal and vertical axes are used as the computational basis and are expressed as the kets $|H\rangle = |0\rangle$ and $|V\rangle = |1\rangle$. There are two other commonly used bases, which are comprised of an equal superposition of $|H\rangle$ and $|V\rangle$: diagonal, $|D\rangle$, and anti-diagonal, $|A\rangle$; and left circular, $|L\rangle$, and right circular, $|R\rangle$, which are defined as follows:

$$|D\rangle = |+\rangle = \frac{1}{\sqrt{2}}\left(|H\rangle + |V\rangle\right) , \tag{1.27a}$$

$$|A\rangle = |-\rangle = \frac{1}{\sqrt{2}}\left(|H\rangle - |V\rangle\right) , \tag{1.27b}$$

$$|L\rangle = \frac{1}{\sqrt{2}}\left(|H\rangle + i|V\rangle\right) , \tag{1.28a}$$

$$|R\rangle = \frac{1}{\sqrt{2}}\left(|H\rangle - i|V\rangle\right) . \tag{1.28b}$$

A general polarization state can be represented using the angles θ and ϕ as in Figure. 1.4,

$$|\psi\rangle = \cos\left(\frac{\theta}{2}\right)|H\rangle + e^{i\phi}\sin\left(\frac{\theta}{2}\right)|V\rangle . \tag{1.29}$$

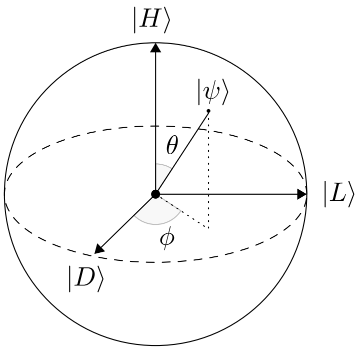

Adapted from a figure created by Sebastiano & cfr. This figure is licensed under CC BY-SA 4.0

Figure 1.4: The Poincaré (or Bloch) sphere is a 3d representation of an arbitrary polarization state [3, 16]. Pure states are represented by vectors with length 1 (on the surface of the sphere) while mixed states have shorter lengths. The Poincaré sphere has been rotated to align $|H\rangle/|V\rangle$ with the computational basis as is the case for the Bloch sphere.

The polarization of light is typically modified by the use of quarter and half wave plates, the effect of which depends on the angle of the optical axis of the wave plate. The Jones matrix for a waveplate with retardation δ with its fast axis at an angle ϑ to horizontal axis is [40]:

$$\begin{pmatrix} \mathrm{e}^{i\delta}\cos^2\vartheta + \sin^2\vartheta & (\mathrm{e}^{i\delta}-1)\sin\vartheta\cos\vartheta \\ (\mathrm{e}^{i\delta}-1)\sin\vartheta\cos\vartheta & \mathrm{e}^{i\delta}\sin^2\vartheta + \cos^2\vartheta \end{pmatrix}, \tag{1.30}$$

where the Jones vectors are:

$$|H\rangle = \begin{pmatrix} 1 \\ 0 \end{pmatrix}, \tag{1.31a}$$

$$|V\rangle = \begin{pmatrix} 0 \\ 1 \end{pmatrix}. \tag{1.31b}$$

1.2.2 The Propagation of Light

A powerful way to understand how light propagates is to use the techniques of Fourier optics [3]. The general principle is that any electromagnetic wave can be considered as a superposition of plane waves – waves with a uniform spatial frequency and direction. How these plane waves then propagate is a comparatively simple problem to solve. This technique is especially relevant for computational modeling of an optical system given the efficiency of fast Fourier transform algorithms.

The propagation of a wave in free space is equivalent to applying a phase shift that depends on spatial frequency. This shift is known as the transfer function:

$$H\left(k_x, k_y, d\right) = \mathrm{e}^{-id\sqrt{k^2-k_x^2-k_y^2}} = \mathrm{e}^{-id\sqrt{\frac{4\pi^2}{\lambda^2}-k_x^2-k_y^2}}\,, \tag{1.32}$$

for propagation by a distance d in the $\hat{\mathbf{z}}$ direction; k_x and k_y are the spatial frequencies in the $\hat{\mathbf{x}}$ and $\hat{\mathbf{y}}$ directions; and k is the wavenumber [3].

When there are no components of the wave at large angles (or equivalently large transverse k), the following approximation can be made:

$$H\left(k_x, k_y, d\right) \approx \mathrm{e}^{-ikd}\mathrm{e}^{i\frac{d}{2k}\left(k_x^2+k_y^2\right)}\,. \tag{1.33}$$

This is known as the Fresnel approximation and is valid for paraxial waves [3].

To make use of this transfer function, a representation of the wave's electric field in k-space (i.e. in terms of its spatial frequency components) is needed. This is done by taking a Fourier transform:

$$\tilde{E}\left(k_x, k_y, z\right) = \int E\left(x, y, z\right)\mathrm{e}^{i\left(k_x x + k_y y\right)}\mathrm{d}x\mathrm{d}y\,. \tag{1.34}$$

The electric field after propagating a distance, d, in free space is then given by:

$$\tilde{E}\left(k_x, k_y, z+d\right) = \tilde{E}\left(k_x, k_y, z\right) \times H\left(k_x, k_y, d\right)\,. \tag{1.35}$$

The electric field in position-space can then be found by taking an inverse Fourier transform.

Performing Fourier Transforms Using a Lens

The action of a lens is to impart a quadratic phase profile on a beam of light [3]. This corresponds to the transmission function:

$$t(x, y) = \mathrm{e}^{i\frac{k}{2f}\left(x^2+y^2\right)}\,, \tag{1.36}$$

where f is the focal length of the lens and k is the wavenumber of the incident light.

In a 2-f system, the wave amplitude, E_2, one focal length, f, after the lens, is proportional to the Fourier transform of the amplitude, E_1, one focal length before the lens,

$$E_2(x, y) = h_l \tilde{E}_1 \left(\frac{kx}{f}, \frac{ky}{f} \right) = h_l \int E_1 \left(x, y\right) \mathrm{e}^{i\left(\frac{kx}{f}x' + \frac{ky}{f}y'\right)} \mathrm{d}x' \mathrm{d}y' \,, \tag{1.37}$$

$$h_l = \tfrac{ik}{2\pi f} \mathrm{e}^{-2ikf} \,. \tag{1.38}$$

For this reason the plane one focal length after a lens is called the 'Fourier plane'.

1.2.3 Optics in This Thesis

The degrees of freedom of photons are used throughout this thesis in both Chapters 2 and 3. In Chapter 2 the propagation of classical light is used in the design of the experiment (for instance to make use of the Fourier plane) and also to perform simulations of the experiment.

1.3 Quantum Optics

Quantum optics is broadly the area where light must be considered in terms of 'photons' – discrete excitations of a propagating electromagnetic field – or where the electric and magnetic field observables must be replaced with operators. A light field is represented in terms of modes [36] (e.g. Hermite-Gauss modes or plane waves) and each mode is considered as a quantum harmonic oscillator, with the excitation number corresponding to the number of photons in the mode [35].

1.3.1 The Quantum Harmonic Oscillator

Before continuing with a very brief outline of quantum optics, it is first necessary to consider the quantum harmonic oscillator [41]. The Hamiltonian for a quantum harmonic oscillator is given by:

$$\hat{\mathcal{H}} = \frac{\hat{p}^2}{2m} + \tfrac{1}{2} m \omega^2 \hat{q}^2 \,, \tag{1.39}$$

where m is the mass of the oscillator, ω is the oscillator's angular frequency, $\hat{q}$ is its position observable, and $\hat{p}$ its momentum observable.

It is useful to introduce the following creation, $\hat{a}^\dagger$, and annihilation, $\hat{a}$, operators (also known as raising and lowering operators):

$$\hat{a}^\dagger = \tfrac{1}{\sqrt{2m\hbar\omega}}\left(m\omega\hat{q} - i\hat{p}\right) \,, \tag{1.40a}$$

$$\hat{a} = \tfrac{1}{\sqrt{2m\hbar\omega}}\left(m\omega\hat{q} + i\hat{p}\right) \,. \tag{1.40b}$$

They have the commutation relationship:

$$\left[\hat{a}, \hat{a}^\dagger\right] = 1\,. \tag{1.41}$$

These allow the Hamiltonian to be rewritten in the form:

$$\hat{\mathcal{H}} = \tfrac{1}{2}\hbar\omega\left(\hat{a}\hat{a}^\dagger + \hat{a}^\dagger\hat{a}\right) = \hbar\omega\left(\hat{a}^\dagger\hat{a} + \tfrac{1}{2}\right) \,. \tag{1.42}$$

An energy eigenstate $|n\rangle$ has energy eigenvalue of:

$$\hat{\mathcal{H}}|n\rangle = E_n|n\rangle = \hbar\omega(n + \tfrac{1}{2})|n\rangle\,. \tag{1.43}$$

The number operator gives the excitation level of the state,

$$\hat{n}|n\rangle = \hat{a}^\dagger\hat{a}|n\rangle = n|n\rangle\,. \tag{1.44}$$

The action of the creation and annihilation operators on an energy eigenstate are:

$$\hat{a}^\dagger|n\rangle = \sqrt{n+1}|n+1\rangle\,, \tag{1.45a}$$

$$\hat{a}|n\rangle = \sqrt{n}|n-1\rangle\,. \tag{1.45b}$$

It is also often useful to use dimensionless equivalents of the position and momentum operators, called quadratures ($\hat{X}$ and $\hat{Y}$), which are found to be:

$$\hat{X} = \sqrt{\frac{m\omega}{2\hbar}}\hat{q} = \tfrac{1}{2}\left(\hat{a}^\dagger + \hat{a}\right) \,, \tag{1.46a}$$

$$\hat{Y} = \tfrac{1}{\sqrt{2m\hbar\omega}}\hat{p} = \tfrac{i}{2}\left(\hat{a}^\dagger - \hat{a}\right) \,. \tag{1.46b}$$

1.3.2 The Quantization of Light

To motivate how electromagnetic waves can be quantized, the energy of a plane wave in terms of its vector potential can be considered [41]:

$$\mathbf{A}(\mathbf{r},t) = \mathbf{e}_\lambda A(\mathbf{r},t) = \left(A\mathrm{e}^{(-i\omega t + i\mathbf{k}.\mathbf{r})} + A^*\mathrm{e}^{(i\omega t - i\mathbf{k}.\mathbf{r})}\right)\mathbf{e}_\lambda\,, \tag{1.47}$$

where $\mathbf{e}_\lambda$ is a unit polarization vector and A is the complex amplitude of the vector potential. The energy of the wave in a volume, V, is then:

$$E = \epsilon_0 V \omega^2 \left(A A^* + A^* A \right) . \tag{1.48}$$

This appears similar to Equation 1.42 and motivates the following quantization:

$$A \rightarrow \sqrt{\frac{\hbar}{2\epsilon_0 V \omega}}\hat{a} , \tag{1.49a}$$

$$A^* \rightarrow \sqrt{\frac{\hbar}{2\epsilon_0 V \omega}}\hat{a}^\dagger . \tag{1.49b}$$

This gives the expression for the electric field operator to be:

$$\hat{\mathbf{E}}(\mathbf{r}, t) = \sqrt{\frac{2\hbar\omega}{\epsilon_0 V}} \left(\hat{X} \cos\left(\mathbf{k}.\mathbf{r} - \omega t\right) + \hat{Y} \sin\left(\mathbf{k}.\mathbf{r} - \omega t\right) \right) \mathbf{e}_\lambda , \tag{1.50}$$

which is comprised of two quadrature observables, $\hat{X}$ and $\hat{Y}$, with a $\pi/2$ phase difference between them.

This allows quantum optical modes to to be considered as having the same Hamiltonian as a quantum harmonic oscillator.

1.3.3 Quantum States of Light

One set of states of light commonly considered are the eigenstates to the Hamiltonian of the quantum harmonic oscillator. These are states with a well-defined number of photons, n, in a mode and are often called number or Fock states. They are typically written as $|n\rangle$.

Another common set of states are the coherent states, $|\alpha\rangle$. This is the state produced by a laser. In terms of the number basis, coherent states are written as [35]:

$$|\alpha\rangle = \mathrm{e}^{-\frac{|\alpha|^2}{2}} \sum_{n=0}^{\infty} \frac{\alpha^n}{\sqrt{n!}} |n\rangle . \tag{1.51}$$

Coherent states have Poissonian statistics in the photon number. These states are minimum uncertainty states in the field quadratures, saturating the uncertainty principle's bound,

$$\Delta \hat{X} = \sqrt{\frac{\hbar}{2}} , \tag{1.52a}$$

$$\Delta \hat{Y} = \sqrt{\frac{\hbar}{2}}\,. \tag{1.52b}$$

They have equal uncertainty in each quadrature.

1.3.4 The Quantum Phase Operator

The classical parameter phase does not map perfectly to any quantum observable. A Hermitian phase operator, $\hat{\phi}$, does not exist [35]. However, it is possible to create Hermitian operators that approximate the behavior of a phase operator.

One approach is to consider states of well known phase (either in a truncated [42] or infinite [35, 43, 44] Hilbert space),

$$|\phi\rangle = \frac{1}{\sqrt{s+1}} \sum_{n=0}^{s} \mathrm{e}^{in\phi_m} |n\rangle\,, \tag{1.53}$$

where $\phi_m = \phi_0 \frac{2\pi m}{s+1}$.

This can then be used to define a phase operator:

$$\hat{\phi} = \sum \phi_{m=0}^{s} |\phi\rangle\langle\phi|\,, \tag{1.54}$$

and can lead to the uncertainty relationship between phase and number:

$$\Delta n \Delta \phi \geq \tfrac{1}{2}\,, \tag{1.55}$$

as would be expected for conjugate observables.

However, care should be taken when interpreting this uncertainty relation. The photon number is discrete and unbounded, whilst the phase is continuous and bounded. This makes it problematic to consider a commutator between their operators, $\left[\hat{\phi}, \hat{n}\right]$, to give a Robertson uncertainty relation. However, for certain states (such as large coherent states) the relationship above does hold.

1.3.5 Nonlinear Quantum Optics Operators

Nonlinear optical phenomena occur when the properties of an optical medium are modified by the presence of light [8]. This enables a number of processes where light in different modes are able to couple together.

The simplest processes to consider are those which are *parametric.* These occur when the state of the optical medium is unchanged by interaction with the light – except for a brief time where it may exist in a virtual level. Parametric processes can be described by a nonlinear susceptibility $\chi^{(n)}$, where n describes how the polarization of the optical medium depends on the electric field, $P^{(n)} = \epsilon_0 \chi^{(n)} E^n$. These nonlinear susceptibilities are often very small, and almost always only the lowest orders $\chi^{(2)}$ and $\chi^{(3)}$ are considered.

To consider the action of these nonlinear interactions on the quantum state of light, we can express the Hamiltonian of the system in terms of the raising and lowering operators of each mode. For $\chi^{(2)}$ there are three modes, $\hat{a}$, $\hat{b}$ and $\hat{c}$ and the Hamiltonian is comprised of the energy in each mode and two interaction terms. [45, 46].

$$\hat{\mathcal{H}}_{\chi^{(2)}} = \hbar\omega\hat{c}^\dagger\hat{c} + \hbar\omega_1\hat{a}^\dagger\hat{a} + \hbar\omega_2\hat{b}^\dagger\hat{b} + \hbar\kappa\left(\hat{a}\hat{b}\hat{c}^\dagger + \hat{a}^\dagger\hat{b}^\dagger\hat{c}\right) \tag{1.56}$$

If we consider the interaction picture, splitting this Hamiltonian into a free part, $\hat{\mathcal{H}}_0$, and interaction part, $\hat{V}$:

$$\hat{\mathcal{H}}_0 = \hbar\omega\,\hat{c}^\dagger\hat{c} + \hbar\omega_1\,\hat{a}^\dagger\hat{a} + \hbar\omega_2\,\hat{b}^\dagger\hat{b}\,, \tag{1.57a}$$

$$\hat{V} = \hbar\kappa\Big(\hat{a}\,\hat{b}\,\hat{c}^\dagger + \hat{a}^\dagger\hat{b}^\dagger\hat{c}\Big)\ . \tag{1.57b}$$

In the interaction picture

$$\hat{O}_I(t) = e^{+\frac{i}{\hbar}H_0 t}\,\hat{O}\,e^{-\frac{i}{\hbar}H_0 t}\,, \tag{1.58a}$$

$$V_I(t) = e^{+\frac{i}{\hbar}H_0 t}\,V\,e^{-\frac{i}{\hbar}H_0 t}\,, \tag{1.58b}$$

and the mode operators acquire simple phases:

$$\hat{a}_I(t) = \hat{a}\,e^{-i\omega_1 t}\,, \tag{1.59a}$$

$$\hat{b}_I(t) = \hat{b}\,e^{-i\omega_2 t}\,, \tag{1.59b}$$

$$\hat{c}_I^\dagger(t) = \hat{c}^\dagger e^{+i\omega t}\,. \tag{1.59c}$$

Hence

$$V_I(t) = \hbar\kappa\Big(\hat{a}\,\hat{b}\,\hat{c}^\dagger\,e^{-i(\omega_1+\omega_2-\omega)t} + \hat{a}^\dagger\hat{b}^\dagger\hat{c}\,e^{+i(\omega_1+\omega_2-\omega)t}\Big) \tag{1.60}$$

For energy conservation, the sum of the two lowest frequencies must be equal to the highest: $\omega = \omega_1 + \omega_2$ and so the interaction Hamiltonian (in the interaction picture) is:

$$\hat{\mathcal{H}}_{\chi^{(2)}} = \hbar\kappa\left(\hat{a}\hat{b}\hat{c}^\dagger + \hat{a}^\dagger\hat{b}^\dagger\hat{c}\right)\ . \tag{1.61}$$

This interaction Hamiltonian describes all possible $\chi^{(2)}$ nonlinear processes.

For spontaneous parametric down-conversion and difference frequency generation, the mode c is the pump and a and b are the signal and idler modes. For sum frequency generation, the photons are generated in mode c from the light in modes a and b. For second-harmonic generation, the modes a and b have the same frequency ($\omega_1 = \omega_2$) and mode c is the pump.

The expression for κ (assuming that time is not directly considered and so the interaction unitary from the Hamiltonian is given by $\hat{U} = \exp(-i\hat{\mathcal{H}}/\hbar)$) is:

$$\kappa^2 = \frac{2d_{eff}^2 \hbar\omega_a\omega_b\omega_c}{n_a n_b n_c \epsilon_0 c^2 V} L^2 \mathrm{sinc}^2\left(\frac{\Delta k L}{2}\right) , \tag{1.62}$$

where n_i is the refractive index of the nonlinear medium for the i^{th} mode, V is the volume of the optical modes, L is the length of the nonlinear medium, $\Delta k = k_c - k_a - k_b$ is the phase mismatch and d_{eff} is the effective nonlinear coefficient. This effectively nonlinear coefficient depends on the precise geometry of the nonlinear medium but is of the same order as $d_{ijk} = \frac{1}{2}\chi^{(2)}_{ijk}$.

For $\chi^{(3)}$, there are four modes. To conserve energy they can be arranged either as $\omega = \omega_1 + \omega_2 + \omega_3$ or as $\omega = \omega_1 + \omega_2 - \omega_3$ (with different permutations of the frequency labels possible). In the first case, the interaction Hamiltonian is given by:

$$\hat{\mathcal{H}}_{\chi^{(3)}} = \hbar\kappa\left(\hat{a}\hat{b}\hat{c}\hat{d}^\dagger + \hat{a}^\dagger\hat{b}^\dagger\hat{c}^\dagger\hat{d}\right) . \tag{1.63}$$

In the second case, the interaction is given by:

$$\hat{\mathcal{H}}_{\chi^{(3)}} = \hbar\kappa\left(\hat{a}\hat{b}\hat{c}^\dagger\hat{d}^\dagger + \hat{a}^\dagger\hat{b}^\dagger\hat{c}\hat{d}\right) . \tag{1.64}$$

The Parametric Approximation

When one, or more, of the modes is an intense coherent beam, it may be treated as a classical wave with constant amplitude [45]. This enables the substitution $\hat{a} \to \alpha$ and $\hat{a}^\dagger \to \alpha^*$.

When this approximation is made, the full trilinear Hamiltonian of a $\chi^{(2)}$ interaction is significantly simplified and enables a much more tractable treatment of the remaining two quantum modes. This is also a highly practical situation, where a classical laser ‘pump’ is able to control the effective strength of an optical nonlinear interaction between the other two modes.

1.3.6 Quantum Optics in This Thesis

The outline of quantum optics presented above is mainly used in Chapter 3, where the nonlinear optical interactions between different quantum optical modes are considered as measurements. However, some of the mathematical tools outlined above (the quantum harmonic oscillator) are used in Chapter 2 to simplify some calculations.

1.4 Quasi-probability Distributions

It can be useful to consider a quantum state in the phase space parameterized by the field quadratures – allowing the state to be represented in a way more similar to a classical probability distribution. This has a number of advantages enabling: the quantum state to be visualized in phase space; calculations of expectation values to more closely parallel the classical approach; and detection of systems behaving non-classically.

There is no unique way to describe a quantum state in phase space – with a range of possible ‘quasi-probability’ distributions. The expectation value of an observable can be written generally as [47]:

$$\langle\hat{O}\rangle = \mathrm{Tr}\left(\hat{O}\hat{\rho}\right) = \sum_{\lambda} T_{\lambda}(\hat{O}) Q_{\lambda}\left(\hat{\rho}\right) , \tag{1.65}$$

where $Q(\hat{\rho}) : \lambda \to Q_{\lambda}\left(\hat{\rho}\right)$ is the quasi-probability distribution, $T(\hat{O}) : \lambda \to T_{\lambda}(\hat{O})$ is the symbol for $\hat{O}$ (the representation of the operator for a specific quasi-probability), and the set of λ depends on the specific quasi-probability distribution (for example, the different a_i and b_j values for the Kirkwood-Dirac (KD) distribution). The function $Q(\hat{\rho})$ acts similarly to a classical probability distribution. However, the function does not need to be positive (or even real) valued, hence it is a ‘quasi-probability’ distribution.

The density matrix, $\hat{\rho}$, is a more general representation of the state of a system that allows for classical uncertainty in the quantum state,

$$\hat{\rho} = \sum_{i} p_i |\psi_i\rangle\langle\psi_i| , \tag{1.66}$$

where p_i is the classical probability of the state being found in the pure quantum state $|\psi_i\rangle$.

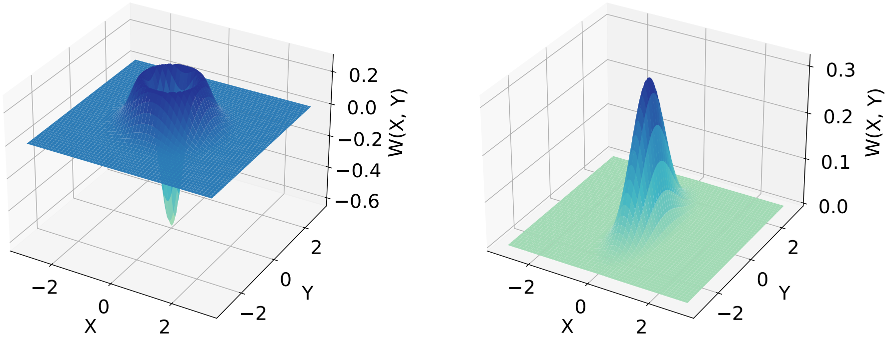

(a) Single photon (b) Squeezed Gaussian state

Figure 1.5: The Wigner distribution for two different quantum states.

1.4.1 The Wigner Distribution

One common choice of quasi-probability distribution is the Wigner representation [35, 48, 49]. The quasi-probability distribution is given by:

$$W(q,p) = \frac{1}{2\pi\hbar}\int_{-\infty}^{\infty}\langle q+\tfrac{1}{2}x|\hat{\rho}|q-\tfrac{1}{2}x\rangle \mathrm{e}^{ipx/\hbar}\mathrm{d}x\,. \tag{1.67}$$

This is the natural choice to evaluate expectation values of symmetrized operators since the symbol of these operators in the Wigner representation is trivial. Hence, for a symmetrized (Weyl ordered) function, G_W, Equation 1.65 becomes (for the continuous case):

$$\langle G_W(\hat{q},\hat{p})\rangle = \int G_W(\hat{q},\hat{p})W(q,p)\mathrm{d}q\mathrm{d}p\,. \tag{1.68}$$

The Wigner distribution is always real, but can have negative values. If a state has any regions with negativity, this is a signature of non-classicality [10, 11]. However, many non-classical states (such as squeezed states) do not have any regions of their Wigner function with a negative value (see Figure 1.5).

Another property of the Wigner function is that the marginals are probability distributions:

$$\int W(q,p)\mathrm{d}q = \langle\hat{p}|\hat{\rho}|\hat{p}\rangle\,, \tag{1.69}$$

which, for a pure state, is equal to $|\langle\hat{p}|\psi\rangle|^2$. Similarly:

$$\int W(q,p)\mathrm{d}p = \langle\hat{q}|\hat{\rho}|\hat{q}\rangle\,. \tag{1.70}$$

In quantum optics, other common quasi-probability distributions are the Glauber-Sudarshan P and Husimi Q representations which act on functions with normal and anti-normal orderings of their operators [35]. However, the marginals of these representations do not have as simple a relationship to classical probability distributions of the state [47].

1.4.2 The Kirkwood-Dirac Distribution

An alternative quasi-probability distribution is known as the Kirkwood-Dirac distribution and applies to left or standard ordered operators (powers of $\hat{x}$ always to the left of powers of $\hat{p}$) [47, 50]. This distribution is also easier to generalize to other observables and, unlike the Wigner distribution, does not require the use of a basis of conjugate (or maximally non-commuting) observables [47, 51]. The distribution also has the property that it is equal to zero wherever the wavefunction of x or p is equal to zero, a property that is especially desirable in signal processing [52] where the Kirkwood-Dirac distribution is known as the Rihazek distribution. Below, the discrete case is considered but this straightforwardly extends to the continuous case.

Consider two orthonormal bases which are the eigen bases of the operators $\hat{A}$ and $\hat{B}$,

$$\hat{A} = \sum_i a_i|a_i\rangle\langle a_i|\,, \tag{1.71a}$$

$$\hat{B} = \sum_j b_j|b_j\rangle\langle b_j|\,. \tag{1.71b}$$

The Kirkwood-Dirac quasi-probability is then expressed as [47]:

$$Q_{i,j}(\hat{\rho}) = \langle b_j|a_i\rangle\langle a_i|\hat{\rho}|b_j\rangle\,, \tag{1.72}$$

with the symbol of $\hat{O}$ being:

$$T_{i,j}(\hat{O}) = \frac{\langle b_j|\hat{O}|a_i\rangle}{\langle b_j|a_i\rangle}\,, \tag{1.73}$$

allowing expectation values to be found using Equation 1.65.

The elements of the Kirkwood-Dirac distribution can be complex as well as

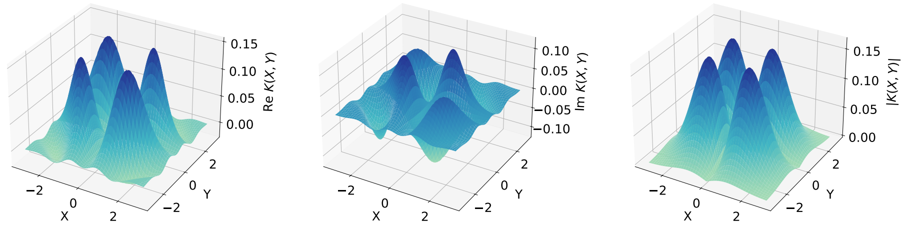

(a) Re$[K]$ (single photon) (b) Im$[K]$ (single photon) (c) $|K|$ (single photon)

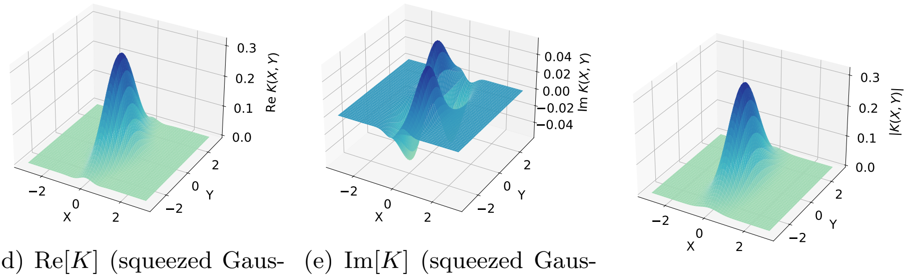

(d) Re$[K]$ (squeezed Gaussian) (e) Im$[K]$ (squeezed Gaussian) (f) $|K|$ (squeezed Gaussian)

Figure 1.6: Kirkwood–Dirac distributions in quadrature space for (top) a single photon and (bottom) a squeezed Gaussian state: real part, imaginary part, and magnitude.

negative valued, which are signs of different forms of nonclassicality[53]. However, as for the Wigner distribution, the marginals of the Kirkwood-Dirac distribution correspond to the Born rule probability distributions expected for $\hat{A}$ or $\hat{B}$. Examples of the KD distribution for a single photon and squeezed (Gaussian state) are shown in Figure 1.6.

An additional property of the Kirkwood-Dirac distribution is that the elements of the distribution are equal to the expectation of the joint value of the two projector operators [28, 47]:

$$Q_{i,j}(\hat{\rho}) = \mathrm{Tr}\left(\Pi_{b_j}\Pi_{a_i}\hat{\rho}\right) = \langle \Pi_{b_j}\Pi_{a_i}\rangle\,, \tag{1.74}$$

where $\Pi_{a_i} = |a_i\rangle\langle a_i|$ and $\Pi_{b_j} = |b_j\rangle\langle b_j|$.

This can be rewritten as:

$$Q_{i,j}(\hat{\rho}) = \langle b_j|a_i\rangle\langle a_i|\hat{\rho}|b_j\rangle\,. \tag{1.72 revisited}$$

Using the resolution of the identity, $\mathbb{1} = \sum_k |a_k\rangle\langle a_k|$, we can rewrite this expression as:

$$Q_{i,j}(\hat{\rho}) = \langle b_j|a_i\rangle\langle a_i|\hat{\rho}.\mathbb{1}|b_j\rangle = \sum_k \langle b_j|a_i\rangle\langle a_i|\hat{\rho}|a_k\rangle\langle a_k|b_j\rangle\,. \tag{1.75}$$

This allows the use of an expression for the density matrix solely in the a basis:

$$\rho(a_i, a_k) = \langle a_i|\hat{\rho}|a_k\rangle \tag{1.76}$$

If we consider the case when a is the position, x, and b the momentum, p, we find that the Kirkood-Dirac distribution for a density matrix $\hat{\rho}$ is given by:

$$D(x_i, p_j) = \mathrm{e}^{-ip_jx_i/\hbar}\sum_k \rho(x_i, x_k)\mathrm{e}^{ip_jx_k/\hbar}\,, \tag{1.77}$$

where $\rho(x_i, x_k) = \langle x_i|\hat{\rho}|x_k\rangle$. For a pure state $|\psi\rangle$, this corresponds to a density matrix of:

$$\rho(x_i, x_k) = \langle x_i|\hat{\rho}|x_k\rangle = \langle x_i|\psi\rangle\langle\psi|x_k\rangle = \psi(x_i)\psi(x_k)^*\,, \tag{1.78}$$

where $\psi(x_i)$ is the wave function of the state.

1.4.3 Quasi-probability Distributions in This Thesis

The quasi-probability distributions outlined above (specifically the Kirkwood-Dirac distribution) are mainly used to motivate and interpret the measurements made by the experiment in Chapter 2.

1.5 Gaussian Quantum Optics

Many relevant quantum optical states (coherent, thermal, squeezed) can be represented as a Gaussian function, where the Wigner distribution of each mode is fully characterized by their first and second moments [54–56]. A Gaussian transformation is then any transformation that changes a Gaussian state to another Gaussian state.

A Gaussian state can be represented by a vector of the quadrature expectations:

$$\mathbf{r} = \begin{pmatrix} \langle \hat{X}_a \rangle \\ \langle \hat{X}_b \rangle \\ \dots \\ \langle \hat{Y}_a \rangle \\ \langle \hat{Y}_b \rangle \\ \dots \end{pmatrix} , \tag{1.79}$$

and a covariance matrix:

$$V_{ij} = \tfrac{1}{2} \langle \Delta \hat{X}_i \Delta \hat{X}_j + \Delta \hat{X}_j \Delta \hat{X}_i \rangle \, , \tag{1.80}$$

where $\Delta \hat{X}_i = \hat{X}_i - \langle \hat{X}_i \rangle$.

A Gaussian transformation is then represented as a symplectic matrix, S and a displacement, $\mathbf{d}$.

$$\mathbf{r} \rightarrow S\mathbf{r} + \mathbf{d} \tag{1.81}$$

$$V \rightarrow SVS^T \tag{1.82}$$

Any Hamiltonian that is at most second order in the field operators, is able to be represented in this way. The matrix S can be found from the purely quadratic part of the Hamiltonian. The matrix H, which satisfies $\hat{\mathcal{H}} = \hat{\mathbf{r}}^T H \hat{\mathbf{r}}$, is used to find S [57]:

$$S = \mathrm{e}^{\Omega H} \, , \tag{1.83}$$

where Ω is the block matrix:

$$\Omega = \begin{pmatrix} 0 & \mathbb{1} \\ -\mathbb{1} & 0 \end{pmatrix} . \tag{1.84}$$

1.5.1 Gaussian Quantum Optics in This Thesis

The Gaussian optics formalism is used in Section 3.1.7 when considering how a von Neumann interaction Hamiltonian can be decomposed into linear operations and single mode squeezers.

Chapter 2

Conditional Measurement of Joint Weak Averages

When two observables do not commute, it is not possible to measure both observables with arbitrary precision – for position and momentum this is the famous uncertainty principle of Heisenberg [58]. More generally this is given by the Robertson uncertainty relation [59, 60],

$$\sigma_A\sigma_B \geq \tfrac{1}{2}|\langle[\hat{A},\hat{B}]\rangle| \,. \tag{2.1}$$

This has consequences when attempting to jointly measure incompatible observables – a strong measurement of $\hat{A}$ will leave no information about $\hat{B}$ [61]. One approach [62] is to simultaneously couple each observable to a different pointer with the Hamiltonian:

$$\hat{\mathcal{H}} = g\left(\hat{A}\hat{p}_1 + \hat{B}\hat{p}_2\right)\,, \tag{2.2}$$

where $\hat{p}_1$ and $\hat{p}_2$ are the conjugate momenta of the two pointers (and commute with $\hat{A}$ and $\hat{B}$ as they act on different systems).

Alternatively, the observables $\hat{A}$ and $\hat{B}$ can be measured on different quantum systems prepared in identical states [16].

Of particular interest is to measure the joint value $\langle\hat{A}\hat{B}\rangle = \mathrm{Tr}\left(\hat{A}\hat{B}\hat{\rho}\right)$. For instance, this is an interesting quantity to understand entanglement [13, 63, 64]. However, when these observables are incompatible, standard approaches no longer work [61] and since $\hat{A}\hat{B}$ is not hermitian, the value $\langle\hat{A}\hat{B}\rangle$ will not be real.

The framework of weak measurement can be applied to these joint measurements. The concept of a joint weak value (analogous to the weak value of a single observable) was introduced by Resch and Steinberg [31] and given by:

$$\mathrm{Re}\left[\tfrac{1}{2}(AB+BA)_W\right] = 2\frac{\langle \hat{q_1}\hat{q_2}\rangle_{fi}}{g_1 g_2} - \mathrm{Re}\left[A_W^* B_W\right] \,, \tag{2.3}$$

where $\langle \hat{q_1}\hat{q_2}\rangle_{fi}$ is the expectation value for the product of the two pointer positions $\hat{q_1}\hat{q_2}$ given a successful postselection and g_i is the interaction strength with the i^{th} pointer. The subscript W indicates this is a weak value. Additional theory for the joint weak value was developed in [32, 65, 66].

It is also possible to consider joint measurements without postselection, even in the case when the joint operator is not Hermitian. These measurements are called the joint weak average and are given by [28]:

$$\langle \hat{A}\hat{B}\rangle_W = \mathrm{Tr}\left(\hat{A}\hat{B}\hat{\rho}\right) \,, \tag{2.4}$$

which is the standard expectation value for an operator acting on a quantum state (although if $\hat{A}\hat{B}$ is not hermitian this value will not be real). As an expectation value (average), this quantity has no fundamental limitation on the uncertainty that can be achieved.

Joint measurements have been made in a number of ways: by sequentially measuring observables [67–69], using optimally cloned states [70, 71], and using fractional Fourier transforms [72]. They have also proven useful investigating phenomena such as: Hardy's paradox [73–75], the quantum Cheshire Cat [76, 77], and the time ordering of measurements [78, 79].

One other application of joint measurements is their use to determine the quantum state of the system [28]. This provides an alternative to standard tomographic techniques [80–83] by allowing the elements of the Kirkwood-Dirac distribution [84, 85] or the density matrix [86] to be found.

However, these schemes all require post-processing of measurements (and often the readout of the states of multiple pointers). This can be avoided by making use of a conditional scheme [28]. By conditionally coupling two pointers – where the second pointer's interaction strength depends on the outcome of the first – the joint operator's weak average can be directly inferred from the shift in the second pointer's position. This has the advantage that the joint weak average can then be directly read off from a single pointer.

This chapter presents, and extends upon, the conditional weak scheme of Lundeen and Bamber [28] in Section 2.1. In Section 2.2 we design an experiment to implement this scheme and present computation simulations of this experiment in Section 2.3. The full experimental setup is described in Section 2.4. Some initial tests are shown in Section 2.5 and results demonstrating the conditional scheme are presented in Section 2.6. Proposed directions for future troubleshooting and refinement are in Section 2.7.

2.1 Conditional Measurement Theory

In Section 2.1.1 we present the proposal of Lundeen and Bamber [28]. In Section 2.1.2 we find the requirements for the weakness of the measurements (clarifying upon the limit suggested in the original proposal) and we show that the first pointer is able to be reused after the conditional measurement with the second pointer in Section 2.1.3. In Section 2.1.4 we show what modifications are required when polarization rather than position is used as the pointer state. Finally in Section 2.1.5 we show that a simpler binary conditionality is able to produce exactly the same type of measurement.

2.1.1 The Lundeen and Bamber Scheme

A conditional joint weak measurement can be made if the unitary evolution of the pointers and the measured state has the form given by Lundeen and Bamber [28]:

$$\hat{U} = \hat{U}_2\hat{U}_1 = \exp\left(-ig_2\hat{q}_1\hat{A}\hat{p}_2/\hbar\right) \times \exp\left(-ig_1\hat{B}\hat{p}_1/\hbar\right) , \tag{2.5}$$

where $\hat{A}$ & $\hat{B}$ are the observables to be jointly measured; $\hat{q}_i$ & $\hat{p}_i$ are the 'position' & conjugate momentum of the ith pointer; and g_i is a measure of the coupling strength to the ith pointer.

This interaction can be seen as comprised of the two different unitary interactions shown in Figure 2.1.

$$\hat{U}_1 = \exp\left(-ig_1\hat{B}\hat{p}_1/\hbar\right) \tag{2.6a}$$

$$\hat{U}_2 = \exp\left(-ig_2\hat{q}_1\hat{A}\hat{p}_2/\hbar\right) \tag{2.6b}$$

The first of these interactions is a typical weak measurement, where the pointer 'position', q_1 is displaced by an amount that depends on the observable $\hat{B}$. The second unitary can be seen also as a von Neumann style measurement interaction to measure $\hat{A}$. However, the strength of this interaction now depends on the position of the first pointer, $g = g_2\hat{q}_1$, making this measurement conditional on

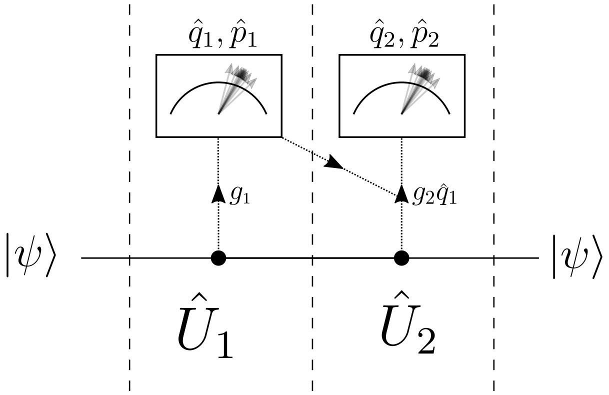

Figure 2.1: A quantum system, represented here by $|\psi\rangle$, interacts weakly with the first pointer in a way described by the unitary operator $\hat{U}_1$ with strength g_1. The first pointer 'position', q_1, is displaced. The system then interacts with a second pointer in a way described by the unitary operator $\hat{U}_2$, displacing the second pointer's 'position', q_2. The strength of this second interaction ($g_2\hat{q}_1$) is conditional on the position of the first pointer, q_1. In the limit of very weak measurements, the quantum system can be arbitrarily undisturbed such that the state after the measurement is the same as before.

the result of the first.

For a system described by this combined unitary, the joint measurement can be performed by finding the expectation value of $\hat{q}_2$.

$$\langle \hat{q}_2 \rangle = g_1 g_2 \mathrm{Re}\left[\langle\psi|\hat{A}\hat{B}|\psi\rangle\right] . \tag{2.7}$$

Derivation

When the pointer wave functions are considered to be pointers centered at zero, the initial state of the system (before measurement) is:

$$|\Psi\rangle = |0\rangle_1 |0\rangle_2 |\psi\rangle \, , \tag{2.8}$$

where the first two terms are the states of the pointers and the final term is the state of the system being measured. After measurement the state will be:

$$|\Psi'\rangle = \hat{U}|\Psi\rangle = \hat{U}|0\rangle_1 |0\rangle_2 |\psi\rangle \, . \tag{2.9}$$

The expectation value of $\hat{q}_2$ is then found to be:

$$\langle \hat{q}_2 \rangle = \langle \Psi' | \hat{q}_2 | \Psi' \rangle = \langle \Psi | \hat{U}^\dagger \hat{q}_2 \hat{U} | \Psi \rangle \,. \tag{2.10}$$

Looking at the $\hat{U}^\dagger \hat{q}_2 \hat{U}$ term:

$$\hat{U}^\dagger \hat{q}_2 \hat{U} = \mathrm{e}^{\left(i g_1 \hat{B} \hat{p}_1 / \hbar\right)} \times \mathrm{e}^{\left(i g_2 \hat{q}_1 \hat{A} \hat{p}_2 / \hbar\right)} \times \hat{q}_2 \times \mathrm{e}^{\left(-i g_2 \hat{q}_1 \hat{A} \hat{p}_2 / \hbar\right)} \times \mathrm{e}^{\left(-i g_1 \hat{B} \hat{p}_1 / \hbar\right)} \,, \tag{2.11}$$

and applying the BCH lemma [87]: $\mathrm{e}^{X} Y \mathrm{e}^{-X} = Y + [X,Y] + \frac{1}{2!}[X,[X,Y]] + ...$

$$\hat{U}^\dagger \hat{q}_2 \hat{U} = \mathrm{e}^{\left(i g_1 \hat{B} \hat{p}_1 / \hbar\right)} \times \left(\hat{q}_2 + \tfrac{i}{\hbar} g_2 \left[\hat{A} \hat{p}_2 \hat{q}_1, \hat{q}_2 \right] + ... \right) \times \mathrm{e}^{\left(-i g_1 \hat{B} \hat{p}_1 / \hbar\right)} \,, \tag{2.12}$$

$$\hat{U}^\dagger \hat{q}_2 \hat{U} = \mathrm{e}^{\left(i g_1 \hat{B} \hat{p}_1 / \hbar\right)} \times \left(\hat{q}_2 + \tfrac{i}{\hbar} g_2 \hat{A} \hat{q}_1 \left[\hat{p}_2, \hat{q}_2 \right] + ... \right) \times \mathrm{e}^{\left(-i g_1 \hat{B} \hat{p}_1 / \hbar\right)} \,, \tag{2.13}$$

$$\hat{U}^\dagger \hat{q}_2 \hat{U} = \mathrm{e}^{\left(i g_1 \hat{B} \hat{p}_1 / \hbar\right)} \times \left(\hat{q}_2 + g_2 \hat{A} \hat{q}_1 \right) \times \mathrm{e}^{\left(-i g_1 \hat{B} \hat{p}_1 / \hbar\right)} \,, \tag{2.14}$$

$$\hat{U}^\dagger \hat{q}_2 \hat{U} = \hat{q}_2 + \mathrm{e}^{\left(i g_1 \hat{B} \hat{p}_1 / \hbar\right)} \times \left(g_2 \hat{A} \hat{q}_1 \right) \times \mathrm{e}^{\left(-i g_1 \hat{B} \hat{p}_1 / \hbar\right)} \,. \tag{2.15}$$

The BCH lemma can then be used again to give:

$$\hat{U}^\dagger \hat{q}_2 \hat{U} = \hat{q}_2 + g_2 \hat{A} \hat{q}_1 + \tfrac{i}{\hbar} g_1 g_2 \left[\hat{B} \hat{p}_1, \hat{A} \hat{q}_1 \right] + \mathcal{O}(g^3) \,. \tag{2.16}$$

The expectation value of the first two terms will be zero for pointer states which have even wave functions (probably the only sensible choice to initialize a pointer state in), since the first two terms are odd and so the expectation integral will be zero. Since the measurements are weak, g_1 and g_2 will be small and hence higher order terms can be neglected. This gives the expression for the expectation of $\hat{q}_2$ to be:

$$\langle \hat{q}_2 \rangle = \frac{i}{\hbar} g_1 g_2 \langle \Psi | \hat{B} \hat{A} \hat{p}_1 \hat{q}_1 - \hat{A} \hat{B} \hat{q}_1 \hat{p}_1 | \Psi \rangle \,. \tag{2.17}$$

To proceed further with this, we can make use of the fact that the pointer can be chosen to start in a specific Gaussian state. The approach used by Martinez et al. [72] of raising and lowering operators is followed.

The wave function of the first pointer in its initial state can be given as:

$$\phi(q_1) = \langle q_1 | 0 \rangle_1 = \frac{1}{(2\pi\sigma_1^2)^{\frac{1}{4}}} \mathrm{e}^{-\frac{q_1^2}{4\sigma_1^2}} \,, \tag{2.18}$$

where σ_1 is the standard deviation of the first pointer probability distribution. This has the same form as the ground state of a quantum harmonic oscillator with a lowering operator given below. There is no actual quantum harmonic oscillator involved, this comparison is simply a mathematical equivalence to enable the use of tools from that framework.

$$\hat{a} = \frac{\hat{q}_1}{2\sigma_1} + i\frac{\hat{p}_1\sigma_1}{\hbar}\,, \tag{2.19}$$

and hence:

$$\hat{q}_1 = \sigma_1(\hat{a} + \hat{a}^\dagger)\,, \tag{2.20a}$$

$$\hat{p}_1 = \frac{i\hbar}{2\sigma_1}(\hat{a}^\dagger - \hat{a})\,. \tag{2.20b}$$

Substituting this result into the Equation 2.17 then gives:

$$\langle\hat{q}_2\rangle = -\frac{1}{2}g_1g_2\langle\Psi|\hat{B}\hat{A}(\hat{a}^\dagger - \hat{a})(\hat{a} + \hat{a}^\dagger) - \hat{A}\hat{B}(\hat{a} + \hat{a}^\dagger)(\hat{a}^\dagger - \hat{a})|\Psi\rangle\,. \tag{2.21}$$

Since we are considering the expectation value of a ‘ground state’ of a quantum harmonic oscillator, only those operators of the form $\hat{a}\hat{a}^\dagger$ will give a non-zero contribution,

$$\langle\hat{q}_2\rangle = \frac{1}{2}g_1g_2\langle\Psi|\hat{B}\hat{A}\hat{a}\hat{a}^\dagger + \hat{A}\hat{B}\hat{a}\hat{a}^\dagger|\Psi\rangle\,, \tag{2.22}$$

$$\langle\hat{q}_2\rangle = \frac{1}{2}g_1g_2\langle\psi|_2\langle 0|_1\langle 0|\hat{B}\hat{A}\hat{a}\hat{a}^\dagger + \hat{A}\hat{B}\hat{a}\hat{a}^\dagger|0\rangle_1|0\rangle_2|\psi\rangle\,, \tag{2.23}$$

$$\langle\hat{q}_2\rangle = \frac{1}{2}g_1g_2\langle\psi|\hat{B}\hat{A} + \hat{A}\hat{B}|\psi\rangle\,. \tag{2.24}$$

With a fairly simple rearrangement, we can then see that this gives the real part of the joint operator $\hat{A}\hat{B}$,

$$\langle\hat{q}_2\rangle = \frac{1}{2}g_1g_2\left(\langle\psi|(\hat{A}^\dagger\hat{B}^\dagger)^\dagger|\psi\rangle + \langle\psi|\hat{A}\hat{B}|\psi\rangle\right)\,. \tag{2.25}$$

Since both $\hat{A}$ and $\hat{B}$ correspond to observables they must be Hermitian operators and so:

$$\langle\hat{q}_2\rangle = \frac{1}{2}g_1g_2\Big(\langle\psi|(\hat{A}\hat{B})^\dagger|\psi\rangle + \langle\psi|\hat{A}\hat{B}|\psi\rangle\Big)\,, \tag{2.26}$$

$$\langle\hat{q}_2\rangle = \frac{1}{2}g_1g_2\Big(\langle\psi|\hat{A}\hat{B}|\psi\rangle^* + \langle\psi|\hat{A}\hat{B}|\psi\rangle\Big)\,, \tag{2.27}$$

$$\langle\hat{q}_2\rangle = g_1g_2\mathrm{Re}\left[\langle\psi|\hat{A}\hat{B}|\psi\rangle\right]\,. \tag{2.28}$$

The real part of the joint weak average is obtained directly by measuring the position of the second pointer.

Imaginary Joint Value

To find the imaginary part of the joint value, the strength of the second interaction should depend on the first pointer's momentum (rather than position).

$$\hat{U}_2 = \exp\left(-ig_2\hat{p}_1\hat{A}\hat{p}_2/\hbar\right) \times \exp\left(-ig_1\hat{B}\hat{p}_1/\hbar\right) \tag{2.29}$$

Using the same procedure as before, this will give the expectation value:

$$\langle\hat{q}_2\rangle = \frac{i}{\hbar}g_1g_2\langle\Psi|\hat{p}_1^2(\hat{B}\hat{A} - \hat{A}\hat{B})|\Psi\rangle\,. \tag{2.30}$$

For a Gaussian pointer and using the raising/lowering operator formalism:

$$\langle\hat{q}_2\rangle = \frac{-i\hbar}{4\sigma_1^2}g_1g_2\langle\Psi|(\hat{a}^\dagger - \hat{a})^2(\hat{B}\hat{A} - \hat{A}\hat{B})|\Psi\rangle\,, \tag{2.31}$$

$$\langle\hat{q}_2\rangle = \frac{i\hbar}{4\sigma_1^2}g_1g_2\langle\psi|(\hat{B}\hat{A} - \hat{A}\hat{B})|\psi\rangle\,. \tag{2.32}$$

Rearranging in a similar way as previously:

$$\langle\hat{q}_2\rangle = \frac{\hbar g_1g_2}{2\sigma_1^2}\mathrm{Im}\left[\langle\psi|\hat{A}\hat{B}|\psi\rangle\right]\,. \tag{2.33}$$

Alternatively, the interaction with the first pointer can shift the pointer's momentum instead of position which would have the unitary:

$$\hat{U}_2 = \exp\left(-ig_2\hat{q}_1\hat{A}\hat{p}_2/\hbar\right) \times \exp\left(-ig_1\hat{B}\hat{q}_1/\hbar\right)\,. \tag{2.34}$$

This would then give the expectation value of the second pointer position to be:

$$\langle\hat{q}_2\rangle = \frac{2g_1g_2\sigma_1^2}{\hbar}\mathrm{Im}\left[\langle\psi|\hat{A}\hat{B}|\psi\rangle\right]\,. \tag{2.35}$$

Momentum of the Second Pointer

When measuring weak values, the imaginary part of the weak value can be found by reading off the momentum of the pointer [21, 27, 31, 32]. However, in the conditional scheme there is no information about the imaginary component of the joint value in the momentum of the second pointer.

Since $\hat{p}_2$ commutes with the unitaries needed for this measurement, the expectation of $\hat{p}_2$ after the interaction will be the initial pointer momentum,

$$\langle\hat{p}_2\rangle = \langle\Psi|\hat{U}^\dagger\hat{p}_2\hat{U}|\Psi\rangle = \langle\Psi|\hat{p}_2\hat{U}^\dagger\hat{U}|\Psi\rangle = \langle\Psi|\hat{p}_2|\Psi\rangle\,. \tag{2.36}$$

Mixed States

The procedure outlined above is simple to generalize for a mixed state of the form:

$$\hat{\rho} = \sum_n p_n |0\rangle_1 |0\rangle_2 |\psi_n\rangle\langle\psi_n|\,{}_2\langle 0|\,{}_1\langle 0|\,. \tag{2.37}$$

Resulting in:

$$\langle \hat{q}_2 \rangle_R = g_1 g_2 \mathrm{Re}\left\{\mathrm{Tr}\left[\hat{\rho}\hat{A}\hat{B}\right]\right\}\,, \tag{2.38a}$$

$$\langle \hat{q}_2 \rangle_I = \frac{\hbar g_1 g_2}{2\sigma_1^2} \mathrm{Im}\left\{\mathrm{Tr}\left[\hat{\rho}\hat{A}\hat{B}\right]\right\}\,, \tag{2.38b}$$

where the first expectation value, $\langle \hat{q}_2 \rangle_R$, is when the strength of the second interaction depends on $\hat{q}_1$, and the second expectation value, $\langle \hat{q}_2 \rangle_I$, is when the strength of the second interaction depends on $\hat{p}_1$.

2.1.2 What Does it Mean to be Weak?

After Equation 2.16, the higher order terms (with respect to coupling between the pointers and system) were neglected since we have assumed that they are small. However, it would be useful to know what 'small' means and hence how strong a signal we can get without unnecessarily disturbing the results. To do this we consider the next terms in power of g. Starting with:

$$\hat{U}^\dagger \hat{q}_2 \hat{U} = \mathrm{e}^{\left(ig_1 \hat{B}\hat{p}_1/\hbar\right)} \times \mathrm{e}^{\left(ig_2 \hat{q}_1 \hat{A}\hat{p}_2/\hbar\right)} \times \hat{q}_2 \times \mathrm{e}^{\left(-ig_2 \hat{q}_1 \hat{A}\hat{p}_2/\hbar\right)} \times \mathrm{e}^{\left(-ig_1 \hat{B}\hat{p}_1/\hbar\right)}\,, \tag{2.11 revisited}$$

we can again apply the BCH lemma – this time explicitly evaluating higher order terms. Identifying $X_1 = \frac{i}{\hbar} g_2 \hat{A}\hat{p}_2\hat{q}_1$ and $Y_1 = \hat{q}_2$,

$$[X_1, Y_1] = \frac{i}{\hbar} g_2 \left[\hat{A}\hat{p}_2\hat{q}_1, \hat{q}_2\right] = \frac{i}{\hbar} g_2 \hat{A}\hat{q}_1 \left[\hat{p}_2, \hat{q}_2\right] = g_2 \hat{A}\hat{q}_1\,, \tag{2.39}$$

$$[X_1, [X_1, Y_1]] = \frac{i}{\hbar} g_2^2 \left[\hat{A}\hat{p}_2\hat{q}_1, \hat{A}\hat{q}_1\right] = 0\,, \tag{2.40}$$

and so the series terminates after only two terms. The application of the BCH lemma in this case gives:

$$\mathrm{e}^{X_1} Y_1 \mathrm{e}^{-X_1} = Y_1 + [X_1, Y_1] + \frac{1}{2!}[X_1, [X_1, Y_1]] + \ldots = \hat{q}_2 + g_2 \hat{A}\hat{q}_1\,. \tag{2.41}$$

Substituting this result into Equation 2.11 then gives:

$$\hat{U}^\dagger \hat{q}_2 \hat{U} = \mathrm{e}^{\left(\frac{i}{\hbar} g_1 \hat{B}\hat{p}_1\right)} \times \left(\hat{q}_2 + g_2 \hat{A}\hat{q}_1\right) \times \mathrm{e}^{\left(-\frac{i}{\hbar} g_1 \hat{B}\hat{p}_1\right)}\,, \tag{2.42}$$

$$\hat{U}^\dagger \hat{q}_2 \hat{U} = \hat{q}_2 + \mathrm{e}^{\left(\frac{i}{\hbar} g_1 \hat{B}\hat{p}_1\right)} \times g_2 \hat{A}\hat{q}_1 \times \mathrm{e}^{\left(-\frac{i}{\hbar} g_1 \hat{B}\hat{p}_1\right)} \,. \tag{2.43}$$

Identifying $X_2 = \frac{i}{\hbar} g_1 \hat{B}\hat{p}_1$ and $Y_2 = g_2 \hat{A}\hat{q}_1$ and applying the BCH lemma again gives the result used in Equation 2.16:

$$[X_2, Y_2] = \frac{i}{\hbar} g_2 g_1 \left[\hat{B}\hat{p}_1, \hat{A}\hat{q}_1\right] \,. \tag{2.44}$$

Now explicitly evaluating the next order term:

$$[X_2, [X_2, Y_2]] = -\frac{1}{\hbar^2} g_2 g_1^2 \left[\hat{B}\hat{p}_1, \left[\hat{B}\hat{p}_1, \hat{A}\hat{q}_1\right]\right] \,. \tag{2.45}$$

This term has odd parity in terms of the $\hat{q}_1$ and $\hat{p}_1$ operators and so will evaluate to zero for an even pointer state. Hence, the next order term will be needed to find a deviation from the $\langle \hat{q}_2 \rangle$ result for weak measurements.

$$[X_2, [X_2, [X_2, Y_2]]] = -\frac{i}{\hbar^3} g_2 g_1^3 \left[\hat{B}\hat{p}_1, \left[\hat{B}\hat{p}_1, \left[\hat{B}\hat{p}_1, \hat{A}\hat{q}_1\right]\right]\right] \tag{2.46}$$

$$\begin{aligned}[X_2, [X_2, [X_2, Y_2]]] = -\frac{i}{\hbar^3} g_2 g_1^3 \Big(&\hat{B}^3 \hat{A} \hat{p}_1^3 \hat{q}_1 - 3\hat{B}^2 \hat{A} \hat{B} \hat{p}_1^2 \hat{q}_1 \hat{p}_1 \\ &+ 3\hat{B}\hat{A}\hat{B}^2 \hat{p}_1 \hat{q}_1 \hat{p}_1^2 - \hat{A}\hat{B}^3 \hat{q}_1 \hat{p}_1^3\Big)\end{aligned} \tag{2.47}$$

To evaluate $\langle \Psi | \, [X_2, [X_2, [X_2, Y_2]]] \, | \Psi \rangle$, we can make use of the same lowering/raising operator formalism as before. Since $\hat{a}|0\rangle = 0$, $\langle 2|0\rangle = 0$ and $\langle 4|0\rangle = 0$ the only combination of lowering and raising terms that won't give a zero expectation value are, $\hat{a}\hat{a}^\dagger\hat{a}\hat{a}^\dagger$ and $\hat{a}^2\hat{a}^{\dagger 2}$. After performing the expansion and evaluating the expectation values we find:

$$\langle \psi | \, [X_2, [X_2, [X_2, Y_2]]] \, | \psi \rangle = -\frac{3}{4\sigma_1^2} g_2 g_1^3 \mathrm{Re}\left[\langle \psi | \hat{A}\hat{B}^3 - \hat{B}\hat{A}\hat{B}^2 | \psi \rangle\right] \,. \tag{2.48}$$

This then gives the result:

$$\langle \hat{q}_2 \rangle = g_1 g_2 \mathrm{Re}\left[\langle \psi | \hat{A}\hat{B} | \psi \rangle\right] - \frac{g_1^3 g_2}{8\sigma_1^2} \mathrm{Re}\left[\langle \psi | \hat{A}\hat{B}^3 - \hat{B}\hat{A}\hat{B}^2 | \psi \rangle\right] \,, \tag{2.49}$$

and hence the condition for the method to work is (assuming that $\frac{\mathrm{Re}\left[\langle \psi | \hat{A}\hat{B}^3 - \hat{B}\hat{A}\hat{B}^2 | \psi \rangle\right]}{\mathrm{Re}\left[\langle \psi | \hat{A}\hat{B} | \psi \rangle\right]}$ is of order unity):

$$\frac{g_1^2}{8\sigma_1^2} << 1 \,. \tag{2.50}$$

This is very similar to the condition that the first measurement is weak – the displacement caused by the first measurement, $g_1\langle\hat{B}\rangle$, must be much smaller than the initial uncertainty in the pointer's position, σ_1.

An equivalent calculation for measuring the imaginary component of the joint weak average (so $X_1 = \frac{i}{\hbar}g_2\hat{A}\hat{p}_2\hat{p}_1$) finds that the same condition is needed.

This condition of weakness has no dependence on any of the parameters of the interaction with the second pointer, including the interaction strength g_2. This second interaction can be of any strength – including strong – enabling larger signals to be measured (and hence improving the signal to noise ratio).

2.1.3 Reuse of the First Pointer

One of the advantages of the conditional scheme is that only a single pointer is read out to find the joint weak average. However, two pointer states are still required to implement this scheme and so it may appear as resource intensive as alternatives. This is not the case, since the first pointer is unused after the second conditional measurement – enabling a subsequent strong measurement to 'overwrite' this pointer.

The unitaries for the conditional weak measurements will be unchanged:

$$\hat{U}_1 = \mathrm{e}^{-ig_1\hat{B}\hat{p}_1/\hbar}\,, \tag{2.51}$$

$$\hat{U}_2 = \mathrm{e}^{-ig_2\hat{q}_1\hat{A}\hat{p}_2/\hbar}\,. \tag{2.52}$$

The unitary for a subsequent strong measurement, using the first pointer, is given by:

$$\hat{U}_3 = \mathrm{e}^{-iG_3\hat{C}\hat{p}_1/\hbar}\,. \tag{2.53}$$

Measuring $\hat{q}_2$

The expectation value of $\hat{q}_2$ will be given by:

$$\langle\hat{q}_2\rangle = \langle\psi|\hat{U}_1^\dagger\hat{U}_2^\dagger\hat{U}_3^\dagger\hat{q}_2\hat{U}_3\hat{U}_2\hat{U}_1|\psi\rangle\,. \tag{2.54}$$

Considering the central 3 'terms' of the expectation value, we can use the BCH lemma to give:

$$\hat{U}_3^\dagger\hat{q}_2\hat{U}_3 = \mathrm{e}^{iG_3\hat{C}\hat{p}_1/\hbar}\hat{q}_2\mathrm{e}^{-iG_3\hat{C}\hat{p}_1/\hbar} = \hat{q}_2 + \frac{i}{\hbar}G_3\left[\hat{C}\hat{p}_1, \hat{q}_2\right] + ... = \hat{q}_2\,. \tag{2.55}$$

Hence the expectation value of $\hat{q}_2$ is unchanged by the additional measurement and will still result in a readout of the joint weak average of $\hat{A}$ and $\hat{B}$.

Measuring $\hat{q}_1$

We can use the same technique to find the expectation of $\hat{q}_1$,

$$\langle\hat{q}_1\rangle = \langle\psi|\hat{U}_1^\dagger\hat{U}_2^\dagger\hat{U}_3^\dagger\hat{q}_1\hat{U}_3\hat{U}_2\hat{U}_1|\psi\rangle\,. \tag{2.56}$$

This time the central three 'terms' give:

$$\hat{U}_3^\dagger\hat{q}_1\hat{U}_3 = \mathrm{e}^{iG_3\hat{C}\hat{p}_1/\hbar}\hat{q}_1\mathrm{e}^{-iG_3\hat{C}\hat{p}_1/\hbar} = \hat{q}_1+\frac{i}{\hbar}G_3\left[\hat{C}\hat{p}_1,\hat{q}_1\right]+... = \hat{q}_1+G_3\hat{C}\,. \tag{2.57}$$

After applying the same technique to the remaining terms we get:

$$\hat{U}_1^\dagger\hat{U}_2^\dagger\hat{U}_3^\dagger\hat{q}_1\hat{U}_3\hat{U}_2\hat{U}_1 = \hat{q}_1 + G_3\hat{C} + g_1\hat{B} + \tfrac{i}{\hbar}G_3g_1\hat{p}_1\left[\hat{B},\hat{C}\right] + ... \tag{2.58}$$

When the first measurement is weak and the second strong such that: $G_3 >> g_1$ and $G_3 >> G_3g_1$, then the expectation for $\hat{q}_1$ will be approximately:

$$\langle\hat{q}_1\rangle \approx \langle\Psi|\hat{q}_1|\Psi\rangle + G_3\langle\Psi|\hat{C}|\Psi\rangle\,, \tag{2.59}$$

which for a pointer initialized with $\langle\hat{q}_2\rangle = 0$ gives:

$$\langle\hat{q}_1\rangle = G_3\langle\psi|\hat{C}|\psi\rangle\,. \tag{2.60}$$

This allows a strong measurement of $\hat{C}$ to be made simultaneously with that of the joint value of $\hat{A}$ and $\hat{B}$.

2.1.4 Using Polarization as a Pointer

Polarization (or any other qubit) is slightly different from the continuous cases considered above – due to the cyclical nature of displacements around the Bloch sphere.

When the second pointer is polarization, the unitary interaction is given by:

$$\hat{U} = \exp\left(-ig_2\hat{q}_1\hat{A}\hat{\sigma}_z/2\right) \times \exp\left(-ig_1\hat{B}\hat{p}_1/\hbar\right)\,, \tag{2.61}$$

where $\hat{p}_2/\hbar$ is replaced with $\hat{\sigma}_z/2$.

We can consider measuring the expectation of $\hat{\sigma}_x$ to be equivalent to measuring the 'position' of the second pointer, $\hat{q}_2$. Using a similar approach as before to find this expectation value:

$$\langle\hat{\sigma}_x\rangle = \langle\Psi|\hat{U}^\dagger\hat{\sigma}_x\hat{U}|\Psi\rangle\,, \tag{2.62}$$

where:

$$\hat{U}^\dagger \hat{\sigma}_x \hat{U} = \mathrm{e}^{ig_1 \hat{B}\hat{p}_1/\hbar} \mathrm{e}^{ig_2 \hat{q}_1 \hat{A}\hat{\sigma}_z/2} \hat{\sigma}_x \mathrm{e}^{-ig_2 \hat{q}_1 \hat{A}\hat{\sigma}_z/2} \mathrm{e}^{-ig_1 \hat{B}\hat{p}_1/\hbar} \,. \tag{2.63}$$

The middle 3 terms can be evaluated with the BCH lemma:

$$\mathrm{e}^{ig_2 \hat{q}_1 \hat{A}\hat{\sigma}_z/2} \hat{\sigma}_x \mathrm{e}^{-ig_2 \hat{q}_1 \hat{A}\hat{\sigma}_z/2} = \cos\left(g_2 \hat{q}_1 \hat{A}\right) \hat{\sigma}_x - \sin\left(g_2 \hat{q}_1 \hat{A}\right) \hat{\sigma}_y \,. \tag{2.64}$$

Making the substitution $g_2 \hat{q}_1 \hat{A} = \hat{\phi}$, gives:

$$\hat{U}^\dagger \hat{\sigma}_x \hat{U} = \mathrm{e}^{ig_1 \hat{B}\hat{p}_1/\hbar} \left(\cos(\hat{\phi})\hat{\sigma}_x - \sin(\hat{\phi})\hat{\sigma}_y\right) \mathrm{e}^{-ig_1 \hat{B}\hat{p}_1/\hbar} \,. \tag{2.65}$$

The BCH lemma can be applied again to give:

$$\begin{aligned} \hat{U}^\dagger \hat{\sigma}_x \hat{U} =& \cos(\hat{\phi})\hat{\sigma}_x - \sin(\hat{\phi})\hat{\sigma}_y \\ &+ \frac{i}{\hbar} g_1 \sigma_x \left[\hat{B}\hat{p}_1, \cos\hat{\phi}\right] - \frac{i}{\hbar} g_1 \sigma_y \left[\hat{B}\hat{p}_1, \sin\hat{\phi}\right] + \mathcal{O}(g_1^2) \,. \end{aligned} \tag{2.66}$$

To evaluate these commutators, we can consider the Taylor expansion of the sine and cosine terms. Neglecting any terms that are third order or higher in the product of g_1 and g_2 gives:

$$\begin{aligned} \hat{U}^\dagger \hat{\sigma}_x \hat{U} =& \cos(\hat{\phi})\hat{\sigma}_x - \sin(\hat{\phi})\hat{\sigma}_y \\ &+ \frac{i}{\hbar} g_1 \sigma_x \left[\hat{B}\hat{p}_1, \mathbb{1}\right] - \frac{i}{\hbar} g_1 \sigma_y \left[\hat{B}\hat{p}_1, \hat{\phi}\right] + \mathcal{O}(g^3) \,, \end{aligned} \tag{2.67}$$

$$\begin{aligned} \hat{U}^\dagger \hat{\sigma}_x \hat{U} =& \cos(g_2 \hat{q}_1 \hat{A})\hat{\sigma}_x - \sin(g_2 \hat{q}_1 \hat{A})\hat{\sigma}_y \\ &- \frac{i}{\hbar} g_1 g_2 \sigma_y \left[\hat{B}\hat{p}_1, \hat{q}_1 \hat{A}\right] + \mathcal{O}(g^3) \,. \end{aligned} \tag{2.68}$$

However, this is only valid when g_2 is small – and so the 2nd measurement can no longer be strong.

For an initial first pointer state which is an even function of $\hat{q}_1$, the expectation value of the odd operator $\sin\left(g_2 \hat{q}_1 \hat{A}\right)$ will be zero. When the second pointer is initialized as circular polarized, $|L\rangle$, an eigenstate of $\hat{\sigma}_y$, then $\langle L|\hat{\sigma}_x|L\rangle = 0$ and $\langle L|\hat{\sigma}_y|L\rangle = 1$. This then gives the expectation value of the second pointer to be:

$$\begin{aligned} \langle\hat{\sigma}_x\rangle =& \langle\Psi|\hat{U}^\dagger \hat{\sigma}_x \hat{U}|\Psi\rangle \\ \approx& \frac{-ig_1 g_2}{\hbar} \langle\psi| \left[\hat{B}\hat{p}_1, \hat{q}_1 \hat{A}\right] |\psi\rangle = -g_1 g_2 \mathrm{Re}\left[\langle\psi|\hat{A}\hat{B}|\psi\rangle\right] \,, \end{aligned} \tag{2.69}$$

very similar to the case of a continuous second pointer given in Equation 2.7.

2.1.5 Binary Conditionality

The original conditional scheme of Lundeen and Bamber [28] proposed that the strength of the second measurement depends linearly on the pointer position. However, a simpler – binary – conditionality is also able to measure the weak joint value.

For the binary conditional scheme, the unitary for the complete interaction is given by:

$$\hat{U} = \exp\left(-ig_2\hat{q}_\pm\hat{A}\hat{p}_2/\hbar\right) \times \exp\left(-ig_1\hat{B}\hat{p}_1/\hbar\right) , \tag{2.70}$$

where $\hat{q}_\pm$ is:

$$\hat{q}_\pm = \begin{cases} 1 & \text{if } \hat{q}_1 > 0 \\ -1 & \text{if } \hat{q}_1 < 0 \,, \end{cases} \tag{2.71}$$

In the position basis, $\hat{q}_\pm$ is represented as:

$$\hat{q}_\pm(q_1) = 2H(q_1) - 1 \,, \tag{2.72}$$

where $H(q_1)$ is the Heaviside step function.

The BCH approach used previously can be applied in the same way until reaching Equation 2.17, but with $\hat{q}_1$ replaced with $\hat{q}_\pm$,

$$\langle\hat{q}_2\rangle = \frac{i}{\hbar} g_1 g_2 \langle\Psi|\hat{B}\hat{A}\hat{p}_1\hat{q}_\pm - \hat{A}\hat{B}\hat{q}_\pm\hat{p}_1|\Psi\rangle \,. \tag{2.73}$$

As before, we consider the pointer state to be in the Gaussian state given by Equation 2.18 – although now evaluated explicitly in the position basis rather than in terms of raising or lowering operators.

$$\begin{aligned} {}_1\langle 0|\hat{q}_\pm\hat{p}_1|0\rangle_1 &= \frac{1}{\sqrt{2\pi\sigma^2}} \int_{-\infty}^{\infty} \mathrm{e}^{\frac{-q_1^2}{4\sigma^2}} \left(2H(q_1) - 1\right) (-i\hbar) \frac{\mathrm{d}}{\mathrm{d}q_1} \mathrm{e}^{\frac{-q_1^2}{4\sigma^2}} \mathrm{d}q_1 && (2.74) \\ &= \frac{i\hbar}{\sqrt{2\pi\sigma^2}} \int_{-\infty}^{\infty} \left(2H(q_1) - 1\right) \frac{q_1}{2\sigma^2} \mathrm{e}^{-\frac{q_1^2}{2\sigma^2}} \mathrm{d}q_1 && (2.75) \\ &= \frac{i\hbar}{\sqrt{2\pi\sigma^2}} \,. && (2.76) \end{aligned}$$

For the other ordering of $q_\pm$ and p_1, the expectation is:

$${}_1\langle 0|\hat{p}_1\hat{q}_\pm|0\rangle_1 = \frac{1}{\sqrt{2\pi\sigma^2}} \int_{-\infty}^{\infty} \mathrm{e}^{\frac{-q_1^2}{4\sigma^2}} (-i\hbar) \frac{\mathrm{d}}{\mathrm{d}q_1} \left(\left(2H(q_1) - 1\right) \mathrm{e}^{\frac{-q_1^2}{4\sigma^2}} \right) \mathrm{d}q_1 \,. \tag{2.77}$$

The derivative of the Heaviside function is a Dirac delta function [88], giving:

$$ {}_1\langle 0|\hat{p}_1\hat{q}_\pm|0\rangle_1 = \frac{-i\hbar}{\sqrt{2\pi\sigma^2}}\int_{-\infty}^{\infty} \mathrm{e}^{\frac{-q_1^2}{2\sigma^2}}\left(2\delta(q_1) + \frac{-q_1}{2\sigma^2}\left(2H(q_1)-1\right)\right)\mathrm{d}q_1 \tag{2.78} $$

$$ = \frac{-i\hbar}{\sqrt{2\pi\sigma^2}}\,. \tag{2.79} $$

Substituting these results into Equation 2.73 gives:

$$ \langle\hat{q}_2\rangle = \frac{g_1g_2}{\sqrt{2\pi\sigma^2}}\langle\Psi|\hat{B}\hat{A}+\hat{A}\hat{B}|\Psi\rangle = \frac{g_1g_2\sqrt{2}}{\sqrt{\pi\sigma^2}}\mathrm{Re}\left[\langle\psi|\hat{A}\hat{B}|\psi\rangle\right]\,. \tag{2.80} $$

This binary scheme has a number of advantages over the original proposal. It allows for a far simpler conditional coupling between the two pointers – rather than requiring the strength of the second interaction to vary linearly with the first pointer 'position', the strength of interaction can take just two values.

This is especially useful when there is experimental noise in the control of the interaction strength. By requiring only two values for the interaction strength, which can be far apart, small fluctuations around these ideal strengths have much less effect than they would in the linear scheme.

Binary Conditionality of Polarization Rotation

The use of the binary conditionality scheme also has the advantage of enabling strong second measurements when using polarization as the second pointer.

Using the same arguments as in Section 2.1.4, we find that for a Gaussian first pointer and the second pointer initialized with the circular polarization $|L\rangle$:

$$ \langle\Psi|\hat{U}^\dagger\hat{\sigma}_x\hat{U}|\Psi\rangle = -\frac{i}{\hbar}g_1\langle\psi|\left[\hat{B}\hat{p}_1, \sin\left(g_2\hat{A}\hat{q}_\pm\right)\right]|\psi\rangle + \mathcal{O}(g_1^2)\,. \tag{2.81} $$

We can consider the full Taylor expansion of the sine term:

$$ \sin\left(g_2\hat{A}\hat{q}_\pm\right) = g_2\hat{A}\hat{q}_\pm + \ldots + \frac{-1^n}{(2n+1)!}g_2^{2n+1}\hat{A}^{2n+1}\hat{q}_\pm^{2n+1} + \ldots \tag{2.82} $$

It is simple to see (for instance by considering the position representation) that $\hat{q}_\pm^{2n+1} = \hat{q}_\pm$. Then for any operator $\hat{A}$, which satisfies $\hat{A}^{2n+1} = \hat{A}$ we find:

$$ \sin\left(g_2\hat{A}\hat{q}_\pm\right) = \sin\left(g_2\right)\hat{A}\hat{q}_\pm\,. \tag{2.83} $$

The restriction on the properties of $\hat{A}$ are not overly limiting. Any idempotent operator will satisfy this condition – including all projectors.

When $\hat{A}$ is of the correct form, this then gives:

$$\langle \hat{\sigma}_x \rangle = \frac{-g_1\sqrt{2}}{\sqrt{\pi\sigma^2}} \sin(g_2)\, \mathrm{Re}\left[\langle\psi|\hat{A}\hat{B}|\psi\rangle\right] . \tag{2.84}$$

There is now no constraint on strength of the second interaction g_2 – with the maximum strength achieved when $g_2 = \frac{\pi}{2}$. This corresponds to a rotation on the Bloch sphere of $+\frac{\pi}{2}$ for $q_1 > 0$ and $-\frac{\pi}{2}$ for $q_1 < 0$.

2.1.6 Conditional Measurement Summary

In this section we presented the proposal of Lundeen and Bamber [28] to perform a conditional joint weak measurement of two observables. By conditionally coupling two pointers – where the second pointer's interaction strength depends on the outcome of the first – joint operator's weak average can be directly inferred from the shift in the second pointer's position. This requires only a single pointer to be readout to obtain the joint weak value. Depending on the exact configuration of the measurement interaction either the real or the imaginary component of the weak joint value can be measured. However, a key disadvantage of this method is that the initial interaction must be weak and performed without postselection, which generates a very small signal, and the conditional coupling introduces greater experimental complexity than alternative sequential measurement schemes.

Building upon this framework, we showed that when a measurement of this form is performed, the first pointer can be 'reused' to perform a strong measurement of another observable. This demonstrates that requiring the readout of a single pointer provides a usable advantage in the degrees of freedom of the optical system available. We also considered the modifications required when one pointer is polarization (i.e. a qubit) rather than a continuous pointer.

Finally, we showed that the conditional scheme does not require that the strength of the second interaction vary linearly with the result of the first. A binary conditional scheme – where the second interaction strength varies only in its sign (and not its strength) – is able to reproduce the results of the original proposal. This has the advantage of being easier to implement – both by no longer requiring a linear variation in interaction strength and also being more robust to noise in the interaction strength.

Key Findings

- A conditional scheme enables the joint weak value to be readout directly using only a single pointer. (Section 2.1)
- After the second interaction, the first pointer is able to be reused to perform a measurement of a different observable. (Section 2.1.3)
- There are only small modifications required if the second pointer is a qubit and no longer continuous. (Section 2.1.4)
- A binary conditional scheme, which only varies the sign of the second interaction, reproduces the key results while being more robust to noise and easier to implement. (Section 2.1.5)

2.2 Experimental Design

In this section, we describe the design of an experiment to measure the joint weak value of the position and momentum projector operators of a photon – using a conditional scheme. The first pointer is the y transverse position and the second pointer is the polarization. The position is coupled to the first pointer using a tilted glass sliver and the momentum is conditionally coupled to polarization using a spatial light modulator (SLM).

It was decided to measure the conjugate projector operators of transverse position, $\hat{\pi}_x$, and momentum, $\hat{\pi}_p$, for a photon to demonstrate the conditional scheme. The primary motivation for selecting these operators is their status as canonical conjugate variables (and hence leaving more degrees of freedom of the photon available to be used as pointers). Measuring their joint average would also enable measurement of the the Kirkwood-Dirac distribution. This distribution offers a complete phase-space characterization of the photon's transverse spatial state, providing an alternative to standard quantum state tomography. In addition, the real part of the Kirkwood-Dirac distribution (which would be directly measured when using a cylindrical lens to perform the Fourier transform in this scheme) is known as the Margenau-Hill distribution [89] and is of interest in its own right.

This choice of measurement observables then allowed the use of y, polarization or frequency as choices for the pointer states (since only the internal degrees of freedom of the photon are easy to couple together). Polarization and y were chosen due to the experimentally simpler equipment to manipulate these degrees of freedom.

Since this scheme should require minimal post processing, and a single value for each x and p value, the readout of the second pointer should be possible to do with a bucket detector. This is more natural when measuring polarization than transverse y position.

This then gives the conceptual arrangement shown in Figure 2.2.

2.2.1 Unitaries Using Y and Polarization as Pointers

For an experiment, measuring the discrete projectors of x and p_x, using the y position as the 1st pointer and the polarization as the second pointer, the

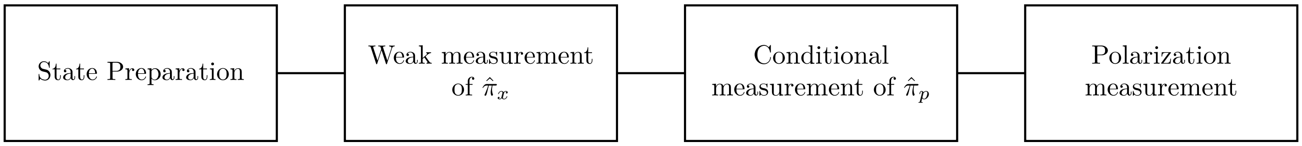

Figure 2.2: A conceptual outline of the components needed to perform a conditional measurement of the joint weak average of the position and momentum projectors. The state to be measured is prepared. Then the x position projector, $\hat{\pi}_x$, is weakly coupled to the first pointer (y transverse position). The x momentum projector, $\hat{\pi}_p$, is then coupled to the second pointer (polarization) in a way that the strength of this interaction depends on the first pointer (y position). The joint weak average is then readout by measuring the second pointer 'position' (polarization).

unitaries must be:

$$\hat{U}_1 = \mathrm{e}^{-ig_1\hat{\pi}_{x_i}\hat{p}_y/\hbar} \approx 1 - ig_1\hat{\pi}_{x_i}\hat{p}_y/\hbar\,, \tag{2.85}$$

$$\hat{U}_2 = \mathrm{e}^{-ig_2\hat{y}\hat{\pi}_{k_j}\hat{\sigma}_z/2} \approx 1 - ig_2\hat{y}\hat{\pi}_{k_j}\hat{\sigma}_z/2\,, \tag{2.86}$$

where g_1 and g_2 are the respective coupling strengths of the two measurement interactions; $\hat{\pi}_{x_i} = |x_i\rangle\langle x_i|$ is the x position projector; $\hat{\pi}_{k_j} = |k_j\rangle\langle k_j|$ is the x momentum projector, where $|k_j\rangle = \sum_i \mathrm{e}^{ik_jx_i}|x_i\rangle$ and $k_j = p_{x_j}/\hbar$; $\hat{p}_y$ and $\hat{y}$ are the momentum and position operators for the y transverse direction; and $\hat{\sigma}_z$ is the Pauli matrix corresponding to measurements on the $|H\rangle/|V\rangle$ axis of the Bloch sphere.

When the second pointer is initialized in a circular polarization state, the expectation value of the polarization state in the diagonal/anti-diagonal basis will be:

$$\langle\Psi'|\hat{\sigma}_x|\Psi'\rangle = -g_1g_2\mathrm{Re}\left[\langle\psi|\hat{\pi}_{k_j}\hat{\pi}_{x_i}|\psi\rangle\right]\,. \tag{2.87}$$

2.2.2 Weak Measurement of $\hat{\pi}_x$

The first measurement shown in Figure 2.3 is that of $\hat{\pi}_x$. The required interaction is that a photon at a position x_i must be displaced by a small amount in the y-direction (compared to the width of the beam in y). This can be accomplished using a tilted 'sliver' of glass as shown in Figure 2.4.

The amount of displacement, g_1, depends on the thickness of the sliver, t;

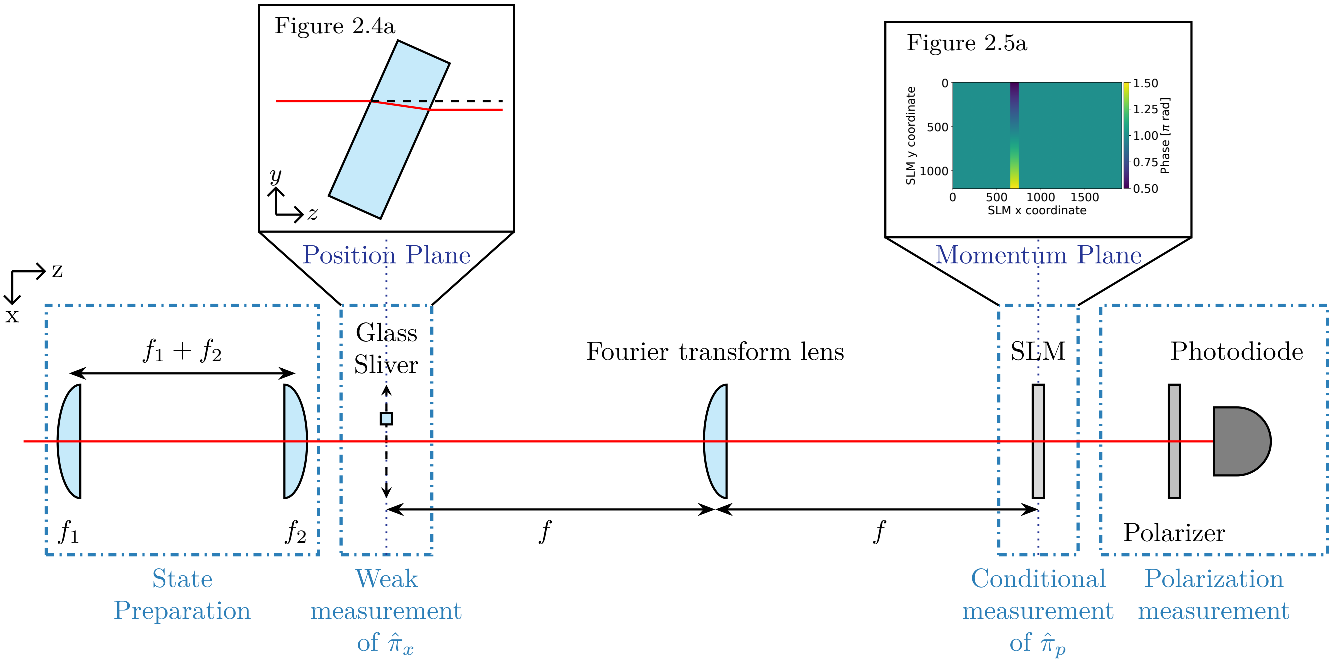

Figure 2.3: A schematic of the key optical components required to perform the conditional measurement of the joint weak value of position and momentum for a photon. The first weak measurement of position is performed by the glass sliver. The second measurement of momentum is performed using the spatial light modulator (SLM). The second pointer 'position' (polarization) is then read out.

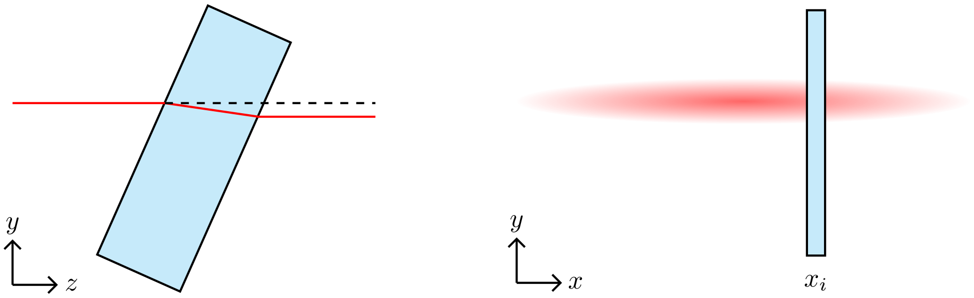

(a) (b)

Figure 2.4: (a) Light passing though a tilted plate of glass will be displaced by refraction. (b) When this glass is a thin 'sliver' at a particular x_i, only the light passing through the sliver will be displaced.

the sliver's refractive index, n; and its angle of tilt, θ:

$$g_1 = t \sin\theta \left(1 - \frac{\cos\theta}{\sqrt{n^2 - \sin^2\theta}}\right) . \tag{2.88}$$

For small angles, this can be approximated as:

$$g_1 \approx t\theta \left(1 - \frac{1}{n}\right) . \tag{2.89}$$

Sliver Parameters

We require that the displacement of the beam is small compared to the y transverse width σ_1.

$$g_1 << 2\sqrt{2}\sigma_1 \tag{2.90}$$

Collimating the light after a single mode fiber, using the aspheric lens readily available, will create a beam with a width of around 1 mm.

A larger displacement will result in a larger (and easier to detect) signal. Hence, there needs to be a balance between a small displacement (so that the measurement is weak), but large enough to have a detectable signal. It was decided that a displacement of around 0.15 of the beam width (0.15 mm) would be used.

For a fused silica (refractive index, $n = 1.45$) sliver with thickness $t = 1$ mm, this would require a tilt angle of 26°. For the experiment, a block with an angle of 24° was used, giving a displacement of $g_1 = 0.140$ mm.

Sliver Phase

Light passing through the glass sliver will pick up a phase, $\Delta\phi$, compared to light that does not pass through the glass,

$$\Delta\phi = \frac{2\pi t(n-1)}{\lambda\cos\theta} , \tag{2.91}$$

where λ is the wavelength of the light.

There will be no effect of this phase if it is an integer number of 2π (and the coherence length of the beam is longer than the path length through the glass sliver). The phase can be fine tuned by small changes to the angle θ until this condition is met.

2.2.3 Operational Measurement of $\hat{\pi}_p$

The second measurement requires the unitary given in Equation 2.86. This unitary describes a process where the polarization of light, at a specific k_j, is rotated about $|H\rangle/|V\rangle$ axis by an amount that depends linearly on its y transverse position. For light with any other value of k, there should be no change to the polarization.

To perform this measurement, it is useful to consider the Fourier plane (introduced in Section 1.2.2) after a lens which is placed one focal length from the plane of the position measurement (as shown in Figure 2.3). In the Fourier plane, the transverse x' position corresponds to the values of k_x or x momentum, p_x, at the plane of the first measurement.

$$x' = \frac{f\lambda k_x}{2\pi} = \frac{f\lambda p_x}{h}\,, \tag{2.92}$$

where λ is the wavelength of the light (in this experiment 809 nm narrow-linewidth laser) and f is the focal length of the lens.

The polarization at a particular k can be rotated using a similar approach as the measurement of position – using a sliver at a particular transverse position in the Fourier plane.

The optical component typically used to rotate polarization, a waveplate, will not be suitable here. This is because the amount of rotation needs to vary with the y-transverse position, while for a typical waveplate it is constant. In principle, it would be possible to create a wedge shaped birefringent crystal that would create the desired rotation. However, it would be very challenging to create this as a very thin sliver.

An alternative is to make use of liquid crystals. These are birefringent fluids where the fast axis of the molecules can vary with position - creating an optical element that imparts a spatially dependent polarization rotation. This has been widely used for the creation of q-plates, but the techniques can be used to produce a generic pattern [90, 91]. There are, however, limits to the feature size that can be written in these plates. This would restrict how thin a sliver can be fabricated and hence the resolution that could be achieved in measuring k.

LCOS Spatial Light Modulator

Another option would be to use a Liquid Crystal on Silicon Spatial Light Modulator (LCOS SLM) [92]. This is also a liquid crystal based device, but the crystals are able to be controlled individually on an array of millions of pixels

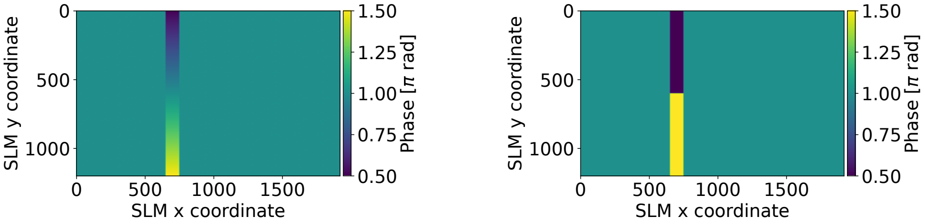

(a) Linear conditional sliver

(b) Binary conditional sliver

Figure 2.5: Phase patterns displayed on the SLM to perform a measurement of momentum that is conditional on the y position.

(1920 × 1200 for the SLM used in this thesis) – each a few microns across (8 µm for the SLM used). These devices are constructed so that the fast axis of the liquid crystals is orientated horizontally so that light polarized in this direction gains an additional phase, ϕ. Typically, LCOS SLMs are used to impart a phase pattern onto light polarized along this axis. This has applications in beam shaping, steering and holography – often making use of blazed gratings [92].

LCOS SLMs can also be used in zeroth order to control the polarization state of light [93–96]. Since light polarized orthogonally to the SLM's fast axis will not experience any phase shift, the Jones matrix representation of the SLM (pixel) will be:

$$\begin{pmatrix} e^{i\phi} & 0 \\ 0 & 1 \end{pmatrix} . \tag{2.93}$$

This has the action of rotating the polarization around the $|H\rangle/|V\rangle$ axis of the Bloch sphere and corresponds to the unitary:

$$\hat{U} = e^{i\frac{\phi}{2}\sigma_z} , \tag{2.94}$$

which is exactly the form required for Equation 2.86 when ϕ varies with y transverse position. This should be easy to accomplish with an SLM since the value of ϕ can be set for each pixel – allowing for the strength of the coupling (amount of polarization rotation) to depend linearly on y position. This corresponds to a linear phase gradient on the SLM as shown in Figure 2.5a. Alternatively the binary conditionality scheme theoretically discussed in Section 2.1.5 can be used, that then requires the 'split' sliver shown in Figure 2.5b to be displayed on the SLM.

An SLM was chosen to implement the second interaction due to its small pixel size (allowing for narrow slivers) and the ease to display gradients of any strength at arbitrary positions.

2.2.4 Polarization Readout

The polarization state of the second pointer is to be readout. To measure $\langle\sigma_x\rangle$, the intensity (or counts) of diagonally, I_D, and anti-diagonally, I_A, polarized light is observed,

$$\langle\sigma_x\rangle = \frac{I_D - I_A}{I_D + I_A}\,. \tag{2.95}$$

This can be performed in two main ways – rotating a polarizer between the $|D\rangle$ and $|A\rangle$ axes and taking a measurement; or using a polarizing beam splitter (PBS) and a half waveplate.

Both of these approaches will be sensitive to imperfect zero phase for the SLM regions outside the phase gradient sliver. This will mean that incoming circular polarized light will experience a small polarization rotation and so the diagonal and anti-diagonal intensities will no longer perfectly balance. This is, at least to some degree, unavoidable – the discretized nature of the phase applied by the SLM means, that on average, the closest to zero phase that can be achieved (for a 10-bit SLM) is: $\phi = \frac{2\pi\mathrm{rad}}{1024\times 2} = 3\,\mathrm{mrad}$. This would result in a measurement of the diagonal polarization $\langle\sigma_x\rangle = 3\times 10^{-3}$. Whilst small, the signals we are expecting to measure are on a similar scale.

Even more troublesome, is that not every pixel on the SLM responds with exactly the same phase – there is some variation between them. This will result in an increase to this background signal. There are multiple ways to address this issue. One approach would be to measure the polarization state with zero phase displayed over the entire SLM and subtract this as a background. An alternative approach is to find a way to keep the background intensity exactly the same for measurements in both polarization bases, and to only vary the signal we want to measure. This can be accomplished if, rather than measuring in two bases, $|D\rangle$ and $|A\rangle$, measurements are only made in one basis and the sign of g_2 (the direction of the phase gradient sliver) is varied between measurements to be subtracted instead.

This approach works since the change in I_D and I_A from the initial state are equal in magnitude and opposite in sign. Hence, when the direction of rotation is flipped, the new I_D will be equal to the measurement of I_A before the direction was flipped. This will result in removing the ‘zero phase’ background mentioned above. In addition, this approach enables the relatively fast switching between two measurements, limited only by the switching speed of the SLM. This is significantly faster than rotating a polarizer between the D and A axes. This also allows for the effect of slow fluctuations in laser intensity to not affect measurements of the polarization state – since the two measurements needed can be made on a timescale much shorter than the slow laser variation.

Compared to using a PBS and half waveplate, the switching gradient scheme has the advantage of not requiring additional polarization optics (which will not work optimally for the non-collimated beam found after the SLM) and only requires one intensity readout.

2.2.5 Beam Initialization

The beam before the first measurement must be initialized into a state to be measured. However, this state is only in the x-direction of the beam. The y-direction must be a Gaussian profile (this is the first pointer state).

We also want to be able to perform high resolution measurements in the x-direction. This requires that the beam is much wider in x than the width of the glass sliver (which practically cannot be smaller than 1 mm since it must be cut from a glass window). To satisfy this, the beam must be initialized to be Gaussian in y and to be wide in x. Once a beam of this form has been created then it will be fairly simple to add additional elements (such as phase jumps) to modify the x wave function.

Creating a Wide Beam

There are 3 main ways to create a wide beam from a small symmetric collimated Gaussian beam (the collimated output of a fiber coupled laser). One way is to make use of cylindrical lenses in a telescope arrangement as shown in Figure 2.6 [3]. This causes the beam to be expanded in one direction by an amount equal to the ratio of the two focal lengths of the lenses. However, cylindrical lenses are more challenging to manufacture than equivalent spherical lenses [97] and lower aberration doublet lenses are not widely available.

An alternative is to use anamorphic prism pairs [98] as shown in Figure 2.7. These systems are, however, limited to relatively small magnifications (generally less than 10).

Another option is not to expand an initial collimated beam, but rather to create a diverging beam and then collimate it once it has reached the desired width. One method to do this, is to make use of diffraction from a single slit. The y profile of the beam is unchanged by a 1 dimensional slit. However, most of the light from the initial beam is blocked by the slit.

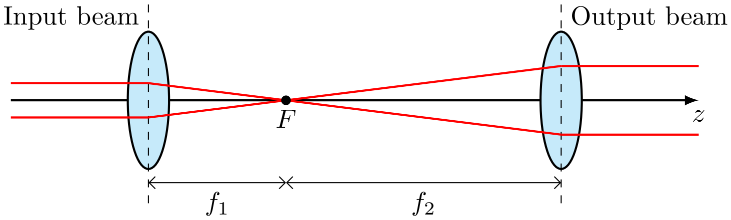

Figure 2.6: Two lenses arranged as a telescope to expand a collimated beam. The expansion magnification is equal to $M = \frac{f_2}{f_1}$.

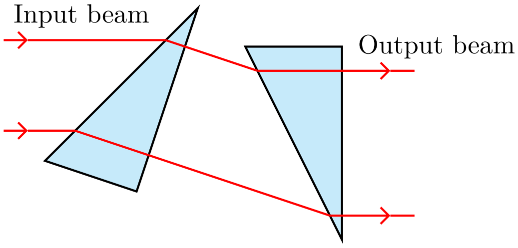

Figure 2.7: A pair of prisms can be arranged to widen a beam by making use of the fact that the width of a beam appears larger when a cross section is not taken perpendicular to the direction of the beam.

It was decided to use a cylindrical lens telescope since this had the flexibility of allowing large magnifications (and hence enabling a high resolution in measurement of x) without the large loss of intensity due to passing through a single slit.

2.2.6 Creating the Fourier Plane

To perform the conditional measurement of $\hat{\pi}_p$, we require access to the Fourier plane. This can be done using a lens as described in Section 1.2.2. When measuring the real part of the joint weak average, only the x-direction should be Fourier transformed and so we require the use of a cylindrical lens. To measure the imaginary part of the joint weak average, the Fourier plane must correspond to momentum for both x and the first pointer y. This requires a standard (spherical) lens.

The momentum, p_x, (in the position measurement plane) corresponds to a position, x', in the Fourier plane:

$$x' = \frac{\lambda f}{2\pi} k_x = \frac{\lambda f}{2\pi\hbar} p_x \, . \tag{2.96}$$

To get a high resolution in momentum measurements, we want the largest possible x' for a given p_x. This is accomplished by using a long focal length lens which is also advantageous since aberrations are typically smaller for these lenses. Since the beam is also wide, in order to achieve high resolution in x, this is limited to a maximum $f = 500\,\mathrm{mm}$ by part availability.

2.2.7 Experimental Design Summary

This section presents the experimental design for conducting conditional weak measurements of position, $\hat{\pi}_x$, and momentum, $\hat{\pi}_k$, projectors in an optical system. The approach utilizes the transverse y position and polarization of a photon as pointer states. The measurement scheme involves two sequential interactions: a weak displacement in the y direction at a particular position, x, using a glass sliver; followed by a polarization rotation at a specific momentum, k, where the strength of the rotation is conditional on the y position, using a liquid crystal spatial light modulator (SLM). This enables the readout of the real part of the joint weak average of the position and momentum projectors, $\mathrm{Re}\left[\hat{\pi}_k\hat{\pi}_x\right]$, by measuring polarization in the diagonal basis.

Several technical considerations are addressed, including the phase due to passing through the glass sliver, beam initialization, and using a switching gradient scheme in the polarization readout to mitigate background signals and fluctuations.

Key Findings

- The unitiaries required to perform a joint measurement of the position and momentum projectors can be achieved with standard optical equipment. (Section 2.2)
- The first measurement interaction uses a tilted glass sliver to displace photons in y at specific x positions, while the second interaction employs an LCOS Spatial Light Modulator to implement polarization rotation dependent on y position in the Fourier plane. (Section 2.2.2 and 2.2.3)
- A polarization readout technique involving switching the gradient direction rather than rotating measurement bases reduces the observed background. (Section 2.2.4)
- The beam is initialized to be a wide Gaussian by making use of a telescope of cylindrical lenses. (Section 2.2.5)

2.3 Simulation

This section presents the computational framework and results of simulations designed to validate our optical setup for measuring joint weak averages of position and momentum. We find a systematic artifact observed near zero momentum and present a way to correct for this. We then examine the simulation results for various experimental configurations and compare them with theoretical Kirkwood-Dirac distributions, demonstrating good agreement when experimental resolution constraints are considered.

The section continues with comparisons between different measurement approaches – two versus one polarization readouts and linear versus binary conditionality – confirming their equivalence. Finally, we introduce a simplified, GPU-accelerated simulation method that significantly reduces computational time while maintaining qualitative agreement with the full model, and explore how beam clipping and phase plates affect the observable features in the Kirkwood-Dirac distribution.

Simulation of All Optical Components

Simulations of the optical components above were performed to confirm that the proposed experiment would enable the measurement of the joint weak average of x and p_x. To perform these simulations, the Fourier optics approach introduced in Section 1.2.2 was used. The code to perform these simulations are in a *Jupyter Notebook* [99] that can be found at `https://gitlab.com/tjbailey/phd-thesis/-/blob/main/SimulationCode/FullExperimentSimulationNotebook.ipynb`.

This code was written in Python [100] and represents the electric field amplitude as a 2d complex NumPy array [101]. When polarization is important, this becomes a 3d array – with each previous array element being replaced by a Jones vector for that position in space.

Propagation in free space is performed using a Fourier optics approach – with the Fourier transforms calculated using the Fast Fourier Transform [102]. These simulations do not make use of the Fresnel approximation (a type of paraxial approximation) and use the full transfer function:

$$H\left(k_x, k_y, d\right) = \mathrm{e}^{-id\sqrt{k^2-k_x^2-k_y^2}} = \mathrm{e}^{-id\sqrt{\frac{4\pi^2}{\lambda^2}-k_x^2-k_y^2}}, \tag{2.97}$$

for propagation by a distance d in the $\hat{\mathbf{z}}$ direction; k_x and k_y are the spatial frequencies in the $\hat{\mathbf{x}}$ and $\hat{\mathbf{y}}$ directions; and k is the wavenumber [3].

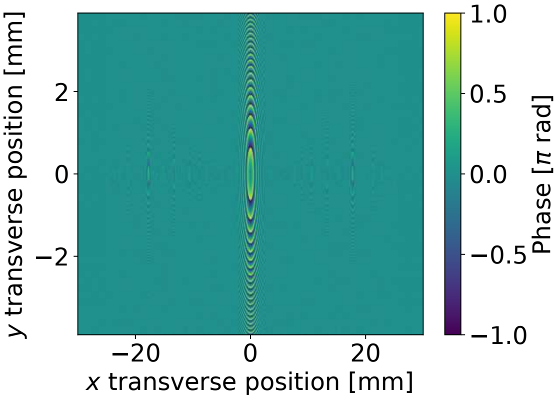

Figure 2.8: An example quadratic phase mask of a ‘normal’ (non cylindrical) lens with a focal length of $f = 500\,\mathrm{mm}$ and for light with a wavelength of $810\,\mathrm{nm}$. The lens has a circular aperture of radius $25\,\mathrm{mm}$ and so the amplitude transmission outside this region is zero (which cannot be clearly shown on a plot of phase). The features seen along the horizontal centerline ($y = 0$) are due to aliasing with the grid discretizing space.

This transfer function is applied to the Fourier transform of the electric field amplitude of the wave:

$$\tilde{E}\left(k_x, k_y, z+d\right) = \tilde{E}\left(k_x, k_y, z\right) \times H\left(k_x, k_y, d\right) \; . \tag{1.35 revisited}$$

However, only beams of light with small transverse momenta were considered and so the results we find should not differ from those that would have been found if we had made the paraxial approximation.

Other optical elements (such as lenses or apertures) are applied as phase and/or amplitude masks (an example for a lens is shown in Figure 2.8). The small displacement from the tilted glass sliver was performed by displacing the relevant columns of the 2d array by an appropriate amount (possibly with a uniform phase shift).

Improved simulation speed was achieved using the Numba [103] (providing very simple to implement just-in-time compilation that significantly increased the speed of some functions) and Joblib [104] (to provide for parallel computation) packages. All visualizations were performed using Matplotlib [105].

The theoretical Kirwood-Dirac distributions were found by calculating the density matrix of the photon position from the beam amplitude (using $\rho(x_i, x_k) =$

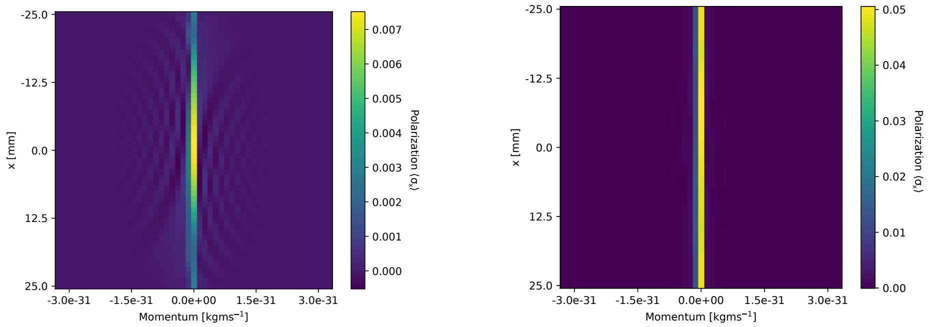

(a) Real

(b) Imaginary

Figure 2.9: The simulated $\langle \sigma_x \rangle$ measurement for the optical arrangements to measure the real and imaginary parts of the weak joint average. These simulations are performed using parameters corresponding to the optical elements outlined in Section 2.4. The key features are an extended positive region along the vertical centerline (corresponding to the region of high intensity on the SLM) and (in the measurement of the real part) fringes to either side.

$\psi(x_i)\psi(x_k)^*$) and then calculating the Kirkwood-Dirac distribution,

$$D(x_i, p_j) = \mathrm{e}^{-ip_j x_i/\hbar} \sum_k \rho(x_i, x_k) \mathrm{e}^{ip_j x_k/\hbar} \,. \qquad \text{(1.77 revisited)}$$

Large Values at Zero Momentum

One reoccurring feature of the simulations is large measured values of $\langle \sigma_x \rangle$ around zero momentum. This can be seen in Figure 2.9 – especially clearly in the imaginary component, although the effect also appears in the real part. This is not expected for these joint weak measurements, as seen by the lack of any such feature in the theoretical Kirkwood-Dirac distributions (such as Figure 2.12).

This effect occurs regardless of the polarization readout scheme used (whether measuring in two bases or one with a flipped conditional strength) and is seen experimentally (as shown in Figure 2.34).

This feature is seen in the region of the beam with high intensity and is due to the discretization of the y position into pixels. This means that the light above and below the $y = 0$ level can never balance exactly and so there will always be a ‘small offset’ in the output that will be proportional to the intensity of the beam at that value of momentum. For regions of the beam far from zero momentum this is negligible – the beam has very low intensity. However, for the region of the beam near zero momentum the intensity is high and this ‘small

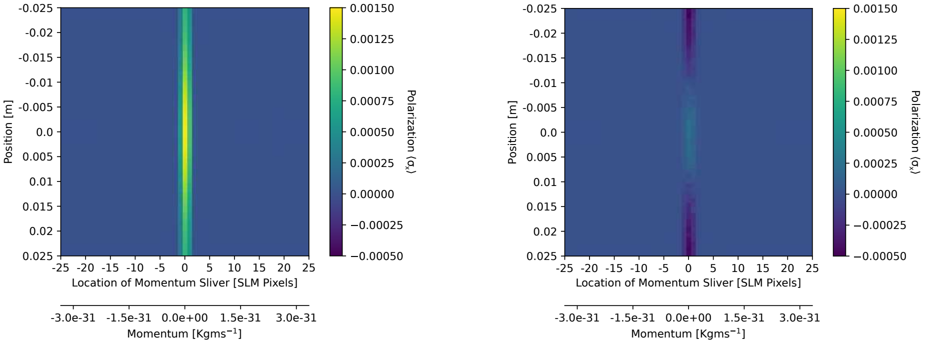

(a) Unshifted

(b) Shifted

Figure 2.10: The simulated (using the scheme of Section 2.3.1) $\langle \sigma_x \rangle$ measurement for a Gaussian beam. (a) is for the best possible approximation of $y = 0$ for the SLM pixel array and (b) is when the SLM pattern is shifted in the y direction by one pixel. Shifting the the SLM pattern by this small amount has a large impact on the size of the measured polarization in the region of high intensity (around zero momentum) showing the sensitivity to the choice of $y = 0$. The change to the polarization measurement is independent of the x measurement, depending only on the intensity of the light at a given momentum.

offset' can become significantly larger than the desired signal itself.

Figure 2.10 shows the effect of this discretization (using the simplified simulation scheme outlined in Section 2.3.1). When the pattern displayed on the SLM is shifted in the y direction by one pixel (8 µm) all these value near zero momentum are reduced by around 1.2×10^{-4}.

This effect is very simple to correct for. Since the joint weak value must be equal to zero when the glass sliver is out of the beam − the values measured at each momentum when the sliver is out of the beam are due to this $y = 0$ misalignment. These can then be subtracted from the rest of the data to give 'corrected' data. Figure 2.11 shows an example of this correction for the simulation of a Gaussian beam and all subsequent simulations results are shown with this 'correction' applied.

Comparison to Theoretical Kirkwood-Dirac Distributions

The values found in the full optical simulation should correspond to the elements of the Kirkwood-Dirac distribution (shown in Figure 2.12). While initially there seems to be some fairly significant differences between the theoretical KD and the simulated measurements, these are actually far smaller than they appear.

When the theoretical distribution is coarse grained, to have the same reso-

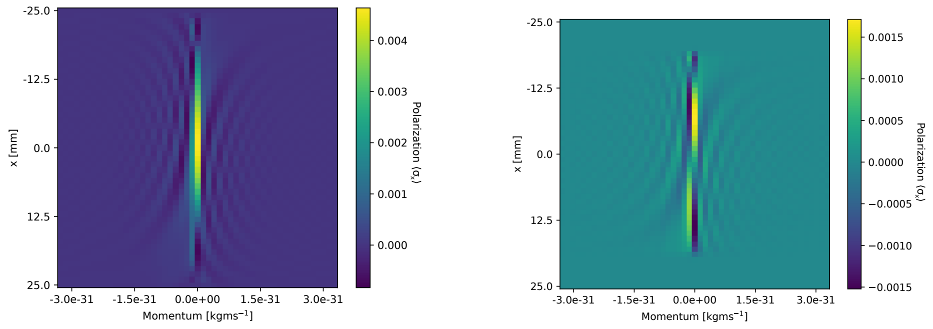

(a) Real – ‘corrected’

(b) Imaginary – ‘corrected’

Figure 2.11: The simulated $\langle \sigma_x \rangle$ measurement for the optical arrangements to measure the real and imaginary parts of the weak joint average. These simulations are performed using parameters corresponding to the optical elements outlined in Section 2.4. They have been ‘corrected’ by subtracting the values found for x out of the beam from all values. The key features are an extended nonzero region along the vertical centerline ($p = 0$), which is positive for the real measurement and shows a two (positive) lobed structure for the imaginary part. Both show fringes to either side of this central region.

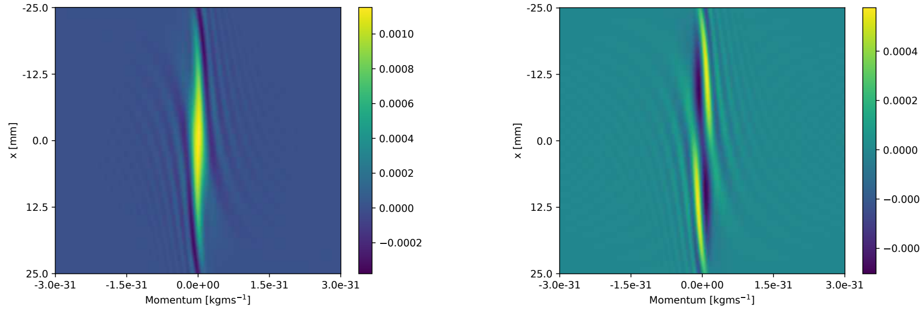

(a) Real

(b) Imaginary

Figure 2.12: The theoretical Kirkwood-Dirac distribution for the ‘Gaussian’ beam considered by the simulation. This shows the same key features as the experimental simulation of an extended nonzero region along the vertical centerline ($p = 0$), which is positive for the real measurement and shows a two (positive) lobed structure for the imaginary part. Both show fringes to either side of this central region.

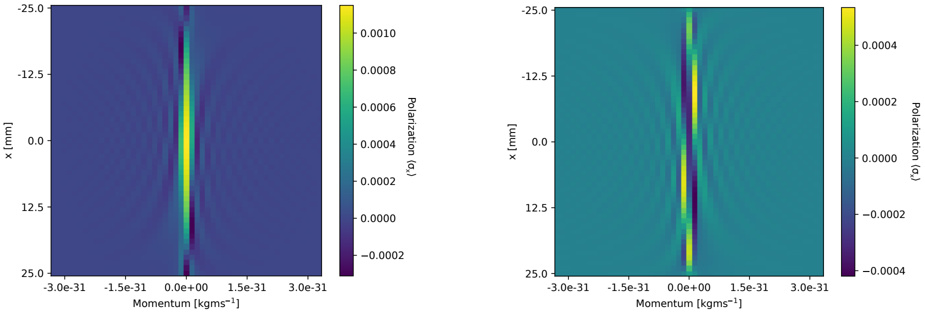

(a) Real

(b) Imaginary

Figure 2.13: The theoretical Kirkwood-Dirac distribution for the 'Gaussian' beam considered by the simulation coarse grained to the same sampling resolution as is optically simulated. This shows a fringe pattern much more similar to the simulated results, showing the difference is due to aliasing with the SLM pixel size.

lution as the simulated experiment, (shown in Figure 2.13) they appear much more similar. The comparison of the simulated experiment and coarse grained theoretical KD distribution is shown in Figure 2.14.

The difference in the magnitude of the two distributions is not meaningful, since the simulated results are showing a measure of the polarization state. To go from the experimental results (whether simulated or physical) to the KD distribution, a normalization needs to be applied.

Two vs. One Polarization Readouts

The simulation can also be used to confirm that measuring in only the diagonal basis and flipping the sign of the conditional interaction is equivalent to measuring $\langle \sigma_x \rangle$. As shown in Figure 2.15, these two approaches give equivalent results.

Linear vs. Binary Conditionality

The simulation can also be used to confirm that measuring with a binary conditionality is equivalent to measuring with a linear one. As shown in Figure 2.16, these two approaches give equivalent results – although the magnitude of the signal with the binary conditionality is around ten times larger.

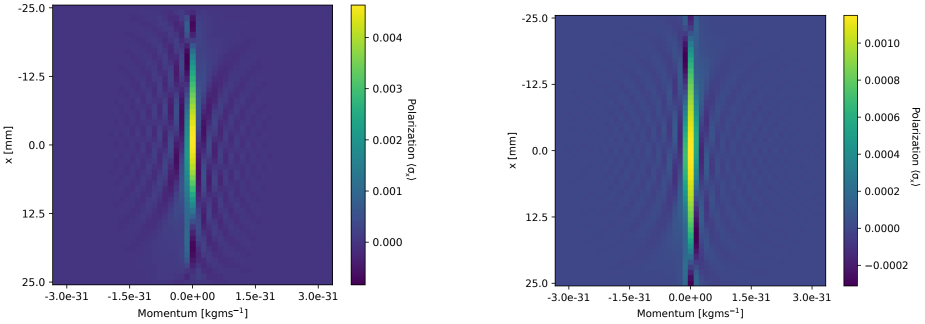

(a) Simulated – ‘corrected’ (b) Theoretical

Figure 2.14: The real parts of the theoretical Kirkwood-Dirac distribution and the simulated experimental measurements for the ‘Gaussian’ beam of the experiment. These are the plots from Figure 2.11a and Figure 2.13a reproduced for ease of comparison.

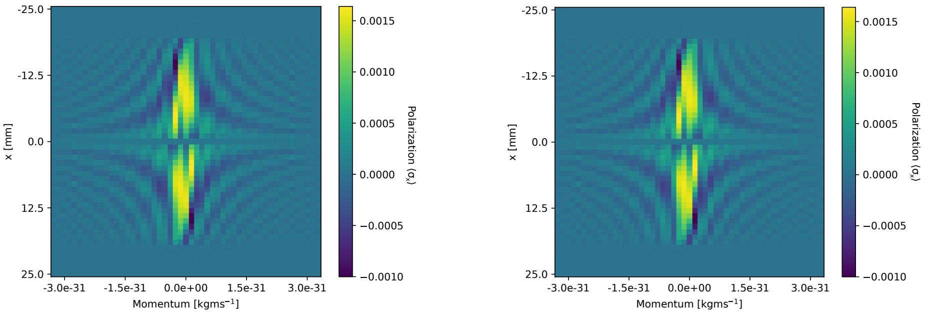

(a) $\langle \sigma_x \rangle$ (b) Flipped sign of conditionality

Figure 2.15: For a Gaussian beam of the experiment with a π phase jump across half the beam, the real parts of the simulated measurement of $\langle \sigma_x \rangle$ and measurements made in only the diagonal basis with the sign of the conditionality flipped are compared. These plots are with the x out of the beam subtraction correction applied. Their similarity indicates that the two measurement schemes give identical results.

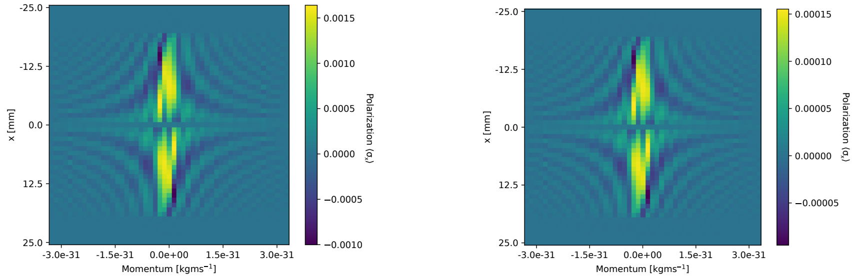

(a) Binary Conditionality

(b) Linear Conditionality

Figure 2.16: For a Gaussian beam of the experiment with a π phase jump across half the beam, the real parts of the simulated measurement of $\langle \sigma_x \rangle$ for binary and linear conditionalities. These plots are with the x out of the beam subtraction correction applied. Their similarity indicates that the two SLM patterns give equivalent results, while the binary pattern results in an order of magnitude larger signal.

2.3.1 Simplified and GPU Accelerated Simulation

The above simulation of all the optical elements in the setup is slow and uses a large amount of memory. This makes it challenging to quickly iterate to see the effect of changing experimental parameters.

The vast majority of the compute time is spent performing operations on arrays – a class of operation which Graphical Processing Units (GPUs) are designed to accelerate [106]. The CuPy package [107] provides a very simple way to run the above code using a GPU with minimal modification.

To further reduce computational time, the simulation of all the optical elements (the initial expansion telescope, finite width of Fourier transform lens and waveplates) were no longer performed. Instead a Fourier transform was applied to the beam after the glass sliver – preventing simulation of misalignment or other imperfections. The effect of the SLM could still be fully considered, and while simplified, some experimental parameters (such as the phase due to passing through the glass sliver) can also be studied. The script used to run these simulations can be found at `https://gitlab.com/tjbailey/phd-thesis/-/blob/main/SimulationCode/SimplifiedSimulationCupy.py`.

Comparison to Full Simulation and Theory

The simplified simulation is able to give qualitatively similar results to the full simulation used in the previous section. A comparison for the results of the three modeling approaches for a Gaussian beam, with a π phase jump half way

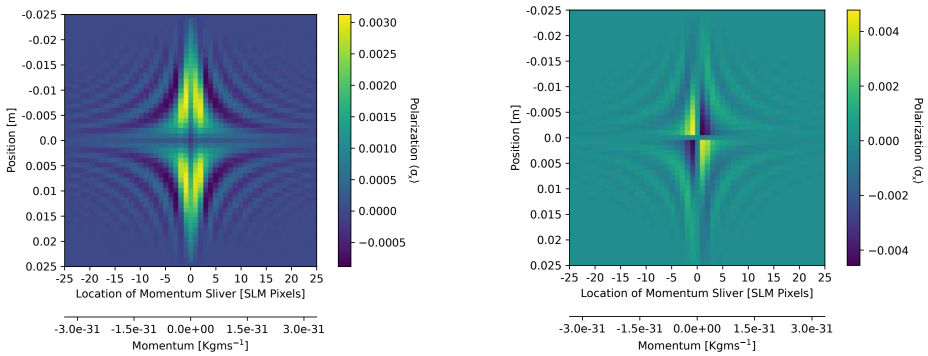

(a) Real – Simplified (b) Imaginary – Simplified

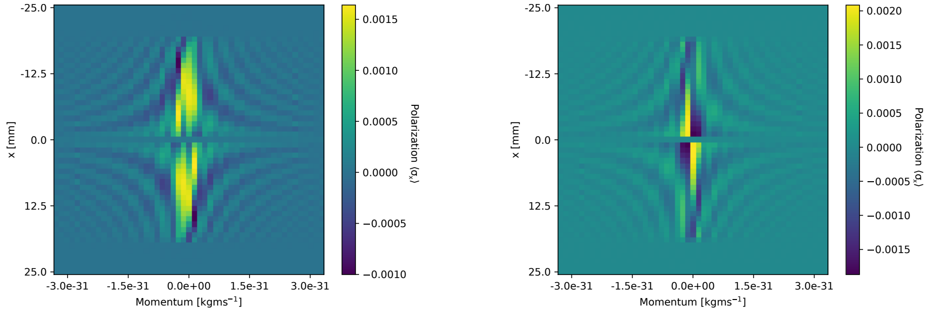

(c) Real – Full (d) Imaginary – Full

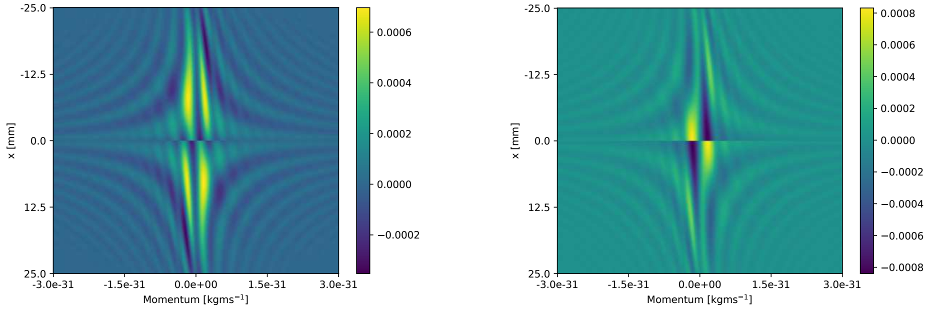

(e) Real – Theory (f) Imaginary – Theory

Figure 2.17: The real and imaginary components of the joint weak average for the two simulation schemes (simplified and full) and the theoretical KD distribution. These simulations are performed for a Gaussian beam with a π phase jump across half the beam. These plots are with the x out of the beam subtraction correction applied. All plots show a good agreement for the imaginary part, with two positive lobes and fringes in each quadrant. However, there are some noticeable differences for the real part, with the four lobed structure being much less clear in the simulations (partially due to the lower momentum resolution of these plots). Some features are common though, such as fringes in each quadrant and zero value along the horizontal centerline (position $x = 0$).

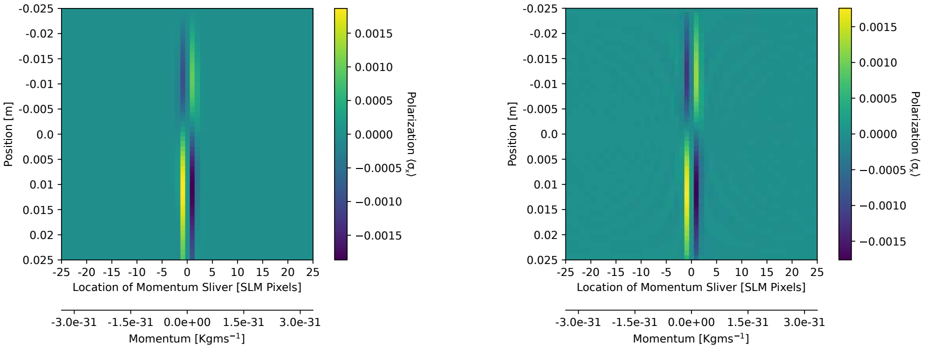

(a) Infinite beam

(b) Clipped beam

Figure 2.18: For a Gaussian beam of the width of the experiment, the imaginary component of the joint weak average when the beam is infinite or 'clipped' to the experimental width. These plots are with the x out of the beam subtraction correction applied. When the beam is clipped we see fringes to either side of the central pattern that are not present for an infinite beam.

across it, are shown in Figure 2.17.

Beam Clipping

For an infinite Gaussian, we would not expect to see fringes around the center. However, when the beam has a finite width (as in the experiment's case due to the finite width of lenses), these fringes start to become apparent – as shown in Figure 2.18.

All the simulations (except Figure 2.18a) where performed in the case of a finite beam 'clipped' to a width of 50 mm.

Phase Plates

The KD distribution of a Gaussian beam is quite simple and narrow in momentum space. This limits how well we can expect the experiment to be able to resolve interesting features. One experimentally simple way to create more complicated features in the KD distribution is to apply a phase shift over one half of the beam. Experimentally this can be done by placing a glass plate (microscope slide) across one half of the beam.

Figure 2.17 shows the KD distributions for when this glass plate imparts a phase of π. However, there are still effects even for smaller phases and Figure 2.19 shows the expected KD distributions when the phase is $\pi/8$.

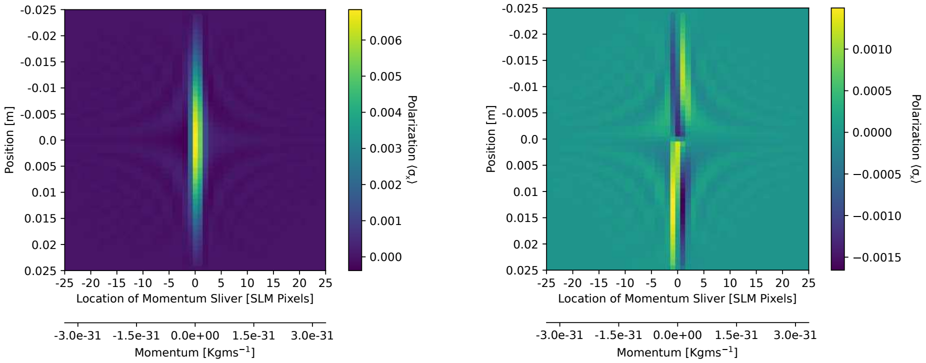

(a) Real (b) Imaginary

Figure 2.19: The real and imaginary components of the joint weak average for a Gaussian beam with a $\pi/8$ phase jump across half the beam. These plots are with the x out of the beam subtraction correction applied. This starts to look a little like when a π phase jump is applied, as in Figure 2.17, with fringes in each quadrant. However largely this distribution looks more similar to when there is no phase jump.

2.3.2 Simulation Summary

The simulation results confirm that our optical setup can successfully measure the joint weak average of position and momentum. Using a Fourier optics approach, we demonstrated that the simulated measurements closely match the theoretical Kirkwood-Dirac distributions when accounting for experimental resolution constraints.

We also confirm: that measuring in a single diagonal basis with flipped conditional interaction is equivalent to a full measurement of $\langle\hat{\sigma}_x\rangle$; that binary conditionality produces results similar to linear conditionality but with approximately ten times larger signal magnitude; and that beam clipping effects introduce a fringe pattern that should be possible to detect.

Our simulations also identified and addressed a systematic artifact in the form of large measurement values around zero momentum, attributable to y-position discretization into pixels. A simple correction method was developed by subtracting reference values measured when the glass sliver is outside the beam.

Additionally, a GPU-accelerated simplified simulation approach was implemented, significantly improving simulation speed while preserving qualitative agreement with both the full simulation and theoretical predictions. This modeling work provides a solid foundation for interpreting experimental results and suggests that phase plates represent a promising method for creating more interesting and experimentally resolvable features in the Kirkwood-Dirac distribution.

Key Findings

- The simulations validate that the optical system designed in Section 2.2 is able to measure the joint weak average and that the simulations closely match the theoretical Kirkwood-Dirac distributions (Section 2.3)
- The artifact of large values at zero momentum, arising from pixelation of the y-position, were mitigated by subtracting measurements taken without the glass sliver. (Section 2.3)
- A GPU-accelerated, simplified simulation offers a faster method to explore parameters, maintaining qualitative accuracy despite reduced complexity. (Section 2.3.1)
- Beam clipping and phase plates introduce fringes and other features that should be resolvable. (Section 2.3.1)

2.4 Experimental Setup

This section details the experimental apparatus and procedures developed to perform conditional weak measurements of position and momentum. We begin by describing the key optical components utilized, including the light source, beam preparation elements, and measurement devices. The alignment procedures required for these components are then outlined, followed by a detailed discussion of the spatial light modulator calibration process. Finally, we analyze the expected signal size and strategies to mitigate sources of noise.

Light Source

A narrow-linewidth fiber coupled diode laser (Thorlabs DBR808PN) was used as the light source. The laser is driven at a constant 100 mA by a Thorlabs KLD101 - K-Cube Laser Diode Driver and its integrated thermoelectric cooler is controlled by a Thorlabs TTC001 - T-Cube TEC Controller.

This laser was chosen since it has a coherence length ($\sim 100\,\mathrm{m}$) much longer than the thickness of the glass sliver, which is needed so that light passing through and around the sliver remain coherent. The laser is coupled to a single mode fiber ensuring that the spatial profile of the beam is initialized as a single mode Gaussian. The wavelength of 809 nm was chosen since this would enable the use of a spontaneous parametric down conversion (SPDC) source pumped as 405 nm as a light source. This would allow the experiment to be modified to be performed with single photon light.

Initial Collimation Lens

After the fiber from the laser, the light is collimated with an aspheric lens (Thorlabs C220TMD-B) with an effective focal length of 11 mm for 633 nm light (or 11.1 mm for 809 nm light [108]).

Collimating light from a single mode optical fiber (Thorlabs 780HP) with a mode field diameter (intensity at $1/\mathrm{e}^2$) of $\phi_{spot} = (5.0 \pm 0.5)\,\mu\mathrm{m}$ with this lens should give a beam with a radius [109]:

$$r = \frac{2\lambda f}{\pi \phi_{spot}} = (1.14 \pm 0.12)\,\mathrm{mm}\,. \tag{2.98}$$

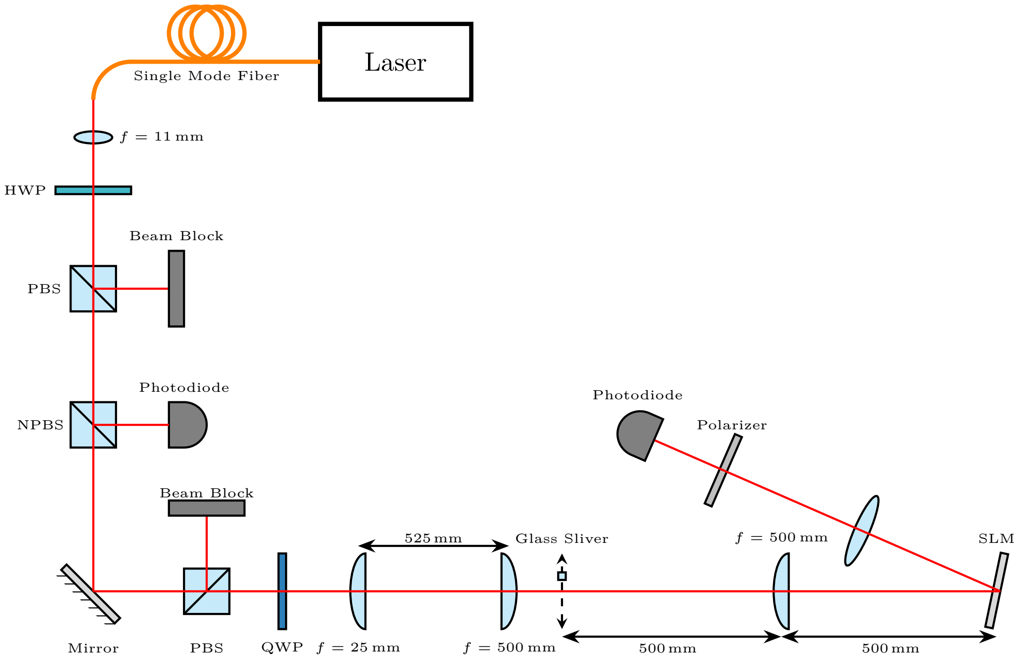

Figure 2.20: The experimental setup to perform a conditional weak measurement of position and momentum. A 809 nm narrow-linewidth laser is used as the light source. After passing through a single mode fiber, the light is collimated by an aspheric lens with focal length 11 mm to create a Gaussian beam profile. The beam then passes through a half waveplate (HWP) to align the polarization of light after the fiber with the polarization axis of the subsequent polarizing beam splitter (PBS). A non-polarizing beam splitter (NPBS) then splits some light off to a photodiode (PD) so the laser's intensity can be monitored. After a mirror and another PBS (to ensure a high purity polarization state), the beam passes through a quarter waveplate (QWP) aligned to create circular polarization.

The light then passes through a telescope made from two cylindrical lenses (focal lengths of 25 mm and 500 mm) to expand the beam in the x direction by a factor of 20 (see Section 2.2.5). A glass sliver that performs the weak measurement of x (see Section 2.2.2), and a 500 mm focal length cylindrical lens is used to perform the Fourier transform (see Section 2.2.6). A reflective liquid crystal on silicon spatial light modulator (LCOS SLM) is then placed in the Fourier plane of this lens and is used to perform the conditional measurement of momentum (see Section 2.2.3).

A lens then images the SLM onto a polarizer, aligned along the diagonal axis, so that the horizontal and vertical components of the beam still overlap correctly. The intensity is then measured with a final photodiode or camera.

Polarization Initialization

The polarization state from the laser is largely linearly polarized. This is rotated to match the axis of the optical table with a zero order half waveplate (HWP), manufactured by Union Optics, before passing through a polarizing beam splitter (PBS), manufactured by Foctek Photonics, to improve the polarization purity.

To monitor the intensity of the laser, a non-polarizing beam splitter (NPBS) is placed directly after the PBS and the intensity is monitored with a silicon photodiode (Thorlabs PDA100A).

The beam is then reflected from a dielectric mirror (Thorlabs BB1-E03) before passing through another PBS (to achieve a higher degree of polarization and mitigate any possible impact of the NPBS and mirror on the polarization state).

To create a circularly polarized beam, it then passes through a quarter waveplate (Meadowlark Optics NQM–100–0809).

Beam Expansion

The width of the beam is expanded with a telescope of two cylindrical lenses. The first has a 25 mm focal length (from Edmund Optics) and the second an uncoated lens with a focal length of 500 mm and a width of 50.8 mm (Idex Optical Technologies SCX-50.8-381.4-UV). The large width of the second lens is required to enable a wide beam to be created – however, it significantly limits the choice and focal length of available lenses.

These lenses result in a magnification in the x direction of 20 times, resulting in a beam with a $1/\mathrm{e}^2$ width of around 22 mm. However, the second lens only has a width of 50.8 mm and so around 2% of the light will not be able to pass though and the beam will be clipped.

Beam Displacement with Glass Sliver

The beam is displaced in a narrow range of x by an approximately 1 mm wide glass sliver (with a length of 25 mm). This was cut out of a (1.0 ± 0.1) mm thick fused silica window anti-reflection coated for wavelengths of 650 nm to 1050 nm (Thorlabs WG41010R-B). This window has a transmitted wavefront error of $\lambda/4$ at 633 nm and a surface quality of 40-20 Scratch-Dig.

It is double-sided taped to a small kinematic mount (Thorlabs KMS) which is at a 24° angle to the vertical due to an angle block (Thorlabs AM24C) as

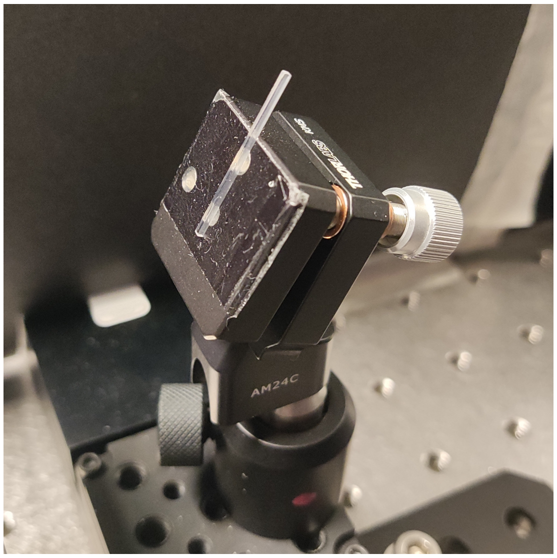

Figure 2.21: A photograph of the glass sliver mounted to a small kinematic mount on an angled block.

shown in Figure 2.21. This is then on a translation stage (Thorlabs MTS50-Z8) that allows the sliver to be translated over a range of 50 mm across the beam.

Fourier Transform Lens

To produce the Fourier plane of the glass sliver plane, a lens is used. To measure the real part of the joint weak average, a wide cylindrical lens is required. An uncoated lens with a focal length of 500 mm and a width of 50.8 mm (Idex Optical Technologies SCX-50.8-381.4-UV) is used. For the imaginary part a spherical (normal) lens is needed.

Spatial Light Modulator

A Santec SLM-200-02 was used as the spatial light modulator. It has a pixel pitch of 8 µm; is 10-bit (1024 grey levels); has a pixel response time of 200 ms; and is anti-reflection coated for wavelengths of 750 nm to 850 nm. The SLM is placed at a small angle to the incident light so the reflected beam can be measured.

Polarization Readout and Camera

After reflecting off the SLM, the polarization of the light is measured. Since the phase on the SLM only affects one component of the polarization (and so can result in different diffraction or beam steering for the two polarizations), the SLM is imaged onto a polarizer (Thorlabs LPVIS050-MP2) using a lens. This polarizer is set so its axis is along the diagonal direction. The intensity of the light is then measured either with a photodiode or a camera (Basler acA2040-55um).

This camera had the glass coverslip on the image sensor removed by Pacific X-ray to reduce interference inside the camera. This was especially useful for various alignment and diagnostic steps. A 1 mm thick glass window, anti-reflection coated for 650 nm to 1050 nm, is then screwed into the camera's C-mount to prevent dust from hitting and potentially damaging the exposed sensor. The threads of the C-mount adapter were coated in silicone grease to reduce the chance of a small shard of metal flaking off and damaging the sensor.

2.4.1 Aligning the Setup

All of the optical components in the above section must be aligned, generally either the separation between two elements or setting some rotation axis. This section provides details on how these alignments were performed.

Collimating Initial Beam

To collimate the beam immediately after the fiber, the standard technique of matching the beam width in the near and far field was used. To accurately determine the width of the beam, a camera was used with a Python script that can be found at `https://gitlab.com/tjbailey/phd-thesis/-/blob/main/ExperimentCode/MeasureBeamWidth.py`.

To align the telescope used to widen the beam is more challenging since the beam afterwards is much larger. This means it is difficult to see changes in size by eye. As well, the small section of the beam that fits in the camera's view is not very useful for giving an estimate of the beam width. It is also challenging to get the beam to propagate for a significant distance due to space constraints in the lab. In addition, since the beam is around 50 mm wide, we do not have mirrors that are large enough to reflect it (due to needing a larger diameter mirror when coming in at an incident angle). However, if this beam is not perfectly collimated, it should not prevent the experiment from working –

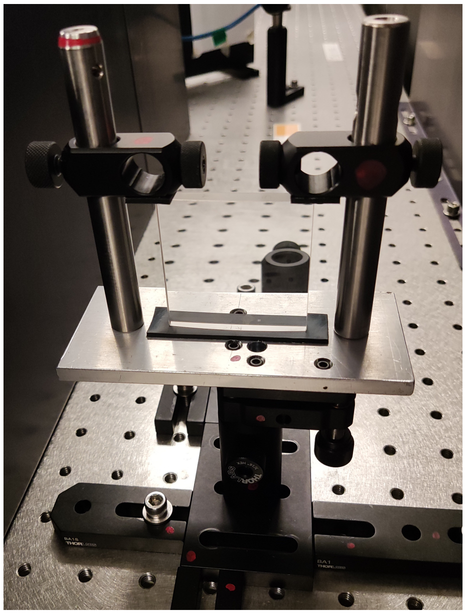

Figure 2.22: A photograph of the custom mount used to hold the large cylindrical lens.

it would just result in measuring the Kirkwood-Dirac distribution for a slightly different state.

Roll Axis of Cylindrical Lenses

Since cylindrical lenses are not rotationally symmetric around their normal (roll) direction, this must be aligned. To enable this, a kinematic platform mount (Thorlabs KM200B) was used. For the large cylindrical lenses, custom mounts were also constructed to reduce any potential strain on the lenses (shown in Figure 2.22).

Aligning the roll axes can be done relatively straightforwardly by looking at the beam near a focus. Figure 2.23 shows the beam when the roll axis is misaligned. The beam should be horizontal when the roll axes are aligned.

Angle of Quarter Waveplate

To find the angle of the quarter waveplate (QWP) that results in circular polarization, a linear polarizer was rotated after the QWP. The QWP angle was then adjusted until the visibility (the difference between the peak and minimum intensity after the polarizer) was minimized. For circular polarized light, half will

Figure 2.23: A photograph of the beam near a focus when the roll axis of the cylindrical lenses of the beam telescope are misaligned. The deviation from a Gaussian shape highlights one challenge when working with cylindrical lenses.

propagate through a linear polarizer regardless of the angle of the polarizer's axis.

Adjusting the Phase of Glass Sliver

The phase of light passing through the sliver must be an integer number of 2π of the light passing around the sliver (as discussed in Section 2.2.2). This can be adjusted by changing the angle of the sliver by a small amount.

To be sensitive to the phase of the light passing through the sliver, a double slit was used. When the sliver was offset from either slit, the normal sine squared double slit interference pattern was seen. When the glass sliver is move behind one of the slits, the position of the interference fringes move (since there is now a phase difference between the light coming from each slit). By adjusting the angle of the glass sliver until there is no shift in the position of the interference pattern, the angle of zero relative phase shift can be determined.

Finding Focal Planes

The Fourier transform lens must be one focal length away from the glass sliver and the SLM must then also be placed one focal length away. To attempt to position these optical elements more accurately than would be possible by simply

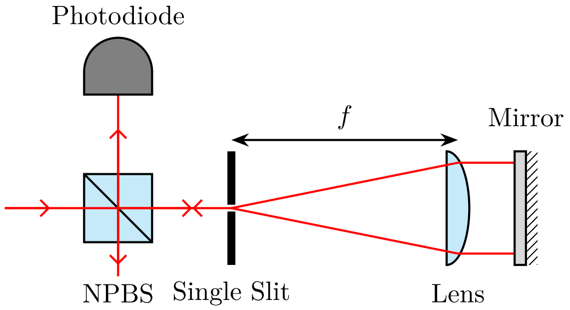

Figure 2.24: An autocollimation scheme to determine the focal plane of a lens. Light is transmitted through a beam splitter and is incident on a narrow slit. It then diffracts and is collimated by a lens when it is one focal length away. This collimated light reflects from a mirror and is focused back on the narrow slit. Reflected light is transmitted through the slit and some is then reflected by the beam splitter. The intensity in this port of the beam splitter will be maximized when the most reflected light can pass through the narrow slit. This will occur when the lens is one focal length away from the slit.

measuring with a ruler, an autocollimation scheme was used. This scheme is show in Figure 2.24.

By placing a slit at the location of the glass sliver, the lens can be adjusted until the best position is found with the autocollimation scheme. Then light can be sent backwards through the system, with a slit positioned roughly one focal length after (now before) the Fourier transform lens. The position of this slit one focal length away from the lens can be found and then the SLM can be placed in this plane.

2.4.2 SLM Calibration

It was found that the SLM did not apply a phase linear to the grey level applied and that there is some uniform phase applied at zero grey level. Hence it was necessary to calibrate the behavior of the SLM before using it to apply phases. In addition the phase offset for zero grey level would occasionally ‘jump’ (shown in Figure 2.25) – requiring that the calibration be performed on a regular basis. Further investigation into how the SLM transforms the polarization are found in Appendix A.

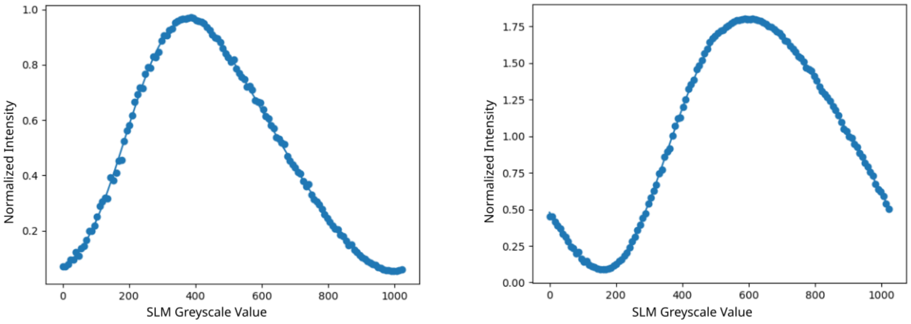

(a) 2024-10-21

(b) 2025-02-21

Figure 2.25: The relationship between SLM grey level and intensity for two different days. The phase offset of the SLM occasionally 'jumps' to an entirely different value.

Calibrating Phase Profile

To calibrate the SLM, we sent in circular polarized light and measured in the diagonal basis. When the horizontal polarization component acquires a phase, ϕ, the intensity measured in the diagonal basis will vary as:

$$I = \frac{I_0}{2} \left(1 + \sin \phi\right) \, . \tag{2.99}$$

The grey levels of SLM do not correspond linearly to the phase applied. We use a quintic polynomial to approximate the true relationship,

$$\phi = a + bG + cG^2 + dG^3 + eG^4 + fG^5 \, , \tag{2.100}$$

where G is the grey level displayed on the SLM.

If the intensity is measured for a variety of grey levels, then the above functions can be fitted to the observations (performed using the SciPy package [110]) as shown in Figure 2.26.

The Python script used to perform this calibration can be found at `https://gitlab.com/tjbailey/phd-thesis/-/blob/main/ExperimentCode/CalibrateSLM.py`.

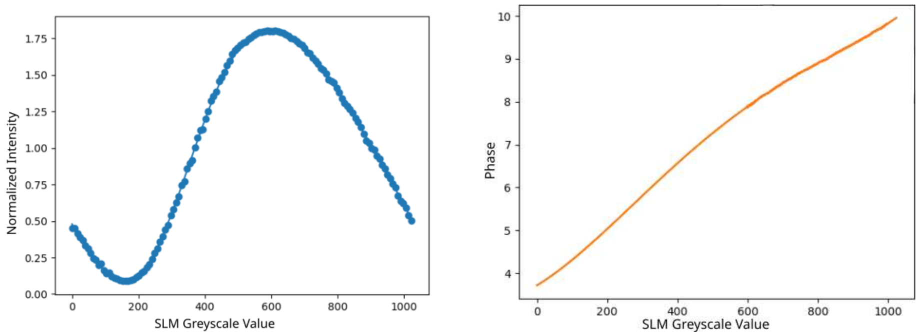

(a) The intensity of diagonal polarization measured for different grey levels displayed on the SLM.

(b) The function between phase (y-axis) and SLM grey level (x-axis) that gave the best fit to the data.

Figure 2.26: The relationship between phase and SLM grey level can be found by measuring the intensity of the diagonal component of polarization for a range of test SLM grey levels when there is circular polarized light incident.

Spatial Phase Variation

The above calibration was performed assuming that every pixel on the SLM applies the same phase for a given grey level. However, we do not actually expect this to be the case – for instance spatial variation in the pixel phase response was seen by Sit et al. while working on using an SLM for general polarization transformations [96].

To check this, we directly imaged the SLM surface using a camera with a polarizer aligned along the diagonal direction. The same phase relationship fitting described above is then performed for every SLM pixel imaged. When only the phase offset, a, is allowed to vary (so the shape of the phase response is assumed the same for each pixel), we see the distribution shown in Figure 2.27. This was done since there is a correlation between the a and b terms of the phase relationship which seems likely to be an artifact of the fitting process rather than representing actual variation between the pixels.

These measurements showed a variation in phase of around $\pm 0.4\,\text{rad}$. However, these phase variations were not random and show the clear structure of a series of fringe patterns. This suggests that some kind of interference effect might be responsible – especially given the long coherence length of the laser being used. The data was retaken with a handheld Oz optics FOSS-21-3S-5/125-810-S-1 laser. This laser has a much shorter coherence length (much less than a millimeter) and so it would be expected that interference from surfaces separated by larger than this distance would be reduced. However, as shown in

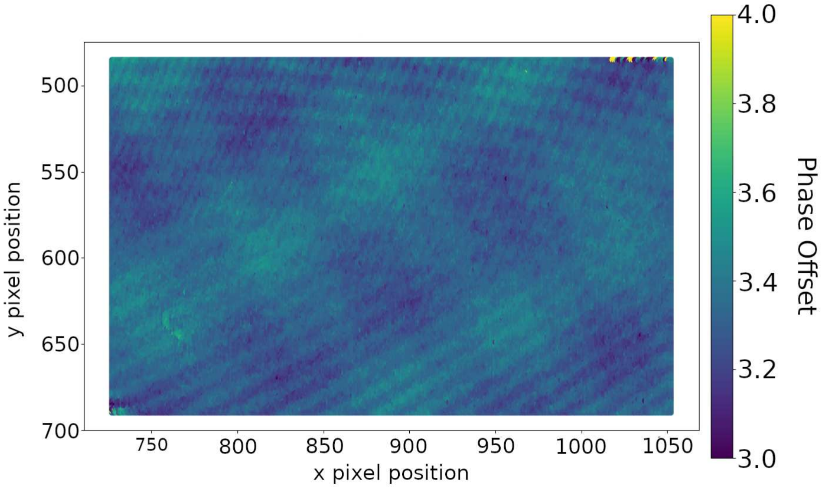

Figure 2.27: The phase offset, a, for the best fit for each pixel on the SLM (the range limited by the area of the SLM imaged by the camera). All other fit parameters were kept constant across all pixels. This shows that there is significant spatial variation (of around $\pm 0.4\,\mathrm{rad}$) from the expected phase.

Figure 2.28, a very similar fringe pattern was seen. This suggests that if interference is responsible then the interfering planes are very close together. The position of some fringes did shift – providing more evidence that this variation is probably due to an interference effect and not entirely intrinsic to the behavior of SLM pixels.

It may be possible to calibrate this phase variation in situ (which appears to be required given the sensitivity to factors such as the light source) using a non polarizing beam splitter (NPBS). However, it would be challenging to image a sufficiently large area of the SLM. Alternatively if a pattern is displayed on the SLM which has values that differ by much larger than $0.4\,\mathrm{rad}$ then this pixel phase response variation would be much less impactful. This is the case for the binary scheme discussed in Section 2.1.5 where the two phases displayed ($\pi/2\,\mathrm{rad}$ and $-\pi/2\,\mathrm{rad}$) differ by $\pi\,\mathrm{rad}$.

Beam Position on the SLM

The location of the beam on the SLM is important to determine. The center of the beam (when there is no glass sliver) set the $y = 0$ and $k = 0$ positions. To determine the center of the beam, a series of different approaches are used.

The first set make use of the fact that when the SLM displays a phase of

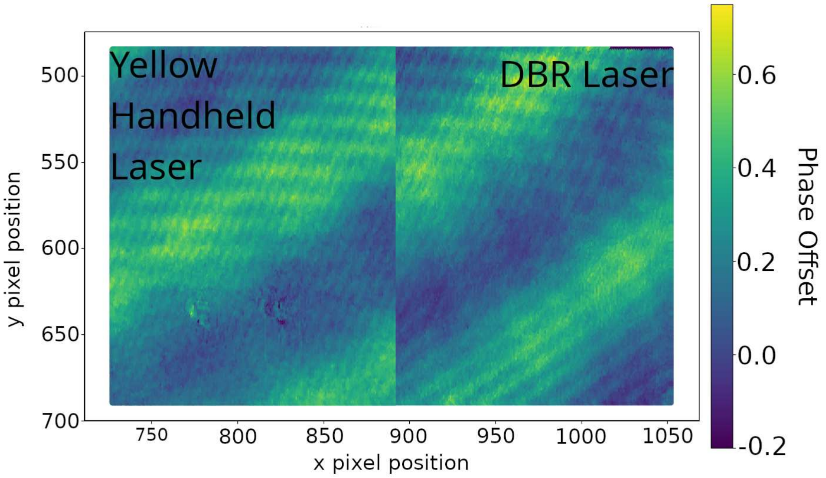

Figure 2.28: The individual SLM pixel phase offset when measured with a long coherence length distributed Bragg grating (DBR) and a shorter coherence length handheld laser. The shift in the pattern depending on light source suggests this is an interference effect rather than intrinsic to each pixel, though the patterns persistence with a short coherence length lase indicates that if interference is responsible the reflecting planes must be very close together.

$\phi = \pi/2$, the incident circular light is rotated to diagonal and will be fully transmitted through the polarizer – making the SLM appear as a mirror. If instead a phase of $\phi = 3\pi/2$ is applied, then the light is rotated to anti-diagonal and none will transmit through the polarizer – making the SLM appear non-reflective. By changing the section of the SLM that acts as a mirror and measuring the total intensity, we can determine the intensity of the light incident on that portion of the SLM.

This then allows us to apply different search patterns to the SLM. One approach is to apply strips in the X and Y directions (an example is shown in Figure 2.29). This allows us to effectively measure the cross section of the beam in these two directions – with the maximum intensity being near the center of the beam.

To get a more precise estimate of the beam location, a series of small square patches can be displayed on the SLM (an example patch is shown in Figure 2.30). This approach is only feasible to use over a small region since it scales quadratically with the resolution – making it inefficient to sample over the entire SLM area. The intensity of light from all these patches can then be fitted with a two dimensional Gaussian function. The results of this fit then gives an estimate for

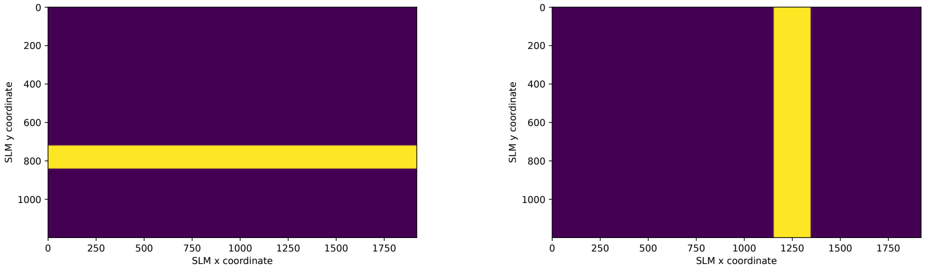

(a) X directed strip

(b) Y directed strip

Figure 2.29: Example X and Y directed strips used to measure the cross sectional intensity of the beam.

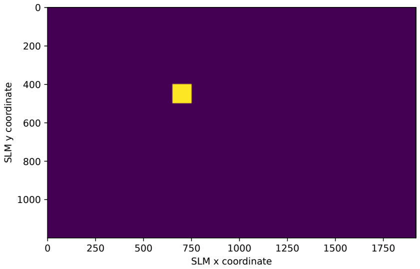

Figure 2.30: An example square patch used to find the beam intensity at a particular location.

the y and k position of the center of the beam.

Another approach to finding the $y = 0$ level is to apply a phase gradient (or split phase) over the entire SLM. When the direction of this gradient is reversed, the amount of light transmitted through the polarizer will change. However, when the gradient is centered on $y = 0$, the situation is symmetric and so should result in no change in measured intensity. By finding the location where the gradient direction has no effect on intensity, $y = 0$ can be found. This technique is more directly useful as the pattern is very similar to the one used to perform the conditional measurement and hence is able to minimize the measured background due to an error in y calibration.

The Python script used to locate the beam on the SLM can be found at `https://gitlab.com/tjbailey/phd-thesis/-/blob/main/ExperimentCode/LocateBeamonSLM.py`.

2.4.3 Expected Signal Size

Only a small portion of the beam is displaced by the glass sliver or hits the SLM at the location of the momentum measurement. Therefore as a proportion of the total beam, the contribution to the signal will be small. This effect is entirely due to the resolution of the x and p momentum measurements – if projectors covering a larger range of x or p are used then the signal is also larger.

To get a sense of the size of this effect, we can consider the maximal amount of light passing through a 1 mm wide sliver of glass. For a beam with a width of 20 mm, this will be a maximum of just less than 4% of the light. A similar factor will occur for momentum measurements – which if we assume we can resolve around 20 discrete momenta projectors – will be on the order of 10%. Hence, we expect that, at most, only around 0.4% of the intensity of the beam can ever contribute to this signal.

This is made even smaller when we consider that the measurement of the position is weak. In the case of a subsequent binary measurement (where the signal would be maximized), for a displacement of 0.14 mm and a beam with a y width of 1 mm, the signal size is around 0.1. It would be significantly smaller if the gradient scheme is used instead.

Together these factors imply that the experiment needs to be sensitive to changes in intensity on the scale of 0.01%. This is certainly achievable, though will require long integration times to average out fluctuations in laser power etc.

One way to reduce the effect of fluctuations is to rapidly switch the direction of the applied polarization rotation. If this is done on a timescale faster than some experimental fluctuations, then the experiment will not be sensitive to them. Another way to reduce a source of noise is to continuously monitor the laser power and to normalize the measured signal by this monitored intensity.

A lock-in amplification scheme was tested varying the strength of the applied polarization rotation. However, due to the response time of the SLM this frequency was limited to around 1 Hz and was unable to remove much noise. The initial polarization state could be altered at a higher frequency (either using a spinning wave plate, a liquid crystal or a Pockels cell) but it was determined that amplification of this type was not required when using the binary conditional scheme.

2.4.4 Experimental Setup Summary

In this section, we have described the implementation of a conditional weak measurement setup using an 809 nm narrow-linewidth laser, polarization optics, cylindrical lenses, a glass sliver, and a spatial light modulator. The experimental design required precise alignment of multiple optical components, particularly the cylindrical lenses, and methods to achieve these alignments are presented.

The spatial light modulator's non-linear phase response is calibrated and its spatial phase variations are characterized. These calibration procedures were essential due to occasional phase 'jumps' observed in the SLM behavior, necessitating regular recalibration.

The expected signal size of approximately 0.01% of the total beam intensity presents a significant experimental challenge. Various strategies to reduce noise or increase the signal strength are considered.

Key Findings

- Methods to align various optical components are presented. (Section 2.4.1)
- The phase response of the spatial light modulator is characterized and the beam position on the SLM is found. (Section 2.4.2)
- The expected signal strength and approaches to reduce noise are considered. (Section 2.4.3)

2.5 Single Measurement Tests

Before attempting the conditional measurement, independent measurements of position and momentum were attempted. This is done largely because the signal strength of the conditional measurement is very small and so requires long ‘integration times’ to reach low enough uncertainties. This can make any required adjustments to the experiment very slow to perform. In addition, the Kirkwood-Dirac distribution is much more complicated than either the position or momentum marginal alone – and so the origin of any errors can be much harder to interpret.

2.5.1 Weak Measurement of $\hat{\pi}_x$

A weak measurement of $\hat{\pi}_x$ was performed without any momentum measurement but using otherwise identical experimental configuration for the full conditional measurement. The weak measurement is initially performed by coupling the x projector to the y traverse position with the glass sliver. The polarization is then rotated by an amount that depends on the y displacement using the SLM. However, unlike in the conditional scheme, this rotation has no dependence on momentum – implemented by applying a gradient over the entire SLM rather than just a sliver. The polarization is then measured in the diagonal basis as for the conditional scheme.

This polarization measurement should correspond to the probability to detect a photon at a given x,

$$p(x) = |\psi(x)|^2 , \tag{2.101}$$

which is equivalent to the intensity profile (up to a normalization). We expect to see a Gaussian with a full width at half maximum (FWHM) of around 20 mm. Figure 2.31 shows two measurements of this profile – when measured with a continuous phase gradient and with a binary phase split. Both find a beam with roughly the width expected. However, the binary approach required much less data to be averaged, as well as appearing to be closer to the shape we would expect – demonstrating its significant advantages over the gradient scheme initially proposed.

2.5.2 Measurement of $\hat{\pi}_p$

A measurement of momentum is equivalent to measuring the position in the Fourier plane. This can be done by displaying vertical ‘slivers’ of $\pi/2$ phase on

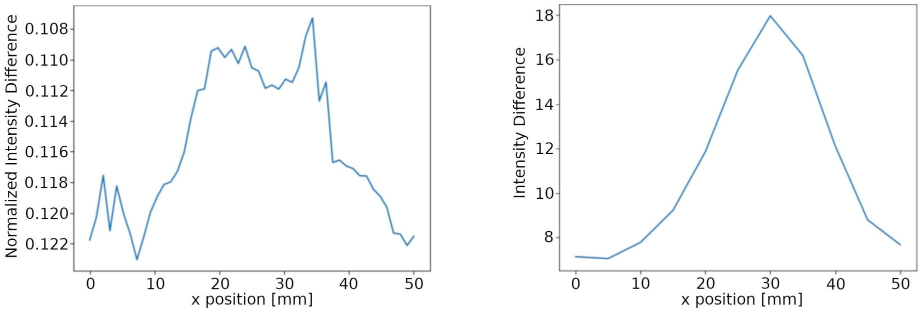

(a) Gradient Approach. The vertical axis goes from high to low to show a positive peak due to the sign convention used when taking the measurements.

(b) Binary Approach. Intensity scale has not been normalized.

Figure 2.31: Measurements of x profile of the beam performed using the glass sliver and the SLM to couple y displacement to polarization. Both measurements plot the difference between the polarization measured in the diagonal basis when the gradient/binary split flips sign. They both show a beam with a width of around 20 mm though the measurement with the gradient approach is much noisier and required significantly longer integration time, showing the advantage of the binary approach to increase signal to the noise ratio.

the SLM (while the rest of the SLM displays $-\pi/2$ phase) as was done to find the beam position in Section 2.4.2.

The results of this measurement is shown in Figure 2.32. The beam asymmetry seen appears to be due to one edge of the beam being clipped by the finite size of the lenses. For a Gaussian beam with the lenses used, we would expect that the FWHM at the focus (which should be where the SLM is placed) is only 8 µm. This would correspond to only a single pixel on the SLM and so we expect that we should see a very narrow peak. The much broader peak we see here suggests that for this measurement the SLM has been placed in the incorrect plane and is not actually at the focus.

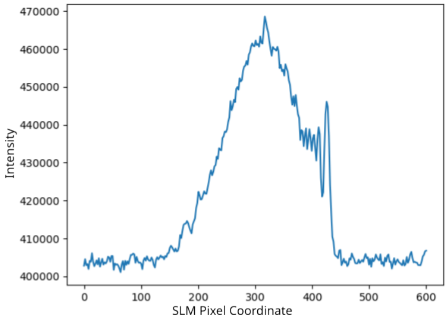

Figure 2.32: The observed intensity of diagonal polarization when a two pixel wide 'sliver' is displayed at the SLM pixel value indicated. This is measuring a the beam profile in the SLM plane. It appears significantly wider than expected, potentially due to the SLM not being placed in the correct plane with respect to the lens. The asymmetry may be due to the beam being clipped by the finite width of the lenses used.

2.6 Joint Weak Measurement

2.6.1 Initial Conditional Measurements

Attempts to measure the joint weak averages using the conditional scheme initially resulted in peak values that showed a strong correlation in x and p (shown in Figure 2.33). This distribution was entirely unexpected, however, subsequent investigations with direct measurements using a camera showed that this was due to the SLM being positioned far from the focal plane of the lens.

2.6.2 Measurements with Camera*

Due to challenges getting the conditional scheme to work, we investigated measuring the joint weak average of the x and p projectors using a camera. The weak measurement of $\hat{\pi}_x$ is performed using a glass sliver as before. However, rather than coupling to the polarization, the y position is measured directly in the Fourier plane using a camera.

For each x projector measurement (camera frame) the joint weak average is then proportional to the weighted average y position for each momentum (x'

---

*This work was done in collaboration with Michael Weil. Data in this section was collected by MW.

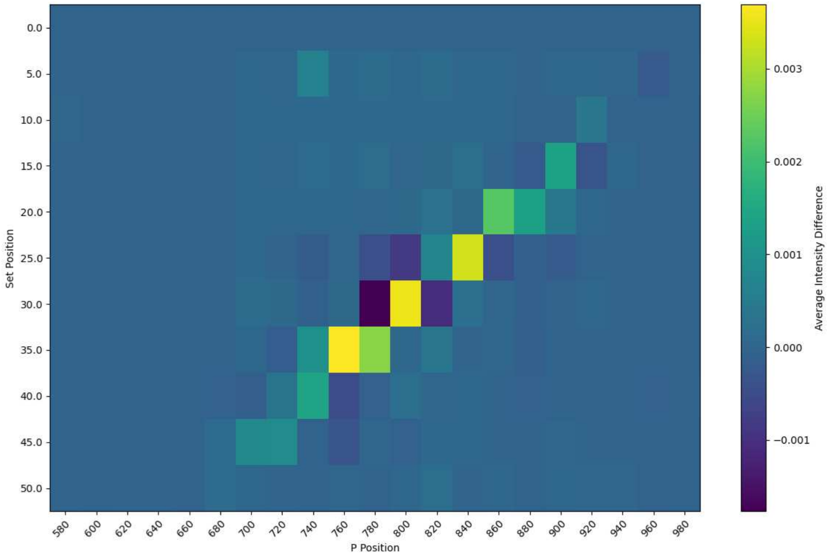

Figure 2.33: The joint weak average for each x and p projector is found using the binary split phase approach. The $x = 0$ row has been subtracted from all columns to remove background effects that have no dependence on x.

position on the camera),

$$\langle \hat{\pi}_p \hat{\pi}_x \rangle \sim \sum_y y I(p, y)\,, \tag{2.102}$$

where $I(p, y)$ is the intensity measured at a camera pixel with height y and which corresponds to momentum p.

When taking these measurements, some momenta have much higher values for all possible x (as shown in Figure 2.34). This is not expected for the Kirkwood-Dirac distribution but was seen in simulations of the conditional scheme (see Section 2.3). To correct for this (and for effects such as a small roll angle between the camera and cylindrical lenses), the $x = 0$ measurement is set as the zero value for all momenta.

The results of these measurements are seen in Figure 2.35a. These look similar to the theoretical prediction of the Kirkwood-Dirac distribution (Figure 2.35b) but there are still some very significant differences (especially around $p = 0$).

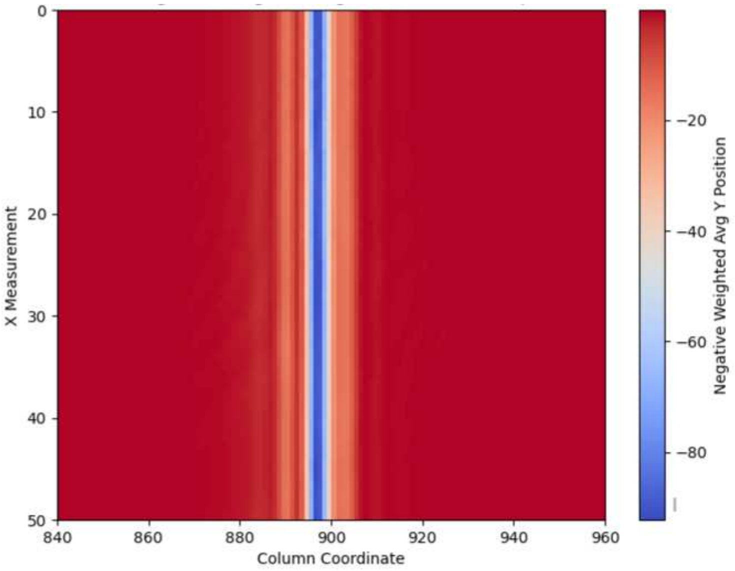

Figure 2.34: The joint weak average for x and p projectors found using a camera before applying a correction for the part of the signal insensitive to x.

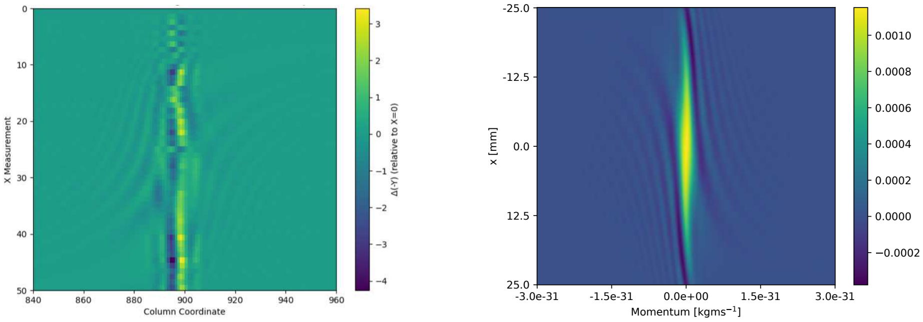

(a) The joint weak averages found using a camera.

(b) The theoretical calculation of the real part of the Kirkwood-Dirac distribution for this beam.

Figure 2.35: The joint weak averages found with a camera compared to our theoretical prediction. There are some similarities, such as the general shape of the fringes, though others (such as the large negative values seen near $p = 0$ experimentally) differ significantly.

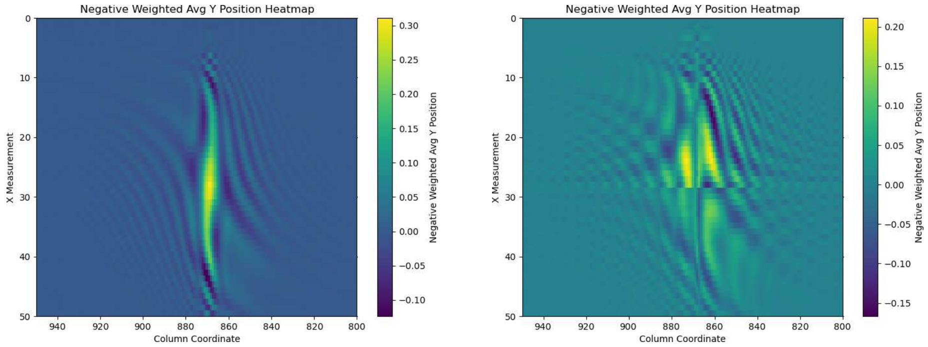

(a) The joint weak averages found for Gaussian beam.

(b) The joint weak averages found with a glass slide across half the beam.

Figure 2.36: The joint weak averages found with a camera after correcting the roll axis. The comparison is much closer to the expected theoretical predication.

Correcting the Roll of the Camera

The camera's roll axis is adjusted so the vertical direction of the pixels align with the beam's vertical direction.

In Figure 2.36a, the measured joint weak averages look far closer to the expected theoretical distribution. When a glass slide is placed over approximately half of the beam (to impart a phase shift), we see the distribution in Figure 2.36b. This shows many of the same features of the theoretical prediction in Figure 2.17e for a π phase shift, such as 4 lobes and more complex fringe structure.

2.6.3 Subsequent Conditional Measurements

When the SLM is placed in the same plane as the camera above, then very similar measurements are achieved using the conditional binary scheme (shown in Figure 2.39). These measurement are lower resolution in momentum (due to the larger pixels of the SLM compared to the camera), but show very similar features and are found by only reading out the polarization of the light with no spatial resolution required at the detector. They have very similar qualitative features to the theoretical KD distributions for the beams shown in Figure 2.37. The estimates for the standard errors for these measurements are shown in Figure 2.40.

For the case of a defocussed beam, as the amount of defocussing increases the large positive vertical feature in the Kirkwood-Diract distribution tilts around as shown in Figure 2.38.

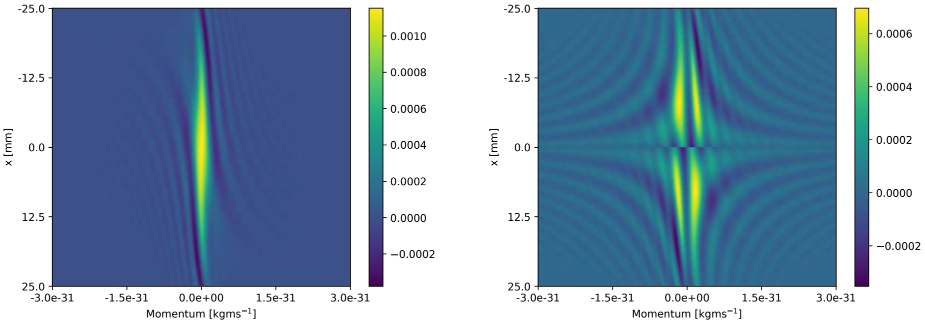

(a) Gaussian beam.

(b) Gaussian with π phase jump.

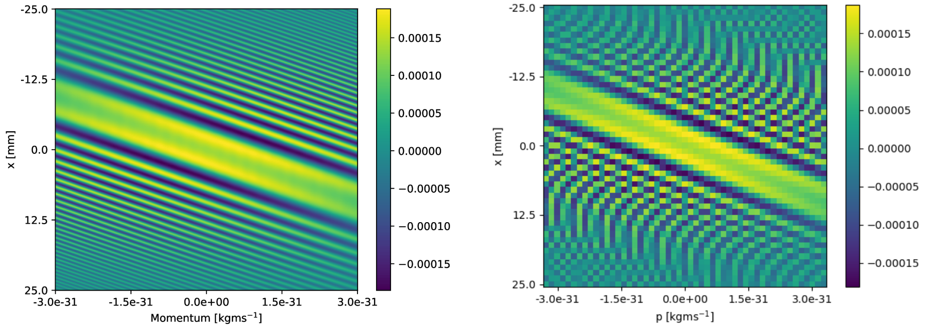

(c) Defocussed Gaussian beam.

(d) Defocussed Gaussian beam measured at momentum resolution of the SLM.

Figure 2.37: The real part of the theoretical Kirkwood-Dirac distribution for the cases experimentally measured. They show good qualitative agreement with the experimental measurements of the joint weak averages of position and momentum projectors made with both the camera and conditional scheme using the SLM. (d) is the same as (c) except that the plot limits momentum resolution to be similar to that imposed by the finite size of SLM pixels. This indicates that the shape we see experimentally is due to aliasing between the fringes and momentum resolution.

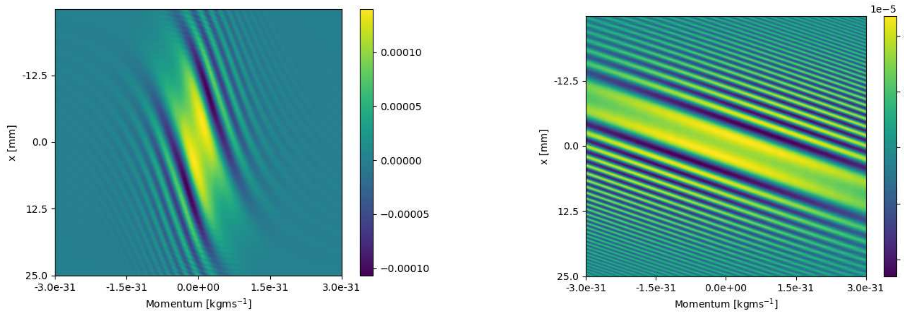

(a) Lens misaligned 1 mm.

(b) Lens misaligned 10 mm.

Figure 2.38: The real part of the theoretical Kirkwood-Dirac distribution two defocussed beams. The additional distance that the second lens has compared to when the beam expansion telescope produces a collimated beam is labeled. We see that as the amount of defocussing increases the large positive vertical feature in the Kirkwood-Diract distribution tilts around.

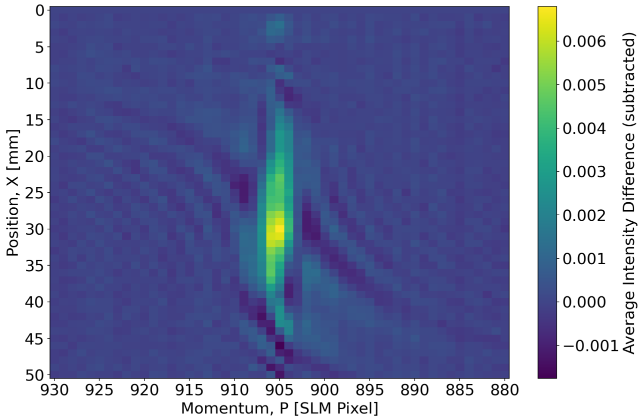

(a) Gaussian beam.

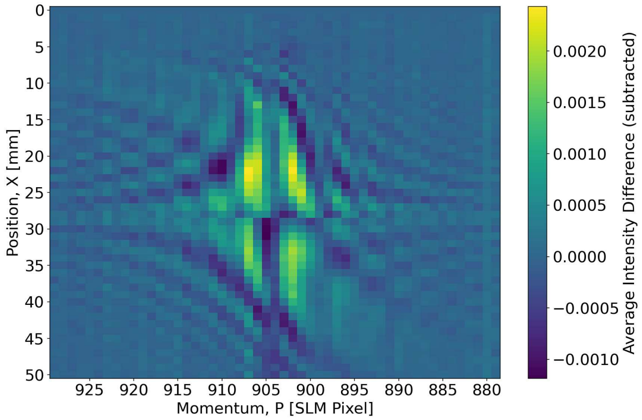

(b) Gaussian beam with a glass slide across half the beam.

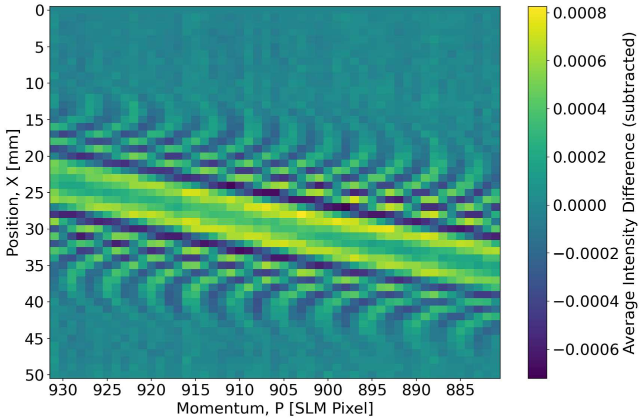

(c) Defocussed Gaussian beam.

Figure 2.39: The real joint weak averages found using a SLM to perform the conditional scheme. They compare well to measurements of the joint weak averages found using a camera and reading out two pointers and have very similar qualitative features to the theoretical plots.

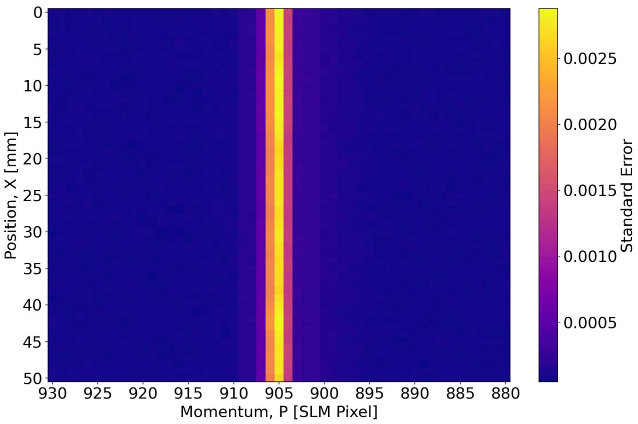

(a) Gaussian beam.

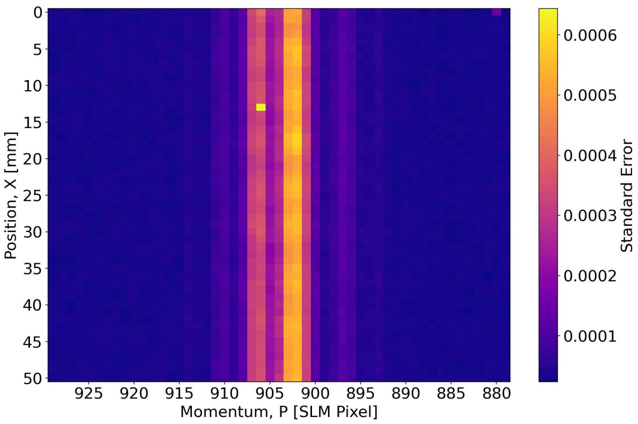

(b) Gaussian beam with a glass slide across half the beam.

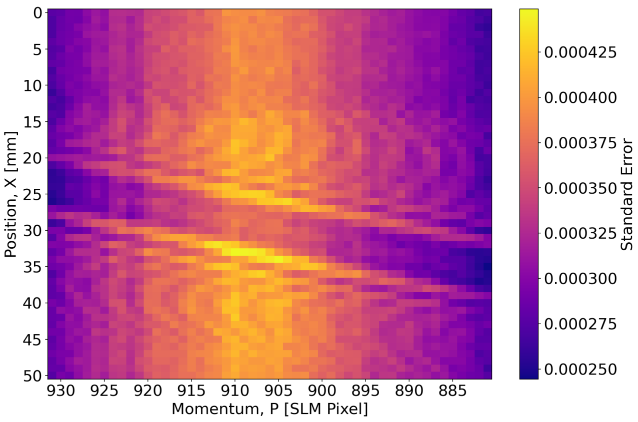

(c) Defocussed Gaussian beam.

Figure 2.40: The estimates for the standard errors in the real joint weak averages found when using a SLM to perform the conditional scheme.

2.6.4 Joint Weak Measurement Summary

In this section, we implement a conditional joint weak measurement of the position and momentum projectors by first weakly displacing the beam in y at a chosen x using a tilted glass sliver, then rotating the polarization at a chosen p_x with a strength that depends on y via a spatial light modulator (SLM). Reading the polarization in the diagonal basis directly yields $\mathrm{Re}\left[\langle\hat{\pi}_p\hat{\pi}_x\rangle\right]$.

After performing tests with a non-conditional approach, we observed qualitative agreement between the theoretical Kirkwood-Dirac distributions for three different input states (truncated Gaussian, truncated Gaussian with a phase step, and a focused Gaussian) and the conditionally measured joint weak averages. The experimental measurements agree in overall structure (e.g. number of bright lobes) as well as the structure of the fringes.

Key Findings

- A non-conditional approach directly imaging the beam in the Fourier plane with a camera enabled making the experimental adjustments required. (Section 2.6.2)
- The joint weak averages of position and momentum projectors qualitatively agree with the theoretical Kirkwood-Dirac distributions for 3 different states. (Section 2.6.3)

2.7 Future Direction

This experiment is still ongoing. We will continue to troubleshoot issues using the camera measurements and suspect that there may still be misalignment to the correct position and momentum planes.

We will also attempt to perform measurements of the imaginary component of the joint weak average. This requires the use of a spherical lens, for which there is far greater choice. This will enable the use of a higher quality lens (eg. a doublet lens) and a longer focal length (enabling greater resolution in the momentum plane). It was initially expected that the signal for the imaginary component of a Gaussian would be smaller than for the real component (hence the real part was attempted to be measured first) but this appears to be much less significant when there are phase jumps across the beam or the beam is clipped.

Chapter 3

Optical Nonlinear Weak Measurements

The use of optical nonlinearities to measure an observable of light would have a number of advantages over current techniques. By enabling the use of an external quantum system as the pointer state, non-demolition measurements would be possible. It would also make all the other degrees of freedom of light available for purposes other than measurement. It is potentially possible that the nonlinear interaction would enable measurement of observables that are not directly available with standard techniques.

Nonlinear interactions are typically very weak [8], unless there are high intensities or very particular arrangements [7]. This makes weak measurement a natural formalism to consider, as the interaction strength between the systems and pointer will be inherently weak. In this context, the ability to use an independent quantum system as the pointer is of particular interest – since most demonstrations of weak value amplification have used internal degrees of freedom and can be explained with classical optics [26].

Previous work has looked at specific cases where a nonlinear interaction can be used for measurement: the cross-Kerr effect to measure photon number [26, 111, 112] (considered in more detail in Section 3.3.1), parametric down-conversion using two pointers to measure field quadratures [113] (presented in Section 3.1.5) and using two pump fields of different frequency [114] (presented in Section 3.1.6).

In this chapter, we shall consider how a range of optical nonlinearities can be used to perform quantum measurements. In Section 3.1, the von Neumann formalism of measurement is used and it is shown that only the Kerr effect will lead to a practical measurement of this type without additional linear elements. We also present the work of Yurke [114] and Braunstein [115] showing how the measurement operation is a Gaussian process that can be decomposed into single mode squeezers and linear processes.

In Section 3.2, the more general framework for quantum measurement of positive operator-valued measures (POVMs) is used. We consider a $\chi^{(2)}$ interaction for a range of different initial pointer states (number and coherent) and readout bases (number, quadrature). We find that measurements of this type can provide information about the quadratures of a quantum state.

Finally in Section 3.3, we consider the impact of postselecting the measured system into a known final state for both von Neumann and POVM style measurements. This can lead to weak value amplification and we show how weak values affect the probabilities of the measurement outcomes for a POVM.

3.0.1 Contributions and Novelty

In this chapter, I demonstrate that for a single $\chi^{(2)}$ or $\chi^{(3)}$ nonlinearity without other elements, and no additional interactions, the only available von Neumann type measurement is photon number via the Kerr effect (Section 3.1). Next, I built upon existing work by extending Yurke's two-pump measurement scheme to the $\chi^{(3)}$ domain (Section 3.1.6) and reframing the Bloch-Messiah decomposition as a measurement interaction (Section 3.1.7).

Moving to a more general framework, I then explicitly derive the Positive Operator-Valued Measures (POVMs) for a variety of $\chi^{(2)}$ scenarios (Section 3.2), considering different pointer initializations and readout bases (number, coherent, and quadrature). This analysis culminates in a novel proposal showing that a coherent pointer and intensity readout can be used to measure field quadratures when the pointer is at the fundamental frequency (Section 3.2.4).

Finally, the chapter explores postselection – presenting a new analysis of Kerr effect measurements postselected on infinitely squeezed states (Section 3.3.1) and considering the outcome probabilities of postselected POVMs (Section 3.3.2).

3.1 Von Neumann Approach

In this section, we explore the feasibility of implementing von Neumann weak measurements in optical systems by examining different optical nonlinearities. We analyze various measurable properties of light – including phase, photon number, field quadratures, and polarization – to identify which can serve effectively as pointer observables in the von Neumann measurement paradigm. Our investigation reveals significant constraints on viable interactions, with only select nonlinear processes (primarily variations of the Kerr effect) satisfying the necessary form of coupling between system observables and pointer variables. While these processes enable measurements of photon number, we find fundamental limitations for measuring other observables, particularly field quadratures, due to energy conservation requirements.

3.1.1 Weak von Neumann Measurements

Typically weak measurements are considered in the formalism of von Neumann measurements where a system couples to a pointer (Section 1.1.1). This coupling is given by the unitary:

$$\hat{U} = \mathrm{e}^{-ig\hat{p}\hat{O}/\hbar} \,. \tag{1.3 revisited}$$

The interaction that leads to this unitary will have a Hamiltonian of the form [18, 21]:

$$\hat{\mathcal{H}} = g\gamma(t)\hat{p}\hat{O} \,, \tag{3.1}$$

where $\gamma(t)$ is a normalized function with compact support near the time of measurement.

This relationship arises since the unitary that provides a solution to the Schrödinger equation is [20]:

$$\hat{U}(t,t_0) = \exp\left(\frac{-i}{\hbar}\int_{t_0}^{t}\hat{\mathcal{H}}(t')\mathrm{d}t'\right) \,. \tag{3.2}$$

When substituting in the measurement Hamiltonian and $\gamma(t)$ is a normalized function with compact support near the time of measurement (and $\hat{p}$ and $\hat{O}$ are time independent), the expression simplifies to:

$$\hat{U}(t,t_0) = \exp\left(\frac{-i}{\hbar}g\hat{p}\hat{O}\int_{t_0}^{t}\gamma(t')\mathrm{d}t'\right) = \exp\left(\frac{-i}{\hbar}g\hat{p}\hat{O}\right) \,. \tag{3.3}$$

To enable a von Neumann measurement, the interaction that couples the system and pointer together must be described by a Hamiltonian of this form – i.e. the Hamiltonian will need to have the conjugate momentum of a pointer observable as a factor.

3.1.2 Observables of Light

Since the pointer is a state of light, we can consider each property that can be experimentally observed and their conjugate momenta. This determines if any optical nonlinearities have a Hamiltonian of a useful form. A list of possible experimentally observable properties of a light beam is given in Table 3.1.

Experimentally Measured Quantity	Conjugate Momenta
Phase	Photon Number [35]
Photon Number (Intensity)	Phase
Field Quadrature ($\hat{X}$)	Field Quadrature ($\hat{Y}$) [41]
Polarization ($\hat{\sigma_x}$)	Polarization ($\hat{\sigma_y}$ or $\hat{\sigma_z}$) [16]
Frequency	Time [3]
Transverse Position	Transverse Momentum

Table 3.1: A table indicating the different properties of a light beam that can be experimentally observed and the conjugate momenta of each.

3.1.3 Phase

Optical phase is not well defined for many quantum systems [35]. However, it is for a coherent state. This is also the experimentally simplest state to use as the pointer and so is highly practical. The conjugate momenta of the phase observable is the photon number operator and so a nonlinear Hamiltonian of the form:

$$\hat{\mathcal{H}} = g\gamma(t)\hat{O}\hat{n} = g\gamma(t)\hat{O}\hat{a}^{\dagger}\hat{a}\,, \tag{3.4}$$

would measure the observable $\hat{O}$.

No second-order nonlinear optical process is able to have a Hamiltonian of this form, since every term of the Hamiltonian must leave the energy of the system unchanged. Since the second-order nonlinear process interaction Hamiltonian (given in Equation 1.61) is trilinear, a term with both raising and lowering operators corresponding to the same frequency can only leave the energy unchanged if the third operator corresponds to zero frequency. This

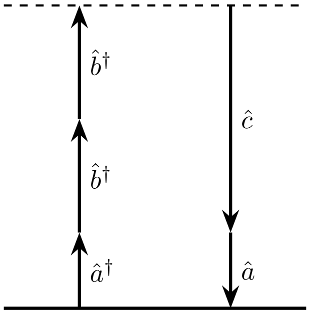

Adapted from a figure created by alchemist. This figure is licensed under CC BY-SA 4.0

Figure 3.1: Energy level diagram corresponding to a $\chi^{(4)}$ interaction given in the first term of Equation 3.6.

is in fact the Hamiltonian for the Pockels effect (considered in Section 3.1.8), but this third mode is no longer considered to be optical.

However, the Hamiltonian in Equation 3.4 matches that of the cross-Kerr effect:

$$\hat{\mathcal{H}} = \hbar\kappa\hat{n}_a\hat{n}_b = \hbar\kappa\hat{a}^\dagger\hat{a}\hat{b}^\dagger\hat{b}\,. \tag{3.5}$$

This interaction would enable the measurement of the number operator, $\hat{n}$, of a quantum system, as previously proposed and demonstrated by Steinberg's research group [26, 111, 112].

No other third-order optical nonlinear processes are able to have a Hamiltonian of the correct form, for similar energy conservation reasons as why no second-order process is able to.

Measuring a Quadrature with $\chi^{(4)}$

For a $\chi^{(4)}$ interaction, it is possible to have a Hamiltonian with the following terms:

$$\hat{\mathcal{H}} = \kappa_4(\hat{a}\hat{a}^\dagger\hat{b}^\dagger\hat{b}^\dagger\hat{c} + \hat{a}\hat{a}^\dagger\hat{b}\hat{b}\hat{c}^\dagger)\,, \tag{3.6}$$

where the frequency of the modes b and c are related by: $\omega_c = 2\omega_b$. This corresponds to an interaction given by the energy level diagram in Figure 3.1. If the parametric approximation is made for mode b, then $\hat{b} \to \beta$:

$$\hat{\mathcal{H}} = \kappa_4(\hat{a}\hat{a}^\dagger\beta^{*2}\hat{c} + \hat{a}\hat{a}^\dagger\beta^2\hat{c}^\dagger)\,. \tag{3.7}$$

If β is real then:

$$\hat{\mathcal{H}} = \kappa_4\beta^2\hat{a}\hat{a}^\dagger(\hat{c} + \hat{c}^\dagger) = 2\kappa_4\beta^2\hat{n}_a\hat{X}_c\,. \tag{3.8}$$

This is the Hamiltonian that would result in measuring a quadrature of c, if the phase of the pointer a is readout.

If the argument of β is $\pi/4$ then the Hamiltonian becomes:

$$\hat{\mathcal{H}} = i\kappa_4\beta^2\hat{a}\hat{a}^\dagger(\hat{c}^\dagger - \hat{c}) = 2\kappa_4\beta^2\hat{n}_a\hat{Y}_c\,, \tag{3.9}$$

which would read out the other quadrature of the field c.

However, it is highly unlikely that this interaction would be useful. Not only are the values of $\chi^{(4)}$ very small, but the phase of mode a is likely to be dominated by other stronger nonlinear processes, such as the cross-Kerr effect.

3.1.4 Photon Number

Using photon number as the readout observable for the pointer system has the issue that the conjugate momenta – which would be phase – is not well defined [35]. Since there is no well defined phase operator, it cannot be a factor of any nonlinear interaction Hamiltonian.

However, approximate operators can be defined, for example the Susskind and Glogower operator [43] (which is very similar to the Barnett and Pegg operators [42, 116]):

$$\mathrm{e}^{i\hat{\phi}} = \sum_0^\infty |n\rangle\langle n+1|\,. \tag{3.10}$$

A unitary of the form $\hat{U} = \mathrm{e}^{-ig\hat{O}\hat{\phi}/\hbar}$ would allow a von Neumann style measurement by measuring $\hat{n}$ of the pointer. However, it is not simple to express the Hamiltonian that would give this unitary in terms of creation and annihilation operators. In addition, doing so would not have the form of the nonlinear interaction Hamiltonians considered in Section 1.3.5.

Bernardo [117] has shown the average and variance of photon number can be used to perform a weak measurement. The Hamiltonian considered in that work had the form $\hat{\mathcal{H}} = g\hat{O}\hat{n}$, exactly the form that was considered in Section 3.1.3 of this thesis. However, rather than measuring the phase, the weak value was obtained from the photon statistics.

3.1.5 Field Quadratures

The quadrature of a field can be measured by homodyne detection [3] and the conjugate momenta is the other field quadrature. In terms of lowering and raising operators, the field quadratures are given by:

$$\hat{X}_a = \tfrac{1}{2}(\hat{a}^\dagger + \hat{a})\,, \tag{3.11a}$$

$$\hat{Y}_a = \tfrac{i}{2}(\hat{a}^\dagger - \hat{a})\,. \tag{3.11b}$$

An interaction Hamiltonian that allows for a weak measurement to be performed by measuring a field quadrature must then have the form:

$$\hat{\mathcal{H}}_X = g\hat{Y}_a\hat{O} = \tfrac{i}{2}g(\hat{a}^\dagger - \hat{a})\hat{O}\,, \tag{3.12a}$$

or

$$\hat{\mathcal{H}}_Y = g\hat{X}_a\hat{O} = \tfrac{1}{2}g(\hat{a}^\dagger + \hat{a})\hat{O}\,. \tag{3.12b}$$

However, there cannot be any parametric nonlinear interaction with this form. Each term of the Hamiltonian needs to correspond to an energy level diagram that conserves the energy across the different optical modes. This means every creation operator must be paired with annihilation operators corresponding to photons with the same total energy, and the reverse for annihilation operators. For example, the Hamiltonian describing the process of second harmonic generation is:

$$\hat{\mathcal{H}} = \kappa\left(\hat{a}^2\hat{c}^\dagger + \hat{a}^{\dagger 2}\hat{c}\right)\,, \tag{3.13}$$

where the second harmonic mode, c, has a frequency twice that of the fundamental mode, a, and so each photon in the second harmonic mode has twice the energy of each photon in the fundamental mode. For each term in the Hamiltonian to correspond to an energy level diagram, shown in Figure 3.2, one raising operator of the second harmonic mode, $\hat{c}^\dagger$ must be paired with two lowering operators of the fundamental, $\hat{a}^2$ (or the reverse).

This is not possible to do for the Hamiltonian given in Equation 3.12 as $\hat{O}$ cannot have the correct form to conserve energy for both the $\hat{a}$ and $\hat{a}^\dagger$ terms. A standard von Neumann measurement, reading the quadrature of an optical field as the pointer 'position', cannot be performed using a parametric nonlinear process.

Optomechanics

One place where a Hamiltonian of this form does appear is in optomechanics – where there is a coupling between a mechanical membrane and an optical field

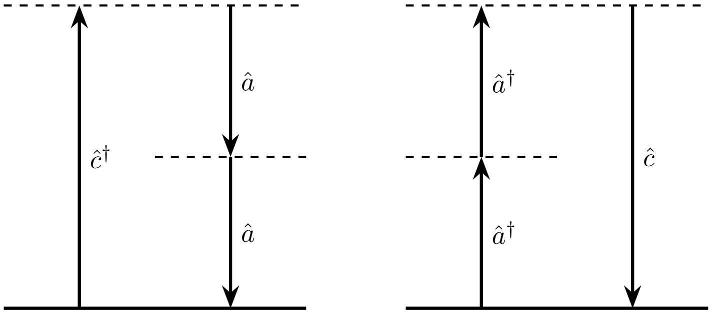

Figure 3.2: Energy level diagrams for the two terms in the Hamiltonian used to describe the process of second harmonic generation (Equation 3.13)

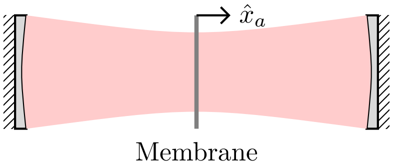

Figure 3.3: A diagram showing a mechanical membrane in an optical cavity. The position of the membrane is given by the operator $\hat{x}_a$ and the number of photons in the cavity by $\hat{n}_b = \hat{b}^\dagger \hat{b}$.

[118] (shown in Figure 3.3). The Hamiltonian of this system is given by:

$$\hat{\mathcal{H}} = \kappa(\hat{a}^\dagger + \hat{a})\hat{b}^\dagger\hat{b} = \kappa\hat{x}_a\hat{b}^\dagger\hat{b}\,, \tag{3.14}$$

where $\hat{b}$ is for the optical mode and $\hat{a}$ is for the membrane vibrational mode. In an optomechanical system, this enables the momentum of the membrane to be used as a pointer to observe the number of photons in the optical mode.

However, translating this Hamiltonian to be purely optical is not obvious. The origin of a Hamiltonian of this form is due to the position dependent frequency of light in the cavity. The Hamiltonian for the optical mode is given by [118]:

$$\hat{\mathcal{H}} = \kappa\omega(\hat{x})\hat{b}^\dagger\hat{b}\,. \tag{3.15}$$

When Taylor expanded to first order, this then gives the Hamiltonian of the form considered above.

$$\hat{\mathcal{H}} = \kappa\left(\omega_0 + \hat{x}\frac{\mathrm{d}\omega}{\mathrm{d}x}\bigg|_{x=0}\right)\hat{b}^\dagger\hat{b} = \kappa\omega_0\hat{b}^\dagger\hat{b} + \kappa\frac{\mathrm{d}\omega}{\mathrm{d}x}\bigg|_{x=0}(\hat{a}^\dagger + \hat{a})\hat{b}^\dagger\hat{b} \tag{3.16}$$

For the same Hamiltonian to be generated by an equivalent nonlinear optical process, the frequency of one mode would need to depend on a quadrature of the other.

The frequency of the light can be shifted if there is a time varying refractive index – as could be created with the Pockels effect. The amount that the frequency changes would depend on the time properties of the refractive index change and would be proportional to the rate of change of the electric field. However, to create a frequency shift of the same type as in an optomechanical cavity, the electric field would need to be varying in time significantly slower than the pointer frequency. This is very similar to case of electro-optic sampling considered in Section 3.1.8 (though leading to a phase rather than polarization change).

Using Two Pointers

Wu and Żukowski [113] propose a scheme where reading the quadrature of an optical pointer state, in combination with an optical nonlinear interaction, does allow weak values to be measured. They consider the case of parametric down-conversion – a $\chi^{(2)}$ process where the pump is treated as classical using the parametric approximation. This gives an interaction Hamiltonian:

$$\hat{\mathcal{H}} = \kappa\left(\hat{a}\hat{b} + \hat{a}^\dagger\hat{b}^\dagger\right) = 2\kappa\left(\hat{X}_a\hat{X}_b - \hat{Y}_a\hat{Y}_b\right) . \tag{3.17}$$

After post-selection, this interaction shifts the pointer 'position', $\hat{X}_a$, by an amount:

$$\begin{aligned}\delta X_a = 4\kappa\mathrm{Im}(X_{bw})\mathrm{Var}(\hat{X}_a) - \kappa\mathrm{Re}(Y_{bw}) \\ - 2\kappa\mathrm{Im}(Y_{bw})\langle\{\hat{X}_a - \langle\hat{X}_a\rangle, \hat{Y}_a - \langle\hat{Y}_a\rangle\}\rangle ,\end{aligned} \tag{3.18}$$

where X_{bw} and Y_{bw} are the weak values of the corresponding observables and $\{\hat{x}, \hat{y}\}$ is the anticommutator of $\hat{x}$ and $\hat{y}$. There is a similar expression for the shift in $\hat{Y}_a$.

By considering two pointers with different variances in $\hat{X}_a$, and assuming that the pointers are in Gaussian states, Wu and Żukowski are able to find expressions for the weak values of $\hat{X}_b$ and $\hat{Y}_b$. For example:

$$\mathrm{Re}(X_{bw}) = \frac{1}{\kappa}\frac{\mathrm{Var}(\hat{Y}_{a2})\delta Y_{a1} - \mathrm{Var}(\hat{Y}_{a1})\delta Y_{a2}}{\mathrm{Var}(\hat{Y}_{a1}) - \mathrm{Var}(\hat{Y}_{a2})} . \tag{3.19}$$

Whilst making use of the von Neumann formalism of measurement, these results clearly are not a typical von Neumann measurement. They require two quantum optical pointer states with different amounts of squeezing and directly make use of the uncertainty in their initial quadrature 'position'.

3.1.6 Two Pump Scheme*

Whilst it is not possible for a single parametric process to have a Hamiltonian of the form given in Equation 3.12, this is not the case if multiple processes occur simultaneously. First proposed by Yurke [114], a $\chi^{(2)}$ medium is able to perform an interaction of the correct form when pumped at the sum and difference frequencies of the system and pointer. Below, we derive this result using the same formalism as elsewhere in this section.

We can consider the case of four frequencies interacting in a $\chi^{(2)}$ medium, where $\omega_c = \omega_a + \omega_b$ and $\omega_d = \omega_a + \omega_c$ (shown in Figures 3.4 and 3.5).

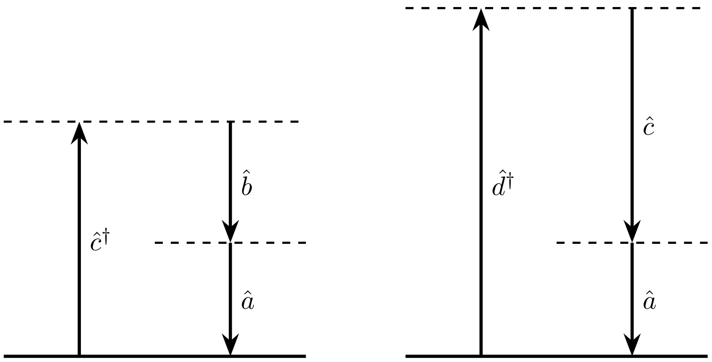

Figure 3.4: Energy level diagrams for the two simultaneous nonlinear processes occurring in the two pump scheme.

The Hamiltonians for the two interactions are given by:

$$\hat{\mathcal{H}}_1 = \kappa_1 \left(\hat{a}\hat{b}\hat{c}^\dagger + \hat{a}^\dagger\hat{b}^\dagger\hat{c} \right) , \tag{3.20a}$$

and

$$\hat{\mathcal{H}}_2 = \kappa_2 \left(\hat{a}\hat{c}\hat{d}^\dagger + \hat{a}^\dagger\hat{c}^\dagger\hat{d} \right) . \tag{3.20b}$$

---

*This work was done in collaboration with Kyle Jordan. KJ proposed that a two pump scheme would give a Hamiltonian of the correct form for a $\chi^{(3)}$ process, the full details for this and extension to $\chi^{(2)}$ was done by Thomas Bailey.

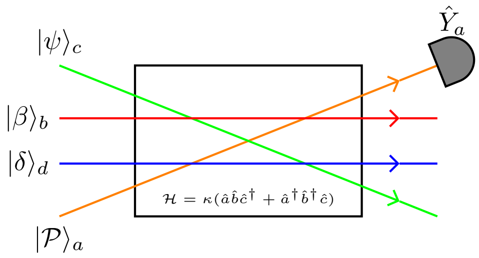

Figure 3.5: A schematic showing the modes interacting for a two pump von Neumann measurement. The state in mode c is measured by reading out the Y quadrature of the pointer mode a. Modes b and d are classical pumps.

If modes b and d are pumped with coherent light (with amplitudes β and δ), such that the parametric approximation can be made, the Hamiltonians become:

$$\hat{\mathcal{H}}_1 = \kappa_1 \left(\beta \hat{a}\hat{c}^\dagger + \beta^* \hat{a}^\dagger \hat{c}\right) \, , \tag{3.21a}$$

and

$$\hat{\mathcal{H}}_2 = \kappa_2 \left(\delta^* \hat{a}\hat{c} + \delta \hat{a}^\dagger \hat{c}^\dagger\right) \, . \tag{3.21b}$$

The total interaction Hamiltonian is given as the sum of these two Hamiltonians,

$$\hat{\mathcal{H}}_T = \hat{a}\left(\kappa_1 \beta \hat{c}^\dagger + \kappa_2 \delta^* \hat{c}\right) + \hat{a}^\dagger \left(\kappa_1 \beta^* \hat{c} + \kappa_2 \delta \hat{c}^\dagger\right) \, . \tag{3.22}$$

If the pump amplitudes are chosen such that $\kappa_1 \beta = \kappa_2 \delta = g$, then the total interaction Hamiltonian becomes:

$$\hat{\mathcal{H}}_T = \left(\hat{a} + \hat{a}^\dagger\right)\left(g\hat{c}^\dagger + g^* \hat{c}\right) \, , \tag{3.23}$$

$$\hat{\mathcal{H}}_T = 2\hat{X}_a \left(g\hat{c}^\dagger + g^*\hat{c}\right) = 4\hat{X}_a \mathrm{Re}\left[g\hat{c}^\dagger\right] \, . \tag{3.24}$$

This has exactly the form of Equation 3.12, where the Y quadrature of the pointer in mode a is readout to give the observable $\hat{O} = 4\mathrm{Re}\left[g\hat{c}^\dagger\right]$ (a quadrature of mode c). The X quadrature of mode a could have been readout instead if $\kappa_1\beta = -\kappa_2\delta = g$.

In practice this approach is likely to be challenging to perform, requiring: setting the amplitude of the two pumps such that the interaction strength of two nonlinear interactions are the same; phase stability between the two pumps; four different frequencies (which will cover a frequency range spanning at least 1.5 octaves); and the challenge of achieving sufficient phase matching for both processes simultaneously.

Extending beyond the result of Yurke, a similar scheme is possible using a $\chi^{(3)}$ nonlinearity. This enables the measurement of observables of the two mode operator,

$$\hat{O} = \left(g^* \hat{a}\hat{b} + g\hat{a}^\dagger \hat{b}^\dagger\right) = 2\mathrm{Re}\left[g\hat{a}^\dagger \hat{b}^\dagger\right] . \tag{3.25}$$

This could be useful either to measure the joint value of two operators on different optical modes or, if mode b is pumped with coherent light, enabling the use of a centrosymmetric nonlinear medium to measure field quadrature.

3.1.7 Combining Linear and Nonlinear Elements

It is possible to consider a more general case where there is an arbitrary linear unitary before and after the nonlinear element. In this expanded space of possible operators, it is possible to find unitaries of the correct form to perform a von Neumann measurement. Yurke [114]; La Porta, Slusher and Yurke [119]; Braunstein [115]; and Salykina, Liamin, Sharapova and Khalil [120] have proposed schemes to measure field quadratures using a $\chi^{(2)}$ nonlinearity.

One way to explore these schemes is to consider the measurement operator in terms of Gaussian optics, as was done by Braunstein [115]. This enables finding the approach proposed by Yurke [114] (using two single mode squeezers of inverse strength) as well as an alternative configuration with two squeezers of identical strength. These schemes have the configuration shown in Figure 3.6.

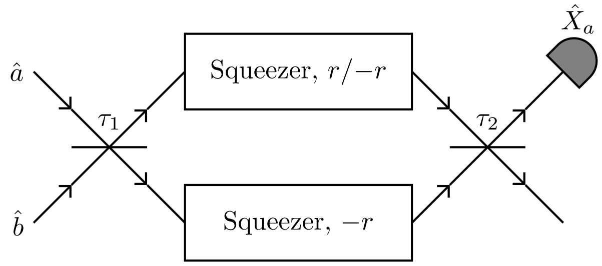

Figure 3.6: A von Neumann measurement of quadrature can be achieved by using linear elements (beam splitters) and single mode squeezers. The quadrature of mode b is measured and the quadrature of pointer a is readout with homodyne detection. Arrangements with squeezers of equal squeezing or inverse squeezing strength (r) [114] enable this scheme – with different linear transformations required for each configuration.

Bloch-Messiah Decomposition

A unitary operator generated by a Hamiltonian which is at most quadratic in the raising and lowering operators, is a Gaussian operation [55, 121]. Since the von Neumann interaction unitary can be of this form, the formalism of Gaussian states and operators (introduced in Section 1.5) is useful as it allows the interaction to be decomposed into passive and single mode active operations.

We can consider when the measurement Hamiltonian is of the form:

$$\hat{\mathcal{H}} = g\hat{Y}_a\hat{O}\,. \tag{3.26}$$

This would displace the X quadrature of the pointer (mode a) to measure $\hat{O}$. When $\hat{O}$ is linear in terms of raising/lowering operators (or quadrature operators), the entire Hamiltonian is quadratic and the Gaussian formalism can be applied.

The symplectic operator corresponding to this interaction is given by [57]:

$$S = \mathrm{e}^{\Omega H}\,, \tag{1.83 revisited}$$

where Ω is the block matrix:

$$\Omega = \begin{pmatrix} 0 & \mathbb{1} \\ -\mathbb{1} & 0 \end{pmatrix}\,. \tag{1.84 revisited}$$

The Hamiltonian used to measure an arbitrary quadrature operator ($\hat{O} = \alpha\hat{X}_b + \beta\hat{Y}_b$),

$$\hat{\mathcal{H}} = g\hat{Y}_a\left(\alpha\hat{X}_b + \beta\hat{Y}_b\right)\,, \tag{3.27}$$

has a H matrix:

$$H = \begin{pmatrix} 0 & 0 & 0 & 0 \\ 0 & 0 & g\alpha & 0 \\ 0 & g\alpha & 0 & g\beta \\ 0 & 0 & g\beta & 0 \end{pmatrix}\,. \tag{3.28}$$

This then gives the symplectic matrix:

$$S = \begin{pmatrix} 1 & g\alpha & 0 & g\beta \\ 0 & 1 & g\beta & 0 \\ 0 & 0 & 1 & 0 \\ 0 & 0 & -g\alpha & 1 \end{pmatrix}\,. \tag{3.29}$$

For simplicity, we will consider the case where we are measuring the X quadrature of the system ($\alpha = 1$ and $\beta = 0$), though all procedures will hold in the more general case.

This symplectic matrix can then be expressed as the product of three matricies by the Bloch-Messiah decomposition,

$$S = O_1 D O_2\,, \tag{3.30}$$

where O_1 and O_2 are orthogonal matrices corresponding to passive transformations (beam splitters and phase shifters) and D is a diagonal matrix representing single mode squeezers.

In principle, this can be done with a singular value decomposition. However, when there are degenerate singular values, the matrices are not uniquely defined and the orthogonal matrices may not have the expected form of Equation 3.35.

Two Identical Squeezers

One possible Bloch-Messiah decomposition is when the two modes have identical squeezers. The decomposition of the symplectic matrix corresponding to the measurement of X is then:

$$O_1 = \begin{pmatrix} \frac{a}{\sqrt{1+a^2}} & 0 & 0 & \frac{1}{\sqrt{1+a^2}} \\ \frac{1}{\sqrt{1+a^2}} & 0 & 0 & \frac{-a}{\sqrt{1+a^2}} \\ 0 & \frac{-1}{\sqrt{1+a^2}} & \frac{a}{\sqrt{1+a^2}} & 0 \\ 0 & \frac{a}{\sqrt{1+a^2}} & \frac{1}{\sqrt{1+a^2}} & 0 \end{pmatrix}, \tag{3.31a}$$

$$D = \begin{pmatrix} a & 0 & 0 & 0 \\ 0 & a & 0 & 0 \\ 0 & 0 & a^{-1} & 0 \\ 0 & 0 & 0 & a^{-1} \end{pmatrix}, \tag{3.31b}$$

$$O_2 = \begin{pmatrix} \frac{1}{\sqrt{1+a^2}} & \frac{a}{\sqrt{1+a^2}} & 0 & 0 \\ 0 & 0 & \frac{-a}{\sqrt{1+a^2}} & \frac{1}{\sqrt{1+a^2}} \\ 0 & 0 & \frac{1}{\sqrt{1+a^2}} & \frac{a}{\sqrt{1+a^2}} \\ \frac{a}{\sqrt{1+a^2}} & \frac{-1}{\sqrt{1+a^2}} & 0 & 0 \end{pmatrix}, \tag{3.31c}$$

where:

$$a = \frac{g + \sqrt{g^2 + 4}}{2}\,. \tag{3.32}$$

The matrix D corresponds to two identical single mode squeezers with strength [55, 121]:

$$r = -\ln a = -\ln\left(\frac{g + \sqrt{g^2+4}}{2}\right). \tag{3.33}$$

Given that the parameter, a, describes the amount of squeezing, it is useful to consider the strength of the measurement achieved with these squeezers,

$$g = \frac{a^2 - 1}{a}. \tag{3.34}$$

For no squeezing ($a = 1$), the measurement strength is 0. As the squeezing is increased (corresponding to $a < 1$), the effective measurement interaction strength increases.

The unitary that leads to the orthogonal matrix, O, is given by the rectangular decomposition [36, 55] where:

$$O = \begin{pmatrix} A & -B \\ B & A \end{pmatrix}, \tag{3.35}$$

and,

$$\hat{U} = A + iB. \tag{3.36}$$

For two modes, any passive transformation can be expressed as a generalized beam splitter [122]:

$$\hat{\tau} = \mathrm{e}^{i\phi_0}\begin{pmatrix} \cos\theta \mathrm{e}^{i\phi_\tau} & \sin\theta \mathrm{e}^{i\phi_\rho} \\ -\sin\theta \mathrm{e}^{-i\phi_\rho} & \cos\theta \mathrm{e}^{-i\phi_\tau} \end{pmatrix}, \tag{3.37}$$

where θ describes the magnitude of the beam splitter, ϕ_0 is a global phase, ϕ_τ is the phase difference between the two transmitted beams and ϕ_ρ is the phase difference between the reflected beams.

For the transformation O_1, the unitary is:

$$\hat{\tau}_1 = \begin{pmatrix} \cos\theta_1 & -i\sin\theta_1 \\ \sin\theta_1 & i\cos\theta_1 \end{pmatrix}, \tag{3.38}$$

where:

$$\cos\theta_1 = \frac{a}{\sqrt{1+a^2}} = \frac{1}{\sqrt{1 + \frac{2}{g^2 + g\sqrt{g^2+4} + 2}}}. \tag{3.39}$$

These beam splitter parameters are: $\phi_{01} = \frac{\pi}{4}$, $\phi_{\tau 1} = \frac{-\pi}{4}$, and $\phi_{\rho 1} = \frac{5\pi}{4}$.

For the transformation O_2, the unitary is:

$$\hat{\tau}_2 = \begin{pmatrix} \cos\theta_2 & \sin\theta_2 \\ i\sin\theta_2 & -i\cos\theta_2 \end{pmatrix}, \tag{3.40}$$

where:

$$\cos\theta_2 = \sin\theta_1 = \frac{1}{\sqrt{1+a^2}} = \sqrt{\frac{2}{g^2 + g\sqrt{g^2+4} + 4}}\,. \tag{3.41}$$

These beam splitter parameters are: $\phi_{02} = \frac{-\pi}{4}$, $\phi_{\tau 2} = \frac{\pi}{4}$, and $\phi_{\rho 2} = \frac{\pi}{4}$.

Two Inverse Squeezers

Another possible Bloch-Messiah decomposition is when the squeezers have inverse squeezing strength. This is exactly the case proposed by Yurke [114]. The decomposition of the symplectic matrix corresponding to the measurement of X is then:

$$O_1 = \begin{pmatrix} \frac{a}{\sqrt{1+a^2}} & \frac{-1}{\sqrt{1+a^2}} & 0 & 0 \\ \frac{1}{\sqrt{1+a^2}} & \frac{a}{\sqrt{1+a^2}} & 0 & 0 \\ 0 & 0 & \frac{a}{\sqrt{1+a^2}} & \frac{-1}{\sqrt{1+a^2}} \\ 0 & 0 & \frac{1}{\sqrt{1+a^2}} & \frac{a}{\sqrt{1+a^2}} \end{pmatrix}, \tag{3.42a}$$

$$D = \begin{pmatrix} a & 0 & 0 & 0 \\ 0 & a^{-1} & 0 & 0 \\ 0 & 0 & a^{-1} & 0 \\ 0 & 0 & 0 & a \end{pmatrix}, \tag{3.42b}$$

$$O_2 = \begin{pmatrix} \frac{1}{\sqrt{1+a^2}} & \frac{a}{\sqrt{1+a^2}} & 0 & 0 \\ \frac{-a}{\sqrt{1+a^2}} & \frac{1}{\sqrt{1+a^2}} & 0 & 0 \\ 0 & 0 & \frac{1}{\sqrt{1+a^2}} & \frac{a}{\sqrt{1+a^2}} \\ 0 & 0 & \frac{-a}{\sqrt{1+a^2}} & \frac{1}{\sqrt{1+a^2}} \end{pmatrix}, \tag{3.42c}$$

where:

$$a = \frac{g + \sqrt{g^2+4}}{2}\,. \tag{3.43}$$

The matrix D corresponds to two single mode squeezers with strengths inverse of each other:

$$r = \pm\ln a = \pm\ln\left(\frac{g+\sqrt{g^2+4}}{2}\right). \tag{3.44}$$

For the transformation O_1, the unitary is:

$$\hat{\tau}_1 = \begin{pmatrix} \cos\theta_1 & \sin\theta_1 \\ -\sin\theta_1 & \cos\theta_1 \end{pmatrix} , \tag{3.45}$$

where:

$$\cos\theta_1 = \frac{a}{\sqrt{1+a^2}} = \frac{1}{\sqrt{1+\frac{2}{g^2+g\sqrt{g^2+4}+2}}} . \tag{3.46}$$

For the transformation O_2, the unitary is:

$$\hat{\tau}_2 = \begin{pmatrix} \cos\theta_1 & \sin\theta_1 \\ -\sin\theta_1 & \cos\theta_1 \end{pmatrix} , \tag{3.47}$$

These are the same beam splitter amplitudes found by Yurke [114].

Use of Block-Messiah Decomposition for Measurement

This approach would enable the measurement of a quadrature operator of one mode, by reading out the quadrature of the pointer. Unlike the other schemes considered in this thesis, the two modes do not directly interact in a nonlinear interaction – instead passing through a beam splitter and then both modes experiencing identical (or inverse) single mode squeezers.

To perform this experimentally would need precise control of the amplitudes of two variable beam splitters to correctly match the strength of the single mode squeezers. When using standard beam splitters, the frequency of the two modes would need to be the same. Whilst making the experiment simpler, it also reduces the possible advantages to this scheme (although it would still enable a non-demolition measurement of quadrature). To use modes of different frequencies would require a 'frequency beam splitter' [123, 124] to superpose these modes.

Other approaches combining linear and nonlinear elements can be more experimentally straightforward, with for instance the use of parametric amplification already demonstrated by La Porta, Slusher and Yurke [119].

3.1.8 Polarization

Polarization acts as a qubit and the observables for polarization states are the Pauli matrices. A measurement in the computational basis is given by $\langle\hat{\sigma}_z\rangle$. This is effectively calculating the average projection of the state's Bloch vector onto the z-axis.

The generators of rotations around the Bloch sphere are given by the Pauli matrices [16]:

$$R_D(\theta) = \mathrm{e}^{-i\theta\hat{\sigma}_x/2}\,, \tag{3.48a}$$

$$R_L(\theta) = \mathrm{e}^{-i\theta\hat{\sigma}_y/2}\,, \tag{3.48b}$$

$$R_H(\theta) = \mathrm{e}^{-i\theta\hat{\sigma}_z/2}\,, \tag{3.48c}$$

where $R_i(\theta)$ is a rotation by an angle θ about an axis i of the Bloch sphere.

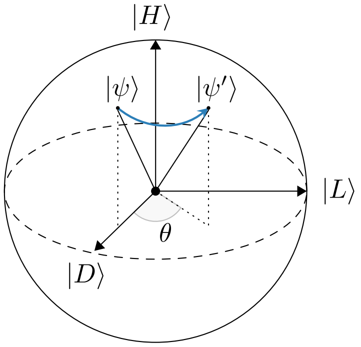

Adapted from a figure created by Sebastiano & cfr. This figure is licensed under CC BY-SA 4.0

Figure 3.7: The state $|\psi\rangle$ is rotated by an angle θ about the $|H\rangle/|V\rangle$ axis to a state $|\psi'\rangle$. This corresponds to the unitary operator $\hat{U} = \mathrm{e}^{-i\theta\hat{\sigma}_z/2}$. This rotation does not maximize the change in state for the rotation amount θ. To achieve a maximal change in state, a rotation about an axis perpendicular to the $|\psi\rangle$ vector is required.

Since a qubit state can be represented on the Bloch sphere (as shown in Figure 3.7), the axis of rotation that would maximize the change in position for a given θ (an axis perpendicular to the state's Bloch vector) depends on the current state. In addition, these rotations are cyclical. As a rotation of 2π would leave a state unchanged. However, for small displacements from an initial state, polarization can be used in the same way as any other pointer – when the pointer is prepared along one basis state, measured in a mutually unbiased basis and then rotated around the 3rd mutually unbiased basis. This gives the von Neumann interaction unitary:

$$\hat{U} = \mathrm{e}^{-i\hat{O}\hat{\sigma}/2}\,. \tag{3.49}$$

In quantum optics, the two orthogonal polarization basis states are considered as different modes. Considering two modes H and V, the Pauli-z operator would be:

$$\hat{\sigma}_z = \frac{\hat{n}_H - \hat{n}_V}{\hat{n}_H + \hat{n}_V} \,. \tag{3.50}$$

From this expression alone it is not clear which, if any, nonlinear interaction could have this term as a factor in their Hamiltonian. However, we typically use a waveplate to rotate a polarization state – a birefringent material whose optic axis is not aligned with that of the polarization state. Hence, any nonlinear optical interaction that induces a birefringence will allow polarization to be used as the readout of the pointer.

Kerr Birefringence

It has long been known that an optical pulse is able to create birefringence in a material through the Kerr effect [125, 126]. This is able to rotate the polarization state of a pointer. The strength of this birefringence depends on the photon number of the measured system and so this would allow a measurement of photon number using polarization as a pointer. In many respects this would be similar to measurements using the pointer phase in Section 3.1.3, also using a $\chi^{(3)}$ Kerr effect.

Electro-optic Sampling

Another nonlinear interaction that can induce birefringence is the Pockels effect [8]. This is a $\chi^{(2)}$ process that occurs with a static electric field. The change to the parameters of the index ellipsoid is:

$$\Delta \left(\frac{1}{n^2} \right)_i = \sum_j r_{ij} E_j \,. \tag{3.51}$$

Typically the effect is small and $r_{ij} E_j << 1$. When this is the case, the change in refractive index is given by:

$$\Delta n \approx -\tfrac{1}{2} n^3 r E \,, \tag{3.52}$$

which is proportional to the electric field amplitude.

When an electromagnetic wave is oscillating at a much lower frequency than the pointer it can be approximated as static. This is the case for electro-optic sampling of terahertz radiation [127–129], and enables the measurement of the radiation's instantaneous electric field. This technique however, would be very challenging to perform at standard optical frequencies – although extensions have been shown into the near-infrared [130].

3.1.9 Other Observables

Other possible observables to measure on the pointer, such as position or frequency, are generally treated as independent modes in quantum optics and so will not appear directly in a nonlinear interaction Hamiltonian.

In these multi-mode cases, the second quantization framework used throughout this chapter is no longer as useful. There is no longer a finite number of modes coupling together – but rather a continuum of states that (in the 2nd quantization formalism) must be expressed in terms of a mode basis. This makes any calculations far more cumbersome and much more challenging to gain insight from them. However, it can be productive to consider these cases in a first quantization framework - where we consider the effect of an environment on a photon's state. To do this, we make use of the known, classical, effects of a particular optical nonlinearity (for instance a refractive index change in the cross Kerr effect) and consider how this will change the pointer state. This was the approach taken in the above discussion regarding the use of polarization as a pointer.

Another example would be changing the refractive index to create a lensing effect – modifying the transverse position of the pointer. Though, as with induced birefringence, for the Kerr effect, this refractive index change will be proportional to the photon number operator and would not enable measurement of a new quantity.

It would also be possible to create a situation with a spatially or temporally varying coupling constant, g (for instance if the nonlinear material was only in a section of the beam). This would enable the use of nonlinear optical measurement techniques to be applied in similar ways to typical measurements of position, but with potential advantages such as non-demolition.

3.1.10 Von Neumann Measurements Summary

This section explored the opportunities of implementing von Neumann weak measurements in optical systems by examining various optical observables and their potential as pointer systems. The key challenge is finding nonlinear optical interactions with Hamiltonians that satisfy the von Neumann measurement formalism – where the interaction Hamiltonian must couple the system observable to the pointer's conjugate momentum.

We see that there are significant constraints on which interactions are able to create coupling of the desired form. While some observables like phase and polarization show potential, most face fundamental limitations. For instance, quadrature measurements cannot be performed directly using parametric nonlinear processes due to energy conservation requirements. The most promising approaches all use some variation of the Kerr effect and so are only suitable for measurements of photon number.

More complicated approaches, such as using two pumps of different frequencies or replacing a single interaction with linear and nonlinear elements, are able perform von Neumann measurements of field quadratures. These approaches have more experimental complexity and requiring fine tuning of several parameters to function, though do provide options to enable non demolition measurements.

The limited number of optical nonlinear interactions that are able to create a von Neumann form interaction suggests that a more general framework of measurement should be considered – as in the next section.

Key Findings

- Implementing von Neumann style weak measurements requires an interaction Hamiltonian that couples the measured observable to the pointer's conjugate momentum. (Section 3.1)

- The Kerr effect has a Hamiltonian of a form that would enable the photon number operator of a system to be measured by reading out the phase of the pointer. (Section 3.1.3, 3.1.8 and 3.1.9)

- There is a $\chi^{(4)}$ interaction that would allow the field quadrature operator of a system to be measured. However, in practice the Kerr effect is likely to dominate the pointer position making this very challenging to implement. (Section 3.1.3)

- Using two pumps with a tuned amplitude relationship enables the measurement of the field quadrature observable. Given the large range in frequencies needed for this scheme, it is likely to be challenging to use. (Section 3.1.6)

- Using the formalism of Gaussian operations, the interaction required to measure a quadrature operator can be decomposed into two generalized beam splitters and two single mode squeezers.

- Other optical nonlinear interactions and possible pointer readout degrees of freedom will not work for von Neumann style measurements.

3.2 POVM Approach

In this section, we explore how optical nonlinearities can be harnessed to perform quantum measurements within the Positive Operator-Valued Measure (POVM) framework. We begin by examining various nonlinear interaction Hamiltonians and their representations in both raising/lowering operators and quadrature space, with particular focus on $\chi^{(2)}$ nonlinearities.

We consider different measurement scenarios, including number state pointers and readout, coherent state pointers with number-basis readout, and quadrature pointer readout. We show that while number state approaches face significant experimental challenges, coherent state pointers offer potentially practical pathways to extracting quadrature information about quantum states.

Notably, we show how observations of the intensity of a coherent pointer after nonlinear interaction can provide quantum non-demolition measurements of field quadratures – potentially offering advantages over traditional homodyne techniques, especially for bright fields.

3.2.1 Optical Nonlinear Hamiltonians

A more general approach to quantum measurement is to use the POVM formalism introduced in Section 1.1.3. This allows us to consider the consequences of any interaction unitary, and avoids the need to find unitaries of a specific form.

There are a number of possible nonlinear interactions that could potentially lead to interesting results. Hamiltonians for these interactions can be written in terms of both raising and lowering operators, as well as using quadrature operators. Each representation offers different insights. Table 3.2 shows a selection of possible Hamiltonians for cases where there are only two quantum modes interacting (and potentially additional classical modes). These are of most interest to us since we want to consider the case of a quantum pointer and measured state interacting and additional quantum modes will complicate the analysis (as well as making an implementation more experimentally challenging and likely resulting in very weak interaction strengths).

3.2.2 Finding Kraus Operators

Nonlinear optical interactions (or any other unitary operator) will result in a POVM. However, the meaning of this POVM, and the information it provides about the measured state, is less clear. More information is needed about the effects, $\hat{E}_k$. The approach in Todd Brun's lecture notes [131] is used.

Interaction	Raising & Lowering Representation	Quadrature Representation
Second Harmonic Generation	$\kappa\left(\hat{a}^{\dagger 2}\hat{c}+\hat{a}^2\hat{c}^\dagger\right)$	$2\kappa\Big(\big(\hat{X}_a^2-\hat{Y}_a^2\big)\hat{X}_c+\big(\hat{X}_a\hat{Y}_a+\hat{Y}_a\hat{X}_a\big)\hat{Y}_c\Big)$
Down Conversion with Classical Pump	$\kappa\left(\gamma^*\hat{a}\hat{b}+\gamma\hat{a}^\dagger\hat{b}^\dagger\right)$	$2\kappa\left(\mathrm{Re}[\gamma]\left(\hat{X}_a\hat{X}_b-\hat{Y}_a\hat{Y}_b\right)+\mathrm{Im}[\gamma]\left(\hat{X}_a\hat{Y}_b+\hat{Y}_a\hat{X}_b\right)\right)$
$\chi^{(2)}$ with Classical Idler	$\kappa\left(\beta^*\hat{a}^\dagger\hat{c}+\beta\hat{a}\hat{c}^\dagger\right)$	$2\kappa\left(\mathrm{Re}[\beta]\left(\hat{X}_a\hat{X}_c+\hat{Y}_a\hat{Y}_c\right)+\mathrm{Im}[\beta]\left(\hat{X}_a\hat{Y}_c-\hat{Y}_a\hat{X}_c\right)\right)$
Kerr Effect	$\kappa\hat{a}^\dagger\hat{a}\hat{b}^\dagger\hat{b}$	$\kappa\left(\hat{X}_a^2+\hat{Y}_a^2-\frac{1}{2}\right)\left(\hat{X}_b^2+\hat{Y}_b^2-\frac{1}{2}\right)$
n^{th} order interaction	$g\left(\hat{a}^n\hat{b}^\dagger+\hat{a}^{\dagger n}\hat{b}\right)$	$g\left(\left(\hat{a}^n+\hat{a}^{\dagger n}\right)\hat{X}_b+i\left(\hat{a}^{\dagger n}-\hat{a}^n\right)\hat{Y}_b\right)$

Table 3.2: Some possible Hamiltonians for the interaction of two quantum modes (there may be additional classical modes where the parametric approximation has been made). These are expressed both in terms of raising/lowering operators and in terms of field quadratures.

The n^{th} order interaction expression applies for both an actual n^{th} order interaction, as well as higher order nonlinearities using classical pumps to achieve a similar effect.

The interaction unitary is partially decomposed in the basis of pointer readout outcomes:

$$\hat{U}=\sum_{k,k'}\hat{A}_{kk'}\otimes|f^k\rangle\langle f^{k'}|\,. \tag{3.53}$$

If this unitary is applied to an initial state where the pointer is prepared as one of the measurement outcomes, $|\mathcal{P}\rangle=|f^c\rangle$, then:

$$\hat{U}|\psi\rangle|f^c\rangle=\sum_k\hat{A}_{kc}|\psi\rangle\otimes|f^k\rangle\,, \tag{3.54}$$

and hence the Kraus operator is:

$$\hat{K}_k=\hat{A}_{kc}\,, \tag{3.55}$$

giving the effect:

$$\hat{E}_k=\hat{A}_{kc}^\dagger\hat{A}_{kc}\,. \tag{3.56}$$

3.2.3 $\chi^{(2)}$ Nonlinearity with Pointer Input and Readout in the Number Basis

To use the approach above we must choose the pointer read-out basis. A natural choice of an orthogonal basis for an optical system are Fock (number) states. Considering the case of a $\chi^{(2)}$ nonlinearity, the interaction unitary is given by:

$$\hat{U} = e^{i\kappa(\hat{a}\hat{b}\hat{c}^\dagger + \hat{a}^\dagger\hat{b}^\dagger\hat{c})}\,, \tag{3.57}$$

which for a weak measurement can be approximated as:

$$\hat{U} \approx \mathbb{1} + i\kappa\left(\hat{a}\hat{b}\hat{c}^\dagger + \hat{a}^\dagger\hat{b}^\dagger\hat{c}\right)\,. \tag{3.58}$$

Represented in the number basis, the raising and lowering operators are:

$$\hat{a} = \sum_i \sqrt{i}|i-1\rangle\langle i|\,, \tag{3.59a}$$

$$\hat{a}^\dagger = \sum_i \sqrt{i+1}|i+1\rangle\langle i|\,. \tag{3.59b}$$

Pointer as the Second Harmonic

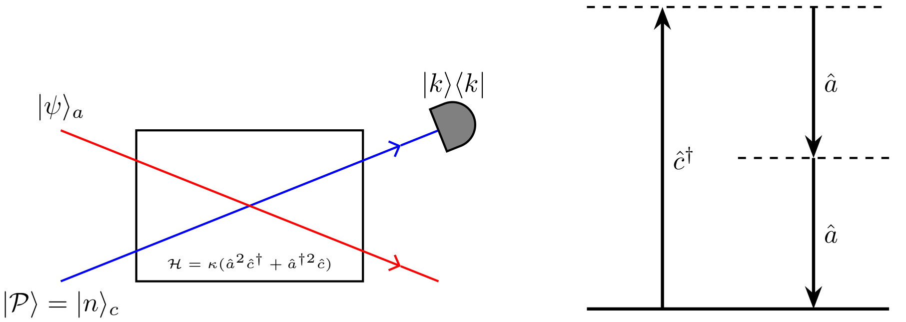

Adapted from a figure created by alchemist.
This figure is licensed under CC BY-SA 4.0

(a) Interacting modes (b) Energy level diagram

Figure 3.8: The modes interacting when the pointer (mode c) is the second harmonic of the measured system (mode a). The initial pointer state is a number state, $|n\rangle$, and is measured in the number basis, $|k\rangle$.

We can consider the case where the pointer is chosen as the second harmonic of the system being measured (so modes a and b are identical). This means that there are only two optical modes interacting: the system, a, and the pointer, c, as shown in Figure 3.8.

$$\hat{U} = \mathbb{1} + i\kappa\left(\hat{a}^2\hat{c}^\dagger + \hat{a}^{\dagger 2}\hat{c}\right) \tag{3.60}$$

The interaction unitary can be partially decomposed in the number basis to give:

$$\hat{U} = \sum_{k,k'} |k\rangle\langle k'| \otimes \left(\mathbb{1}\delta_{k,k'} + i(\hat{a}^{\dagger 2}\kappa\sqrt{k'}\delta_{k,k'-1} + i\hat{a}^2\kappa\sqrt{k'+1}\delta_{k,k'+1}\right)\,. \tag{3.61}$$

To proceed with the analysis, we also need to consider a specific pointer state initialization. When the initial pointer state is a number state, $|\mathcal{P}\rangle = |n\rangle_c$, this gives the Kraus operators:

$$\hat{K}_{n-1} = i\kappa\sqrt{n}\hat{a}^{\dagger 2}\,, \tag{3.62a}$$

$$\hat{K}_n = \mathbb{1}\,, \tag{3.62b}$$

$$\hat{K}_{n+1} = i\kappa\sqrt{n+1}\hat{a}^2\,, \tag{3.62c}$$

and the generalized measurement operators are:

$$\hat{E}_{n-1} = \kappa^2 n\hat{a}^2\hat{a}^{\dagger 2}\,, \tag{3.63a}$$

$$\hat{E}_n = \mathbb{1}\,, \tag{3.63b}$$

$$\hat{E}_{n+1} = \kappa^2(n+1)\hat{a}^{\dagger 2}\hat{a}^2\,. \tag{3.63c}$$

The probability to find that the pointer mode contains k photons is:

$$p_k = \langle\psi|\hat{E}_k|\psi\rangle\,, \tag{3.64}$$

and so:

$$p_{n-1} = \kappa^2 n\langle\psi|\hat{a}^2\hat{a}^{\dagger 2}|\psi\rangle\,, \tag{3.65a}$$

$$p_n \approx 1\,, \tag{3.65b}$$

$$p_{n+1} = \kappa^2(n+1)\langle\psi|\hat{a}^{\dagger 2}\hat{a}^2|\psi\rangle\,. \tag{3.65c}$$

Due to the assumption of a weak interaction, the only possible measurements are $n-1$, n and $n+1$. As discussed in more detail in Section 3.2.3, this result is probably not very useful due to needing precise number state information.

Pointer as the Fundamental

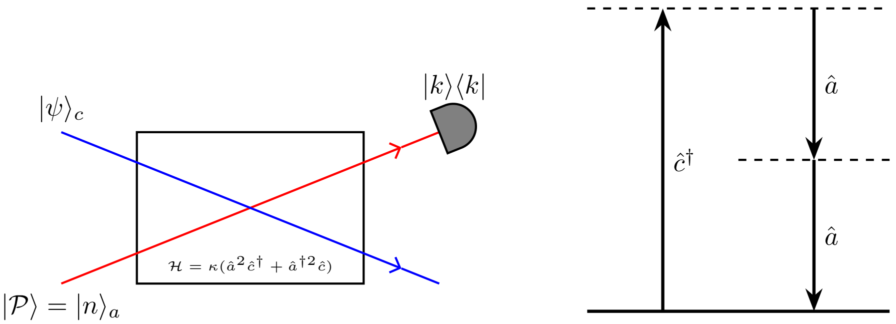

Adapted from a figure created by alchemist.
This figure is licensed under CC BY-SA 4.0

(a) Interacting modes (b) Energy level diagram

Figure 3.9: The modes interacting when the measured system (mode c) is the second harmonic of the pointer (mode a). The initial pointer state is a number state, $|n\rangle$, and is measured in the number basis, $|k\rangle$.

If the pointer is chosen as the fundamental frequency and the system is the second harmonic (so that modes a and b are identical and correspond to the pointer and mode c to the measured system, as shown in Figure 3.9) then the interaction unitary is:

$$\hat{U} = \mathbb{1} + i\kappa\left(\hat{c}^\dagger\hat{a}^2 + \hat{c}\hat{a}^{\dagger 2}\right) . \tag{3.66}$$

For the initial pointer state $|\mathcal{P}\rangle = |n\rangle_a$, this then gives the POVM:

$$\hat{E}_{n-2} = \kappa^2 n(n-1)\hat{c}\hat{c}^\dagger \,, \tag{3.67a}$$

$$\hat{E}_n = \mathbb{1} \,, \tag{3.67b}$$

$$\hat{E}_{n+2} = \kappa^2(n+1)(n+2)\hat{c}^\dagger\hat{c} \,. \tag{3.67c}$$

The probability to detect a change in photon number will be proportional to the number of photons in the measured system.

Other Second Order Processes

Another option is to consider the full trilinear Hamiltonian. To continue considering only two quantum modes, we will consider when one mode is a coherent state, enabling the parametric approximation to be made.

When the parametric approximation is made for the mode at the highest frequency (mode c) and the coherent state in this mode has an amplitude γ, the unitary of the interaction will be:

$$\hat{U} = \mathbb{1} + i\kappa\left(\gamma^*\hat{a}\hat{b} + \gamma\hat{a}^\dagger\hat{b}^\dagger\right)\ . \tag{3.68}$$

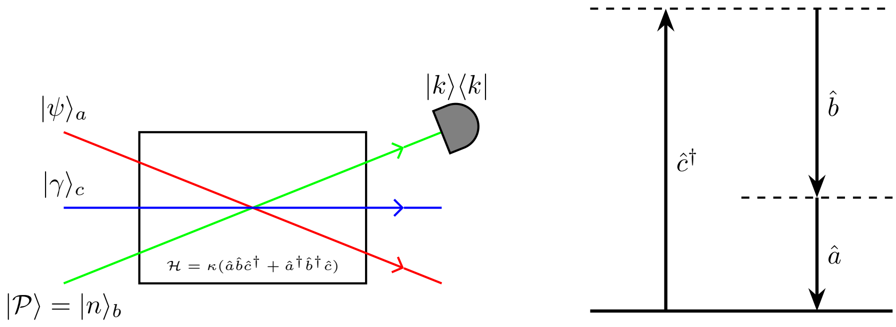

Adapted from a figure created by alchemist.
This figure is licensed under CC BY-SA 4.0

(a) Interacting modes

(b) Energy level diagram

Figure 3.10: The modes interacting when the highest frequency mode, c, is pumped with a coherent state with amplitude γ for a measured system in mode a the pointer in mode b. The initial pointer state is a number state, $|n\rangle$, and is measured in the number basis, $|k\rangle$.

When the measured state is mode a and the pointer is mode b, initialized as a number state, $\mathcal{P} = |n\rangle_b$ (shown in Figure 3.10), this would give the POVM:

$$\hat{E}_{n-1} = \kappa^2 n|\gamma|^2\hat{a}^\dagger\hat{a}\,, \tag{3.69a}$$

$$\hat{E}_n = \mathbb{1}\,, \tag{3.69b}$$

$$\hat{E}_{n+1} = \kappa^2(n+1)|\gamma|^2\hat{a}\hat{a}^\dagger\,. \tag{3.69c}$$

This is a very similar result to using the pointer as the fundamental frequency, except that the probability of a change in outcome has $n|\gamma|^2$ dependence rather than n^2. Since $|\gamma|^2$ is likely to be much larger than n, this would correspond to larger changes in probability. The unitary is symmetric between modes a and b and so would have the same result if the measured state was in mode b instead.

When mode a has a coherent state with amplitude α (and the parametric approximation is made) the unitary is:

$$\hat{U} = \mathbb{1} + i\kappa\left(\alpha\hat{b}\hat{c}^\dagger + \alpha^*\hat{b}^\dagger\hat{c}\right)\ . \tag{3.70}$$

When the measured state, $|\psi\rangle$, is in mode b and the pointer is in mode c initialized as a number state, $|\mathcal{P}\rangle = |n\rangle_c$ (shown in Figure 3.11), the POVM is:

$$\hat{E}_{n-1} = \kappa^2 n|\alpha|^2 \hat{b}\hat{b}^\dagger\,, \tag{3.71a}$$

$$\hat{E}_n = \mathbb{1}\,, \tag{3.71b}$$

$$\hat{E}_{n+1} = \kappa^2 (n+1)|\alpha|^2 \hat{b}^\dagger \hat{b}\,. \tag{3.71c}$$

This is a very similar result to when the coherent state is in the highest frequency mode, as considered above, with the change in probability still proportional to the photon number of the measured system.

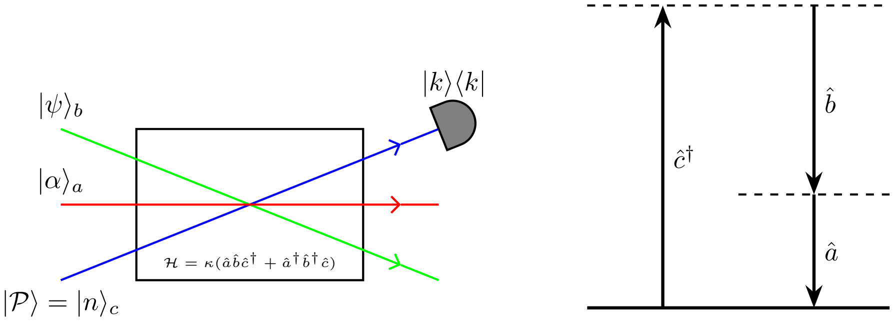

Adapted from a figure created by alchemist.
This figure is licensed under CC BY-SA 4.0

(a) Interacting modes

(b) Energy level diagram

Figure 3.11: The modes interacting when the pointer is the highest frequency mode, c, the measured system is in mode b, and mode a is pumped with coherent light with amplitude α. The initial pointer state is a number state, $|n\rangle$, and is measured in the number basis, $|k\rangle$.

Limitations with Number Basis Approach

There are very challenging experimental obstacles to overcome to be able to use a number state pointer. Generating precise number states (especially higher than 1) is non trivial. Photon number resolving detectors are expensive and have a limit to how many photons they can distinguish.

Perhaps more fundamental is that the interaction will typically be very weak if the pointer has a small number of photons. Precise generation and detection of a large photon number state does not look possible in the foreseeable future. For this reason we do not consider any arrangements with the pointer initialized as a number state.

Whilst photon number is the most natural orthonormal basis, other properties of a light field can be used. In addition, the POVM formalism does not require that the input pointer state is a member of the outcome basis.

3.2.4 $\chi^{(2)}$ Nonlinearity with Coherent Pointer Input and Number Basis Readout

Another option would be to use coherent states as the pointer but still measure in the number basis. This may well be the simplest to achieve experimentally, given lasers produce coherent states and photon number is equivalent to intensity (although the issue of detecting multiple photons still remains).

In this case the combined input state is given by $|\psi\rangle|\alpha\rangle$ and the same first order expansion of the $\chi^{(2)}$ unitary can be used as before.

Pointer as the Second Harmonic

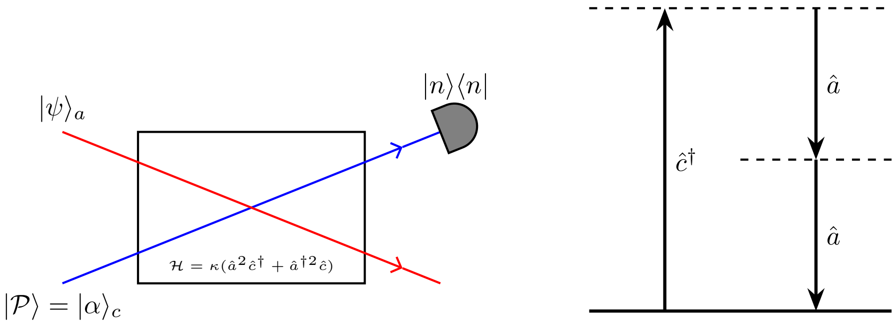

Adapted from a figure created by alchemist.
This figure is licensed under CC BY-SA 4.0

(a) Interacting modes (b) Energy level diagram

Figure 3.12: The modes interacting when the pointer (mode c) is the second harmonic of the measured system (mode a). The initial pointer state is a coherent state, $|\alpha\rangle$, and is measured in the number basis, $|n\rangle$.

Consider the case where the pointer (mode c) is at double the frequency of the measured system (mode a), as shown in Figure 3.12. After the nonlinear interaction, the state will be:

$$|\Psi'\rangle = \hat{U}|\psi\rangle_a|\alpha\rangle_c \approx \left(\mathbb{1} + i\kappa\left(\hat{a}^2\hat{c}^\dagger + (\hat{a}^{\dagger 2}\hat{c})\right)\right)|\psi\rangle_a|\alpha\rangle_c\,. \tag{3.72}$$

The initial pointer state in the number basis is:

$$|\mathcal{P}\rangle = |\alpha\rangle_c = \mathrm{e}^{-\frac{|\alpha|^2}{2}} \sum_n \frac{\alpha^n}{\sqrt{n!}} |n\rangle_c \,, \tag{3.73}$$

hence after the nonlinear interaction the state will be:

$$|\Psi'\rangle = \mathrm{e}^{-\frac{|\alpha|^2}{2}} \left(\sum_n \frac{\alpha^n}{\sqrt{n!}} \left(\mathbb{1} + i\kappa \left((\hat{a}^\dagger)^2 \alpha + \hat{a}^2 \frac{n}{\alpha} \right) \right) |n\rangle |\psi\rangle \right) . \tag{3.74}$$

This gives the Kraus operators:

$$\hat{K}_n = \mathrm{e}^{-\frac{|\alpha|^2}{2}} \frac{\alpha^n}{\sqrt{n!}} \left(\mathbb{1} + i\kappa \left((\hat{a}^\dagger)^2 \alpha + \hat{a}^2 \frac{n}{\alpha} \right) \right) , \tag{3.75}$$

and the generalized measurement operator to first order:

$$\hat{E}_n = \mathrm{e}^{-|\alpha|^2} \frac{|\alpha|^{2n}}{n!} \left(\mathbb{1} + i\kappa \left((\frac{n}{\alpha} - \alpha^*) \hat{a}^2 + (\alpha - \frac{n}{\alpha^*})(\hat{a}^\dagger)^2 \right) \right) , \tag{3.76}$$

hence the probability of measuring n photons will be:

$$p_n = \mathrm{e}^{-|\alpha|^2} \frac{|\alpha|^{2n}}{n!} \left(1 - 2\kappa \mathrm{Im} \left[\left(\frac{n}{\alpha} - \alpha^* \right) \langle \psi | \hat{a}^2 | \psi \rangle \right] \right) . \tag{3.77}$$

These probabilities depend on the square of quadrature operators. Subsequent sections will discuss how these probability changes could be used to perform practical measurements.

Pointer as Fundamental

If the pointer (mode a) is at the fundamental frequency (shown in Figure 3.13), then after the nonlinear interaction, the state will be:

$$|\Psi'\rangle = \mathrm{e}^{-\frac{|\alpha|^2}{2}} \left(\sum_n \frac{\alpha^n}{\sqrt{n!}} \left(\mathbb{1} + i\kappa \left(\hat{c}^\dagger \alpha^2 + \hat{c} \frac{n(n-1)}{\alpha^2} \right) \right) |n\rangle |\psi\rangle \right) , \tag{3.78}$$

giving the Kraus operators:

$$\hat{K}_n = \mathrm{e}^{-\frac{|\alpha|^2}{2}} \frac{\alpha^n}{\sqrt{n!}} \left(\mathbb{1} + i\kappa \left(\hat{c}^\dagger \alpha^2 + \hat{c} \frac{n(n-1)}{\alpha^2} \right) \right) , \tag{3.79}$$

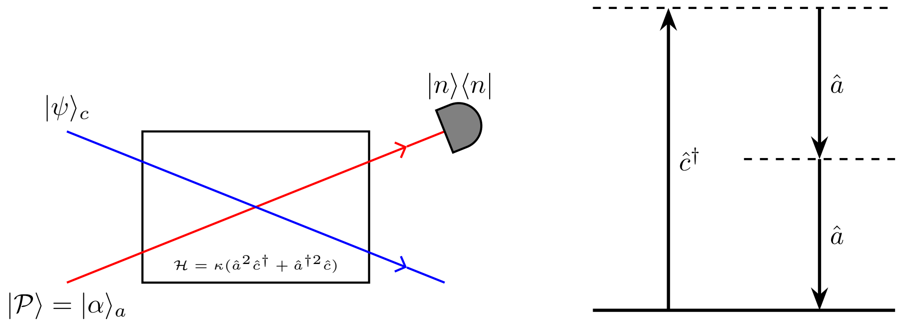

Adapted from a figure created by alchemist.
This figure is licensed under CC BY-SA 4.0

(a) Interacting modes (b) Energy level diagram

Figure 3.13: The modes interacting when the measured system (mode c) is the second harmonic of the pointer (mode a). The initial pointer state is a coherent state, $|\alpha\rangle$, and is measured in the number basis, $|n\rangle$.

and the generalized measurement operator:

$$\hat{E}_n = \mathrm{e}^{-|\alpha|^2}\frac{|\alpha|^{2n}}{n!}\left(\mathbb{1} + i\kappa\left(\left(\frac{n(n-1)}{\alpha^2} - \alpha^{*2}\right)\hat{c} + \left(\alpha^2 - \frac{n(n-1)}{\alpha^{*2}}\right)\hat{c}^\dagger\right)\right), \tag{3.80}$$

and probabilities:

$$p_n = \mathrm{e}^{-|\alpha|^2}\frac{|\alpha|^{2n}}{n!}\left(1 - 2\kappa\mathrm{Im}\left[\left(\frac{n(n-1)}{\alpha^2} - \alpha^{*2}\right)\langle\psi|\hat{c}|\psi\rangle\right]\right). \tag{3.81}$$

Simultaneous Readout of Quadratures?

These effects look interesting, since the change in probability of measuring each specific number of photons depends linearly on the expectation value of the lowering operator (or its square). However, the expressions also have dependence on both the number of measured photons and the coherent state amplitude – suggesting that it might be possible that different quadratures of $|\psi\rangle$ affect the probability to measure each photon number differently.

We can consider the fractional difference in probability for measuring n photons – the change in the probability to measure n photons in the pointer state after the interaction as compared to before, divided by the initial probability to measure n photons in the pointer.

$$\Delta p_n = \frac{p_n - \lim_{\kappa\to 0}(p_n)}{\lim_{\kappa\to 0}(p_n)}, \tag{3.82}$$

where $\lim_{\kappa\to 0}(p_n)$ is the initial probability to measure n photons in the pointer (the number that would be detected if the interaction strength was zero).

This shows that the quadratures affect the probability to measure all photon numbers in the same way – with a single coherent state measuring a single quadrature of $|\psi\rangle$.

For the pointer as the fundamental frequency, this is equal to:

$$\Delta p_n = -2\kappa \mathrm{Im}\left[\left(\frac{n(n-1)}{\alpha^2} - \alpha^{*2}\right)\langle\psi|\hat{c}|\psi\rangle\right] . \tag{3.83}$$

For $\alpha = |\alpha|\mathrm{e}^{i\theta}$, this then simplifies to:

$$\begin{aligned}\Delta p_n = 2\kappa &\left(|\alpha|^2 - \frac{n(n-1)}{|\alpha|^2}\right) \\ &\times \left(\cos(2\theta)\mathrm{Im}\left[\langle\psi|\hat{c}|\psi\rangle\right] - \sin(2\theta)\mathrm{Re}\left[\langle\psi|\hat{c}|\psi\rangle\right]\right) .\end{aligned} \tag{3.84}$$

It is clear that the change in probability depends on $\langle\psi|\hat{a}|\psi\rangle$ in the same way, regardless of the number of photons measured. Therefore, unfortunately, the simultaneous determination of more than one phase is not possible. Only a change in the phase of the coherent state would allow different quadratures to be measured. However, it also indicates that this scheme will be able to be used to perform quadrature measurements as outlined below.

When the pointer is the second harmonic frequency then the equivalent expression is:

$$\Delta p_n = 2\kappa\left(|\alpha| - \frac{n}{|\alpha|}\right)\left(\cos(\theta)\mathrm{Im}\left[\langle\psi|\hat{a}^2|\psi\rangle\right] - \sin(\theta)\mathrm{Re}\left[\langle\psi|\hat{a}^2|\psi\rangle\right]\right) . \tag{3.85}$$

Whilst these measurements would provide information about the quadratures of the state $|\psi\rangle$, it appears to require detecting the change in probabilities of observing a specific number of photons. This would require photon number resolving measurements, and thus, many of the same challenges discussed in Section 3.2.3 would still apply. However, as we show below, there is not the same limitation.

‘Classical’ Measurements of the Pointer

We can also consider finding average properties of the pointer states, rather than observing the full probability distribution of measuring different outcomes. For light, the most natural measurement to consider is average intensity, which corresponds to the expectation of the photon number operator. This also has the advantage that it can be performed simply with standard laboratory equipment.

For an input coherent state with amplitude $|\alpha|\mathrm{e}^{i\theta}$, the intensity measured after the interaction with the system, $|\psi\rangle$, when the pointer is the second harmonic, is:

$$\langle\hat{n}\rangle_d = |\alpha|^2 - 2\kappa|\alpha|\mathrm{Im}\left[\mathrm{e}^{-i\theta}\langle\psi|\hat{a}^2|\psi\rangle\right] \ , \tag{3.86}$$

which is a fractional change from the initial pointer state:

$$\frac{\langle\hat{n}\rangle_d - \langle\hat{n}\rangle_c}{\langle\hat{n}\rangle_c} = -\frac{2\kappa}{|\alpha|}\mathrm{Im}\left[\mathrm{e}^{-i\theta}\langle\psi|\hat{a}^2|\psi\rangle\right] \ . \tag{3.87}$$

When the pointer has the fundamental frequency, the corresponding expressions are:

$$\langle\hat{n}\rangle_d = |\alpha|^2 - 4\kappa|\alpha|^2\mathrm{Im}\left[\mathrm{e}^{-2i\theta}\langle\psi|\hat{c}|\psi\rangle\right] \ , \tag{3.88}$$

$$\frac{\langle\hat{n}\rangle_d - \langle\hat{n}\rangle_c}{\langle\hat{n}\rangle_c} = -4\kappa\mathrm{Im}\left[\mathrm{e}^{-2i\theta}\langle\psi|\hat{c}|\psi\rangle\right] \ . \tag{3.89}$$

While the weakness of the nonlinear interaction means that these changes are likely to be small, the phase of the pointer state could be varied with time. This would create a time varying signal, that would be suitable for lock-in amplification.

The signal of any such measurement would still be proportional to the intensity of the initial beam, $\langle\hat{n}\rangle_c$. Whilst this may not be especially problematic – the intensity is a straightforward property to measure – this can be avoided by considering the variance of the photon number statistics.

For the case when the pointer is the fundamental frequency, the variance of the pointer intensity will be:

$$\mathrm{Var}(\hat{n})_d = \langle\hat{n}^2\rangle_d - \langle\hat{n}\rangle_d^2 = |\alpha|^2\left(1 - 8\kappa\mathrm{Im}\left[\mathrm{e}^{-2i\theta}\langle\psi|\hat{c}|\psi\rangle\right]\right) \ . \tag{3.90}$$

The ratio of the variance in the intensity to the mean of intensity can be considered. For a coherent beam – following Poissonian statistics – this ratio is 1. However, for the pointer after the interaction this ratio is:

$$\frac{\mathrm{Var}(\hat{n})_d}{\langle\hat{n}\rangle_d} = \frac{1 - 8\kappa\mathrm{Im}\left[\mathrm{e}^{-2i\theta}\langle\psi|\hat{c}|\psi\rangle\right]}{1 - 4\kappa\mathrm{Im}\left[\mathrm{e}^{-2i\theta}\langle\psi|\hat{c}|\psi\rangle\right]} \, , \tag{3.91}$$

which can be rearranged to give:

$$\mathrm{Im}\left[\mathrm{e}^{-2i\theta}\langle\psi|\hat{c}|\psi\rangle\right] = \frac{1}{2\kappa}\frac{\mathrm{Var}(\hat{n}) - \langle\hat{n}\rangle}{\mathrm{Var}(\hat{n}) - 2\langle\hat{n}\rangle} \, . \tag{3.92}$$

The expectation of $\hat{c}$ can in turn be represented in terms of quadrature operators:

$$\mathrm{e}^{-2i\theta}\langle\psi|\hat{c}|\psi\rangle = \mathrm{e}^{-2i\theta}\langle\psi|\hat{X} + i\hat{Y}|\psi\rangle \,, \tag{3.93}$$

and so, depending on the initial phase of the pointer, the expectation of the two field quadratures can be found.

Non-demolition Measurement of Quadrature

The above shows how by using a coherent pointer (one of the easiest states to create experimentally) and a $\chi^{(2)}$ interaction, it is possible to perform quantum non-demolition measurements of the field quadratures. This is done by detecting the intensity of the pointer (somewhat similarly to the scheme considered by Wiseman and Milburn [132]). This could provide an experimentally feasible alternative to using homodyne techniques to measure field quadratures – which could be especially useful for bright fields that would otherwise saturate photodetectors.

3.2.5 Measuring Pointer Quadrature for $\chi^{(2)}$ Nonlinearity with Coherent Input

An alternative to measuring the number state of the pointer is to measure its quadrature values. Considering this as an idealized measurement, the probability density that the pointer is found in state with quadrature value X will be:

$$p(X) = |\langle X|\Psi'\rangle|^2 = |\langle X|\hat{U}|\psi\rangle|\mathcal{P}\rangle|^2 \,. \tag{3.94}$$

The Hamiltonian for nonlinear interactions is often written in terms of raising and lowering operators. However, it can also be written in terms of quadrature operators. For the case with a fundamental and second harmonic frequency:

$$\hat{\mathcal{H}} = \kappa\left(\hat{a}^{\dagger 2}\hat{c} + \hat{a}^2\hat{c}^{\dagger}\right) = 2\kappa\Big((\hat{X}_a^2 - \hat{Y}_a^2)\hat{X}_c + (\hat{X}_a\hat{Y}_a + \hat{Y}_a\hat{X}_a)\hat{Y}_c\Big) \,, \tag{3.95}$$

where:

$$\hat{a} = \hat{X}_a + i\hat{Y}_a \,, \tag{3.96a}$$

$$\hat{a}^{\dagger} = \hat{X}_a - i\hat{Y}_a \,. \tag{3.96b}$$

This results in the unitary:

$$\hat{U} = \mathrm{e}^{2i\kappa\left((\hat{X}_a^2 - \hat{Y}_a^2)\hat{X}_c + (\hat{X}_a\hat{Y}_a + \hat{Y}_a\hat{X}_a)\hat{Y}_c\right)} \,. \tag{3.97}$$

This can be Taylor expanded to first order to give:

$$\hat{U} \approx \mathbb{1} + 2i\kappa \Big((\hat{X}_a^2 - \hat{Y}_a^2)\hat{X}_c + (\hat{X}_a\hat{Y}_a + \hat{Y}_a\hat{X}_a)\hat{Y}_c \Big) \,. \tag{3.98}$$

Pointer as Second Harmonic

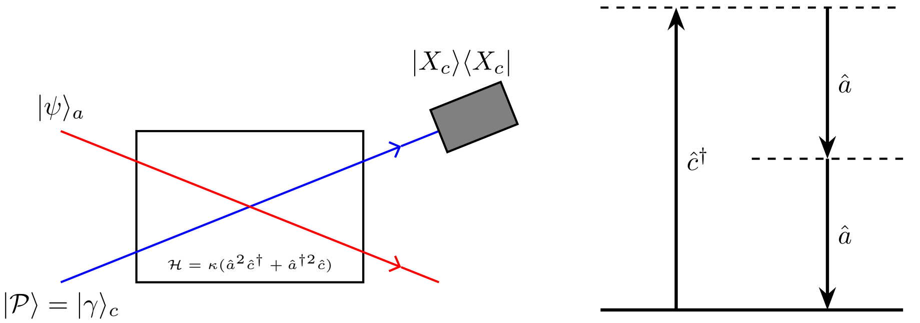

Adapted from a figure created by alchemist.
This figure is licensed under CC BY-SA 4.0

(a) Interacting modes (b) Energy level diagram

Figure 3.14: The modes interacting when the pointer (mode c) is the second harmonic of the measured system (mode a). The initial pointer state is a coherent state, $|\gamma\rangle$, and has it's quadrature, $|X_c\rangle$, measured.

When the pointer in mode c is prepared as a coherent state, with amplitude γ, $|\mathcal{P}\rangle = |\gamma\rangle_c$ (shown in Figure 3.14), the initial state before the nonlinear interaction is:

$$|\Psi\rangle = |\psi\rangle_a|\gamma\rangle_c \,, \tag{3.99}$$

and after the interaction the state will be:

$$\begin{aligned}\hat{U}|\Psi\rangle = |\psi\rangle_a|\gamma\rangle_c + 2i\kappa\Big(&\big(\hat{X}_a^2 - \hat{Y}_a^2\big)|\psi\rangle_a\hat{X}_c|\gamma\rangle_c \\ &+ \big(\hat{X}_a\hat{Y}_a + \hat{Y}_a\hat{X}_a\big)|\psi\rangle_a\hat{Y}_c|\gamma\rangle_c\Big) \,.\end{aligned} \tag{3.100}$$

After measuring the pointer's quadrature state, the state will then be:

$$\begin{aligned}\langle X_c|\hat{U}|\Psi\rangle = |\psi\rangle_a\langle X_c|\gamma\rangle_c + 2i\kappa\Big(&(\hat{X}_a^2 - \hat{Y}_a^2)|\psi\rangle_a\langle X_c|\hat{X}_c|\gamma\rangle_c \\ &+ (\hat{X}_a\hat{Y}_a + \hat{Y}_a\hat{X}_a)|\psi\rangle_a\langle X_c|\hat{Y}_c|\gamma\rangle_c\Big) \,.\end{aligned} \tag{3.101}$$

The coherent state can be represented in position space as [35]:

$$\langle X|\gamma\rangle = \frac{1}{\pi^{\frac{1}{4}}}\mathrm{e}^{2\gamma X - X^2 - \mathrm{Re}[\gamma]\gamma}\,. \tag{3.102}$$

The following expectation values are then:

$$\langle X|\hat{X}|\gamma\rangle = \frac{X}{\pi^{\frac{1}{4}}}\mathrm{e}^{2\gamma X - X^2 - \mathrm{Re}[\gamma]\gamma}\,, \tag{3.103}$$

$$\langle X|\hat{Y}|\gamma\rangle = \frac{i(X-\gamma)}{\pi^{\frac{1}{4}}}\mathrm{e}^{2\gamma X - X^2 - \mathrm{Re}[\gamma]\gamma}\,, \tag{3.104}$$

making use of the expressions: $\hat{Y} = \frac{i}{2}(\hat{a}^\dagger - \hat{a})$; $\hat{a}^\dagger = 2\hat{X} - \hat{a}$; $\hat{X}|X\rangle = X|X\rangle$; and $\hat{a}|\alpha\rangle = \alpha|\alpha\rangle$.

Evaluating all the expectation values above then gives the state after the interaction and after measuring the pointer in state $|X\rangle_c$ to be:

$$\begin{aligned}\langle X_c|\hat{U}|\Psi\rangle = \frac{1}{\pi^{\frac{1}{4}}}\mathrm{e}^{2\gamma X_c - X_c^2 - \mathrm{Re}[\gamma]\gamma}\Big(|\psi\rangle_a + 2i\kappa\Big(X_c\big(\hat{X}_a^2 - \hat{Y}_a^2\big)|\psi\rangle_a \\ + i(X_c-\gamma)\big(\hat{X}_a\hat{Y}_a + \hat{Y}_a\hat{X}_a\big)|\psi\rangle_a\Big)\Big)\,.\end{aligned} \tag{3.105}$$

The probability of measuring this state is then:

$$\begin{aligned}|\langle X_c|\hat{U}|\Psi\rangle|^2 = \frac{1}{\sqrt{\pi}}\mathrm{e}^{4X_c\mathrm{Re}[\gamma] - 2X_c^2 - 2\mathrm{Re}[\gamma]^2} \\ \times\Big(1 - 4\kappa\big(X_c - \mathrm{Re}[\gamma]\big)\langle\psi|\hat{X}_a\hat{Y}_a + \hat{Y}_a\hat{X}_a|\psi\rangle_a\Big)\,.\end{aligned} \tag{3.106}$$

Pointer as Fundamental

When the pointer is a coherent state, $|\mathcal{P}\rangle = |\alpha\rangle_a$, at the fundamental frequency in mode a (shown in Figure 3.15), the probability to measure $|X\rangle_a$ for a state $|\psi\rangle_c$ is:

$$\begin{aligned}|\langle X_a|\hat{U}|\Psi\rangle|^2 = |\langle X_a|\alpha\rangle|^2\Big(1{+}4\kappa\big(2X_a\mathrm{Im}[\alpha] - \mathrm{Im}[\alpha^2]\big)\langle\psi|\hat{X}_c|\psi\rangle_c \\ - 2\kappa\big(4X_a^2 - 4X_a\mathrm{Re}[\alpha] - 1\big)\langle\psi|\hat{Y}_c|\psi\rangle_c\Big)\,.\end{aligned} \tag{3.107}$$

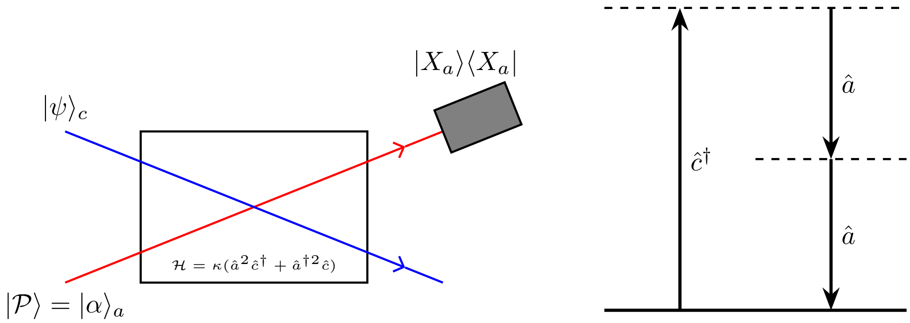

Adapted from a figure created by alchemist.
This figure is licensed under CC BY-SA 4.0

(a) Interacting modes

(b) Energy level diagram

Figure 3.15: The modes interacting when the measured system (mode c) is the second harmonic of the pointer (mode a). The initial pointer state is a coherent state, $|\alpha\rangle$, and has it's quadrature, $|X_a\rangle$, measured.

Coherent Pump

When the pointer is a coherent state, $|\alpha\rangle$, in mode a and the pump mode, c, is a large coherent state with amplitude γ (so the parametric approximation can be made), the probability to measure $|X\rangle_a$ for a state $|\psi\rangle_b$ is:

$$\begin{aligned}|\langle X_a|\hat{U}|\Psi\rangle|^2 = |\langle X_a|\alpha\rangle|^2 \Big(1 - 4\kappa\big(X_a - \mathrm{Re}[\alpha]\big)\Big(&\mathrm{Im}[\gamma]\langle\psi|\hat{X}_b|\psi\rangle_b \\ &- \mathrm{Re}[\gamma]\langle\psi|\hat{Y}_b|\psi\rangle_b\Big)\Big)\,. \end{aligned} \tag{3.108}$$

This situation is shown in Figure 3.16.

Advantage of these Quadrature Measurements?

It is unclear what the advantage of reading out the quadrature of the pointer has over number state or intensity readouts. Not only is reading out the quadrature much more experimentally challenging than intensity, but it also feels somewhat counter intuitive to determine information about the quadrature of a quantum system by directly measuring the quadrature of the pointer.

However, it is possible that there could be some cases where coupling to the pointer would have some advantages. For instance, it would enable the quadrature measurement to be performed at a different frequency (where there may be more efficient detectors) or with minimal disturbance.

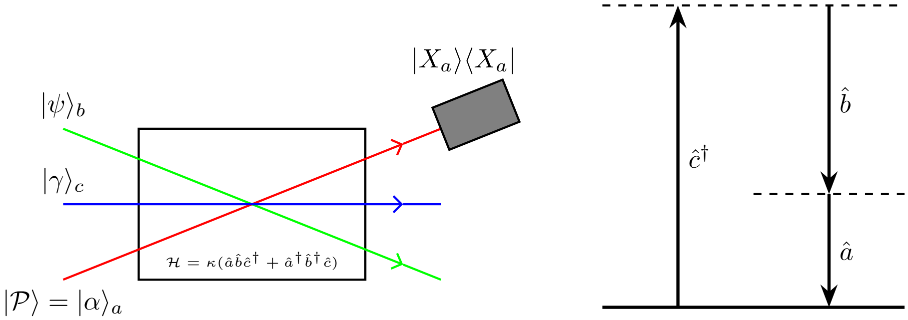

Adapted from a figure created by alchemist.
This figure is licensed under CC BY-SA 4.0

(a) Interacting modes

(b) Energy level diagram

Figure 3.16: The modes interacting when mode c is pumped with coherent light with amplitude γ, the pointer is in mode a and the measured system in mode b. The initial pointer state is a coherent state, $|\alpha\rangle$, and has it's quadrature, $|X_a\rangle$, measured.

3.2.6 Measuring Squeezed Photon Number State

Yanagimoto, Nehra, Hamerly, Ng, Marandi and Mabuchi [133] propose a non-destructive scheme to measure the projectors of the squeezed photon number states,

$$|N_a\rangle = 1/(\sqrt{N_a!})\hat{A}^{\dagger N_a}|0\rangle\,, \tag{3.109}$$

where,

$$\hat{A} = \hat{a}\mathrm{cosh}u + \hat{a}^\dagger\mathrm{sinh}u\,. \tag{3.110}$$

This is done using a frequency detuned second harmonic interaction,

$$\hat{\mathcal{H}} = \kappa\left(\hat{a}^{\dagger 2}\hat{c} + \hat{a}^2\hat{c}^\dagger\right) + \delta\hat{a}^\dagger\hat{a}\,, \tag{3.111}$$

where $\delta = \omega_a - \omega_c/2$, and a coherent state in mode c with amplitude γ is used as the pointer. The squeezing parameter of the measurement basis, u, is then given by:

$$u = \tanh^{-1}(2\kappa\gamma/\delta)\,. \tag{3.112}$$

When the Y-quadrature of the pointer is measured, this gives a POVM with effects:

$$\hat{E}(Y_c) = \sum_{N_a=0}^{\infty} |\mathrm{e}^{-i\Delta N_a t}\langle Y_c - d(N_a+1/2)|\mathcal{P}\rangle|^2 |N_a\rangle\langle N_a|\,, \tag{3.113}$$

where $\Delta = \sqrt{\delta^2 - 4\kappa^2\gamma^2}$ and $d = \kappa \sinh(2u)t$.

This result is somewhat similar to the work presented here – making use of a $\chi^{(2)}$ nonlinearity to find a POVM. However, there are some notable differences: this scheme requires a frequency detuning between the two modes (versus the perfect frequency matching assumed to be required throughout this thesis), and the analysis is performed in a displaced frame.

3.2.7 POVM Measurements Summary

In this section, we investigated the application of the Positive Operator-Valued Measure (POVM) formalism to nonlinear optical weak measurements, with a particular focus on $\chi^{(2)}$ nonlinearities. The POVM approach provides a generalized framework for quantum measurements, enabling the analysis of a variety of nonlinear interactions between optical modes, such as second harmonic generation and parametric down-conversion.

We explored initializing the pointer in different states – Fock (number) states and coherent states – and assessed their effectiveness in extracting information about the system's quadratures through measurements in the number basis, intensity (photon number expectation), and quadrature bases.

For pointers prepared as a number state, we derived Kraus operators and POVM elements, showing they provide information about the operators $\hat{a}^\dagger\hat{a}$ or $\hat{a}^{\dagger 2}\hat{a}^2$. However, experimental challenges, including the difficulty of generating and detecting precise photon numbers, especially for large n, limit their practicality.

Considering coherent state pointers, which are more experimentally accessible via laser sources, we found that intensity measurements yield signals proportional to quadrature expectation values (for example, $\mathrm{Im}\left[\langle\hat{a}\rangle\right]$ or $\mathrm{Im}\left[\langle\hat{a}^2\rangle\right]$). Direct quadrature measurements of the pointer also provide information about the quadrature operators of the measured system.

In summary, this section showed how there is significant potential to use $\chi^{(2)}$ nonlinearities to determine quadrature information about quantum optical states.

Key Findings

- The Positive Operator-Valued Measure (POVM) formalism provides a flexible approach to quantum measurements, allowing the analysis of various nonlinear optical interactions, without being limited to a unitary of a specific form. (Section 3.2.2)

- Pointers prepared as Fock (number) states would provide information about the system being measured. However, measurements of this type would be very challenging to perform experimentally due to needing precise photon number generation and detection. (Section 3.2.3)
- Pointers initialized as coherent states are both more experimentally practical and would enable measurements of quadrature operators of the system. (Section 3.2.4 and 3.2.5)
- There is not a clear advantage to reading out the quadrature of a pointer state rather than its intensity given both provide information about the quadrature operators of a quantum system. (Section 3.2.4 and 3.2.5)

3.3 Postselection

The approaches considered thus far (with the exception of Wu and Żukowski's method outlined in Section 3.1.5) have been considering weak measurements without any postselection. Not only does this mean that the signal for any of these potential measurements is going to be inherently very weak, but also many of the advantages that postselection can provide are not being utilized. For instance, weak value amplification [21] (or other postselection schemes) enable the quantum Fisher information obtained from a weak measurement to reach the quantum limit [30, 134]. In certain situations, postselected weak measurements have advantages over standard techniques. For example, in the presence of certain types of noise [30] or for measurements of some non-classical states [135]. In addition, the complex nature of weak values can enable additional information to be found [22, 27–29].

This section explores the enhancement of weak measurements via postselection in nonlinear optical systems. We focus on how postselecting on states with small overlap to the initial state can amplify measurement signals – a phenomenon known as weak value amplification. For von Neumann measurements using the Kerr effect, we present the amplification achieved by Steinberg's research group [26, 111, 112] and investigate alternative postselection strategies, such as quadrature measurements. Additionally, we analyze postselection after POVMs, revealing how weak values appear in outcome probabilities.

3.3.1 Postselection of Von Neumann Measurements Using the Kerr Effect

To make use of weak value amplification [21], the interaction between the pointer and the system must take the form of a von Neumann measurement as investigated in Section 3.1.

The case of using the Kerr effect to measure the photon number of a state using the phase of another system is considered. This is the experiment and theory performed by Steinberg's research group [26, 111, 112], where the state was postselected into a near orthogonal state. Below we consider in detail this result, as well as the effect of an alternative choice of postselection and measured states.

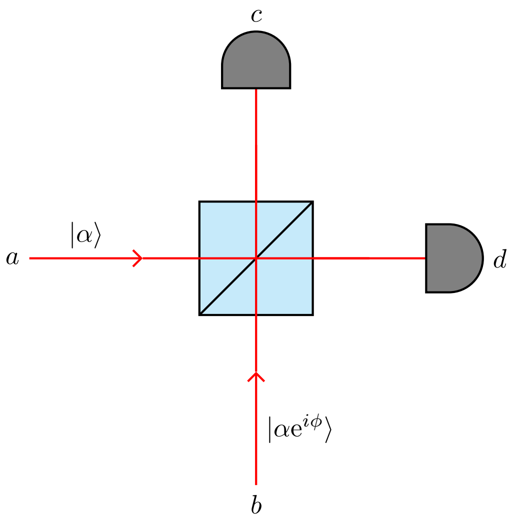

Figure 3.17: An interferometer configured to be sensitive to small phases, ϕ, of the beam entering in port b. The inputs in ports a and b are coherent beams with equal amplitude magnitude. The intensity of the beams in port c and d are measured.

Operational Phase Measurement

As has come up several times in this thesis (Section 1.3.4 and Section 3.1.3), there is no well defined quantum phase operator. However, we are experimentally able to measure optical phase (at least for coherent light) and this procedure can be described in terms of quantum operators.

Phase can be measured by considering the interference between two coherent beams. For the experimental configuration shown in Figure 3.17, the difference in intensity between the two output ports of a beam splitter is considered (normalized by the total intensity to give a visibility).

$$\bar{\phi} = \frac{\langle \hat{M}_- \rangle}{\langle \hat{M}_+ \rangle} = \frac{\langle \hat{n}_c - \hat{n}_d \rangle}{\langle \hat{n}_d + \hat{n}_c \rangle}\,, \tag{3.114}$$

where the difference and sum intensity operators are given by:

$$\hat{M}_- = \hat{n}_c - \hat{n}_d\,, \tag{3.115a}$$

$$\hat{M}_+ = \hat{n}_d + \hat{n}_c\,. \tag{3.115b}$$

The relationship between the modes of the input and output ports of the beam splitter are given by [35]:

$$\hat{c} = \frac{1}{\sqrt{2}}\left(i\hat{a} + \hat{b}\right) , \tag{3.116a}$$

$$\hat{d} = \frac{1}{\sqrt{2}}\left(\hat{a} + i\hat{b}\right) , \tag{3.116b}$$

where these operators correspond to the annihilation operators for the beam at the corresponding port.

The difference and sum count operators, $\hat{M}_-$ and $\hat{M}_+$ are then found to be:

$$\hat{M}_- = \hat{n}_c - \hat{n}_d = i\left(\hat{a}\hat{b}^\dagger - \hat{a}^\dagger\hat{b}\right) , \tag{3.117a}$$

$$\hat{M}_+ = \hat{n}_d + \hat{n}_c = \hat{a}^\dagger\hat{a} + \hat{b}^\dagger\hat{b} . \tag{3.117b}$$

When a reference state $|\alpha\rangle$ enters in port a and a state with a phase to be measured $|\alpha\mathrm{e}^{i\phi}\rangle$ enters in port b, the count operators are evaluated to be:

$$\langle\hat{M}_-\rangle = \langle\alpha|\langle\alpha\mathrm{e}^{i\phi}|\hat{M}_-|\alpha\mathrm{e}^{i\phi}\rangle|\alpha\rangle = 2|\alpha|^2\sin\phi , \tag{3.118a}$$

$$\langle\hat{M}_+\rangle = \langle\alpha|\langle\alpha\mathrm{e}^{i\phi}|\hat{M}_+|\alpha\mathrm{e}^{i\phi}\rangle|\alpha\rangle = 2|\alpha|^2 . \tag{3.118b}$$

For small angles, the visibility gives an estimate for the unknown phase:

$$\bar{\phi} = \frac{\langle\hat{M}_-\rangle}{\langle\hat{M}_+\rangle} = \sin\phi \approx \phi . \tag{3.119}$$

Kerr Measurements Without Postselection

For the case considered in Section 3.1.3 of a cross-Kerr shift, we can confirm that this operational phase measurement gives the result we would expect. For a pointer input state $|\mathcal{P}\rangle = |\alpha\rangle$ and a measured state $|\psi\rangle = \sum c_n|n\rangle$, we find that the total system after the interaction is:

$$|\Psi'\rangle = \sum c_n|\alpha\mathrm{e}^{in\phi_0}\rangle|n\rangle , \tag{3.120}$$

where ϕ_0 is the cross-Kerr phase shift due to a single photon.

If the pointer phase is now measured by interference with a reference beam, of equal amplitude, we find that the expectation of the count operators are:

$$\langle\hat{M}_+\rangle = \sum_{n,m} c_m^* c_n \langle\alpha|\langle\alpha\mathrm{e}^{im\phi_0}\langle m|\hat{M}_+|n\rangle|\alpha\mathrm{e}^{im\phi_0}\rangle|\alpha\rangle = \sum_n 2|c_n|^2|\alpha|^2 , \tag{3.121}$$

$$\langle \hat{M}_+ \rangle = 2|\alpha|^2 \,, \tag{3.122}$$

and

$$\langle \hat{M}_- \rangle = \sum_{n,m} c_m^* c_n \langle \alpha | \langle \alpha \mathrm{e}^{im\phi_0} \langle m | \hat{M}_- | n \rangle | \alpha \mathrm{e}^{im\phi_0} \rangle | \alpha \rangle \,, \tag{3.123}$$

$$\langle \hat{M}_- \rangle = \sum_n 2|c_n|^2 |\alpha|^2 \sin(n\phi_0) \,. \tag{3.124}$$

When all $n\phi_0$ are small, the phase estimate evaluates to be:

$$\bar{\phi} = \frac{\langle \hat{M}_- \rangle}{\langle \hat{M}_+ \rangle} = \sum_n |c_n|^2 n\phi_0 = \phi_0 \langle \psi | n | \psi \rangle \,, \tag{3.125}$$

which is proportional to the number observable of the state $|\psi\rangle$ as expected.

Postselection on Near Orthogonal State

When postselecting, typically interesting effects occur when the overlap between the initial and postselected states is small (so that the denominator of the weak value is small). This is exactly the case considered by Steinberg's research group [111], where the initial state is:

$$|\psi_i\rangle = \frac{1}{\sqrt{2}}(|0\rangle + |1\rangle) \,, \tag{3.126}$$

and the postselected state is:

$$|\psi_f\rangle = \frac{1}{\sqrt{2}} \left((1+\delta)|1\rangle - (1-\delta)|0\rangle \right) \,, \tag{3.127}$$

where δ is small.

The probability of postselection is then found to be δ^2 (ignoring measurement back-action) and the normalized pointer state after postselection is:

$$|\mathcal{P}_p'\rangle = \frac{1}{\delta} \left(\tfrac{1+\delta}{2} |\alpha \mathrm{e}^{i\phi_0}\rangle - \tfrac{1-\delta}{2} |\alpha\rangle \right) \,. \tag{3.128}$$

This is the state considered by Steinberg's research group [26, 111].

To find the average phase shift measured, we evaluate the expectation of

$\hat{M}_{\pm}$:

$$\langle \hat{M}_- \rangle = \frac{1}{\delta^2}\langle\alpha|\Bigg(\left(\frac{1+\delta}{2}\right)^2 \langle \alpha \mathrm{e}^{i\phi_0}|\hat{M}_-|\alpha \mathrm{e}^{i\phi_0}\rangle + \left(\frac{1+\delta}{2}\right)^2 \langle\alpha|\hat{M}_-|\alpha\rangle - \frac{1-\delta^2}{4}\langle\alpha|\hat{M}_-|\alpha \mathrm{e}^{i\phi_0}\rangle - \frac{1-\delta^2}{4}\langle\alpha \mathrm{e}^{i\phi_0}|\hat{M}_-|\alpha\rangle\Bigg)|\alpha\rangle\,, \tag{3.129}$$

$$\langle \hat{M}_- \rangle = \frac{i|\alpha|^2}{4\delta^2}\Big(-2i\,(1+\delta)^2\sin\phi_0 - (1-\delta^2)\Big(\langle\alpha|\alpha \mathrm{e}^{i\phi_0}\rangle - \mathrm{e}^{i\phi_0}\langle\alpha|\alpha \mathrm{e}^{i\phi_0}\rangle + \mathrm{e}^{-i\phi_0}\langle\alpha \mathrm{e}^{i\phi_0}|\alpha\rangle - \langle\alpha \mathrm{e}^{i\phi_0}|\alpha\rangle\Big)\Big)\,. \tag{3.130}$$

The overlap between two coherent states is given by: $\langle\alpha|\beta\rangle = \mathrm{e}^{\alpha^*\beta - \frac{1}{2}(|\alpha|^2+|\beta|^2)}$ and so $\langle\alpha|\alpha \mathrm{e}^{i\phi_0}\rangle = \mathrm{e}^{|\alpha|^2(\mathrm{e}^{i\phi_0}-1)}$.

$$\langle \hat{M}_- \rangle = \frac{i|\alpha|^2}{4\delta^2}\Big(-2i\,(1+\delta)^2\sin\phi_0 - (1-\delta^2)\Big(\mathrm{e}^{|\alpha|^2(\mathrm{e}^{i\phi_0}-1)} - \mathrm{e}^{i\phi_0}\mathrm{e}^{|\alpha|^2(\mathrm{e}^{i\phi_0}-1)} + \mathrm{e}^{-i\phi_0}\mathrm{e}^{|\alpha|^2(\mathrm{e}^{-i\phi_0}-1)} - \mathrm{e}^{|\alpha|^2(\mathrm{e}^{-i\phi_0}-1)}\Big)\Big) \tag{3.131}$$

When ϕ_0 is small:

$$\langle \hat{M}_- \rangle = \frac{i|\alpha|^2}{4\delta^2}\Big(-2i\,(1+\delta)^2\,\phi_0 - (1-\delta^2)\Big(\mathrm{e}^{i|\alpha|^2\phi_0} - \mathrm{e}^{i\phi_0}\mathrm{e}^{i|\alpha|^2\phi_0} + \mathrm{e}^{-i\phi_0}\mathrm{e}^{-i|\alpha|^2\phi_0} - \mathrm{e}^{-i|\alpha|^2\phi_0}\Big)\Big)\,, \tag{3.132}$$

$$\langle \hat{M}_- \rangle = \frac{i|\alpha|^2}{4\delta^2}\Big(-2i\,(1+\delta)^2\,\phi_0 - (1-\delta^2)\Big(\mathrm{e}^{i|\alpha|^2\phi_0} - \mathrm{e}^{i(|\alpha|^2+1)\phi_0} + \mathrm{e}^{-i(|\alpha|^2+1)\phi_0} - \mathrm{e}^{-i|\alpha|^2\phi_0}\Big)\Big)\,. \tag{3.133}$$

When the phase shift imparted by the pointer on the measured system is small, $|\alpha|^2\phi_0 << 1$, we then find:

$$\langle \hat{M}_- \rangle = \frac{i|\alpha|^2}{4\delta^2}\Big(-2i\,(1+\delta)^2\,\phi_0 - (1-\delta^2)\Big(i|\alpha|^2\phi_0 - i(|\alpha|^2+1)\phi_0 - i(|\alpha|^2+1)\phi_0 + i|\alpha|^2\phi_0\Big)\Big)\,, \tag{3.134}$$

$$\langle \hat{M}_- \rangle = \frac{i|\alpha|^2}{4\delta^2}\Big(-2i\,(1+\delta)^2\,\phi_0 + 2i(1-\delta^2)\phi_0\Big)\,, \tag{3.135}$$

$$\langle \hat{M}_- \rangle = \frac{|\alpha|^2}{\delta^2}\Big(\delta\phi_0 + \delta^2\phi_0\Big) \approx \frac{|\alpha|^2\phi_0}{\delta}\,. \tag{3.136}$$

$\langle \hat{M}_+ \rangle$ evaluates to $2|\alpha|^2$ and so we find the phase estimate to be:

$$\bar{\phi} = \frac{\langle \hat{M}_- \rangle}{\langle \hat{M}_+ \rangle} \approx \frac{\phi_0}{2\delta}\,. \tag{3.137}$$

This is the probability found by Steinberg's research group [111] in the case of small back-action (as we assumed here). While this is able to show a significant weak value amplification of the phase measured, it is somewhat less clear how useful this is for measuring properties of a quantum system. It can be used to provide 'which-way' information about a photon (as in the proposal by Steinberg's research group) but is limited to cases where a great deal of information is already known about the quantum state (so that a nearly orthogonal state can be selected). This can still be valuable – but inevitably results in the useful postselections being much more particular to specific situations than a more general scheme (such as finding operator expectations).

Additionally, postselecting in the eigenbasis of the observable being measured (for Kerr measurements, the number basis) will not provide any amplification. Hence, it can be useful to consider postselecting in a different basis – for instance quadratures.

Postselecting with Quadrature Measurements

If the measured state is postselected into an infinitely squeezed state, $|X\rangle$, then the normalized pointer state after postselection, for an arbitrary input state represented in the number basis, $|\psi_i\rangle = \sum_n c_n|n\rangle$, is found to be:

$$|\mathcal{P}'_p\rangle = \frac{\langle X|\Psi\rangle}{\langle X|\psi_i\rangle} = \frac{1}{\psi_i(X)}\sum_n c_n \pi^{-1/4}(2^2 n!)^{-1/2}\mathrm{e}^{-X^2/2}H_n(X)|\alpha \mathrm{e}^{in\phi_0}\rangle\,, \tag{3.138}$$

where $H_n(X)$ is the n$^{\text{th}}$ Hermite polynomial evaluated at X, $\psi_i(X)$ is the measured state's initial wave function.

The expectation of the count operators ($\hat{M}_\pm$) are then:

$$\begin{aligned}\langle M_- \rangle = \frac{1}{\psi_i(X)}\sum_{n,m} & c_n c_m^* (2^{n+m}\pi n! m!)^{-1/2}\mathrm{e}^{-X^2}H_n(X)H_m(X) \\ & \times |\alpha^2| \left(\mathrm{e}^{-im\phi_0} - \mathrm{e}^{in\phi_0}\right)\langle \alpha \mathrm{e}^{im\phi_0}|\alpha \mathrm{e}^{in\phi_0}\rangle\,,\end{aligned} \tag{3.139}$$

which when the phase shift imparted by the pointer on the measured system is small, $\phi_0|\alpha|^2 << 1$, gives:

$$\langle M_- \rangle = \frac{|\alpha^2|}{\psi_i(X)} \sum_{n,m} c_n c_m^* \frac{1}{\sqrt{2^{n+m}\pi n! m!}} \mathrm{e}^{-X^2} H_n(X) H_m(X) \phi_0 (n+m) \,. \quad (3.140)$$

$\langle \hat{M}_+ \rangle$ evaluates to:

$$\langle M_+ \rangle = \frac{2|\alpha^2|}{\psi_i(X)} \sum_{n,m} c_n c_m^* \frac{1}{\sqrt{2^{n+m}\pi n! m!}} \mathrm{e}^{-X^2} H_n(X) H_m(X) \,. \quad (3.141)$$

This gives the phase estimate to be:

$$\bar{\phi} = \frac{\langle \hat{M}_- \rangle}{\langle \hat{M}_+ \rangle} \approx \frac{\phi_0 \sum_{n,m} c_n c_m^* \frac{1}{\sqrt{2^{n+m} n! m!}} H_n(X) H_m(X)(n+m)}{2 \sum_{n,m} c_n c_m^* \frac{1}{\sqrt{2^{n+m} n! m!}} H_n(X) H_m(X)} \,. \quad (3.142)$$

This expression is very ‘messy’, and it is not immediately obvious what kind of advantage could be achieved. We can consider an initial state to see how the measurement would be affected.

One option would be to send in a Fock state, $|\psi_i\rangle = |n\rangle$. If this is done then the expression for the phase estimate becomes:

$$\bar{\phi} = \frac{\langle \hat{M}_- \rangle}{\langle \hat{M}_+ \rangle} \approx n\phi_0 \,, \quad (3.143)$$

the same as if there had been no postselection.

An other example would be to consider the states $|\psi_i\rangle = \frac{1}{\sqrt{2}}\left(|0\rangle \pm |1\rangle\right)$. The phase estimate then is:

$$\bar{\phi} = \frac{\langle \hat{M}_- \rangle}{\langle \hat{M}_+ \rangle} \approx \phi_0 \frac{H_1(x)^2 \pm \sqrt{2} H_0(X) H_1(X)}{H_1(X)^2 \pm 2\sqrt{2} H_0(X) H_1(X) + 2 H_0(X)^2} \,. \quad (3.144)$$

Substituting in the Hermite polynomials then gives:

$$\bar{\phi} = \frac{2X^2 \pm \sqrt{2}X}{1 \pm 2\sqrt{2} + 2X^2} \phi_0 \,. \quad (3.145)$$

As shown in Figure 3.18, this results in significant amplification around $X = \mp\frac{\sqrt{2}}{2}$. Hence, this technique may be useful to discriminate between states such as these. However, given that these states are orthogonal and can already be distinguished by interference with a coherent state, it is unclear when there could be any advantage.

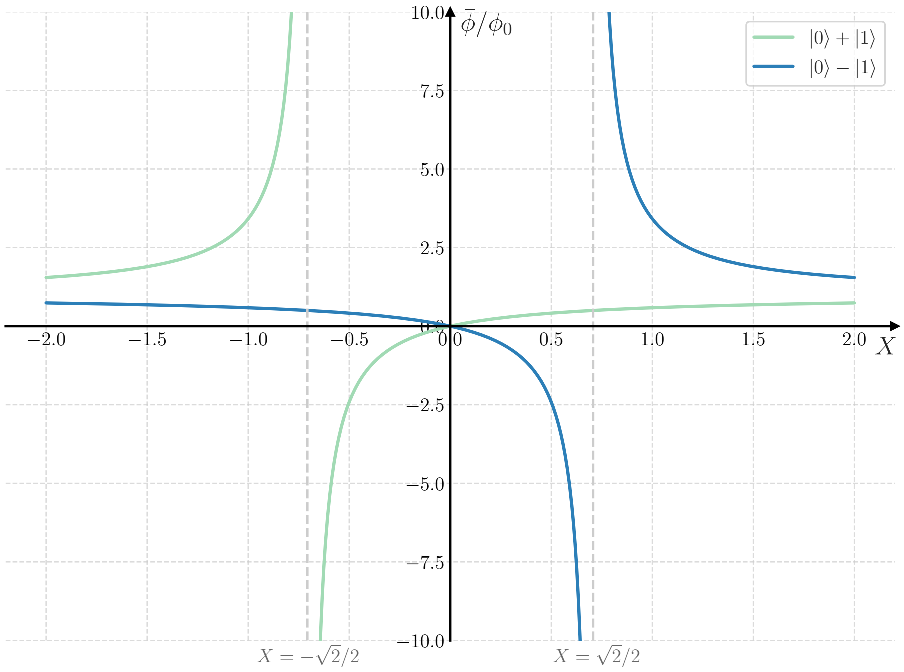

Figure 3.18: The measured phase shows significant amplification around $X = \mp\frac{\sqrt{2}}{2}$ for the state $|\psi_i\rangle = \frac{1}{\sqrt{2}}(|0\rangle \pm |1\rangle)$ when postselected by an infinite squeezed state $|X\rangle$. Measurements around these points are highly sensitive to discrimination between these two states.

3.3.2 Postselection of POVMs

It is also possible to postselect for POVM measurements using the formalism shown in Section 1.1.4. We now use this approach to examine the different combinations of pointer and readout bases considered in Section 3.2.

$\chi^{(2)}$ Nonlinearity in the Number Basis

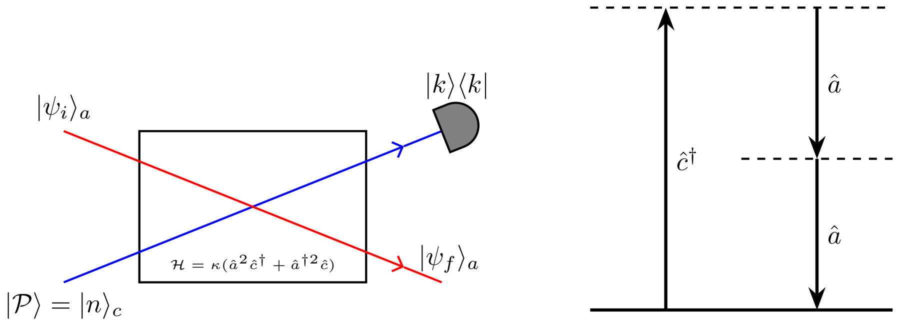

Adapted from a figure created by alchemist.

(a) Interacting modes

(b) Energy level diagram

Figure 3.19: The modes interacting when the pointer (mode c) is the second harmonic of the measured system (mode a). The initial pointer state is a number state, $|n\rangle$, and is measured in the number basis, $|k\rangle$. The measured state, $|\psi_i\rangle$ is postselected into $|\psi_f\rangle$.

When the pointer is initialized in a Fock state, $|\mathcal{P}\rangle = |n\rangle_c$, measured in the number basis, and is the second harmonic of the state $|\psi\rangle_a$ (shown in Figure 3.19), the postselected probabilities to readout n photons are:

$$p^f_{n-1} = \kappa^2 n \frac{|\langle\psi_f|\hat{a}^{\dagger 2}|\psi_i\rangle|^2}{|\langle\psi_f|\psi_i\rangle|^2} = \kappa^2 n \left|\left(a^{\dagger 2}\right)_w\right|^2 , \tag{3.146a}$$

$$p^f_n \approx 1 , \tag{3.146b}$$

$$p^f_{n+1} = \kappa^2 (n+1) \frac{|\langle\psi_f|\hat{a}^2|\psi_i\rangle|^2}{|\langle\psi_f|\psi_i\rangle|^2} = \kappa^2 (n+1) \left|\left(a^2\right)_w\right|^2 , \tag{3.146c}$$

where $(a^{\dagger 2})_w$ and $(a^2)_w$ are the weak values of the raising and lowering operators squared given by:

$$(a^{\dagger 2})_w = \frac{\langle\psi_f|\hat{a}^{\dagger 2}|\psi_i\rangle}{\langle\psi_f|\psi_i\rangle} , \tag{3.147a}$$

$$(a^2)_w = \frac{\langle\psi_f|\hat{a}^2|\psi_i\rangle}{\langle\psi_f|\psi_i\rangle} \,. \tag{3.147b}$$

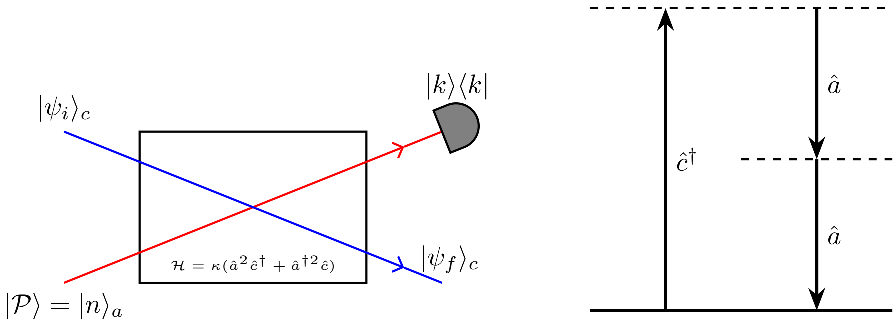

Adapted from a figure created by alchemist.
This figure is licensed under CC BY-SA 4.0

(a) Interacting modes (b) Energy level diagram

Figure 3.20: The modes interacting when the measured system (mode c) is the second harmonic of the pointer (mode a). The initial pointer state is a number state, $|n\rangle$, and is measured in the number basis, $|k\rangle$. The measured state, $|\psi_i\rangle$ is postselected into $|\psi_f\rangle$.

When the state being measured is the second harmonic (shown in Figure 3.20), the postselected probabilities to readout n photons are:

$$p^f_{n-2} = \kappa^2 n(n-1)\frac{|\langle\psi_f|\hat{c}^\dagger|\psi_i\rangle|^2}{|\langle\psi_f|\psi_i\rangle|^2} = \kappa^2 n(n-1)\left|\left(c^\dagger\right)_w\right|^2 \,, \tag{3.148a}$$

$$p^f_n \approx 1 \,, \tag{3.148b}$$

$$p^f_{n+2} = \kappa^2 (n+1)(n+2)\frac{|\langle\psi_f|\hat{c}|\psi_i\rangle|^2}{|\langle\psi_f|\psi_i\rangle|^2} = \kappa^2 (n+1)(n+2)\left|(c)_w\right|^2 \,. \tag{3.148c}$$

The probability to measure these different photon numbers correspond to the absolute square of the weak value of the raising and lowering operators (or their squares).

$\chi^{(2)}$ Nonlinearity with Coherent Pointer

When the pointer is initialized in the coherent state $|\mathcal{P}\rangle = |\alpha\rangle_c$; measured in the number basis; and is the second harmonic of the state $|\psi\rangle_a$ (shown in Figure 3.21), the postselected probabilities are:

$$p^f_n = \mathrm{e}^{-|\alpha|^2}\frac{|\alpha|^{2n}}{n!}\left(1 - 2\kappa\mathrm{Im}\left[\left(\alpha a^{\dagger 2} + \frac{n}{\alpha}a^2\right)_w\right]\right) \,, \tag{3.149}$$

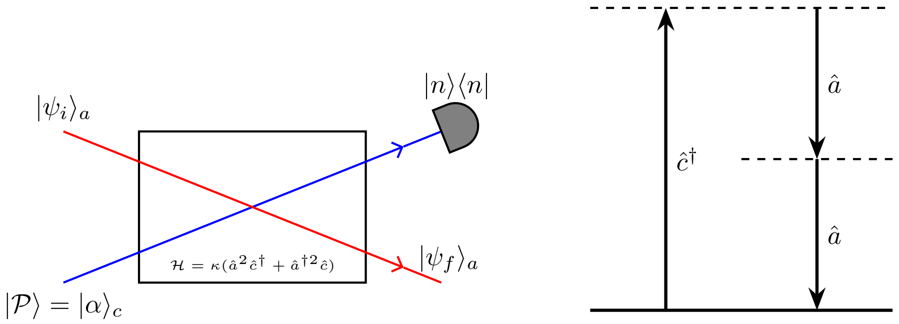

Adapted from a figure created by alchemist.
This figure is licensed under CC BY-SA 4.0

(a) Interacting modes (b) Energy level diagram

Figure 3.21: The modes interacting when the pointer (mode c) is the second harmonic of the measured system (mode a). The initial pointer state is a coherent state, $|\alpha\rangle$, and is measured in the number basis, $|n\rangle$. The measured state, $|\psi_i\rangle$ is postselected into $|\psi_f\rangle$.

where:

$$\left(\alpha a^{\dagger 2} + \frac{n}{\alpha} a^2\right)_w = \frac{\langle\psi_f|\alpha\hat{a}^{\dagger 2} + \frac{n}{\alpha}\hat{a}^2|\psi_i\rangle}{\langle\psi_f|\psi_i\rangle} \,. \tag{3.150}$$

The fractional difference in intensity, compared to when there is no measurement is:

$$\Delta p_n^f = \frac{p_n^f - \lim_{\kappa\to 0}\left(p_n^k\right)}{\lim_{\kappa\to 0}\left(p_n^k\right)} = -2\kappa \mathrm{Im}\left[\left(\alpha a^{\dagger 2} + \frac{n}{\alpha}a^2\right)_w\right] \,. \tag{3.151}$$

For the state where $\alpha = |\alpha|\mathrm{e}^{-\theta}$, the average intensity is found to be:

$$\langle\hat{n}\rangle = |\alpha|^2 - 2\kappa\left(|\alpha|^3 \mathrm{Im}\left[\mathrm{e}^{i\theta}(a^{\dagger 2})_w + \mathrm{e}^{-i\theta}(a^2)_w\right] + |\alpha|\mathrm{Im}\left[\mathrm{e}^{-i\theta}(a^2)_w\right]\right) \,. \tag{3.152}$$

When the state being measured is the second harmonic (and the pointer is the fundamental frequency, as shown in Figure 3.22), the postselected probabilities to readout n photons are:

$$p_n^f = \mathrm{e}^{-|\alpha|^2}\frac{|\alpha|^{2n}}{n!}\left(1 - 2\kappa\mathrm{Im}\left[\alpha^2 c_w^\dagger + \frac{n(n-1)}{\alpha^2}c_w\right]\right) \,. \tag{3.153}$$

This then has an average photon number after postselection:

$$\langle\hat{n}\rangle = |\alpha|^2 - 2\kappa\left(|\alpha|^4\mathrm{Im}\left[\mathrm{e}^{2i\theta}c_w^\dagger + \mathrm{e}^{-2i\theta}c_w\right] + 2|\alpha|^2\mathrm{Im}\left[\mathrm{e}^{-2i\theta}c_w\right]\right) \,. \tag{3.154}$$

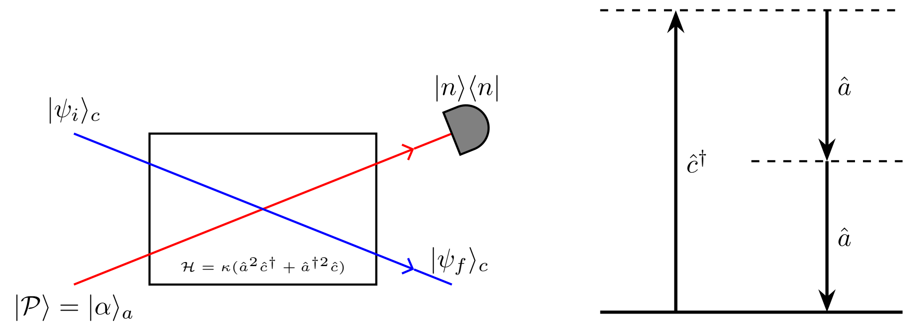

Adapted from a figure created by alchemist.
This figure is licensed under CC BY-SA 4.0

(a) Interacting modes (b) Energy level diagram

Figure 3.22: The modes interacting when the measured system (mode c) is the second harmonic of the pointer (mode a). The initial pointer state is a coherent state, $|\alpha\rangle$, and is measured in the number basis, $|n\rangle$. The measured state, $|\psi_i\rangle$ is postselected into $|\psi_f\rangle$.

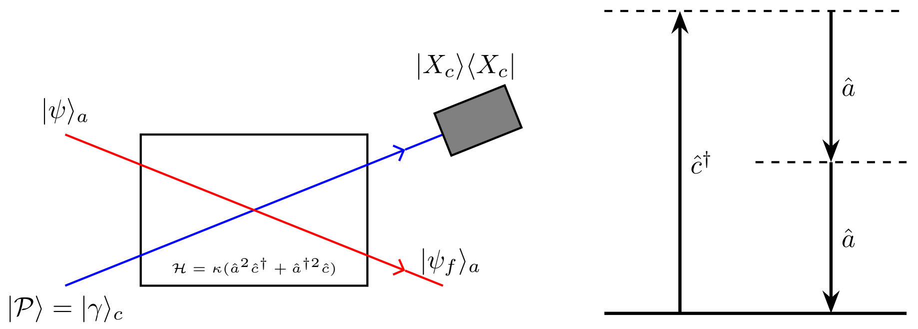

Adapted from a figure created by alchemist.
This figure is licensed under CC BY-SA 4.0

(a) Interacting modes (b) Energy level diagram

Figure 3.23: The modes interacting when the pointer (mode c) is the second harmonic of the measured system (mode a). The initial pointer state is a coherent state, $|\gamma\rangle$, and has it's quadrature, $|X_c\rangle$, measured. The initial measured state, $|\psi_i\rangle$, is postselected into state $|\psi_f\rangle$.

Again the probability to measure these different photon numbers correspond to the weak value of the raising and lowering operators (or their squares).

Measuring Pointer Quadrature for $\chi^{(2)}$ Nonlinearity

When the pointer is initialized in a coherent state, $|\mathcal{P}'\rangle = |\gamma\rangle_c$, at the second harmonic frequency (shown in Figure 3.23), the postselected probability to measure the state in quadrature $|X_c\rangle$ will be:

$$\begin{aligned}\frac{|\langle\psi_f|\langle X_c|\hat{U}|\gamma\rangle|\psi_i\rangle|^2}{|\langle\psi_f|\psi_i\rangle|^2} = |\langle X_c|\gamma\rangle|^2\Big(1 - 4\kappa X_c \mathrm{Im}\left[\left(X_a^2 - Y_a^2\right)_w\right] \\ - 4\kappa \mathrm{Re}\left[\left(X_c - \gamma\right)\left(X_a Y_a + Y_a X_a\right)_w\right]\Big),\end{aligned} \tag{3.155}$$

where:

$$\left(X_a^2 - Y_a^2\right)_w = \frac{\langle\psi_f|\hat{X}_a^2 - \hat{Y}_a^2|\psi_i\rangle_a}{\langle\psi_f|\psi_i\rangle}, \tag{3.156a}$$

$$\left(X_a Y_a + Y_a X_a\right)_w = \frac{\langle\psi_f|\hat{X}_a\hat{Y}_a + \hat{Y}_a\hat{X}_a|\psi_i\rangle_a}{\langle\psi_f|\psi_i\rangle}. \tag{3.156b}$$

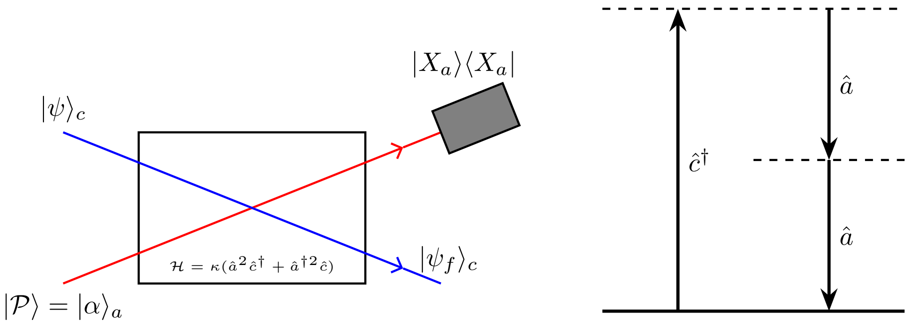

Adapted from a figure created by alchemist.
This figure is licensed under CC BY-SA 4.0

(a) Interacting modes

(b) Energy level diagram

Figure 3.24: The modes interacting when the measured system (mode c) is the second harmonic of the pointer (mode a). The initial pointer state is a coherent state, $|\alpha\rangle$, and has it's quadrature, $|X_a\rangle$, measured. The initial measured state, $|\psi_i\rangle$, is postselected into state $|\psi_f\rangle$.

When the pointer is at the fundamental frequency and the system being measured is the second harmonic (shown in Figure 3.24), then the postselected probability to measure the pointer in $|X_a\rangle$ is:

$$\frac{|\langle\psi_f|\langle X_a|\hat{U}|\alpha\rangle|\psi_i\rangle|^2}{|\langle\psi_f|\psi_i\rangle|^2} = \\ |\langle X_a|\alpha\rangle|^2\Big(1 - 4\kappa\mathrm{Im}\left[\left(2X_a^2 - 2\alpha X_a + \alpha^2\right)(X_c)_w\right] \\ - 2\kappa\mathrm{Re}\left[\left(4X_a^2 - 4\alpha X_a - 1\right)(Y_c)_w\right]\Big)\,, \tag{3.157}$$

where:

$$(X_c)_w = \frac{\langle\psi_f|\hat{X}_c|\psi_i\rangle_c}{\langle\psi_f|\psi_i\rangle}\,, \tag{3.158a}$$

$$(Y_c)_w = \frac{\langle\psi_f|\hat{Y}_c|\psi_i\rangle_c}{\langle\psi_f|\psi_i\rangle}\,. \tag{3.158b}$$

Interpreting These Weak Values

To understand what the postselected POVM results above can provide information about, it is insightful to consider some possible examples for the weak values found in the probabilities above.

Postselecting on Number State

If the postselected state is chosen to be a number state, $|\psi_f\rangle = |m\rangle$, and the initial state is expressed in the number basis as $|\psi_i\rangle = \sum_j c_j|j\rangle$, then the weak values will be:

$$(a)_w = \frac{\langle m|\hat{a}|\psi_i\rangle}{\langle m|\psi_i\rangle} = \frac{c_{m+1}}{c_m}\sqrt{m+1}\,, \tag{3.159a}$$

$$(a^\dagger)_w = \frac{\langle m|\hat{a}^\dagger|\psi_i\rangle}{\langle m|\psi_i\rangle} = \frac{c_{m-1}}{c_m}\sqrt{m}\,, \tag{3.159b}$$

$$(a^2)_w = \frac{\langle m|\hat{a}^2|\psi_i\rangle}{\langle m|\psi_i\rangle} = \frac{c_{m+2}}{c_m}\sqrt{(m+1)(m+2)}\,, \tag{3.159c}$$

$$(a^{\dagger 2})_w = \frac{\langle m|\hat{a}^{\dagger 2}|\psi_i\rangle}{\langle m|\psi_i\rangle} = \frac{c_{m-2}}{c_m}\sqrt{m(m-1)}\,. \tag{3.159d}$$

This provides information about the relative magnitude and phase of different photon number coefficients of the initial state (with the coefficient being probed depending on the value of the postselection). There will be a large amplification when c_m is small – when the initial state has a low probability of having the postselected number of photons.

The weak values of the quadrature operators are found to be:

$$(X)_w = \frac{\langle m|\hat{X}|\psi_i\rangle}{\langle m|\psi_i\rangle} = \frac{c_{m+1}\sqrt{m+1} + c_{m-1}\sqrt{m}}{2c_m}\,, \tag{3.160a}$$

$$(Y)_w = \frac{\langle m|\hat{Y}|\psi_i\rangle}{\langle m|\psi_i\rangle} = \frac{c_{m+1}\sqrt{m+1} - c_{m-1}\sqrt{m}}{2ic_m}\,, \tag{3.160b}$$

$$(XY+YX)_w = \frac{c_{m+2}\sqrt{(m+1)(m+2)} - c_{m-2}\sqrt{m(m-1)}}{2ic_m}\,, \tag{3.160c}$$

$$(X^2 - Y^2)_w = \frac{\langle m|\hat{X}^2 + \hat{Y}^2|\psi_i\rangle}{\langle m|\psi_i\rangle} = \frac{2m+1}{2}\,. \tag{3.160d}$$

These weak values provide information about the ‘interference’ between different photon number amplitudes (either separated by 2 or 4 photons). The exception to this is the weak value $(X^2 - Y^2)_w$, which provides no information about the measured system when the postselection is performed in the number basis.

Postselecting with Quadratures

If the postselected state is chosen to be an infinitely squeezed state (a quadrature projector state), $|\psi_f\rangle = |X\rangle$, and the initial state is expressed in the quadrature basis as $|\psi_i\rangle = \int \psi_i(X')|X'\rangle \mathrm{d}X$, then the weak values will be:

$$(X)_w = \frac{\langle X|\hat{X}|\psi_i\rangle}{\langle X|\psi_i\rangle} = X\,, \tag{3.161a}$$

$$(Y)_w = \frac{\langle X|\hat{Y}|\psi_i\rangle}{\langle X|\psi_i\rangle} = \frac{i}{2\psi_i(X)}\frac{\mathrm{d}\psi_i}{\mathrm{d}X}\,, \tag{3.161b}$$

$$(XY+YX)_w = \frac{\langle X|\hat{X}\hat{Y} + \hat{Y}\hat{X}|\psi_i\rangle}{\langle X|\psi_i\rangle} = \frac{i}{2\psi_i(X)}\left(2X\frac{\mathrm{d}\psi_i}{\mathrm{d}X} + \psi_i(X)\right)\,, \tag{3.161c}$$

$$(X^2 - Y^2)_w = \frac{\langle X|\hat{X}^2 - \hat{Y}^2|\psi_i\rangle}{\langle X|\psi_i\rangle} = \frac{1}{\psi_i(X)}\left(X^2 + \frac{1}{4}\frac{\mathrm{d}^2\psi_i}{\mathrm{d}X^2}\right)\,. \tag{3.161d}$$

The weak values for the raising and lowering operators can be written either in terms of the quadrature results above (using $\hat{a} = \hat{X} + i\hat{Y}$) or the initial state can be considered in the number basis ($|\psi_i\rangle = \sum_j c_j|j\rangle$) and the results written as sums of Hermite polynomials.

$$(a)_w = \frac{\langle X|\hat{a}|\psi_i\rangle}{\langle X|\psi_i\rangle} = X - \frac{1}{2\psi_i(X)}\frac{\mathrm{d}\psi_i}{\mathrm{d}X} = \frac{\sum_j c_{j+1}\frac{\sqrt{j+1}}{\sqrt{j!2^j}}H_j(X)}{\sum_j c_j\frac{1}{\sqrt{j!2^j}}H_j(X)}\,, \tag{3.162a}$$

$$(a^\dagger)_w = \frac{\langle X|\hat{a}^\dagger|\psi_i\rangle}{\langle X|\psi_i\rangle} = X + \frac{1}{2\psi_i(X)}\frac{\mathrm{d}\psi_i}{\mathrm{d}X} = \frac{\sum_j c_{j-1}\frac{1}{\sqrt{(j-1)!2^j}}H_j(X)}{\sum_j c_j\frac{1}{\sqrt{j!2^j}}H_j(X)}\,, \tag{3.162b}$$

$$\begin{aligned}(a^2)_w = \frac{\langle X|\hat{a}^2|\psi_i\rangle}{\langle X|\psi_i\rangle} &= \frac{1}{\psi_i(X)}\left(X^2 - \frac{\psi_i(X)}{2} - X\frac{\mathrm{d}\psi_i}{\mathrm{d}X} + \frac{1}{4}\frac{\mathrm{d}^2\psi_i}{\mathrm{d}X^2}\right)\\ &= \frac{\sum_j c_{j+2}\frac{\sqrt{(j+1)(j+2)}}{\sqrt{j!2^j}}H_j(X)}{\sum_j c_j\frac{1}{\sqrt{j!2^j}}H_j(X)}\,,\end{aligned} \tag{3.162c}$$

$$\begin{aligned}(a^{\dagger 2})_w = \frac{\langle X|\hat{a}^{\dagger 2}|\psi_i\rangle}{\langle X|\psi_i\rangle} &= \frac{1}{\psi_i(X)}\left(X^2 + \frac{\psi_i(X)}{2} + X\frac{\mathrm{d}\psi_i}{\mathrm{d}X} + \frac{1}{4}\frac{\mathrm{d}^2\psi_i}{\mathrm{d}X^2}\right)\\ &= \frac{\sum_j c_{j-2}\frac{\sqrt{j(j-1)}}{\sqrt{j!2^j}}H_j(X)}{\sum_j c_j\frac{1}{\sqrt{j!2^j}}H_j(X)}\,.\end{aligned} \tag{3.162d}$$

Unsurprisingly, when postselecting on an infinite squeezed state, representing the state in the number basis results in a fairly ‘messy’ expression. However, in the ‘quadrature position’ representation, these look more interesting – providing information about the gradient of the wave function. These weak values will be large either when the gradient is large or when the wave function value is small at the postselected X.

These measurements are unlikely to be useful for determining the full state (wave function) of the system – since to find the gradient at a given X requires a measurement of the field quadrature at that X to postselect upon. It would be much simpler to perform tomography directly using these quadrature measurements. However, if the gradient was only required for a single X then there may be some use for this scheme.

3.3.3 Postselection Summary

In this section, we explored the role of postselection in enhancing the sensitivity and information gained from weak measurements in nonlinear optical systems. Postselection, particularly when the overlap between the initial and postselected states is small, can significantly amplify the measurement signal, a phenomenon known as weak value amplification.

We examined postselection for the von Neumann style Kerr measurements. The example of postselecting on near-orthogonal states as proposed and demonstrated by Steinberg’s research group is presented. Postselecting with quadrature measurements is considered and shows advantages for distinguishing between certain states. However, a postselection is only able to provide useful amplification when the postselected and measured eigenstates have small overlaps – and hence requires some knowledge of the initial measured state.

Additionally, we discussed the implications of postselecting after a Positive Operator-Valued Measure (POVM). This results in expressions for the weak values of various operators appearing in the probability distribution of the outcomes. Various postselection strategies – such as number states or quadrature states – reveal distinct information about the quantum state, from Fock state amplitudes to wave function derivatives

Key Findings

- Postselections can provide weak value amplification for Kerr effect based measurements of number states. These effects are large only when the overlap between the initial and postselected states is small. (Section 3.3.1)
- Postselecting with quadrature measurements provides amplification that can help distinguish between certain states. (Section 3.3.1)
- Postselecting Positive Operator-Valued Measurements (POVMs) results in weak values appearing in the probability to obtain each measurement outcome. (Section 3.3.2)
- The weak values of the raising and lowering operators (or quadratures) provide information about the interference of photon number amplitudes or the derivatives of the wave function. (Section 3.3.2)

Chapter 4

Conclusions

The finite number of degrees of freedom of optical modes restricts the simultaneous measurement of multiple observables. This is of increasing relevance as we develop the technology to engineer ever more complex quantum systems [136–138]. Weak measurement offers approaches that can overcome these limitations. One way, is as a framework used to analyze coupling to external systems with nonlinear interactions. Alternatively, they can enable novel methods to measure joint observables. In addition, weak measurements allow for a sequence of measurements, which can be used to find quantum trajectories and the development of a system over time [9].

In Chapter 2 we designed, simulated and built an experiment to find the joint weak average of the position and momentum projectors using the conditional scheme proposed by Lundeen and Bamber [28]. This scheme allows the joint weak average to be readout directly from a single pointer. We showed that a binary conditionality is able to result in the same measurement outcome as a proportional conditionality – enabling simpler experimental designs and stronger signals. Whilst qualitative demonstrations of the scheme have been made for the real part of the Kirkwood-Dirac distribution, the experiment is still in progress and a conclusive quantitative demonstration remains forthcoming. Additional work that could be performed in this area would be: taking measurements of different states, performing measurements at the single photon level, and performing a third strong measurement using the first pointer after the joint weak average has been ‘encoded’ onto the second pointer. It could also be interesting to consider how the conditional scheme could be applied to other situations, perhaps considering discrete systems that have quantum information processing applications, such as optical beam arrays.

In Chapter 3, we considered how bulk optical nonlinearities can be used to perform measurements. In the von Neumann formalism, only photon number (using the Kerr effect) and, potentially, field quadrature (using a very weak $\chi^{(4)}$ interaction resulting in a signal that would almost certainly be dominated by $\chi^{(3)}$ processes) can be measured. When linear process are combined with nonlinear interactions, von Neumann style measurements of field quadratures are possible using $\chi^{(2)}$ processes. It could be an area for further exploration to see what other measurements would be possible using these 'hybrid' interactions. In the more general Positive Operator-Valued Measure (POVM) formalism, other observables affect the probabilities of measurement outcomes. Whilst the relevant observables were all a combination of quadrature or raising/lowering operators – these are nevertheless useful quantities to measure. Most promisingly we showed that, using a $\chi^{(2)}$ nonlinearity and detecting the intensity of the pointer, it would be possible to measure the quadrature of a quantum system. This potentially provides an alternative to using homodyne detection and would be performed as a non-demolition measurement. There remains significant scope for future work in this area. Other nonlinearities beyond $\chi^{(2)}$ could be analyzed in the POVM framework and alternative initial pointer states (for instance squeezed states) could be considered. There could also be more detailed treatment of multimode light – using pointers such as position or frequency. Finally, the use of optical nonlinearities created by postselection (of the type first proposed by Knill, Laflamme and Milburn [139]) could be considered.

Weak measurements remain an area of opportunity – enabling measurement schemes that may naively appear to be forbidden by quantum theory. This is the case regardless of whether postselection is performed, although postselection is needed to see weak value amplification. In particular, weak measurements provide a useful tool to find measurements that function in a fundamentally different way to standard strong projective measurements. While in most cases standard measurement schemes will prove more useful, with much larger signals than (non-postselected) weak measurements, this is not always the case. In this thesis, we have shown how the framework of weak measurement enables optical nonlinearities to yield information about useful observables. Additionally, we demonstrate how weak measurements allow for more direct and efficient use of degrees of freedom when measuring joint values and characterizing system states.

Appendix A

Appendix: SLM Process Tomography

A.1 Motivation

During the use of the SLM for the conditional weak measurement experiment, very strange behavior was observed numerous times. For instance, at one point the phase was found to vary almost sinusoidally with the grey scale value of the SLM with one laser but linearly with another laser (see Figure A.1).

Due to these strange effects, we decided to conduct a more thorough investigation of the transformations the SLM was performing – and see if these depended on the properties of the laser used.

A.2 Polarization Measurement Scheme

To determine the effect of any SLM grey scale value on any polarization input state is to perform process tomography [140] on the SLM. We need to perform quantum state tomography on the system after interaction with the SLM, for a range of different input polarizations – and this process needs to be repeated for each SLM grey scale value.

A.2.1 Quantum Tomography of Polarization State

To perform quantum tomography on a polarization state is fairly simple to do. One approach is to measure in the three typical bases (horizontal, diagonal and

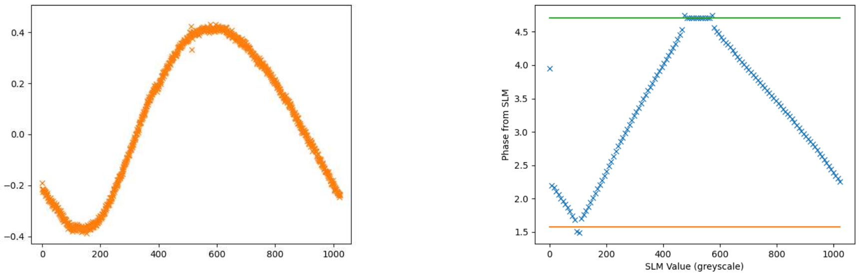

(a) Narrowband DBR laser

(b) Broader band laser

Figure A.1: The measured phase variation with SLM grey scale value. We would expect this to be linear. The limited range seen in (b) is due to an artifact of the fitting process used to determine the phase at this time.

circular) and then reconstruct the state from these measurements [141].

However, more classical approaches can be used to measure polarization when we are not at the single photon level. One way is to continuously rotate a quarter waveplate and measure the intensity after a fixed polarizer [142]. This has the advantage of enabling the polarization state to be determined in a very short amount of time (around the time it takes for the quarter waveplate to rotate once) – which is especially useful for this process tomography where tomography is going to have to be performed on many quantum states.

Reconstruction Approaches

There are a number of ways to determine the Stokes parameters (which correspond to coordinates in the Poincaré sphere). One is to multiply the measured intensity signals by sinusoids of the appropriate phase and frequency to ‘pick out’ each component.

Alternatively, a more complex fitting algorithm can be used to find the best fit of Stokes parameters to the measured intensity data. When this is done, there are a range of constraints that can be imposed on the fit – such as imposing the states be physical, that they be pure or no constraints on their physicality. These different fits correspond to the different colours used in Figure A.4.

A.3 Polarization Dependent Loss

Due to the pixel array of the SLM, some light is diffracted out of the zeroth order even when a uniform grey scale is displayed on the SLM. For the hor-

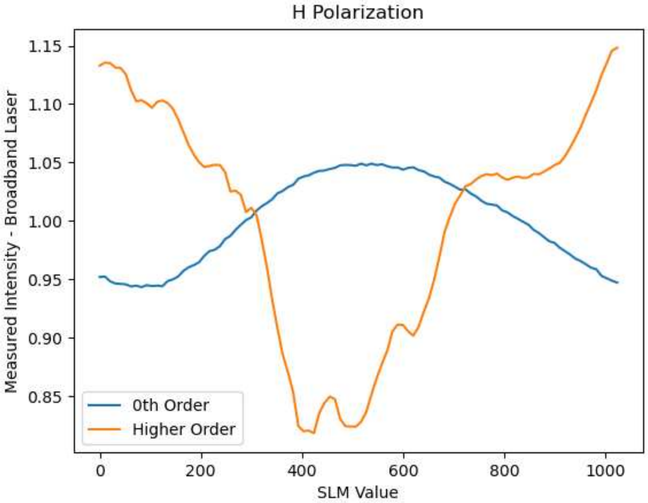

Figure A.2: The intensity of horizontal polarized light measured after the SLM for different grey scale values. Vertical polarized light does not see this variation.

izontally polarized light, the amount that diffracts depends on the grey scale displayed on the pixels as shown in Figure A.2. The vertical polarized light does not experience a phase change due to the liquid crystals and so the amount of light diffracted has no dependence on the grey scale values displayed. The consequence of these differences is that the SLM will appear to have a polarization dependent loss that varies with the grey scale value displayed.

A.3.1 Impact of Polarization Dependent Loss

When there is polarization dependent loss, the effective polarization rotation changes. The rotation now depends on the input state. This limits the range of possible rotations, for instance, it is not possible to rotate from circular to diagonal polarization. Some possible examples are shown in Figure A.3.

A.4 Process Tomography Results

To determine how the SLM will change an arbitrary state, we consider a range of different input states. Figure A.4 shows the measured output states for a range of different linear polarization input states. As shown in Figure A.5, the effect of the SLM is largely to rotate the input state about the horizontal/vertical

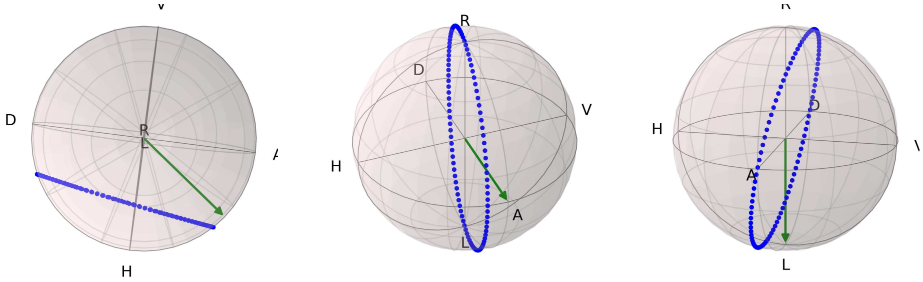

Figure A.3: The theoretical range of polarization states that can be reached for different input polarizations when there is polarization dependent loss. These plots show an effect around 4 times larger than seen experimentally, to make the difference more visible.

polarization axis of the Poincaré sphere by an amount that depends on the grey scale value displayed on the SLM.

This is exactly the kind of transformation to the polarization states that would be expected by theory and the only major correction needed is to relate the strength of this rotation to the grey scale value. This was already done in Section 2.4.2 when finding the relationship between the phase and the grey scale value. We did not observe any noticeable difference depending on the bandwidth of the laser used.

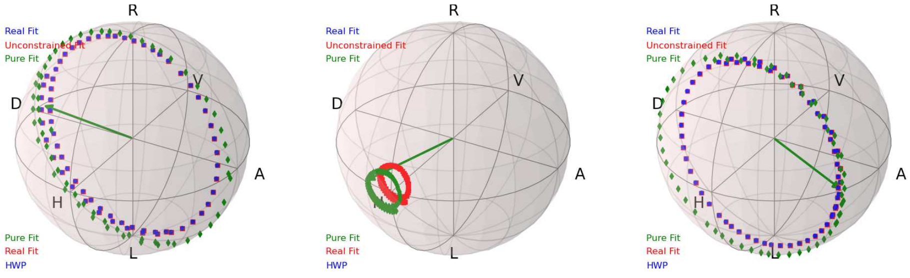

(a) Input near $|D\rangle$ (b) Input near $|H\rangle$ (c) Input near $|H\rangle + |A\rangle$

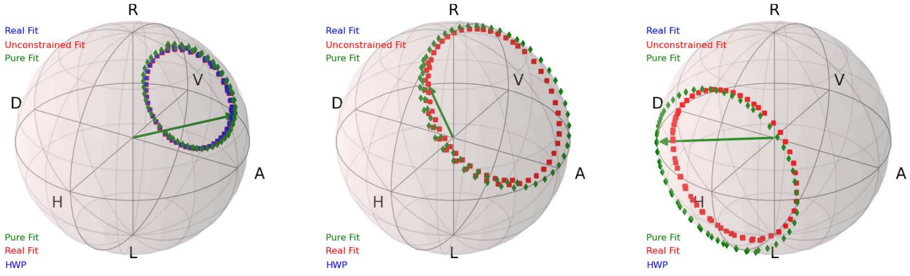

(d) Input near $|V\rangle + |A\rangle$ (e) Input near $|V\rangle + |D\rangle$ (f) Input near $|D\rangle + |H\rangle$

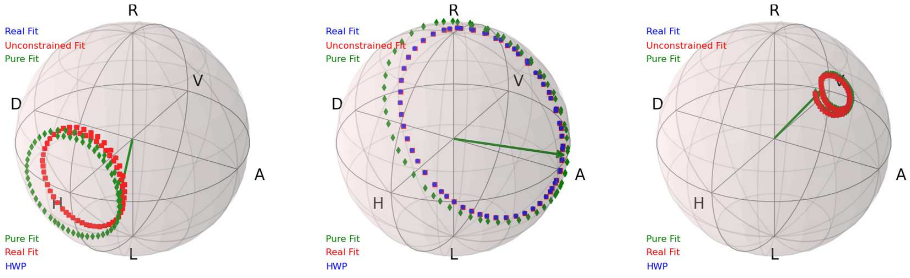

(g) Input near $|A\rangle + |H\rangle$ (h) Input near $|A\rangle$ (i) Input near $|V\rangle$

Figure A.4: The measured polarization states for different SLM grey scale values for a range of different input polarization inputs. These are measured for a HeNe laser with wavelength of 633 nm.

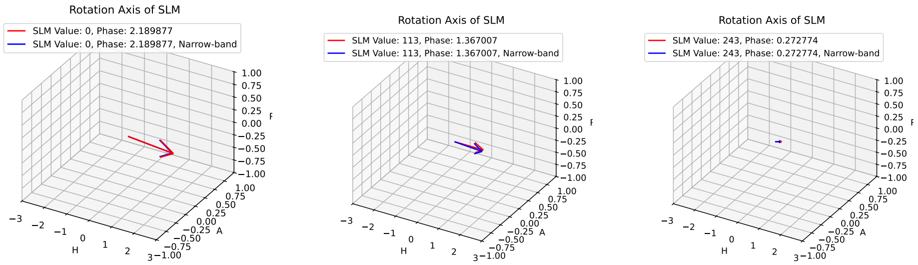

(a) SLM Grey = 0 (b) SLM Grey = 113 (c) SLM Grey = 243

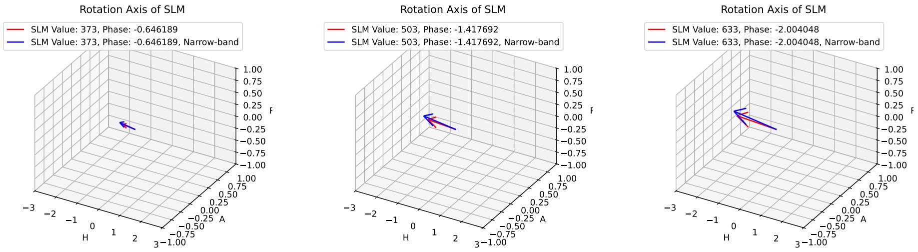

(d) SLM Grey = 373 (e) SLM Grey = 503 (f) SLM Grey = 633

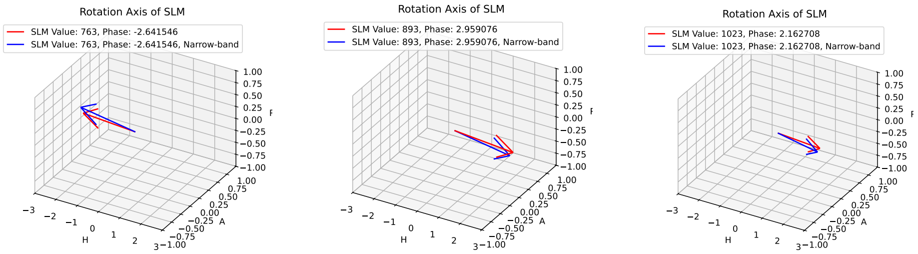

(g) SLM Grey = 763 (h) SLM Grey = 893 (i) SLM Grey = 1023

Figure A.5: For a range of different SLM grey scale values, the rotation axis in the Poincaré and strength of the transformation is plotted. This rotation is found for a narrowband and a broader band 810 nm laser. An animation of these plots can be found here.

Additional Work: Graduate Student Finances

In addition to my primary research in quantum optics, I have also contributed to empirical work examining the financial realities of graduate students in Canada. Conducted as a member of the Ottawa Science Policy Network and Support Our Science, this research used survey and publicly accessible data to better understand the financial situation of graduate students and their intentions to remain in Canada. While distinct from the core scientific content of this thesis, this work was positively received and had significant impact.

Analysis of Financial Challenges Faced by Graduate Students in Canada[*]

This paper [143] presents the results of a national survey of graduate student finances that was conducted from the end of 2021 until April 2022. The survey received 1305 responses from graduate students representing various geographical locations, years of study, fields of education, and demographic backgrounds. The results capture a snapshot into graduate student finances, including an in-depth analysis of stipends, scholarships, debt, tuition, and living expenses.

This paper had significant impact: becoming the most read article of the journal [144] (with over 21,000 downloads), the runner-up for the publisher's top article of the year [145] and cited by the House of Commons Standing Committee on Science and Research in their report on graduate scholarships and

---

[*] This work was done in collaboration with many other authors in the Ottawa Science Policy Network. As second author I lead the data analysis team and contributed to conceptualization; data curation; formal analysis; investigation; methodology; project administration; resources; supervision; validation; visualization; writing – original draft; and writing – review & editing. I contributed equally with Sarah Laframboise, Anh-Thu Dang, Mercedes Rose, and Zier Zhou.

post-doctoral fellowships [146]. This helped contribute to the $2.6 billion of additional investment in federal research grants and scholarships (and the significant increase in the value of federal graduate scholarships and post-doctoral fellowships) allocated in federal budget 2024 [147].

An abridged version of this paper is presented in this section. Figures AW.1 to AW.18 and all text in this section are reproduced from Laframboise et al. [143] under a CC BY 4.0 license.

Introduction

Graduate students play a large role in the research and innovation ecosystem in Canada. These students have already completed a bachelor's degree and are enrolled in a master's or doctoral degree. Most graduate degrees include full-time, independent research in collaboration with a Principal Investigator or supervisor, who is a faculty member at a university. This work requires laborious training and creates the foundation of research in Canada. Research has shown that one-third of publications feature PhD students as either authors or co-authors [148], exemplifying the crucial role that graduate students play in research and academic publications.

Since graduate students are often enrolled in full-time studies, many receive a stipend intended to offset living costs so that they can focus on their studies. The source of this funding for graduate students can be complex. In Canada, funding comes from two main sources: (1) directly through scholarships, such as those provided by the three federal granting agencies, known as the Tri-Council (Natural Sciences and Engineering Research Council (NSERC), Social Science and Humanities Research Council (SSHRC), and the Canadian Institute for Health Research (CIHR)) or (2) indirectly through their supervisor's research grants and(or) department funding. As such, graduate student pay is often referred to as a stipend, since it is often a fixed pay, independent from work performed. Stipends can vary among graduate students and depend on many factors. For example, some students may be required to complete teaching assistantships (TAs) in which they assist a professor with instructional responsibilities or research assistantships (RAs) in which they assist a professor or instructor with additional research activities such as performance of clerical, laboratory, or technical tasks as part of their stipend.

The value of graduate student stipends can be set by universities, faculties, departments, and supervisors. It appears that, in the absence of any other government guidance, federal Tri-Council scholarship values have set the precedent for stipend values. However, it is important to acknowledge that these scholarships have not changed in value since 2003. Additionally, there has been little increase in the number of available Canadian scholarships over the years. A 2018 report from the Science and Policy Exchange (SPE) revealed that 91% of graduate students were largely displeased with the number of Tri-Council scholarships available for graduate students [149]. Furthermore, 79% replied that they would like to see an increase in the value of the awards. This 2018 report eloquently displayed the dissatisfaction among graduate students in regard to the value and number of federal scholarships, as well as the perceived financial security that comes with obtaining these scholarships.

During the COVID-19 pandemic, financial concerns of graduate students became even more prominent, with Statistics Canada reporting that over two-thirds of continuing postsecondary students were very or extremely concerned about the financial impacts of the pandemic [150]. The Toronto Science Policy Network's COVID-19 Graduate Student Report has also revealed that finances were at the forefront of worries for graduate students during the pandemic [151].

These financial concerns for graduate students have continued, with inflation recently hitting a 40-year high, causing an increase in everyday expenses [152]. While inflation affects all those in Canada, graduate students can be considered a particularly vulnerable group because their stipend values do not reflect average living costs. The Canadian housing market has also witnessed a large increase in real-estate prices. While the majority of graduate students are not in a position to purchase their own homes, rental prices across Canada are increasing at unprecedented rates [153].

There is a lack of national data on graduate student finances, especially for the vast majority of graduate students who do not hold a federal scholarship. This survey aimed to investigate the state of graduate student finances in Canada. From 1305 responses of graduate students representing various geographical locations, years of study, fields of education, and demographic backgrounds, we examined costs, tuition, debt, sources of funding, reported financial struggle, and other financial indicators.

Results

Demographics

One aim of our survey was to assess the financial situation of graduate students across Canada, including students from varying programs, fields of study, and ages. We received a total of 1305 responses, 1030 of which were in English

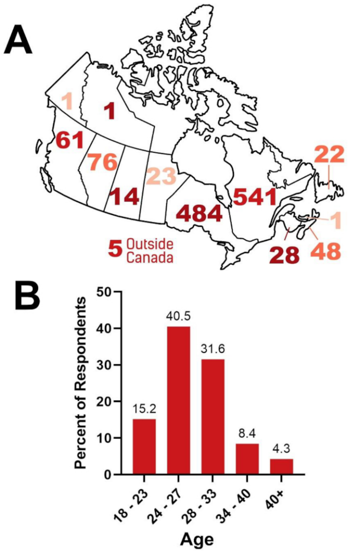

Figure AW.1: Geographic location and age: (A) number of respondents from each province and territory ($n = 1305$) and (B) age category of respondents by % ($n = 1305$).

and 275 in French. Nearly all respondents were registered as full-time students (96.7%), with only a small percentage registered in part-time programs (2.3%). Students that resided in QC and ON made up 78.6% of respondents, with 484 respondents from ON and 541 from QC (Figure AW.1A). This is consistent with Statistics Canada data from the National Graduates Survey that showed QC and ON made up 73.8% and 73.7% of master's and PhD graduates, respectively [154]. Additionally, over 70% of respondents were between the ages of 24 and 33 (Figure AW.1B). Again, this is consistent with the Statistics Canada data that showed an average graduate student's age was 31 and 35 upon graduation from master's and PhD programs, respectively [154]. This provides confidence that the conclusions made in this survey are a valid representation of the overall graduate student profile in Canada.

A majority of respondents (57.6%) were pursuing a doctoral degree and nearly all were in a research-stream program (Figure AW.2A). Similarly, the majority (60.9%) of master's student respondents were in the research stream, while the remaining were in course-based (19.8%) and professional master's programs (19.3%) (Figure AW.2A). Responses across years of study were evenly dispersed (Figure AW.2B). Survey respondents were primarily in science-based programs, including physical science (26.3%), medical sciences (23.8%), life sci-

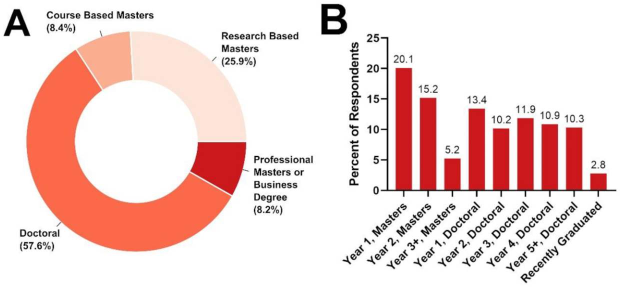

Figure AW.2: Level and year of study: (A) program and current study level of survey respondents by % ($n = 1303$). The doctoral category includes professional doctoral (e.g., EdD, PharmD, and DBA), research stream doctoral (PhD), course-based doctoral, and MD PhD. (B) Current year of study of survey respondents by % ($n = 1297$).

ences (23.5%), and social sciences (16.4%) (Figure AW.3). Arts and humanities students comprised 7.7% of respondents (Figure AW.3). A small percentage of business students (1.6%) and law students (0.5%) also responded to the survey (Figure AW.3). As such, our overall findings are most representative of graduate students in STEM-related fields, which encompassed 73% of our respondents.

Financial Stress

We asked survey respondents to identify their comfort levels with their current financial situation. Our team examined how concerned students were about various financial stresses, including living expenses, debt, and emergency funds. To investigate students' financial status, we asked participants to choose which most appropriately defined their current financial situation: comfortable (I am very comfortable financially. I have enough money that I do not need to worry about monthly expenses and spend as I would like.), enough (I have enough. My finances are a bit tight but I live within my means and can afford to provide for myself.), tight (every month is tight, but I am getting by. I am often making sacrifices to pay for necessities.), and struggling (I am struggling financially. I often do not have enough to make ends meet.) Nearly half of all respondents (43.4%) identified that they were either frequently struggling to make ends meet or that their tight finances forced them to make sacrifices to afford necessities (Figure AW.4A). Less than 10% of students stated that they were very comfortable with their current financial situation (Figure AW.4A). Unsurprisingly, those who identified as struggling to make ends meet generally had the lowest stipend values, whereas those who identified as being very comfortable with

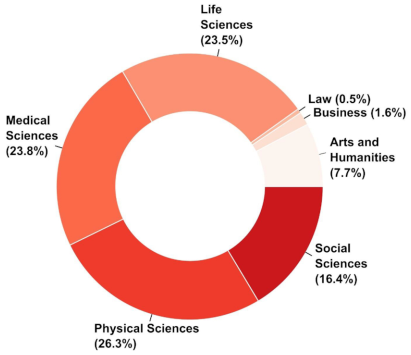

Figure AW.3: Field of study. Respondents self-reported their field of study from seven categories: arts and humanities, business, law, life sciences, medical sciences, physical sciences (engineering, physics, mathematics, etc.) and social sciences ($n = 1305$). If respondents indicated multiple fields of study or an option not listed in the survey, they were categorized into one of the seven categories based on their answers for analysis purposes.

their financial situation had the highest (Figure AW.4B).

The majority of respondents (85.7%) expressed experiencing stress/anxiety about finances at some point during their graduate studies. Meanwhile, 54.7% experienced difficulty budgeting, and 30.7% have considered leaving their studies due to financial struggles alone (Figure AW.5A). Concern about insufficient funds for living expenses was common among respondents, with over 30% having experienced concern about rent and food (Figure AW.5A) and 27.2% either "always" or "often" worrying about their ability to pay for bills (Figure AW.5B). The standard advice from financial experts and the recommendation by the Financial and Consumer Agency of Canada is to ideally have at least 3–6 months of savings for living expenses [155]. Only half of our survey respondents met this recommendation, with 52.3% having only 0–3 months of living expenses saved (Figure AW.5C) and 53.7% of students either "always" or "often" worrying about their ability to pay for emergency expenses (Figure AW.5B). These findings highlight that graduate students are vulnerable to unexpected financial challenges.

As an expected consequence, graduate students worry about their future financial security. Nearly 60% of respondents indicated that they either "always" or "often" worry about future financial security, and a similar number (57%) indicated "always" or "often" worrying about their ability to obtain a job in the future (Figure AW.5B).

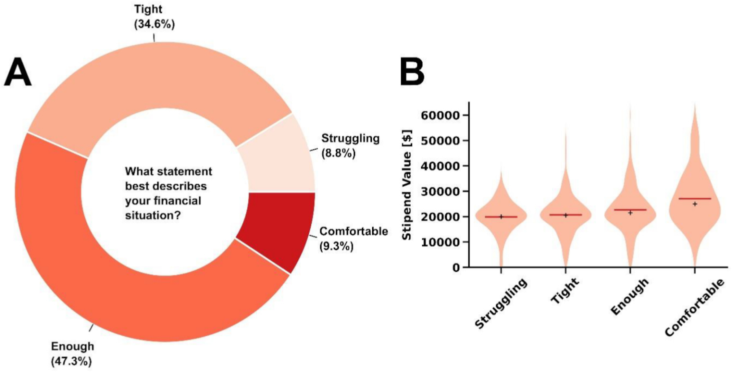

Figure AW.4: Financial situation. (A) Respondents were asked what best describes their financial situation: comfortable (I am very comfortable financially. I have enough money that I do not need to worry about monthly expenses and spend as I would like.), enough (I have enough. My finances are a bit tight but I live within my means and can afford to provide for myself.), tight (every month is tight, but I am getting by. I am often making sacrifices to pay for necessities.), and struggling (I am struggling financially. I often do not have enough to make ends meet.). Data are shown by % ($n = 1303$). (B) Violin plot of respondents' financial situation and stipend value ($n = 1303$). The red line and + sign represent the mean and median stipend value of respondents in each group, respectively.

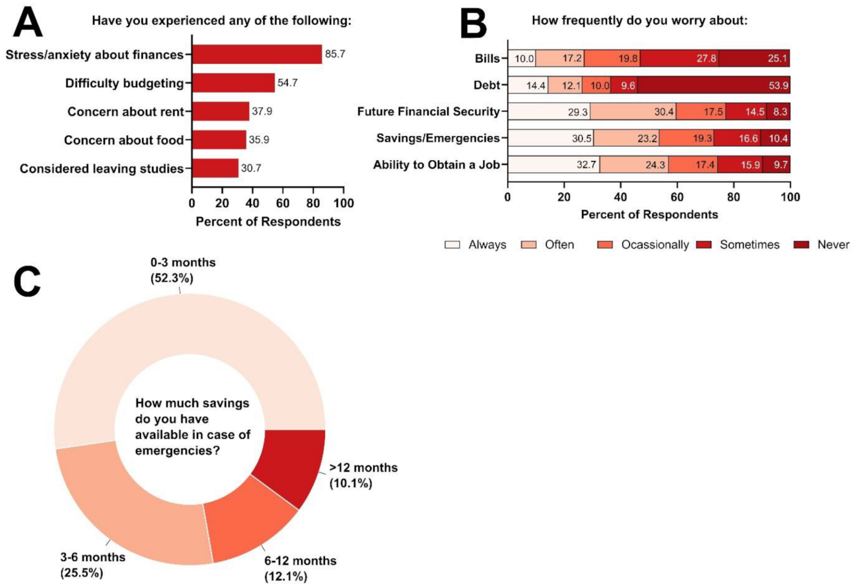

Figure AW.5: Financial stressors. (A) Concerns and stress experienced by respondents (multiple selections possible) by % ($n = 1178$). (B) Respondents were asked how frequently they worry about their ability to obtain a future job in their chosen field, savings/ability to pay for emergency expenses, future financial security, ability to pay back their student debt, and ability to pay bills. Data are shown by % in each category ($n = 1305$). (C) Amount of savings, measured by months of living expenses, that respondents have available for emergencies, by % ($n = 1264$).

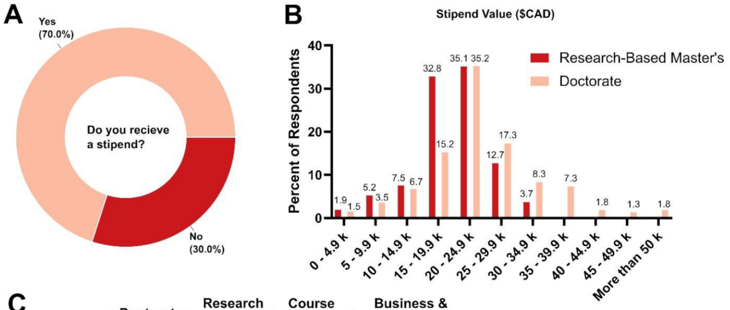

C

	Doctorate	Research Master's	Course Master's	Business & Professional
Average	$23,749.68	$19,724.69	$16,812.63	$13,113.19
Standard Deviation	$9,024.50	$6,065.99	$12,144.30	$5,983.74
Median	$22,000.00	$20,000.00	$13,000.00	$13,577.00

Figure AW.6: Stipend status. (A) Respondents were asked whether they received a stipend, by % ($n = 1305$). (B) Stipend value of respondents in research-based master's ($n = 268$) or doctorate ($n = 600$) studies. Data are shown by the % of students in the respective level of study. (C) Average and median stipend value of respondents in research-based master's ($n = 268$), course-based master's ($n = 19$), business or professional master's ($n = 21$), or doctorate ($n = 600$) studies.

Stipends

Funding for graduate students in Canada is complex as it comes from various sources and is regulated on multiple levels. While some universities set minimum funding levels for student stipends, this can vary greatly between departments and even faculty within a university.

Over 70% of respondents declared that they received a stipend (Figure AW.6A).

The average stipend reported was $23,750 for doctoral students, $19,725 for research-based master's students, $16,813 for course-based master's students, and $13,113 for business and professional master's students (Figure AW.6B). If we consider the context of a typical 40h work week, this becomes an average hourly pay of $9.18/h for a master's student and $11.43/h for a PhD student. This is well below the $15/h minimum wage implemented by the federal government [156] and does not account for the many graduate students who work over the average 40h standard.

When asked about their ideal stipend values, respondents reported an average of $33,619 for doctoral students, $29,213 for research-based master's students, $26,912 for course-based master's students, and $22,705 for business and

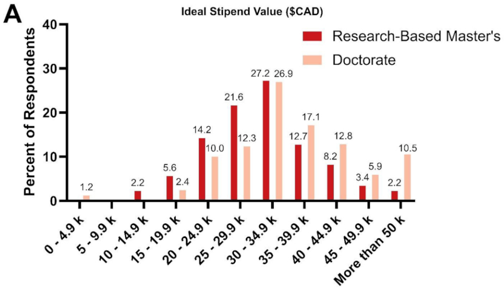

B

	Doctorate	Research Master's	Course Master's	Business & Professional
Average	$33,619.16	$29,212.93	$26,911.76	$22,704.76
Standard Deviation	$10,525.67	$11,046.15	$12,535.24	$21,661.38
Median	$32,000.00	$30,000.00	$24,000.00	$20,000.00

Figure AW.7: Ideal stipend. (A) The ideal stipend value shared by respondents in research-based master's ($n = 267$) or doctorate ($n = 592$) studies who responded "yes" to receiving a stipend. Data are shown by the % of students in the respective level of study. (B) Average and median of ideal stipend value of respondents in research-based master's ($n = 267$), course-based master's ($n = 17$), business or professional master's ($n = 21$), or doctorate ($n = 592$) studies.

professional master's students (Figure AW.7). The SPE's Rethinking Federal Research Funding Report found that respondents' ideal value of federal scholarships was $21,000 for a master's student and $35,000 for a PhD student [149]. In our results, master's students reported a much higher ideal stipend value compared to their current average funding, which puts them well below the poverty line [157]. Further, the ideal value of $21,000 from the SPE survey would still fall below the poverty line in the vast majority of the country.

We asked respondents to share the source of their stipend. The majority of respondents (67%) were funded through their supervisor (Figure AW.8A). Less than half (45.2%) were funded from their department/faculty. While national and provincial awards exist, only 20% were funded through federal awards, and 11.5% of respondents were funded through provincial awards. Most respondents (77%) reported only having 1–2 funding sources (Figure AW.8D). The length of funding also varied from under 6 months to 4 years (Figure AW.8C).

Scholarships

In Canada, awards are granted to students who display a high level of academic achievement and are intended to encourage graduate students to dedicate more time to their studies. The awards are primarily distributed by three federal research funding groups: the NSERC, the SSHRC, and the CIHR, which together

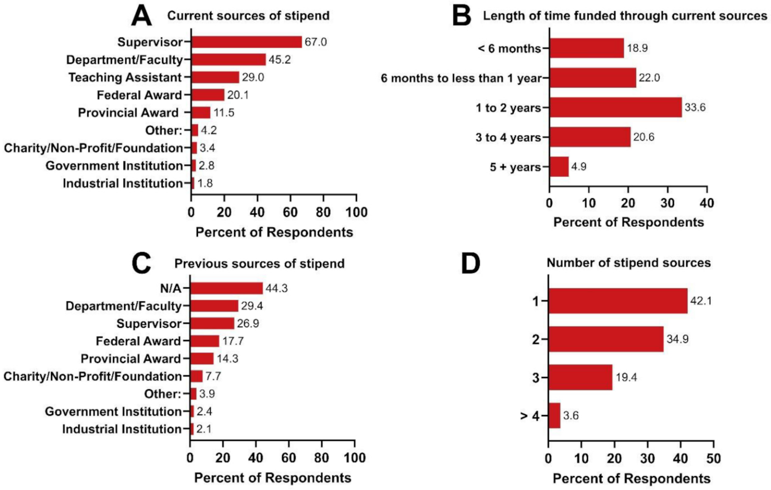

Figure AW.8: Stipend sources. (A) Current sources of stipend of respondents (multiple selections possible) (n = 914). Other includes institutional scholarships, research assistantships, and university scholarships. (B) Length of time funded through current sources of stipend (n = 914). (C) Previous sources of stipend, not including current stipend sources (multiple selections possible) (n = 914). Other includes Mitacs and institutional scholarships. (D) Number of current stipend sources (n = 914). Data are shown by percentage.

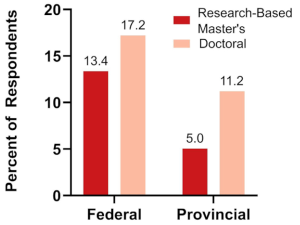

Figure AW.9: Federal and provincial award holders. Percent of respondents who have received an award based on level of study: research-based master's ($n = 337$) and doctoral ($n = 750$). Award-holder status is defined as being selected to receive a federal or provincial award. This does not include any other awards that were indicated (admission scholarships, institutional scholarships, etc.).

form the Tri-Councils Agency. In addition to federal research awards, there are also provincial awards for graduate students.

Of 1305 survey respondents, 17.2% of doctoral and 13.4% of research-based master's students reported receiving a federal award, while 11.2% of doctoral and 5.0% of research-based master's students reported receiving a provincial award (Figure AW.9).

When asked to describe their current financial situation, award holders were less than half as likely to respond as "struggling" and more than twice as likely to respond as "comfortable" compared to non-award holders, a significant difference at the $P < 10^{-5}$ level (χ^2 test) (Figure AW.10). Overall, 48.4% of non-award holders and 38% of award holders responded as either "struggling" or "tight" to describe their current financial situation. These survey findings are not surprising, considering that awards can help guarantee an income for graduate students that may or may not be provided to non-awardees.

Gender and Ethnic Identity

Diversity is essential among graduate students to foster generations of scientists with diverse perspectives and ideas. This will be vital to innovation as we tackle future challenges in society. Per the Dimensions charter: "equity, diversity and inclusion strengthen the research community, the quality, relevance and impact of research, and the opportunities for the full pool of potential participants." [158].

Despite the presence and increasing prevalence of diverse groups, women, Indigenous peoples, and visible minorities still face inequities and barriers to inclusion in graduate programs, including lack of representation among those

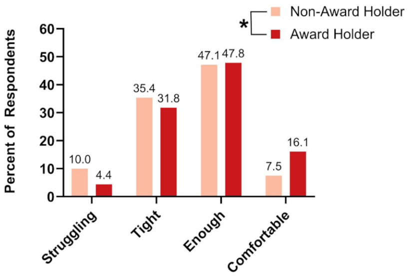

Figure AW.10: Financial situation by award holder status. Financial situation of non-award holder ($n = 1031$) and award holder ($n = 274$) respondents. Data are shown by the % of respective award statuses. Award holder status is defined as being selected to receive a federal or provincial award. This does not include any other awards that were indicated (admission scholarships, institutional scholarships, etc.). $^{*}P < 0.05, \chi^2$ test (award holder vs. non-award holder).

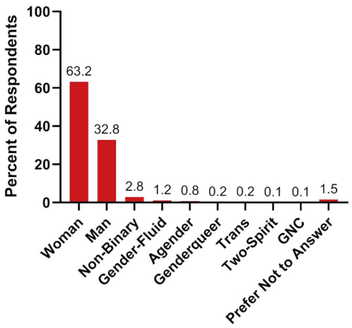

Figure AW.11: Gender identity. Gender identity of all respondents by % ($n = 1305$) (multiple selections possible). Definitions are located in Supplementary file. GNC, gender non-conforming.

who receive federal doctoral and master's level scholarships [159]. Additionally, it has been found that those who identified as women, visible minorities, individuals with disabilities, and Indigenous were all less likely to receive research funding [160]. Factors such as eligibility, duration of awards, and evaluation criteria are significant barriers to promoting equity, diversity, and inclusion (EDI) in graduate programs.

Women composed the majority of the survey sample (63.2%), followed by men (32.8%) and respondents who identified as non-binary, gender-fluid, agender, genderqueer, trans, two-spirit, or gender non-conforming (4.0%) (Figure AW.11). There were no significant differences in average stipend values among gender groups (KW test, $P = 0.78$) (Figure AW.12).

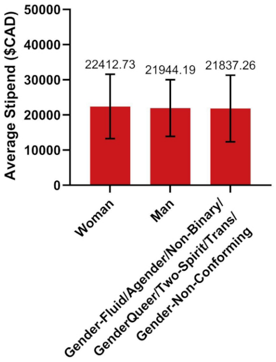

Figure AW.12: Average stipend by gender identity. Average stipend value of respondents by their gender identity: woman ($n = 547$), men ($n = 328$), and gender-fluid/agender/non-binary/genderqueer/two-spirit/trans/gender non-conforming ($n = 37$). Bars represent mean±SD.

Respondents largely identified as White (66.5%) (Figure AW.13). No significant differences in average stipend values were found for domestic students (KW test, $P = 0.35$) (Figure AW.14). There were significant differences (χ^2 test, $P = 0.043$) in the reported level of financial struggle of domestic students with Black, Latin American, Middle Eastern, and South Asian students more likely to report struggling or feeling tight financially than East Asian, Southeast Asian, or White students (Figure AW.15). Among international students, there were also significant differences (χ^2 test, $P = 1.7 \times 10{-}4$), with Middle Eastern, South Asian, and Southeast Asian (not shown in the figure due to small sample size) students reporting financial struggle at a much higher rate. The discrepancy between the financial stress of domestic and international Southeast Asian students may be due to a small sample (with only 17 students and 11 international students).

International Students

International students composed 21% of master's and 37% of doctoral students in Canada, with this proportion rising to nearly 50% for those studying in STEM [161]. This is comparable to the 31.6% of survey respondents to our survey who were international students.

International students can face additional challenges compared to domestic students, such as legal limits on the number of hours they can work off campus, which has recently been suspended until the end of 2023 [162], ineligibility for most Canadian government scholarships, as well as other struggles.

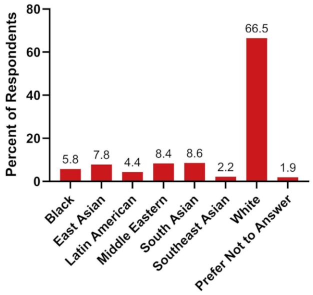

Figure AW.13: Ethnic identity. The % of respondents reporting selected ethnic identity (multiple selections possible) ($n = 1300$).

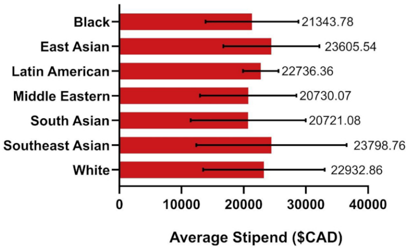

Figure AW.14: Average stipend by ethnic identity. Average stipend value of domestic student respondents by their ethnic identity: Black ($n = 23$), East Asian ($n = 54$), Latin American ($n = 11$), Middle Eastern ($n = 29$), South Asian ($n = 36$), Southeast Asian ($n = 11$), and White ($n = 415$).

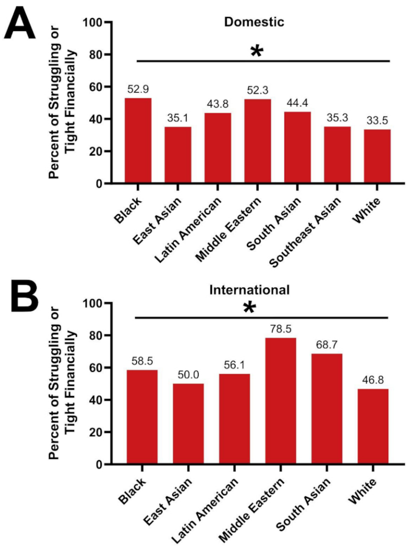

Figure AW.15: Financial situation by ethnic identity. (A) The financial situation of domestic student respondents by their ethnic identity: Black ($n = 34$), East Asian ($n = 74$), Latin American ($n = 16$), Middle Eastern ($n = 44$), South Asian ($n = 45$), Southeast Asian ($n = 17$), White ($n = 695$). (B) The financial situation of international student respondents by their ethnic identity: Black ($n = 41$), East Asian ($n = 28$), Latin American ($n = 41$), Middle Eastern ($n = 65$), South Asian ($n = 67$), White ($n = 173$). Southeast Asian excluded due to too few responses. Tight/struggling responses were combined to ensure more than five responses in the grouped categories. $^*P < 0.05, \chi^2$ test.

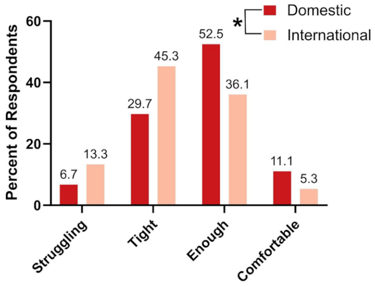

Figure AW.16: Financial situation of domestic and international students. The % of respondents who are struggling financially and often do not have enough to make ends meet (struggling); every month is tight and often making sacrifices to pay for necessities (tight); have enough and are able to afford to provide for themselves (enough); or very comfortable and can spend as they like (comfortable), separated by domestic ($n = 892$) and international ($n = 413$) students. $^{*}P < 0.05, \chi^2$ test (domestic vs. international).

International students were found to be significantly (χ^2 test, $P < 10^{-5}$) more likely to report that they are "struggling" to make ends meet or that their finances are "tight," with over 50% falling into these categories (Figure AW.16). Concerns over one's ability to pay for bills, financial security, and emergency expenses were also significantly higher (χ^2 test, P values of $< 10^{-5}$, 0.002, and $< 10^{-5}$, respectively). The survey reported 44% of international students were "always worried" about their ability to pay for emergency expenses compared to 24% of domestic students (Figure AW.17).

Far fewer international student respondents indicated receiving stipends larger than $27,000 compared to domestic students, which may be due to the lack of access to federal scholarships (Figure AW.18).

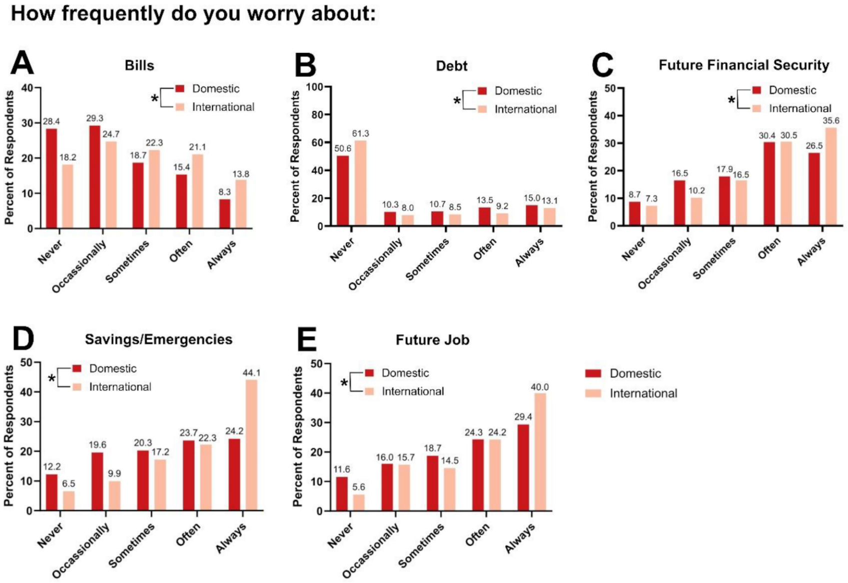

Figure AW.17: Financial stresses of domestic and international students. The response for domestic ($n = 892$) and international ($n = 413$) students on how frequently they worry about their (A) ability to pay bills, (B) ability to pay back their student debt, (C) future financial security, (D) savings/ability to pay for emergency expenses, and (E) ability to obtain a future job in their chosen field. Data are shown by % in each category. $^*P < 0.05, \chi^2$ test (domestic vs. international).

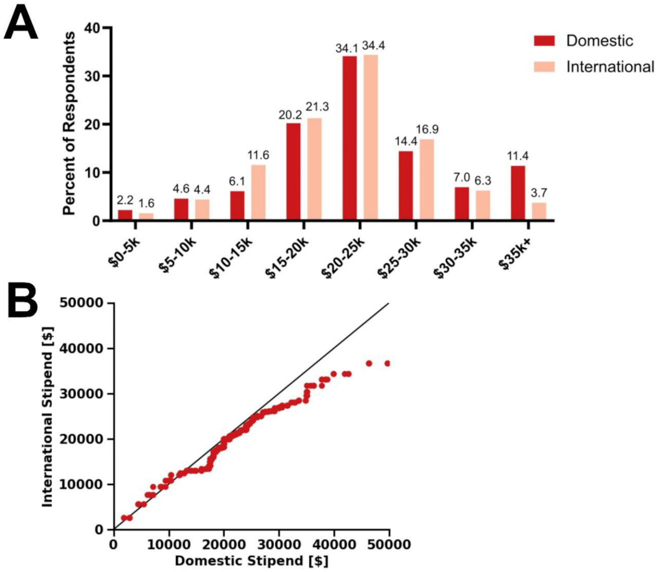

Figure AW.18: Stipend levels of domestic and international students. The annual stipend received by domestic ($n = 589$) vs. international ($n = 320$) student respondents. (A) The percentage of respondents in each category who receive a stipend of this amount. (B) A QQ-plot (binned into groups of five to maintain de-identification) showing how the distribution of stipends for domestic and international students differ. A QQ-plot is such that the same quantile for each data set is plotted against each other (e.g., the 5th percentile of both distributions is one point). If the two distributions were the same they would follow the line indicated.

Conclusions

We propose six recommendations to better support graduate students and enable them to more fully focus on research.

1. Increase federal funding (through the Tri-Councils) for graduate students in the form of research grants and scholarships.
2. Implement a standard for stipends in Canada and establish transparency practices for university departments.
3. Expand the eligibility of Tri-Council graduate student scholarships to help provide better funding for international students and underrepresented groups.
4. Index and evaluate graduate student funding on a regular basis to ensure the sustainability of research infrastructure in Canada.
5. Remove limits on work outside of studies for graduate students.
6. Further investigate the role of EDI factors in financial struggle.

Canadian Science Graduate Stipends Lie Below the Poverty Line[†]

This paper [163] presents the minimum stipend levels and tuition fees for all university graduate programs in Canada in Ecological Sciences/Biology and Physics, along with cost of living measures for the cities in which they reside. We show Canadian minimum stipends are at values almost exclusively below the poverty threshold. Only two of 140 degree programs offered stipends which meet cost of living measures after subtracting tuition and fees. For graduate programs which offered a minimum guaranteed stipend, the average minimum domestic stipend is short ∼Can$9,584 (international ∼Can$16,953) of the poverty threshold after accounting for payment of tuition and fees. While international comparison is difficult, the highest Canadian minimum stipend is roughly equivalent or lower than the lowest stipend within the largest dataset of United States of America (US) Biology stipends [164], and lower than the United Kingdom (UK) stipend. University endowment correlates with minimum stipend amount but intra- and inter-institutional differences suggest it is not solely institutional wealth which improves graduate pay.

An abridged version of this paper is presented in this section. Figures AW.19 and AW.20 and all the text in this section are reproduced from Fraass et al. [163] under a CC BY 4.0 license.

Introduction

The following is a general description of the financial model of Canadian graduate studies in natural science: stipends provide financial assistance to students for living expenses (e.g., tuition, rent), as opposed to financial support for the costs associated with the research itself (e.g., reagents, equipment) [165]. Graduate students in Canada pay tuition and fees to their institution; waivers are rarely provided. When a stipend is provided, tuition and fees are paid by the student to their institution using their stipend, which itself was previously paid by the institution to the student.

Departments or equivalent academic units frequently set minimum stipend levels but individual principal investigators (PIs) can choose to exceed that amount. Stipends are typically funded from multiple sources: the institution

---

[†] This work was done in collaboration with Andrew Fraass, Kayona Karunakumar and Andrea Wishart. As joint first author, I contributed to conceptualization, project administration, project design, data and code management, data collection, analysis and writing. I contributed equally with Andrew Fraass and Andrea Wishart.

(e.g., faculty of graduate studies provides the department funds based on number of students in their programs), a PI's research grants (see below), student awards, and/or teaching assistantships. TAships are frequently a core part of funding packages, with the pay earned from this job (which can be on the order of \$3-6k/term) often included in the value of the minimum stipend.

The Natural Sciences and Engineering Research Council of Canada (NSERC) Discovery Grant (DG) is a 5-year operating grant awarded to individual PIs and the foundation of most academic Canadian natural science graduate funding and research. Grant applications are judged evenly across three categories: a record of past research, highly qualified personnel (HQP; students, postdocs, and other mentees) produced by the researcher, and a proposed project [166]. Quality mentorship is therefore paramount in acquiring funding. Policy requires NSERC panels to not judge a researcher based on the number of HQP [166]; rather, applicants are judged on mentorship quality, post-mentorship careers, and so on. However, an incentive still remains to have more students, as publications and citations correlate positively with the number of HQP [167]. This pressure to train a large number of students with the relatively small operating grants may contribute to the suppression of stipend minimum support.

As a case study, we examined whether the guaranteed minimum stipends for graduate students in Physics and Ecological Sciences/Biology are a) enough to live on, b) comparable between programs and fields, c) related to the financial size of universities, and d) similar with those in two peer nations (US and UK).

Results

Accessibility

Determining accurate annual stipends was difficult, despite two of four authors possessing PhDs. It was rare for tuition and fees to be displayed in logical and easily interpretable ways. For example, most institutions split fees into different categories (e.g., bus pass, graduate association fees), but they commonly use different units of time to display each: some fees appeared per term, some per year, some per credit, while others had different values during fall, winter, and summer or for part-time vs. full-time students, and so on. This complexity made it extremely easy to make simple errors due to the number of parameters and unclear language/presentation. Many institutions include certain fees (e.g., healthcare) on their fee lists, others do not. Furthermore, several institutions put dollar amounts behind several menus and/or 'opt-out/opt-in' paperwork, or even private intranet pages.

Whatever the factors contributing to low discoverability and transparency in tuition and stipend data may be, the impact is obfuscated financial information prior to being enrolled in a program. A solution for these issues would be to have a "Finances" page clearly indicated on department websites, with a table laying out common funding scenarios, minimum stipends, durations, costs, and how much of the stipend is left after fees and tuition. A department that models this well is the University of British Columbia Physics Department website (`https://web.archive.org/web/20240501083537/https://phas.ubc.ca/graduate-program-financial-support`).

Stipend Amounts

We collected tuition, fee, and stipend data from public-facing program and/or university websites for both domestic and international MSc and PhD students. We focus our main analysis on domestic students due to the complexity and uncertainty around much of the international student data that was available.

Data analysis was performed in R (v. 4.4.0 [168]). All code and data are publicly archived on GitHub (`https://github.com/UVicMicropaleo/Canadian-Minimum-Graduate-Stipends`). We defined Gross Minimum Stipend (GMS) as the minimum annual stipend, Net Minimum Stipend (NMS) as the minimum annual stipend after both tuition and fees are repaid to the institution, and MBM Shortfall as NMS minus the inflation-adjusted Market Basket Measure poverty threshold (MBM), for a single individual with no dependents assessed by Statistics Canada [169]. The dataset contains 140 programs from 38 institutions. We found 95 programs providing a guaranteed minimum stipend, while 21 programs provide no minimum stipend. We could not identify minimums and received no response to email requests from 24 programs. Only considering departments which guarantee support, the mean domestic GMS in Canada is Can\$23,933, and mean NMS is Can\$16,528 (Figure AW.19). An average program with a minimum stipend charges Can\$7,585 in tuition and fees to domestic graduate students, with a mean ~33% (range: 18% - 61%) of the GMS repaid to their institution.

We compared stipend values to the governmental (MBM threshold [169], Figure AW.19). Only two programs (University of Toronto Physics PhD and MSc) appear to have domestic net minimum stipends which reached MBM thresholds, though these were estimated as fees were hidden behind an intranet page. The average department would need to raise their guaranteed minimum stipend by ~Can\$9,584 for domestic students and ~Can\$16,953 for international students to reach the MBM threshold.

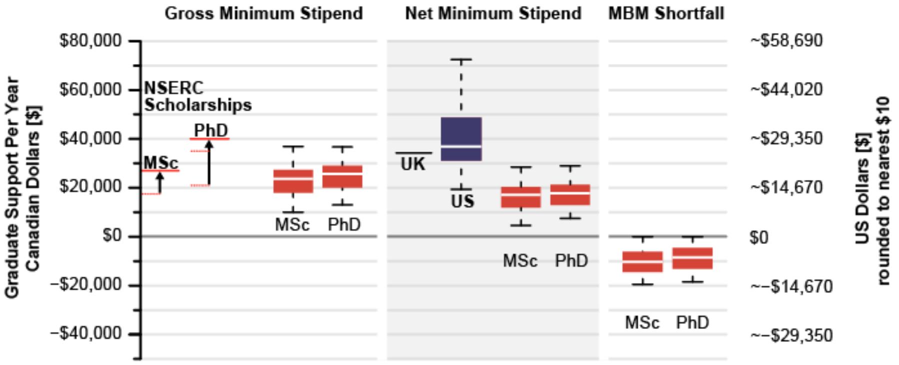

Figure AW.19: Annual financial support in Canadian and US dollars to graduate students (MSc and PhD in physics and biology). Red lines correspond to recently increased federal NSERC scholarships. Gross Minimum Stipend (GMS) is the guaranteed minimum funding for an MSc or PhD student provided by the institution. Net Minimum Stipend (NMS) is the GMS minus tuition and fees for an institution. MBM Shortfall is the NMS minus the Market Basket Measure (MBM), a poverty threshold, for an institution's location. US Biology stipends are from [164] and should be considered a rough approximation of the US stipends, without accounting for fees or taxes (see text).

NMS best demonstrates the disparity between Canadian, US [170–172], and UK stipends for PhD students (Figure AW.19a) as tuition waivers are normally included for US or UK graduate studies. Notably, US data [164] (n=215) is considerable, but not exhaustive, while the UK funding agency sets a single national stipend level. It is difficult to reasonably compare various indices of poverty in an unbiased way across national borders. Poverty metrics generated by different governments vary due to numerous factors (e.g., national and regional differences, political impacts of declaring a 'line of poverty'). Further, the non-TA portion of Canadian stipends are untaxed while US stipends are taxed. US stipend data from [164] do not include ancillary fees, though it is extremely unlikely that fees or taxes are enough to erase the Can$23,759/yr difference between the means of the two countries (eg. the federal tax on a US$37k stipend for a single person would be around US$2,500). This difference is essentially the same as the mean GMS, suggesting in order to compete with the US or UK Canadian stipends would need to double, compared to only increasing by ∼1.5 times to meet the cost of living.

To identify if net stipend is driven by available institutional funding, we compared NMS against each university's endowment (n = 26 universities with

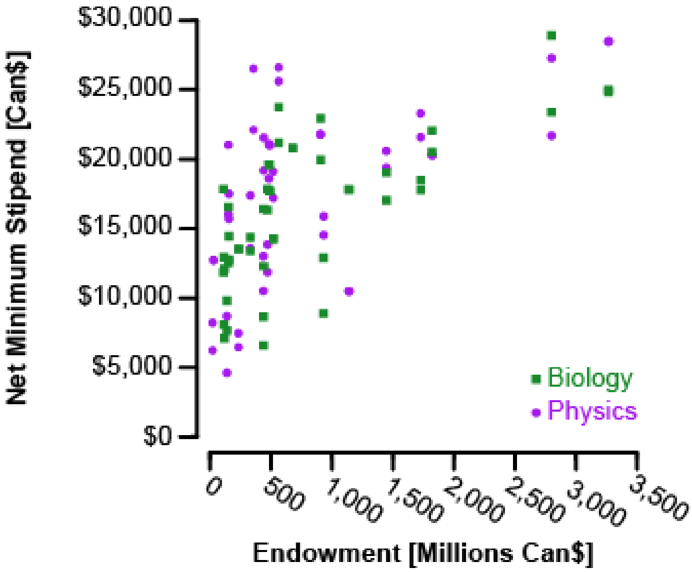

Figure AW.20: Net minimum stipends in Canadian dollars to MSc and PhD graduate students in biology (green squares) and physics (purple circles) in relation to their institution's endowment in millions of Canadian dollars.

n=80 programs; Figure AW.20). We fit a generalized linear mixed model (package lme4 v.1.1.26 [173]) with university endowment (log10 transformed due to skewness of raw data), program (MSc or PhD), and field (Biology or Physics) as fixed effects, and university nested within province as a random effect because postsecondary funding falls within provincial jurisdiction. Endowment accounts for significant variation in NMS, suggesting a larger endowment generally results in higher stipends. We see similar effects when considering total expenses rather than endowment, suggesting that this is an effect predominantly of financial size of the institution rather than specific use of endowments (although these parameters are highly correlated with larger institutions generally having larger endowments). Yet, substantial residual variation remains, even with accounting for variation across program and field within provinces (e.g., Ontario and Quebec demonstrate inter-institutional variation). Variation in stipends may result from a number of processes; e.g., different levels of support allocated to departments from the institution, different departmental budget priorities, or perhaps lagged responses to the increased expenses faced by students.

All analysis here is based on minimum stipend levels. Many graduate students do receive stipends higher than these levels, e.g. via top-ups from PI grants, additional TA hours, or external scholarships such as NSERC doctoral awards. However, the distribution of actual stipend values awarded is not publicly available and would require departments to report all stipend values, rather than simply department policies around guaranteed minimums (when they exist). Nevertheless, like minimum wage, minimum stipends are important to consider because they represent a lower bound that at least some graduate students experience. The purpose of setting a minimum is to ensure that all students receive financial support to enable them to focus on their studies without needing to seek employment elsewhere. If this is no longer being satisfied then the minimum level must be adjusted. Our mean/median minimum stipend levels are very similar to results from a recent survey [143], suggesting many students are, or are close to, receiving their departments minimum stipend.

Conclusions

The complexity and opaque nature of the Canadian graduate funding system is likely to be unclear to potential graduate students evaluating program options. This is exacerbated by a lack of transparency around stipends and tuition at institutional and departmental levels, making comparison between departments difficult, along with other potential consequences (for example possibly posing a further barrier to recruiting underrepresented students [174]). It also, given the dissimilarity with other similar nations, makes it incredibly challenging for international students to make informed decisions due to the overly-complex nature of Canadian tuition and fee structures. While individual departments are unable to transform this system, they can improve their own transparency to allow for more informed choices by future graduate students.

Canadian and foreign students receiving the observed minimum stipend levels are poised to incur substantial debt to undertake graduate education, unless otherwise wealthy. This presents a series of problems; for example: equity, incurred health costs of poverty on the next generation of scientists, and the breadth of scientific inquiry [175]. Students would benefit from significant changes at whatever level is possible [176]. Governments have the ability to tweak aspects or alter the entire national system at once. However, within the current Canadian system, institutions, departments, or individual PIs can adjust minimum stipend levels. There is ample anecdotal evidence that this is already occurring at least at the departmental level, as several departments had increased stipends while we were performing quality control checks on our data. That minimum stipends are low, however, suggests that individual departments probably cannot do this on their own, and may require assistance from institutions and/or government.

It is clear that Canada is behind competing countries when it comes to funding the next generation of scientists. Canadians who desire higher STEM education have three options: hope for significantly higher guaranteed support from a supervisor, department, or awards; incur substantial debts; or emigrate.

Graduate students, both in Canada and around the world, help drive academic advances in science [148]. Providing adequate financial support to these researchers enables this work to be done most effectively and boosts the ability of the entire scientific community to make progress. Not providing adequate support is damaging [177]. How best to provide this support is a global challenge, with countries offering a range of different systems and amounts. Regardless of the financial model offered, there is a potential for participation in science and innovation to be reduced when junior scientists are expected to live below the poverty line.

International Mobility of Canadian Graduate Students: An Investigation Into Brain Drain[‡]

This report [178] presents survey data from current and recent graduate students who studied in Canada on their likelihood and reasons for looking to remain in or to leave Canada. It was met with significant interest in the Canadian science and research advocacy community and I was invited to give a presentation on our findings at Research Canada's annual stakeholder action roundtable.

An abridged version of this report is presented in this section. Figures AW.21 to AW.24; Tables AW.1 and AW.2; and all text of this section are reproduced from Ottawa Science Policy Network's *International Mobility of Canadian Graduate Students* [178] under a CC BY 4.0 license.

Introduction

The term 'brain drain' refers to the permanent outflow of highly educated and skilled individuals such as researchers, technologists, and experts, out of the country in pursuit of better opportunities abroad. Historically, this phenomenon has led to a loss of intellectual and human capital exerting a profound influence on the nation's workforce, impeding economic growth, and directly shaping the innovation landscape.

In the contemporary landscape of Canada's intellectual and economic growth, graduate students play a pivotal role. While working as graduate students they perform much of academic research - working closely with professors and other more senior researchers to push the frontier of human knowledge. Once completing these programs these highly qualified personnel may continue in academia as a postdoctoral scholar or move into the wider economy bringing their skills and expertise with them.

Their commitment to research and development not only fuels economic growth but also spawns novel enterprises, generates employment opportunities, and elevates productivity [148]. Notably, Canada's rich history of impactful innovations, exemplified by discoveries like insulin, underscores the importance of Canadian research and discovery in shaping the nation's identity and global influence.

[‡] This work was done in collaboration with Stephen Holland, Mercedes Rose, Sarah Laframboise, Alexa D'Addario, Keaton Sinclair and Mariam Hakoum at the Ottawa Science Policy Network. As first author, I contributed to conceptualization, project administration, project design, data and code management, data collection, analysis and writing.

In this survey conducted by the Ottawa Science Policy Network, we delve into the dynamics surrounding the departure of graduate students from Canada. We explore the motivations driving their decisions to leave, with a specific focus on the impact of financial considerations and the role of scholarships. Additionally, we consider the plans and reasoning of international students, offering a comparative lens to improve our understanding. As our investigation extends beyond national borders, we provide a global context, shedding light on where these departing students are heading and international comparisons of remuneration for academic researchers.

Results

Survey Demographics

Our survey received a total of 582 responses, comprised of 411 students currently enrolled in a graduate program at a Canadian university, and 171 respondents who recently (within the past 10 years) completed a graduate program at a Canadian university. Of the current students, 293 are enrolled in a PhD program and 116 in a Masters program and 26% are international students. Of the recent graduates, the majority (60%) graduated between the years of 2020-2023. Entering the workforce was the most common position currently held by recent graduates (42%), followed by postdoctoral scholar (35%) and faculty/teaching positions (17%). For both recent graduates and current students, life sciences was the most common field of study (39%) followed by medical sciences (24%), physical sciences (23%), social sciences (8%), computer sciences (3%) and arts and humanities (3%).

Intent to Leave

A substantial portion of respondents either have left or are considering leaving Canada (Figure AW.21). Of students currently enrolled in a graduate program, 64% indicated they were likely or very likely to leave Canada following completion of their degree. 36% of recent graduates have left Canada following their degree, 15% intend to leave Canada, and 49% do not intend to leave Canada. The proportion of those reporting a desire to leave or who have already left are likely to be somewhat elevated due to a response bias to this survey, however they do indicate that large numbers of graduate students and those who have completed graduate studies are seriously considering moving away from Canada.

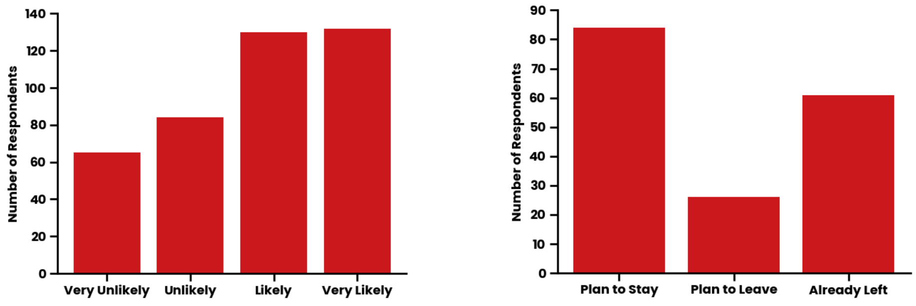

(a) (b)

Figure AW.21: Likelihood of graduate students to leave Canada. A) The proportion of current graduate students reporting their likelihood of leaving Canada following completion of their degree. B) The proportion of recent graduates by whether they have left or intend to leave Canada.

Factors for Leaving

What drives so many graduate students to look beyond Canada for their futures? A key part of this survey was to determine which factors graduate students were most concerned about and had the biggest effect on their career choices. Survey respondents were asked to score from 1-5 (1 being the least important, 5 being the most important) the extent to which various factors influenced their decision to leave or stay in Canada (Figure AW.22).

Between those likely to leave and those unlikely to leave, the former scored "Available Opportunities/Jobs", "Finances/Salary", and "Infrastructure/Facilities" the highest. Conversely, those unlikely to leave Canada rated all other factors more highly, with the largest differences in scoring being "Family/Friends", "Significant Other", and "Healthcare". The factor "Available Opportunities/Jobs" was scored highest on average, while "Prestige" was the lowest average score overall.

This suggests that those graduate students who leave are incentivised towards financial stability and academic institutional reputation more than any other listed factor. By contrast, those who stay are driven mainly by their social connections with partners, families, and friends.

Those patterns remain when considering those who have recently completed graduate studies. Those who have left Canada or plan to do so both scored "Available Opportunities/Jobs" and "Finances/Salary" higher on average than other factors, whereas the highest-scored factors on average were "Significant Other", "Healthcare", and Family/Friends" for those planning to stay in Canada

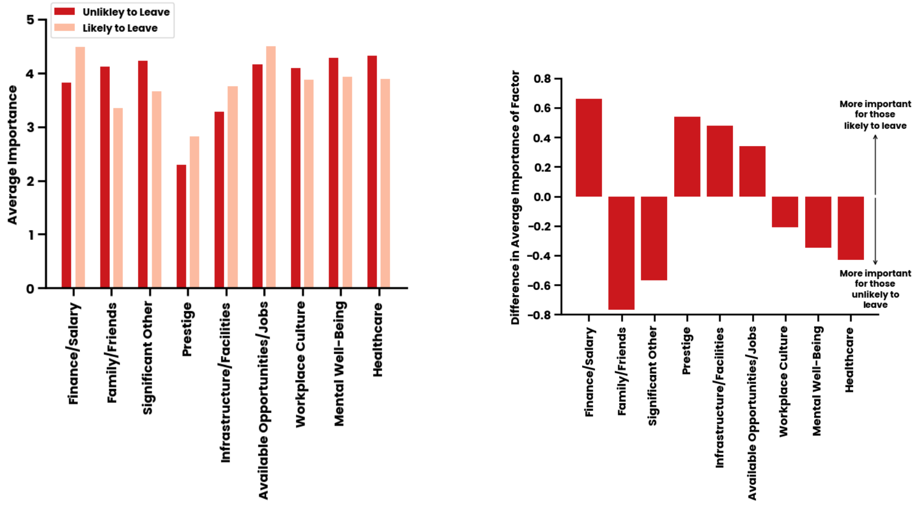

(a) (b)

Figure AW.22: Importance of various factors in graduate student decisions to leave or stay in Canada. A) Average importance and B) the difference in average importance between those two groups. Factors were scored on a scale of 1-5, where a score of 1 was unimportant and 5 was very important. Responses of “likely” and “very likely” were grouped together, as were “unlikely” and “very unlikely”. For each factor except “Workplace Culture”, the difference in average score between “leaving” and “staying” groups was significant.

Left	Planning to Leave	Planning to Remain
Available Opportunities/Jobs (4.6)	Available Opportunities/Jobs (4.7)	Significant Other (4.5)
Finances/Salary (4.3)	Finances/Salary (4.6)	Healthcare (4.1)
Infrastructure/Facilities (3.6)	Mental Well Being (4.4)	Family/Friends (4.1)

Table AW.1: he three highest-scored factors (on average) by recent graduates current status in Canada.

Woman	Man	Agender/Gender-Fluid/Non-Binary
Available Opportunities/Jobs (4.3)	Available Opportunities/Jobs (4.5)	Healthcare (4.1)
Healthcare (4.2)	Finances/Salary (4.4)	Mental Well Being (4.1)
Mental Well Being (4.2)	Workplace Culture (3.8)	Available Opportunities (4.0)

Table AW.2: The three highest-scored factors (on average) by graduate students' self-declared gender, categorised as "Woman", "Man", "Agender", "Gender-Fluid", and/or "Non-Binary".

(Table AW.1).

Interestingly, the gender of the survey respondents appeared to also have an influence on which three factors scored highest (Table AW.2). Respondents from all categories valued "Available Opportunities/Jobs" highly, but respondents self- identifying as women or agender/non-binary/gender-fluid both valued "Healthcare" and "Mental Well-Being" higher than other factors. Men scored "Finances/Salary" on average higher than any other gender, which suggests that they are more willing or able to move abroad for the sake of financial stability and career opportunities.

Impact of Finances

Future financial stability was the most important decision factor incentivising students to consider leaving Canada following completion of their degree, as described in the previous section. To further understand the extent to which a

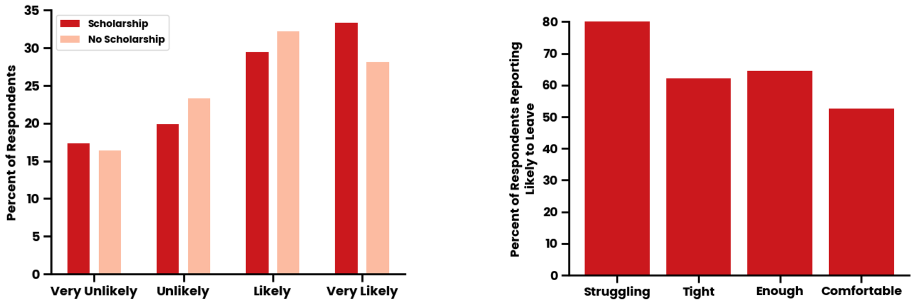

(a) Likelihood of current students considering leaving Canada by whether they hold a federal scholarship.

(b) Likelihood of current students considering leaving Canada by their reported level of financial struggle.

Figure AW.23: Impact of stipend values, scholarship values, and financial situation on likelihood to leave Canada. A) The likelihood of current students to consider leaving Canada by whether they hold a federal scholarship. B) The proportion of current students considering themselves Likely or Very Likely to leave Canada after completing their studies by their reported financial struggle.

student's current financial status plays a role in their decision to move outside Canada, we investigated the impact of self-reported salaries, stipends and scholarship status on the likelihood of leaving Canada following degree completion

Self-reported stipend values and scholarship status appeared to have no impact on the extent to which current students are considering leaving Canada post-graduation. Despite scholarship status not being associated with likelihood to leave (Figure **??**), student's level of reported financial struggle do have a significant correlation (Figure AW.23b; $p = 0.03$). Students who reported that they were struggling financially tended to be more likely to consider leaving Canada (80%) than those who reported being comfortable financially (53%).

Given the low value of stipends for Canadian graduate students [143] as well as low federal scholarship amounts at the time this survey was conducted ($17,500 for Master's students, $21,000 – $35,000 for PhD students) it's possible that lack of impact of stipend or scholarship status on likelihood to leave reflects an insufficiency of federal scholarships and current stipend values to prevent students from struggling financially and looking for international opportunities to find a better financial future.

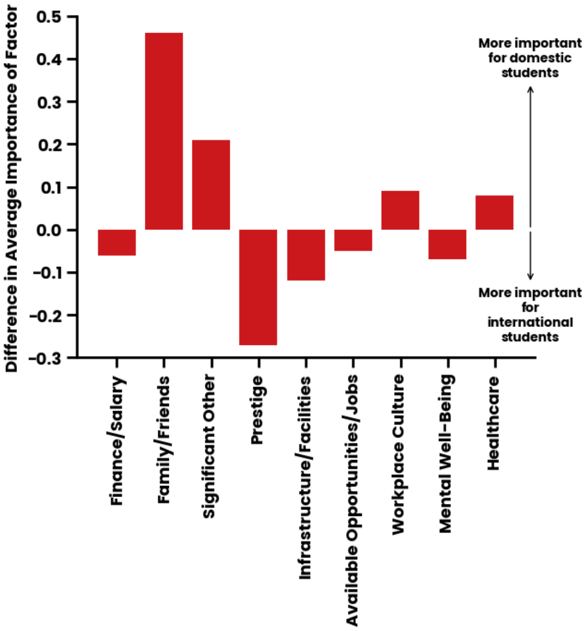

Figure AW.24: The difference in the average importance of factors on their decision to remain or leave Canada between Domestic and International students.

International Students

A greater proportion of international student respondents reported that they were considering moving to another country (65%) than remaining in Canada (53%) or returning to their home country (34%). In addition, upon comparison to domestic students, current international students are more likely to consider leaving Canada compared to domestic students (71% to 62%, respectively).

For international graduate students the most important factors in their decision to remain in or leave Canada were broadly similar to domestic students. However international students reported “Proximity to Family and Friends” as less important as compared with domestic students and placed a relatively higher value on “Prestige”. This can likely be explained due to international students moving away from family and friends to pursue their education, this was a choice made before enrolling and may then have less of an impact on whether they leave Canada after graduating (Figure AW.24).

International students are a vital part of the future economy, they bring aspirations and knowledge to sectors of the economy that are often overlooked. They choose Canada to start their academic career, opening up opportunities for them that they might not have access to from their home country. However, based on our data, international students are more likely to leave Canada than domestic students. So where do international graduate students go to pursue their career?

It appears that international graduate students are using Canada as a stepping stone for better opportunities elsewhere. Just like domestic students, international graduates are looking for better financial opportunities. Since Canada is lacking the necessary investment into research and development, both domestic and international students are looking for better financial well-being in their future career, but international students do not have the strong ties of friends and family to retain them in Canada.

Conclusions

The study's findings illuminate the key factors behind the international mobility of holders of Canadian graduate degrees, with the appeal of better financial support and job opportunities being the most prominent factors for why graduates are considering leaving Canada.

On the global stage, graduate students are considering immigrating to countries such as the United States, EU nations (such as Germany and Denmark), and the UK due to their consistent investment in research and development, better support for emerging researchers and a more diverse research intensive private sector.

For instance, Canadian graduates have historically favoured employment in the United States, where a typical PhD salary can range from Can$52,800 to Can$65,500, compared to Can$21,000 in Canada. Similarly, postdoc salaries in the US can range from Can$70,000 to Can$85,000, surpassing the Can$45,000 typically offered in Canada (before announcements in the federal budget 2024). This trend underscores the importance of addressing this financial discrepancy and improving Canada's appeal as a compelling destination through increased research investment and competitive financial incentives, ultimately retaining top-tier talent and mitigating brain drain.

However, our survey found that many respondents were at least open to the idea of returning to Canada, with the vast majority of current students considering themselves likely or very likely to return to Canada if they did leave and just over half of recent graduates who had left or were planning to leave reporting the same. This suggests that targeted programs to increase the opportunities in research in Canada could be effective (similar to the Canada

Research Chairs in the 1990s and early 2000s).

Those who have completed Canadian graduate programs are globally some of the best highly qualified personnel and could provide many of the skills that Canadian research, innovation and industry require. However, our survey suggests that Canada's lack of investment in R&D may be causing many of these people to look elsewhere for opportunities - which if unaddressed could lead to a large brain drain and harm to the Canadian economy and society.

In the realm of research and development, the departure of graduates poses a threat to the country's capabilities and global competitiveness. The solution lies in conducive policy changes that cultivate an environment where talented graduates find encouragement to anchor themselves within the Canadian landscape. A multifaceted approach, involving increased funding for research and development, fostering collaboration between diverse sectors, and promoting a seamless transition from academia to the workforce, is critical to stemming this brain drain.

Bibliography

[1] Jonathan P Dowling and Gerard J Milburn. “Quantum technology: the second quantum revolution”. In: *Philosophical Transactions of the Royal Society of London. Series A: Mathematical, Physical and Engineering Sciences* 361 (2003), pp. 1655–1674.

[2] David P. DiVincenzo. “The Physical Implementation of Quantum Computation”. In: *Fortschritte der Physik* 48.9-11 (2000), pp. 771–783.

[3] Bahaa E. A. Saleh and Malvin Carl Teich. *Fundamentals of Photonics*. John Wiley & Sons, Inc., 1991.

[4] Keisuke Goda and Bahram Jalali. “Dispersive Fourier transformation for fast continuous single-shot measurements”. In: *Nature Photonics* 7 (2013), pp. 102–112.

[5] Philippe Grangier, Juan Ariel Levenson, and Jean-Philippe Poizat. “Quantum non-demolition measurements in optics”. In: *Nature* 396 (1998), pp. 537–542.

[6] Gilles Nogues et al. “Seeing a single photon without destroying it”. In: *Nature* 400 (1999), pp. 239–242.

[7] Darrick E Chang, Vladan Vuletić, and Mikhail D Lukin. “Quantum nonlinear optics—photon by photon”. In: *Nature Photonics* 8 (2014), pp. 685–694.

[8] Robert W. Boyd. *Nonlinear Optics*. Fourth Edition. Academic Press, 2020.

[9] John Steinmetz. “Weak measurement: applications to quantum computing and parameter estimation”. PhD thesis. University of Rochester, 2023.

[10] R.L. Hudson. “When is the wigner quasi-probability density non-negative?” In: *Reports on Mathematical Physics* 6.2 (1974), pp. 249–252.

[11] Anatole Kenfack and Karol Życzkowski. “Negativity of the Wigner function as an indicator of non-classicality”. In: *Journal of Optics B: Quantum and Semiclassical Optics* 6.10 (2004), p. 396.

[12] Amit Devra et al. “Wigner state and process tomography on near-term quantum devices”. In: *Quantum Information Processing* 23.10 (2024), p. 359.

[13] Ryszard Horodecki et al. “Quantum entanglement”. In: *Rev. Mod. Phys.* 81 (2009), pp. 865–942.

[14] Víctor Zapatero et al. “Advances in device-independent quantum key distribution”. In: *npj quantum information* 9.1 (2023), p. 10.

[15] Howard M. Wiseman and Gerard J. Milburn. *Quantum Measurement and Control*. Cambridge University Press, 2009.

[16] Michael A. Nielsen and Isaac L. Chuang. *Quantum Computation and Quantum Information*. 10th Anniversary Edition. Cambridge University Press, 2010.

[17] Walther Gerlach and Otto Stern. “Der experimentelle Nachweis der Richtungsquantelung im Magnetfeld”. In: *Zeitschrift für Physik* 9 (1922), pp. 349–352.

[18] John von Neumann and Robert T. Beyer. *Mathematical Foundations of Quantum Mechanics: New Edition*. Princeton University Press, 2018.

[19] Ramamurti Shankar. *Principles of quantum mechanics*. 2nd ed. Springer, 2012.

[20] J. J. Sakurai and Jim Napolitano. *Modern Quantum Mechanics*. 3rd ed. Cambridge University Press, 2020.

[21] Yakir Aharonov, David Z. Albert, and Lev Vaidman. “How the result of a measurement of a component of the spin of a spin-1/2 particle can turn out to be 100”. In: *Phys. Rev. Lett.* 60 (1988), pp. 1351–1354.

[22] Jeff S Lundeen et al. “Direct measurement of the quantum wavefunction”. In: *Nature* 474 (2011), pp. 188–191.

[23] I. M. Duck, P. M. Stevenson, and E. C. G. Sudarshan. “The sense in which a ”weak measurement” of a spin-½ particle’s spin component yields a value 100”. In: *Phys. Rev. D* 40 (6 1989), pp. 2112–2117.

[24] A. J. Leggett. “Comment on “How the result of a measurement of a component of the spin of a spin-(1/2 particle can turn out to be 100””. In: *Phys. Rev. Lett.* 62 (19 1989), pp. 2325–2325.

[25] P. Ben Dixon et al. "Ultrasensitive Beam Deflection Measurement via Interferometric Weak Value Amplification". In: *Phys. Rev. Lett.* 102 (2009), p. 173601.

[26] Matin Hallaji et al. "Weak-value amplification of the nonlinear effect of a single photon". In: *Nature Physics* 13 (2017), pp. 540–544.

[27] Richard Jozsa. "Complex weak values in quantum measurement". In: *Phys. Rev. A* 76 (2007), p. 044103.

[28] Jeff S. Lundeen and Charles Bamber. "Procedure for Direct Measurement of General Quantum States Using Weak Measurement". In: *Phys. Rev. Lett.* 108 (2012), p. 070402.

[29] J. Dressel and A. N. Jordan. "Significance of the imaginary part of the weak value". In: *Phys. Rev. A* 85 (2012), p. 012107.

[30] Andrew N. Jordan, Julián Martínez-Rincón, and John C. Howell. "Technical Advantages for Weak-Value Amplification: When Less Is More". In: *Phys. Rev. X* 4 (2014), p. 011031.

[31] K. J. Resch and A. M. Steinberg. "Extracting Joint Weak Values with Local, Single-Particle Measurements". In: *Phys. Rev. Lett.* 92 (2004), p. 130402.

[32] K J Resch. "Practical weak measurement of multiparticle observables". In: *Journal of Optics B: Quantum and Semiclassical Optics* 6.11 (2004), p. 482.

[33] Robert B. Griffiths. *Quantum Channels, Kraus Operators, POVMs.* Accessed: 2024-12-06. (2012).

[34] Hayato Arai and Masahito Hayashi. *Quantum Implementation of Non-Positive-Operator-Valued Measurements in General Probabilistic Theories by Post-Selected POVMs.* (2024). arXiv: `2411.01873`.

[35] Christopher Gerry and Peter Knight. *Introductory Quantum Optics.* Cambridge: Cambridge University Press, 2004.

[36] C. Fabre and N. Treps. "Modes and states in quantum optics". In: *Rev. Mod. Phys.* 92 (2020), p. 035005.

[37] Andrew Forbes, ed. *Laser beam propagation: generation and propagation of customized light.* CRC Press, 2014.

[38] L Allen, Stephen M Barnett, and Miles J Padgett. *Optical Angular Momentum.* CRC Press, 2003.

[39] Rafael de la Madrid Modino. “Quantum mechanics in rigged Hilbert space language”. PhD thesis. University of Valladolid, 2001.

[40] Pericles S Theocaris and Emmanuel E Gdoutos. *Matrix Theory of Photoelasticity*. Springer, 1979.

[41] Rodney Loudon. *The Quantum Theory of Light*. Oxford University Press, 2000.

[42] DT Pegg and SM Barnett. “Phase properties of the quantized single-mode electromagnetic field”. In: *Physical Review A* 39 (1989), pp. 1665–1675.

[43] Leonard Susskind and Jonathan Glogower. “Quantum mechanical phase and time operator”. In: *Physics Physique Fizika* 1 (1964), pp. 49–61.

[44] P. Carruthers and Michael Martin Nieto. “Phase and Angle Variables in Quantum Mechanics”. In: *Rev. Mod. Phys.* 40 (2 1968), pp. 411–440.

[45] Daniel F. Walls. “Topics in non linear quantum optics”. PhD thesis. Harvard University, 1969.

[46] Mark Hillery. “An introduction to the quantum theory of nonlinear optics”. In: *Acta Physica Slovaca* 59.1 (2009), pp. 1–80.

[47] David Roland Miran Arvidsson-Shukur et al. “Properties and applications of the Kirkwood–Dirac distribution”. In: *New Journal of Physics* 26 (2024), p. 121201.

[48] Marlan O. Scully and M. Suhail Zubairy. *Quantum Optics*. Cambridge University Press, 1997.

[49] E. Wigner. “On the Quantum Correction For Thermodynamic Equilibrium”. In: *Phys. Rev.* 40 (1932), pp. 749–759.

[50] Paul Adrien Maurice Dirac. “On the analogy between classical and quantum mechanics”. In: *Reviews of Modern Physics* 17.2-3 (1945), pp. 195–199.

[51] Gunnar Björk, Andrei B. Klimov, and Luis L. Sánchez-Soto. “Chapter 7 The discrete Wigner function”. In: ed. by E. Wolf. Vol. 51. Progress in Optics. Elsevier, 2008, pp. 469–516.

[52] Boualem Boashash. “Time-Frequency Signal Analysis and Processing: A Comprehensive Reference”. In: (2003).

[53] David R M Arvidsson-Shukur, Jacob Chevalier Drori, and Nicole Yunger Halpern. "Conditions tighter than noncommutation needed for nonclassicality". In: *Journal of Physics A: Mathematical and Theoretical* 54.28 (2021), p. 284001.

[54] Christian Weedbrook et al. "Gaussian quantum information". In: *Rev. Mod. Phys.* 84 (2 2012), pp. 621–669.

[55] Xanadu. *Decompositions — Stawberry Fields.* Accessed: 2025-07-17. (2020).

[56] Alessandro Ferraro, Stefano Olivares, and Matteo G. A. Paris. *Gaussian States in Quantum Information.* Napoli: Bibliopolis, 2005.

[57] Mark M. Wilde and Kevin Valson Jacob. *PHYS 7895: Gaussian Quantum Information. Lecture 16.* University Lecture. Accessed: 2025-07-17. (2019).

[58] Werner Heisenberg. "Über den anschaulichen Inhalt der quantentheoretischen Kinematik und Mechanik". In: *Zeitschrift für Physik* 43 (1927), pp. 172–198.

[59] H. P. Robertson. "The Uncertainty Principle". In: *Phys. Rev.* 34 (1929), pp. 163–164.

[60] Debashis Sen. "The uncertainty relations in quantum mechanics". In: *Current Science* 107.2 (2014), pp. 203–218.

[61] Paul Busch et al. *Quantum measurement.* Vol. 23. Springer, 2016.

[62] E. Arthurs and J. L. Kelly Jr. "On the Simultaneous Measurement of a Pair of Conjugate Observables". In: *Bell System Technical Journal* 44.4 (1965), pp. 725–729.

[63] A. Einstein, B. Podolsky, and N. Rosen. "Can Quantum-Mechanical Description of Physical Reality Be Considered Complete?" In: *Phys. Rev.* 47 (1935), pp. 777–780.

[64] J. S. Bell. "On the Einstein Podolsky Rosen paradox". In: *Physics Physique Fizika* 1 (1964), pp. 195–200.

[65] J.S. Lundeen and K.J. Resch. "Practical measurement of joint weak values and their connection to the annihilation operator". In: *Physics Letters A* 334.5-6 (2005), pp. 337–344.

[66] Graeme Mitchison, Richard Jozsa, and Sandu Popescu. "Sequential weak measurement". In: *Phys. Rev. A* 76 (2007), p. 062105.

[67] F. Piacentini et al. "Measuring Incompatible Observables by Exploiting Sequential Weak Values". In: *Phys. Rev. Lett.* 117 (2016), p. 170402.

[68] Yosep Kim et al. “Direct quantum process tomography via measuring sequential weak values of incompatible observables”. In: *Nature communications* 9 (2018), p. 192.

[69] Jiang-Shan Chen et al. “Experimental realization of sequential weak measurements of non-commuting Pauli observables”. In: *Opt. Express* 27.5 (2019), pp. 6089–6097.

[70] G M D’Ariano, C Macchiavello, and M F Sacchi. “Joint measurements via quantum cloning”. In: *Journal of Optics B: Quantum and Semiclassical Optics* 3.2 (2001), p. 44.

[71] G. S. Thekkadath et al. “Determining Complementary Properties with Quantum Clones”. In: *Phys. Rev. Lett.* 119 (2017), p. 050405.

[72] Aldo C Martinez-Becerril et al. “Theory and experiment for resource-efficient joint weak-measurement”. In: *Quantum* 5 (2021), p. 599.

[73] Lucien Hardy. “Quantum mechanics, local realistic theories, and Lorentz-invariant realistic theories”. In: *Physical Review Letters* 68.20 (1992), pp. 2981–2984.

[74] Kazuhiro Yokota et al. “Direct observation of Hardy’s paradox by joint weak measurement with an entangled photon pair”. In: *New Journal of Physics* 11 (2009), p. 033011.

[75] J. S. Lundeen and A. M. Steinberg. “Experimental Joint Weak Measurement on a Photon Pair as a Probe of Hardy’s Paradox”. In: *Phys. Rev. Lett.* 102 (2009), p. 020404.

[76] Yakir Aharonov et al. “Quantum Cheshire Cats”. In: *New Journal of Physics* 15 (2013), p. 113015.

[77] Tobias Denkmayr et al. “Observation of a quantum Cheshire Cat in a matter-wave interferometer experiment”. In: *Nature communications* 5 (2014), p. 4492.

[78] Adam Bednorz, Kurt Franke, and Wolfgang Belzig. “Noninvasiveness and time symmetry of weak measurements”. In: *New Journal of Physics* 15 (2013), p. 023043.

[79] D. Curic et al. “Experimental investigation of measurement-induced disturbance and time symmetry in quantum physics”. In: *Phys. Rev. A* 97 (2018), p. 042128.

[80] K. Vogel and H. Risken. “Determination of quasiprobability distributions in terms of probability distributions for the rotated quadrature phase”. In: *Phys. Rev. A* 40 (1989), pp. 2847–2849.

[81] D. T. Smithey et al. “Measurement of the Wigner distribution and the density matrix of a light mode using optical homodyne tomography: Application to squeezed states and the vacuum”. In: *Phys. Rev. Lett.* 70 (1993), pp. 1244–1247.

[82] Gerd Breitenbach, S Schiller, and J Mlynek. “Measurement of the quantum states of squeezed light”. In: *Nature* 387 (1997), pp. 471–475.

[83] G. Mauro D’Ariano, Matteo G.A. Paris, and Massimiliano F. Sacchi. “Quantum Tomography”. In: ed. by Peter W. Hawkes. Vol. 128. Advances in Imaging and Electron Physics. Elsevier, 2003, pp. 205–308.

[84] Jeff Z Salvail et al. “Full characterization of polarization states of light via direct measurement”. In: *Nature Photonics* 7.4 (2013), pp. 316–321.

[85] Charles Bamber and Jeff S. Lundeen. “Observing Dirac’s Classical Phase Space Analog to the Quantum State”. In: *Phys. Rev. Lett.* 112, 070405 (2014).

[86] G. S. Thekkadath et al. “Direct Measurement of the Density Matrix of a Quantum System”. In: *Phys. Rev. Lett.* 117, 120401 (2016).

[87] Brian C Hall. *Lie groups, Lie algebras, and Representations.* 2nd ed. Springer Cham, 2015.

[88] K. F. Riley, M. P. Hobson, and S. J. Bence. *Mathematical Methods for Physics and Engineering: A Comprehensive Guide.* 3rd ed. Cambridge University Press, 2006.

[89] Henry Margenau and Robert Nyden Hill. “Correlation between Measurements in Quantum Theory”. In: *Progress of Theoretical Physics* 26.5 (1961), pp. 722–738.

[90] L. Marrucci, C. Manzo, and D. Paparo. “Optical Spin-to-Orbital Angular Momentum Conversion in Inhomogeneous Anisotropic Media”. In: *Phys. Rev. Lett.* 96 (2006), p. 163905.

[91] Andrea Rubano et al. “Q-plate technology: a progress review [Invited]”. In: *J. Opt. Soc. Am. B* 36.5 (2019), pp. D70–D87.

[92] Yiqian Yang, Andrew Forbes, and Liangcai Cao. “A review of liquid crystal spatial light modulators: devices and applications”. In: *Opto-Electronic Science* 2 (2023), p. 230026.

[93] Mark A. A. Neil et al. “Method for the generation of arbitrary complex vector wave fronts”. In: *Opt. Lett.* 27.21 (2002), pp. 1929–1931.

[94] Christian Maurer et al. “Tailoring of arbitrary optical vector beams”. In: *New Journal of Physics* 9 (2007), p. 78.

[95] Ignacio Moreno et al. “Complete polarization control of light from a liquid crystal spatial light modulator”. In: *Opt. Express* 20.1 (2012), pp. 364–376.

[96] Alicia Sit et al. “General lossless spatial polarization transformations”. In: *Journal of Optics* 19.9 (2017), p. 094003.

[97] Grant M. Miles and Robert F. Limoges. “Manufacture Of Cylindrical Lenses”. In: *Optical Systems in Engineering I*. Ed. by Paul R. Yoder Jr. Vol. 0193. International Society for Optics and Photonics. SPIE, 1979, pp. 268–275.

[98] Rudolf Kingslake. “Chapter 1 - Dispersing Prisms”. In: *Optical Instruments*. Ed. by Rudolf Kingslake. Vol. 5. Applied Optics and Optical Engineering. Elsevier, 1969, pp. 1–16.

[99] Thomas Kluyver et al. “Jupyter Notebooks - a publishing format for reproducible computational workflows”. In: *Positioning and Power in Academic Publishing: Players, Agents and Agendas*. Ed. by Fernando Loizides and Birgit Scmidt. Netherlands: IOS Press, 2016, pp. 87–90.

[100] Python Core Team. *Python: A dynamic, open source programming language*. Python Software Foundation.

[101] Charles R. Harris et al. “Array programming with NumPy”. In: *Nature* 585 (2020), pp. 357–362.

[102] James W. Cooley and John W. Tukey. “An Algorithm for the Machine Calculation of Complex Fourier Series”. In: *Mathematics of Computation* 19 (1965), pp. 297–301.

[103] Siu Kwan Lam, Antoine Pitrou, and Stanley Seibert. “Numba: a LLVM-based Python JIT compiler”. In: LLVM ’15. Austin, Texas: Association for Computing Machinery, 2015.

[104] The joblib developers. *joblib*.

[105] J. D. Hunter. “Matplotlib: A 2D graphics environment”. In: *Computing in Science & Engineering* 9.3 (2007), pp. 90–95.

[106] John Nickolls et al. “Scalable Parallel Programming with CUDA: Is CUDA the parallel programming model that application developers have been waiting for?” In: *Queue* 6.2 (2008), pp. 40–53.

[107] Ryosuke Okuta et al. “CuPy: A NumPy-Compatible Library for NVIDIA GPU Calculations”. In: *Proceedings of Workshop on Machine Learning Systems (LearningSys) in The Thirty-first Annual Conference on Neural Information Processing Systems (NIPS).* 2017.

[108] Mikhail N Polyanskiy. “Refractiveindex. info database of optical constants”. In: *Scientific Data* 11 (2024), p. 94.

[109] R. Paschotta. *Fiber Collimators.* RP Photonics Encyclopedia. Accessed: 2025-04-07. (2013).

[110] Pauli Virtanen et al. “SciPy 1.0: Fundamental Algorithms for Scientific Computing in Python”. In: *Nature Methods* 17 (2020), pp. 261–272.

[111] Amir Feizpour, Xingxing Xing, and Aephraim M Steinberg. “Amplifying single-photon nonlinearity using weak measurements”. In: *Physical review letters* 107 (2011), p. 133603.

[112] Amir Feizpour et al. “Observation of the nonlinear phase shift due to single post-selected photons”. In: *Nature Physics* 11.11 (2015), pp. 905–909.

[113] Shengjun Wu and Marek Żukowski. “Feasible optical weak measurements of complementary observables via a single Hamiltonian”. In: *Physical Review Letters* 108 (2012), p. 080403.

[114] B Yurke. “Optical back-action-evading amplifiers”. In: *Journal of the Optical Society of America B* 2.5 (1985), pp. 732–738.

[115] Samuel L. Braunstein. “Squeezing as an irreducible resource”. In: *Phys. Rev. A* 71 (5 2005), p. 055801.

[116] S M Barnett and D T Pegg. “Phase in quantum optics”. In: *Journal of Physics A: Mathematical and General* 19, 3849.18 (1986).

[117] Bertúlio de Lima Bernardo. “Photon statistics as a probe for weak measurements”. In: *Journal of the Optical Society of America B* 31.7 (2014), pp. 1494–1498.

[118] Markus Aspelmeyer, Tobias J. Kippenberg, and Florian Marquardt. “Cavity optomechanics”. In: *Rev. Mod. Phys.* 86 (2014), pp. 1391–1452.

[119] A La Porta, RE Slusher, and B Yurke. “Back-action evading measurements of an optical field using parametric down conversion”. In: *Physical review letters* 62.1 (1989), p. 28.

[120] D. I. Salykina et al. *Quantum non-demolition measurement of optical quadratures using quadratic nonlinearity.* (2025). arXiv: `2507.15508`.

[121] Jonatan Bohr Brask. *Gaussian states and operations – a quick reference.* (2022). arXiv: `2102.05748 [quant-ph]`.

[122] Richard A. Campos, Bahaa E. A. Saleh, and Malvin C. Teich. "Quantum-mechanical lossless beam splitter: SU(2) symmetry and photon statistics". In: *Phys. Rev. A* 40 (3 1989), pp. 1371–1384.

[123] Hsuan-Hao Lu et al. "Electro-Optic Frequency Beam Splitters and Tritters for High-Fidelity Photonic Quantum Information Processing". In: *Phys. Rev. Lett.* 120 (3 2018), p. 030502.

[124] Kao-Fang Chang et al. "Low-loss high-fidelity frequency beam splitter with tunable split ratio based on electromagnetically induced transparency". In: *Phys. Rev. Res.* 3 (1 2021), p. 013096.

[125] G Mayer and F Gires. "Action of an intense light beam on the refractive index of liquids". In: *Comptes Rendus* 258 (1964), pp. 2039–2042.

[126] M. A. Duguay and J. W. Hansen. "AN ULTRAFAST LIGHT GATE". In: *Applied Physics Letters* 15.6 (1969), pp. 192–194.

[127] Qi Wu and X-C Zhang. "Free-space electro-optic sampling of terahertz beams". In: *Applied Physics Letters* 67 (1995), pp. 3523–3525.

[128] A. Leitenstorfer et al. "Detectors and sources for ultrabroadband electro-optic sampling: Experiment and theory". In: *Applied Physics Letters* 74 (1999), pp. 1516–1518.

[129] Kai Liu, Jingzhou Xu, and X.-C. Zhang. "GaSe crystals for broadband terahertz wave detection". In: *Applied Physics Letters* 85 (2004), pp. 863–865.

[130] Sabine Keiber et al. "Electro-optic sampling of near-infrared waveforms". In: *Nature Photonics* 10 (2016), pp. 159–162.

[131] Todd Brun. *EE520: Introduction to Quantum Information Processing. Lecture 8.* University Lecture. Accessed: 2025-04-25. (2017).

[132] H. M. Wiseman and G. J. Milburn. "Quantum theory of field-quadrature measurements". In: *Phys. Rev. A* 47 (1993), pp. 642–662.

[133] Ryotatsu Yanagimoto et al. "Quantum Nondemolition Measurements with Optical Parametric Amplifiers for Ultrafast Universal Quantum Information Processing". In: *PRX Quantum* 4 (1 2023), p. 010333.

[134] Jing Yang. "Theory of Compression Channels for Postselected Quantum Metrology". In: *Phys. Rev. Lett.* 132 (2024), p. 250802.

[135] David RM Arvidsson-Shukur et al. "Quantum advantage in postselected metrology". In: *Nature communications* 11 (2020), p. 3775.

[136] Han-Sen Zhong et al. "Quantum computational advantage using photons". In: *Science* 370.6523 (2020), pp. 1460–1463.

[137] Elizabeth Gibney. "This billion-dollar firm plans to build giant quantum computers from light. Can it succeed?" In: *Nature* 635 (2024), pp. 800–803.

[138] H Aghaee Rad et al. "Scaling and networking a modular photonic quantum computer". In: *Nature* (2025), pp. 912–919.

[139] Emanuel Knill, Raymond Laflamme, and Gerald J Milburn. "A scheme for efficient quantum computation with linear optics". In: *Nature* 409 (2001), pp. 46–52.

[140] Isaac L. Chuang and M. A. Nielsen and. "Prescription for experimental determination of the dynamics of a quantum black box". In: *Journal of Modern Optics* 44.11-12 (1997), pp. 2455–2467.

[141] Muhammad Hamza Waseem, Faizan-e-Ilahi, and Muhammad Sabieh Anwar. "Quantum state tomography". In: *Quantum Mechanics in the Single Photon Laboratory*. 2053-2563. IOP Publishing, 2020. Chap. 6.

[142] Beth Schaefer et al. "Measuring the Stokes polarization parameters". In: *American Journal of Physics* 75.2 (2007), pp. 163–168.

[143] Sarah Jane Laframboise et al. "Analysis of financial challenges faced by graduate students in Canada". In: *Biochemistry and Cell Biology* 101.4 (2023), pp. 326–360.

[144] Canadian Science Publishing. *Most Read Articles – Biochemistry and Cell Biology*. `https://cdnsciencepub.com/journal/bcb#pane-mostread01`. Accessed: 2025-04-24.

[145] Canadian Science Publishing. *The runner-up in our Top Articles of 2023*. `https://x.com/cdnsciencepub/status/1741474780656587016`. Posted on December 31, 2023. Accessed: 2025-04-24.

[146] House of Commons Standing Committee on Science and Research. *Government of Canada's Graduate Scholarship and Post-Doctoral Fellowship Programs*. 8th Report, 44th Parliament, 1st Session. (2023).

[147] Department of Finance Canada. *Budget 2024: Fairness for Every Generation*. (2024).

[148] Vincent Larivière. “On the shoulders of students? The contribution of PhD students to the advancement of knowledge”. In: *Scientometrics* 90.2 (2012), pp. 463–481.

[149] Science & Policy Exchange. *Rethinking federal research funding: towards more equitable funding for Canada’s next generation.* Accessed: 2023-01-07. (2020).

[150] Statistics Canada. *COVID-19 Pandemic: Financial impacts on postsecondary students in Canada.* (2020).

[151] Toronto Science Policy Network. *The early impacts of COVID-19 on graduate students across Canada.* Accessed: 2023-01-08. (2020).

[152] S. Scherer and F. Smith. *Canada annual inflation gallops to near 40-year high of 7.7% in May.* Accessed: 2023-01-07. (2022).

[153] C. Chen. *Canadian rent report.* Accessed: 2023-01-07. (2022).

[154] Statistics Canada. *Postsecondary graduates, by province of study and level of study.* Accessed: 2023-01-08. (2019).

[155] Financial Consumer Agency of Canada. *Setting up an emergency fund.* Accessed: 2023-01-05. (2022).

[156] Employment and Social Development Canada. *Federal minimum wage of $15 per hour to come into effect on December 29, 2021.* Accessed: 2025-04-28. (2021).

[157] Statistics Canada. *Market Basket Measure (MBM) thresholds for economic families and persons not in economic families, 2020.* Accessed: 2025-04-28. (2022).

[158] Government of Canada. *Dimensions: equity, diversity and inclusion Canada.* Accessed: 2023-01-05. (2019).

[159] Sivani Baskaran et al. “Improving the accessibility of Federal Graduate Research Awards in Canada”. In: *J. Sci. Policy Governance* 18.04 (2021).

[160] Statistics Canada. *Survey of Postsecondary Faculty and Researchers, 2019.* Accessed: 2023-01-08. (2020).

[161] Statistics Canada. *Proportion of Canadian and international student enrolments, by International Standard Classification of Education.* Accessed: 2023-01-08. (2022).

[162] Immigration, Refugees and Citizenship Canada. *International students to help address Canada’s labour shortage.* Accessed: 2023-01-05. (2022).

[163] Andrew J. Fraass et al. “Canadian natural science graduate stipends lie below the poverty line”. In: *PLoS One* 20.5 (2025), e0313972.

[164] M. L. Gaynor and R. M. Rautsaw. *Biology Ph.D. Stipends.* (2022).

[165] Government of Canada, Natural Sciences & Engineering Research Council of Canada. *NSERC - Inter-agency, Tri-agency Financial Administration, Tri-agency Guide on Financial Administration.* (2019).

[166] Government of Canada, Natural Sciences & Engineering Research Council of Canada. *Discovery Grants (individual) program.* (2016).

[167] G. S. Patience and B. A. Patience. “NSERC discovery grants and a tribute to Leo A. Behie”. In: *Can. J. Chem. Eng.* 99 (2021), pp. 2282–2293.

[168] R Core Team. *R: A Language and Environment for Statistical Computing.* Vienna, Austria, (2021).

[169] Government of Canada and Statistics Canada. *Census of Population, 2021 – Table 2.2 Market Basket Measure (MBM) thresholds for economic families and persons not in economic families, 2020.* (2021).

[170] C. Woolston. “PhD students face cash crisis with wages that don’t cover living costs”. In: *Nature* 605 (2022), pp. 775–777.

[171] K. Langin. *Ph.D. students demand wage increases amid rising cost of living.* (2022).

[172] M. Kirchner and J. Petzoldt. “Entomology graduate stipends fail to cover necessities”. In: *Am. Entomol.* 68 (2022), pp. 22–23.

[173] Douglas Bates et al. “Fitting linear mixed-effects models using lme4”. In: *Journal of statistical software* 67 (2015), pp. 1–48.

[174] M. A. Cadena and et al. “Insights and strategies for improving equity in graduate school admissions”. In: *Cell* 186 (2023), pp. 3529–3547.

[175] K. Rembrand, S. Samila, and J. Ferguson. “Who do we invent for? Patents by women focus more on women’s health, but few women get to invent”. In: *Science* 372 (2021), pp. 1345–1348.

[176] Fabian Rohden, Thomas Bailey, and Sarah Laframboise. “20 years of choices: a fight for increased funding for graduate students”. In: *Biochemistry and Cell Biology* 102.5 (2024), pp. 346–350.

[177] A. N. Osiecka et al. “Being ECR in marine science: Results of a survey among early-career marine scientists and conservationists”. In: *Front. Mar. Sci.* 9 (2022), p. 835692.

[178] Thomas Bailey et al. *International Mobility of Canadian Graduate Students: An Investigation into Brain Drain*. Ottawa Science Policy Network. (2024).